USC-SIPI REPORT #365

Nanotubes for Noisy Signal Processing

by

Ian YenYin Lee

May 2005

Signal and Image Processing Institute
UNIVERSITY OF SOUTHERN CALIFORNIA
Viterbi School of Engineering
Department of Electrical Engineering-Systems
3740 McClintock Avenue, Suite 400
Los Angeles, CA 90089-2564 U.S.A.

Dedication

to my Family

Contents

List of Figures

List of Tables

Abstract

Nanotubes can process noisy signals. We present two central results in support of this general thesis and make an informed extrapolation that uses nanotubes to improve body armor.

The first result is that noise can help nanotubes detect weak signals. The finding confirmed a stochastic-resonance theoretical prediction that noise can enhance detection at the nano-level. Laboratory experiments with nanotubes showed that three types of noise improved three measures of detection.

Small amounts of Gaussian, uniform, and Cauchy additive white noise increased mutual-information, cross-correlation, and bit-error-rate measures before degrading them with further increases in noise. Nanotubes can apply this noise-enhancement and nanotube electrical and mechanical properties to improve signal processing. Similar noise-enhancement may benefit a proposed nanotube-array cochlear-model spectral processing.

The second result is that nanotube antennas can directly detect narrowband electromagnetic (EM) signals. The finding showed that nanotube and thin-wire dipoles are similar: They are resonant and narrowband and can implement linear-array designs if the EM waves in the nanotubes propagate at or near the free-space velocity of light.

The nanotube-antenna prediction is based on a Fresnel-zone or near-zone analysis of antenna impedance using a quantum-conductor model. The analysis also predicts a

failure to resonate if the nanotube EM-wave propagation is much slower than free-space light propagation.

We extrapolate based on applied and theoretical analysis of body armor. Field experiments used a baseball comparison and statistical and other techniques to model body-armor bruising effects. A baseball comparison showed that a large caliber handgun bullet can hit an armored chest as hard as a fast baseball can hit a bare chest. Adaptive fuzzy systems learned to predict a bruise profile directly from the experimental data and also from statistical analysis of the data. Nanotube signal processing should help disguise armor by adapting camouflage to match changing backgrounds while nanotube additives should strengthen armor materials.

Chapter 1

Introduction

Nanotubes can process noisy signals in a variety of contexts. We present two key results in support of this general thesis and propose a related research direction that uses nanotubes to improve body armor.

The first result is an empirical finding based on laboratory experiments with carbon nanotubes. It showed that electrical noise can help carbon nanotubes detect subthreshold pulse-train signals. Similar noise enhancement may benefit a proposed nanotube-array architecture for cochlear spectral processing.

The second result is a theoretical finding based on *near*-field analysis of nanotube antennas. The antennas detect narrowband electromagnetic (EM) signals. The finding showed that nanotubes can act as narrowband resonant antennas that are similar to thin-wire dipoles if the EM waves in the nanotube antenna propagate at or near the free-space velocity of light.

The proposed research direction arose from applied and theoretical analysis of body armor. Field experiments used statistical and other techniques to model body-armor bruising effects. Nanotube signal processing should help armor camouflage adapt to changing circumstances just as nanotube additives should strengthen armor materials.

1.1 Noise Can Help Nanotubes Detect Signals

A singlewall-nanotube transistor exhibited noise-enhanced signal detection. Our experiments found that small amounts of electrical noise can help a nanotube transistor

detect subthreshold pulse-train voltage signals. This observation confirms a stochastic-resonance (SR) theoretical prediction that a threshold exhibits SR [254].

The experiments interpreted the nanotube transistor (such as in [492]) as a threshold detector. The detector had a threshold-like input-output characteristic in Figure 1.1(a): It produced little current for subthreshold input voltages that fed its gate. The figure also shows that additive noise helped the subthreshold input voltages generate larger currents.

Figure 1.1(b) presents a sample of the nanotube-SR findings. Three measures of nanotube-detector performance showed the SR effect: Shannon's mutual information $I(X,Y)$ [427], a normalized correlation measure $C(X,Y)$ [87] [88], and an inverted bit error rate (1−BER) compared the input and output discrete-time random sequences.

Three types of synchronized white noise corrupted the subthreshold Bernoulli sequences that fed the detector. The Gaussian, the uniform, and the impulsive Cauchy [254] noise combined with the random input voltage sequences to help the detector produce random output current sequences.

The experiments applied different Bernoulli input sequences that used different combinations of subthreshold gate voltages as their ON/OFF symbols. *Synchronized* Gaussian, uniform, and infinite-variance Cauchy noise added to the input sequences and produced the SR effect: They helped the nanotube transistor detect the subthreshold input.

Figure 1.1(b) shows the nonmonotonic signature of SR for white Gaussian noise. The modes of the three SR curves occurred for nonzero noise strength with a standard deviation of at least 0.01. The three SR curves correlated with each other and the correlation coefficients were $R = 0.9830$ for the information and the correlation curves, $R = 0.9774$ for the information and the bit-error-rate curves, and $R = 0.9877$ for the correlation and the bit-error-rate curves with p-value< 0.001 for each. We observed

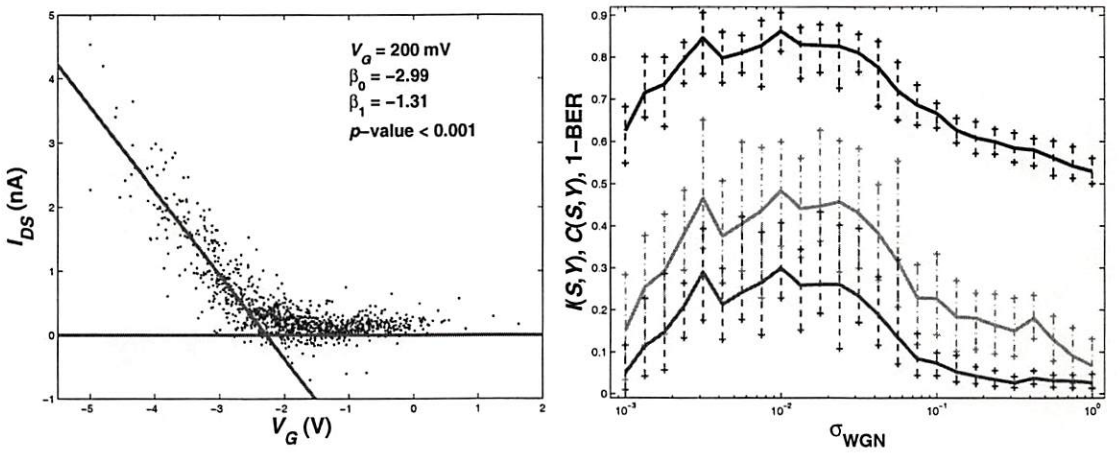

(a) Threshold Detector (b) Nanotube SR

Figure 1.1: Noise enhances the performance of a nanotube detector. (a) The stochastic I-V_G curve shows a threshold-like gate effect of the p-type nanotube detector. (b) Experiments gave the nonmonotonic stochastic-resonance signature for additive white Gaussian noise.

the nanotube SR-effect despite the nanotube instabilities that caused fluctuations in the stochastic I-V_G curve in Figure 1.1(a).

The noise-enhanced detection at the nanolevel can have applications in signal processing because circuits and sensors can exhibit SR. Researchers have reported an example of noise-enhanced signal processing: Bartz et al. demonstrated an SR-effect in analog-to-digital converters [40]. Researchers have reported SR-effects in electrical systems that include Chua's circuit [18], [17], comparators [178], coupled diode resonators [291], tunnel diodes [311] [310], Schmitt triggers [323], superconducting quantum interference devices (SQUIDs) [401] [470] [204], and Josephson junctions [205] [59]. Other researchers have found that noise helps mammalian cochleae [224] and cochlear implants [339] detect faint sounds.

Nanotubes can also enhance signal processing by improving transistor circuits. Researchers have reported that nanotube transistors can be better than silicon transistors. Nanotube transistors can be small and so can increase device density: Rochefort et al.

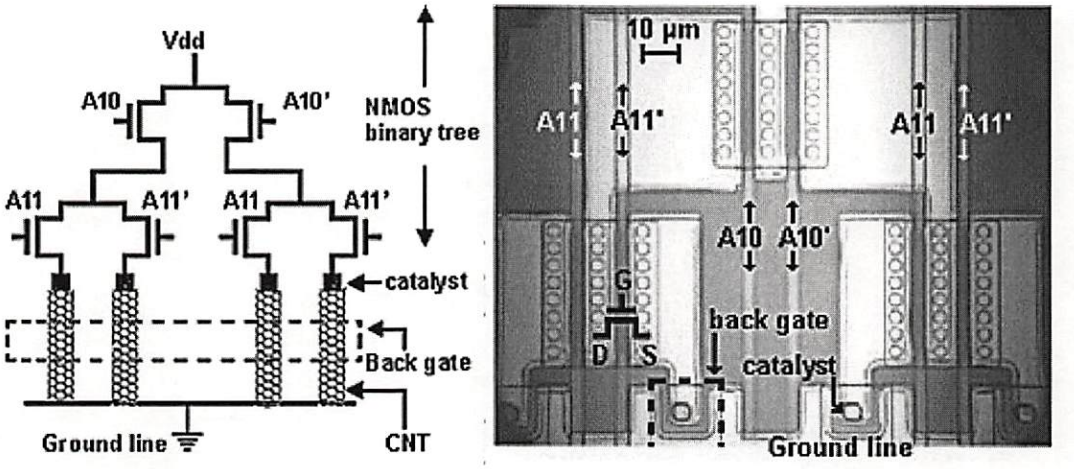

(a) (b)

Figure 1.2: Carbon nanotube and silicon transistors are compatible. (a) Circuit schematic of the nanotube decoder in [444]. The back gate modulates the conductance of the CNTs. (b) Optical micrograph of part of the circuit that corresponds to the schematic in (a). Images courtesy of Tseng et al., [444].

predicted that nanotube transistors can have nanometer-size channel length [398]. And singlewall nanotubes have nanometer-size diameters [386] [431].

Nanotube transistors can operate at high speeds. Dürkop et al. measured higher carrier mobility that suggests faster switching speeds in nanotubes than in silicon [132]. Burke et al. predicted that nanotube transistors can operate at GHz to THz speeds [67].

Nanotube transistors have high gain [27] and can resist break down. Wei et al. observed that multiwall nanotubes had high break-down currents and so had large current densities [463].

Nanotubes are compatible with silicon and electromechanical technologies. Tseng et al. integrated nanotubes with silicon transistors [444] (see Figure 1.2) and demonstrated that nanotube transistors are compatible with silicon transistors. Sazonova et al. produced a nanotube electromechanical oscillator based on a suspended-nanotube transistor architecture [410] and demonstrated that nanotube electronic circuits are compatible with electromechanical devices.

Nanotube-enhanced transistors should improve both analog and digital signal-processing circuits. Nanotube transistors can improve logic gates [31] [114] [228] [317] and so make digital signal processing faster [67], smaller [398] [386] [431], and tougher [27] [463]. Nanotube transistors can improve multipliers and amplifiers and so make analog signal processing more sensitive (large current gain [27]).

1.2 Nanotube Antennas Can Directly Detect EM Signals

Nanotubes can directly detect electromagnetic (EM) signals because they can act as narrowband resonant dipole antennas. Nanotube impedance resembles thin-wire dipole impedance if the EM waves in the nanotube dipoles propagate at or near the free-space velocity of light. So nanotube antennas are resonant and narrowband. The nanotube-antenna prediction is based on a mathematical analysis of nanotube-antenna impedance.

The nanotube-antenna analysis estimates the induced Fresnel-zone (or near-zone) electric field due to a current distribution in the nanotube antenna. A key modification of the induced electromagnetic field (EMF) method alters the assumed current distribution and replaces a single parameter $k_p \neq k_0$ that summarizes the change from a perfect-conductor model to a quantum-conductor model. The analysis applies to quantum conductors in general and so the prediction can apply to single-crystal metallic nanowires [478].

Nanotube dipoles have thin-wire-like resonant length and radiation resistance for small quantum-induced changes in EM-wave propagation. Figure 1.3 plots nanotube self impedance versus normalized nanotube length and compares the perfect-conductor case $k_p = k_0$ and a limited quantum-conductor case $k_p \approx k_0$. Nanotube dipoles can have a fundamental resonant length that is approximately half free-space wavelength $l \approx \lambda/2$ for small changes in the velocity of EM-wave propagation $k_p \approx k_0$. The estimated

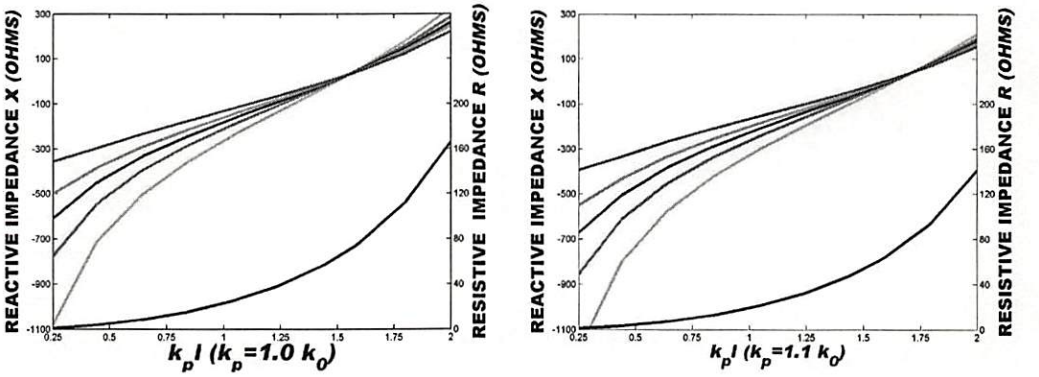

(a) $k_p = k_0$ (b) $k_p \approx k_0$

Figure 1.3: Similarity between nanotube and thin-wire dipole impedance for $k_p \approx k_0$. The figures plot the real and imaginary parts of impedance versus a normalized dipole length $k_p l$. (a) $k_p = k_0$ corresponds to the perfect-conductor case. (b) $k_p = 1.1 \cdot k_0$ corresponds to a weak quantum-conductor case. The top five color curves are nanotube input reactance for five different dipole diameters as a function of compressed wavelength. The five diameters a/λ_p are 0.009525 (red), 0.006350 (green), 0.004763 (blue), 0.003175 (magenta), and 0.001588 (cyan) from top to bottom. The bottom-most black curve is the nanotube input reactance.

nanotube impedance has zero reactance (or imaginary part of impedance) so that the dipole resonates [382] for approximately half-wave dipole lengths.

Resonant nanotube dipoles can have narrower bandwidths than thin-wire dipoles due to smaller diameter-to-length ratios. Nanotubes have smaller ratios because they are nanometers in diameter [431] and can be many micrometers [492] to millimeters [212] in length.

The estimated impedance has resistance (or real part of impedance) that resembles free-space resistance for the fundamental resonant-dipole length. So nanotube dipoles have thin-wire like radiation efficiency for $k_p \approx k_0$.

Nanotube dipoles can fail to resonate for large changes in the velocity of EM wave propagation $k_p >> k_0$. Figure 1.4(a) plots nanotube reactance as a function of normalized dipole length for $k_p = 1.45 \cdot k_0$. The estimated nanotube reactance

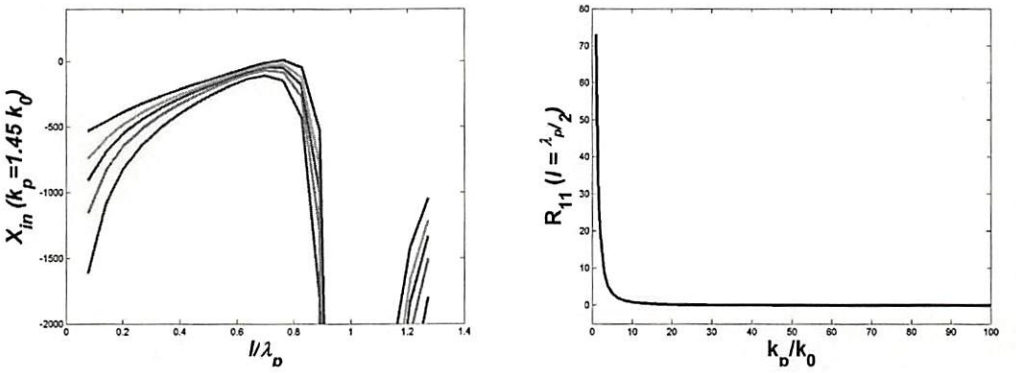

(a) No Resonance for $k_p = 1.45 \cdot k_0$ (b) Radiation Resistance

Figure 1.4: Nanotube antenna input impedance for $k_p >> k_0$. (a) Nanotube reactance is all negative and so the nanotube antenna does not resonate for larger k_p. (b) Nanotube input resistance falls rapidly with increasing k_p. The input resistance is the nanotube radiation resistance for the lossless case.

becomes more negative with small increases in k_p (Figure 1.3) and eventually becomes all negative (Figure 1.4(a)). Nanotube dipoles do not resonate for $k_p >> k_0$ due to nonzero estimated reactance.

Figure 1.4(b) plots nanotube resonant resistance as a function of k_p. The radiation resistance falls rapidly as k_p increases. Nanotube dipoles can become very inefficient for large k_p because the estimated resistance becomes many orders of magnitude smaller than free-space resistance.

Nanotube antennas can be an attractive design choice for small changes in EM-wave propagation. Multiwall nanotube and single-crystal nanowire antennas can be better than nanometer-size thin wires because poly-crystal metal wires can have high intrinsic resistive-losses and act as poor antennas: Oxidation [335], heating and electromigration [201] [446], and grain-boundary effects [46] can reduce conductivity for nm-diameter poly-crystal metal wires. The nanotube (or nanowire) antennas are also better than poly-crystal wires because they can interface with nanotube (or nanowire) circuits without high-impedance junctions.

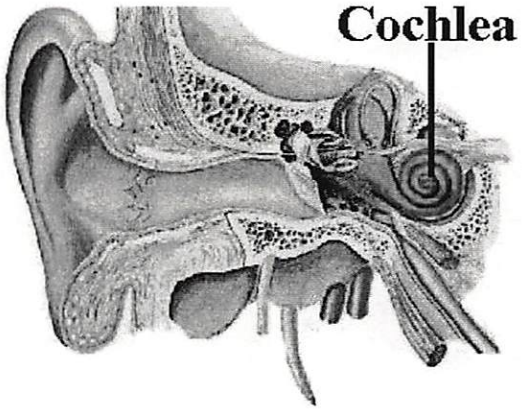

Figure 1.5: The human cochlea in the inner ear. Image courtesy of Alec N. Salt [406].

A proposed nanotube cochlear-model architecture samples a signal's spectra with nanotube antennas and processes the signal with nanotube circuits. Mammalian cochlea separates an input acoustic signal into overlapping frequency bands and samples the frequency spectrum of the acoustic signal for transduction into electrical nerve impulses [12]. The cochlea spatially isolates and filters each frequency component of a signal [453].

The proposed nanotube cochlear-model architecture uses a bank of nanotube antennas to sample a signal's spectrum and uses nanotube circuits to filter the sampled spectrum in the frequency domain. The proposed spectral-processing architecture can implement signal processing techniques that require an estimate of a signal's spectrum or its autocorrelation. The cochlear-model architecture is an example of how nanotube antennas and circuits can benefit signal processing.

The proposed architecture may also benefit from noise-enhanced detection. This expectation is an informed extrapolation. The proposed architecture uses nanotube antennas and transistors for signal processing. Our SR experiments on nanotubes show that noise-enhancement can benefit nanotube detectors. Noise may also help nanotube-array antennas detect faint signals. And mammalian cochleae [224] and cochlear

implants [339] use noise to detect faint sounds. So noise should enhance the proposed nanotube cochlear-model architecture.

1.3 Nanotubes Can Enhance Body-Armor Stealth and Strength

Nanotube signal processing should help armor adapt camouflage and nanotube additives should strengthen armor materials. Adaptive camouflage enhances armor performance by improving disguise. Nanotube signal processing should improve armor stealth by changing camouflage brightness, color, and pattern to match changing background conditions.

Stronger armor materials enhance armor performance by resisting bullet impacts and reducing physiological costs such as bruising. Nanotube additives can increase breaking strength of fibers and increase toughness of ceramics. Other nano-additives can program and increase armor stiffness and include silica-nanoparticle shear-thickening fluids and iron-nanoparticle magneto-rheologic fluids. The nano-enhanced materials can reduce bullet-armor deformations that can bruise the underlying tissue.

Handgun experiments tested soft body armor and modeled body-armor bruising effects. We modeled the bruising effects with a baseball comparison, statistical analysis, and adaptive fuzzy systems. The Appendix contains a detailed report of the field experiments. The modeling techniques can also apply to nano-enhanced armor.

Nanotubes can adapt camouflage patterns on a nano-strengthened body armor to increase its stealth. A proposed adaptive camouflage models octopus species such as *Octopus vulgaris* and uses nanotubes to coordinate artificial color organs. Nanotube signal processing can speed up [132] and optimize the camouflage adaptation that matches a background. Nanotube-enhanced optical detector arrays can have a higher

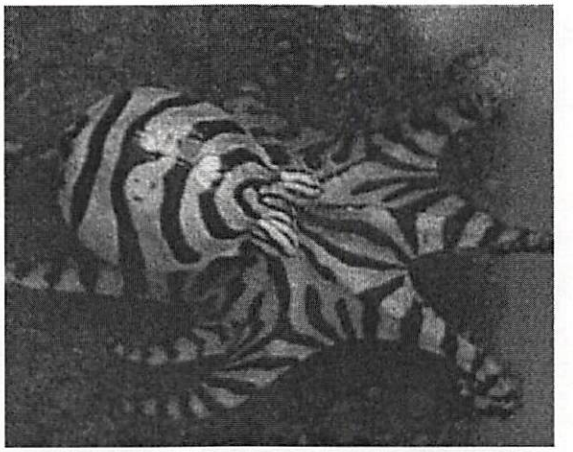

Figure 1.6: An octopus displays disruptive camouflage. Photo courtesy of John B. Messenger [325].

sensitivity [484] and a smaller size [398] and so can sample the background with a higher resolution.

The artificial color organs model octopus chromatomotor fields [325]. A chromatomotor cell can selectively display its color by stretching and contracting pigment sacs. Large arrays of chromatomotor cells form a chromatomotor field that can display different colors or reflect ambient light. The coordinated display can match background colors, patterns, and brightness.

The artificial color organs can model the chromatomotor fields with semiconductor quantum dots, retro-reflectors, and electromechanical actuators. The quantum dots can be better pigments because they are brighter than chemical dyes and resist breakdown [385]. Retro-reflectors are brighter than untreated reflectors because micro-size beads returns incident light rays to their source [393]. And electromechanical actuators [192] can shutter the artificial pigments and retro-reflectors to program color and reflectivity.

Nanotubes can improve body-armor performance by strengthening polymer fibers [264] [6] and ceramic plates [371] [428] [482] [481] [489] in body armor. Researchers have demonstrated that nanotube additives strengthen Zylon fibers [264] that are already

stronger than Kevlar fibers and that nanotube additives toughen alumina ceramics [428] [489]. Other nanomaterials can also strengthen armor.

Nanoparticle rheologic materials can enhance body armor. They can make body armor programmable and adaptive to optimize armor performance. Lee et al. have shown that silica nanoparticles in a shear thickening fluid (STF) help Kevlar fabric stiffen on impact [272]. The STF-treated armor is adaptive and allows less armor deformation with less armor materials [272].

Deshmukh et al. have predicted that iron nanoparticles in a magneto-rheologic (MR) fluid can stiffen fabric in a magnetic field [231] [116]. The MR-treated armor can have programmable toughness. The armor can remain flexible until an applied magnetic field stiffens it.

Field experiments evaluated body-armor bruising effects. Impact experiments on Kevlar fabric and gelatin blocks used a bruise profile to measure body armor performance in terms of a physiological cost. Handguns shot different caliber bullets at Kevlar-clad ordnance gelatin blocks. A bruise profile models a bullet's bruising effects based on the deformation in the Kevlar fabric against a gelatin backing material that simulates tissue.

We modeled the bruising effects with a baseball comparison and with statistical and fuzzy techniques. The analysis techniques can also evaluate nano-enhanced armor that can reduce a bullet's bruising effects. The baseball comparison found that a .45 caliber handgun bullet hits an armored chest as hard as a 90 MPH baseball hits a bare chest. And a .22 caliber bullet can hit an armored chest as hard as a 40 MPH baseball can hit a bare chest.

Statistical analysis of the experimental data found that armor deformation correlated with bullet weight, momentum, and kinetic energy. Deformation correlated the least with kinetic energy and did not correlate with bullet speed for experiments that varied

both bullet weight and speed. The experimental data also tuned adaptive fuzzy systems that can predict bruise profiles for bullets.

The organization of the remaining chapters is as follows: Chapter 2 reviews the electronic and mechanical properties of nanotubes and their effects in nonlinear devices.

Chapter 3 presents the first key result that noise helps nanotubes detect weak voltage signals. Section 3.1 discusses how nanotubes can enhance analog and digital signal processing. And Section 3.2 reports the results of nanotube SR experiments. Noise enhances nanotube detection at the nano-level.

Chapter 4 presents the second key result that nanotube dipole antennas resemble thin-wire dipoles and can directly detect electromagnetic signals. Section 4.1 presents an impedance estimate for nanotube antennas. And Section 4.2 proposes an architecture that uses nanotube antennas in a cochlear-model signal processing.

Chapter 5 presents the proposed research direction for nanotube-enhanced armor. Section 5.1 discusses how nanotubes and nanoparticles can enhance body armor. Section 5.2 summarizes the results of handgun bullet-armor experiments. We evaluated armor performance with a bruise profile. The Appendix contains the detailed report. And Section 5.3 proposes an octopus-model adaptive camouflage that applies nanomaterials to disguise armor.

Chapter 6 discusses some future work.

Chapter 2

Nanotubes for Nonlinear Devices

Nanotube-based nonlinear devices can be compact, fast, and sensitive because nanotubes are strong, stable, and uniquely conductive. Researchers have demonstrated that nanotube transistors can have a large current density, a high gain, and a high carrier mobility. Prototype nanotube sensors have demonstrated high sensitivity and detection of electromagnetic and acoustic signals as well as different chemicals. This chapter reviews the mechanical and electronic properties of carbon nanotubes and how researchers have applied nanotubes to enhance transistors, sensors, antennas, and single-electron transistors.

2.1 Nanotube Materials and Electronic Properties

Carbon nanotubes have a unique combination of materials properties due to its size, shape, and carbon bonds. A carbon nanotube is a cylindrical molecular carbon that is narrow and long. Singlewall nanotubes can be 0.4 nanometers (nm) to 2 nm in diameter [431], [386] and many millimeters in length [212]. Researchers reported the first multiwall carbon nanotubes (MWNT) in 1991 [220] and observed singlewall carbon nanotubes (SWNT) within two years [219]. Other researchers reported that arc-discharge grown nanotubes are crystallization of liquid or glass-phase carbon [110].

Singlewall carbon nanotubes have good mechanical and electrical properties due to their shapes and their sp^2 carbon-carbon bonds [92] (see Figure 2.1). The carbon atoms form hexagons along the length of a perfect nanotube and form both hexagons and

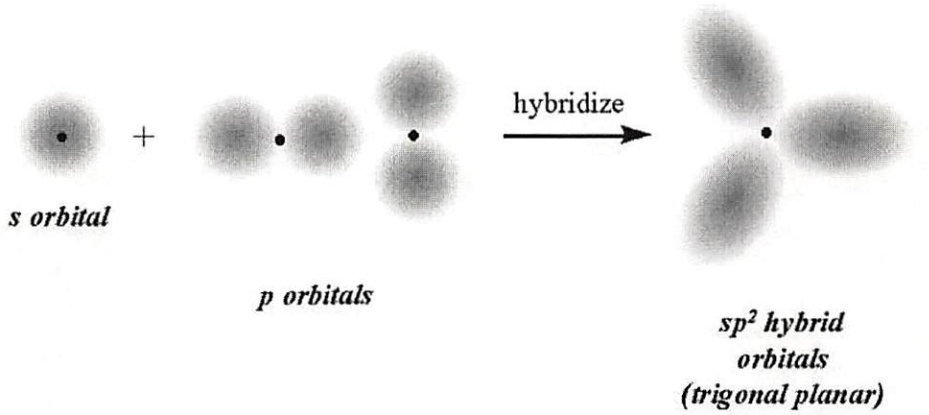

Figure 2.1: The sp^2 hybrid orbitals that form covalent bonds. Each carbon atom uses three of its four available electrons (one s and two p orbitals) to form three sp^2 hybrid orbitals that are coplanar and 120° apart. M. Blaber 1996 [47]

pentagons on the hemispherical end caps (similar to Bucky balls). The hexagons have ring currents in the graphene structure and can interact with electric and magnetic fields. Perfect nanotubes are chemically non-reactive because all chemical bonds of the carbon atoms are satisfied in the graphene structure. The hollow cylinders have a low density of 1.33 to 1.40 grams per cubic centimeter. This and the carbon bonds give nanotubes large strength-to-weight ratios.

The sp^2 carbon-carbon covalent bonds give high mechanical and thermal stability and resistance to electromigration [27] or degradation from electric currents that displace atoms and often break fine metal lines in integrated circuits. Nanotubes are thermally stable up to 2800 degrees Celsius in vacuum and up to 750 °C in air, have tensile strength of up to 45 billion pascals and Young's modulus about ten times higher than that of steel ($\geq$ 1 TPa) [486], and are resilient–nanotubes can bend and restraighten without damage [286]. Nanotubes transmit heat at greater than 3,000 watts per Kelvin per meter (W/K m) at room temperature [246] and can transmit at a predicted 6,600 W/K m at room temperature [440].

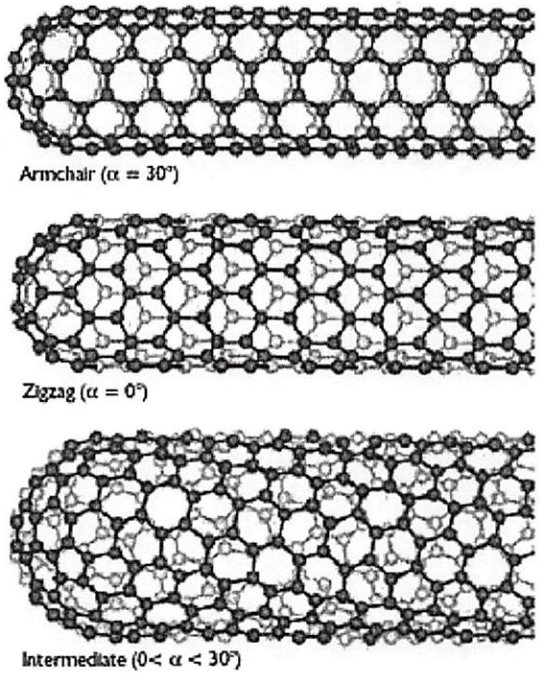

Figure 2.2: Carbon-atom model of singlewall carbon nanotubes. Singlewall carbon nanotubes exist in a variety of structures corresponding to the many ways a sheet of graphite can be wrapped into a seamless tube. Each structure has a specific diameter and chiral (or wrapping) angle α. The armchair structures ($\alpha = 30°$) have metallic character. The zigzag tubes ($\alpha = 0°$) can be either semimetallic or semiconducting. Nanotubes with chiral angles $\alpha \in [0°, 30°]$ include both semimetals and semiconductors. From Weisman 2004 [465].

Nanotube additives strengthen polymer and ceramic composites by adding small weight percentages of MWNT [134], [482], [489]. Researchers estimate that nanotubes are 40–50 times stronger than steel wires for a given weight [486]. Some lab-made nanotube-polymer fibers have tensile strength of 1.8 gigapascals (GPa) that matches spider silk, Young's modulus of 80 GPa, and breaking-energy of 570 joules per gram (J/g) [104] [105]. The fiber's breaking energy is much greater than that for spider dragline silk (165 J/g), Kevlar fibers (33 J/g), and graphite (12 J/g). The nanotube fiber's Young's modulus is twice that of steel wire after normalizing for density and twenty times tougher than steel wires. [104]. Pure singlewall carbon nanotube fibers [150]

have a Young's modulus of 120 $\pm$ 10 GPa and a tensile strength of 116 $\pm$ 10 MPa. In comparison, laboratory-grade PBO or Zylon fibers possess a Young's modulus of 138 GPa and a tensile strength of 2.6 GPa.

The electrical resistivity of the pure SWNT fibers is around $\rho = 0.2$ milliohm cm (mΩ cm), with an order of magnitude increase upon high-temperature annealing [150]. The thermal conductivity of ether-coagulated fibers is 21 W/Km [150].

A SWNT is structurally similar to a rolled-up sheet of graphite and can conduct electricity as a metal or a semiconductor based on its chiral angle or the angle that the cylindrical axis makes with the graphene lattice [125]. The electronic structure of a single graphite layer or graphene sheet gives nanotubes their electrical properties [120], [320], [111], [92], [125], [330]. A single sheet of graphite is a semiconductor with a zero bandgap [27] despite having valence (π) and conduction (π*) states that intersect the Fermi level. This is because the two-dimensional structure results in a vanishing density of states when integrating over the Fermi surface.

A SWNT can conduct electricity as a metal or a semiconductor depending on how the graphite rolls about the sheet direction. A pair of integers (n, m) specifies the sheet direction in a chiral vector

$$C_h = n\hat{a}_1 + m\hat{a}_2 \tag{2.1}$$

The chiral vector C_h expresses the nanotube circumference and connects two crystallographically equivalent sites on a two-dimensional graphene sheet where $\hat{a}_1$ and $\hat{a}_2$ are unit vectors. These integers can fix the sheet direction in the chiral angle

$$\theta = \tan^{-1}\left(\frac{\sqrt{3}n}{(2m+n)}\right) \tag{2.2}$$

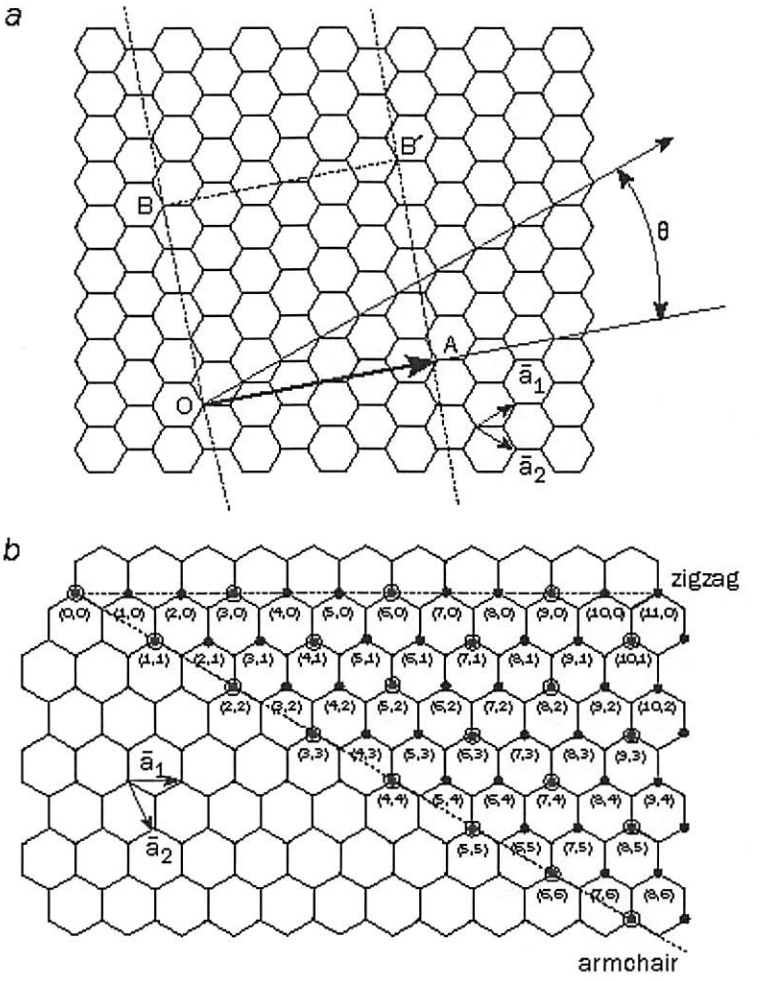

Figure 2.3: A carbon nanotube is based on a two-dimensional graphene sheet. (a) The chiral vector is defined on the hexagonal lattice as $C_h = n\hat{a}_1 + m\hat{a}_2$, where $\hat{a}_1$ and $\hat{a}_2$ are unit vectors, and n and m are integers. The chiral angle q (or θ in the text) is measured relative to the direction defined by $\hat{a}_1$. This diagram has been constructed for $(n, m) = (4, 2)$, and the unit cell of this nanotube is bounded by OAB'B. To form the nanotube, imagine that this cell is rolled up so that O meets A and B meets B', and the two ends are capped with half of a fullerene molecule. Different types of carbon nanotubes have different values of n and m. (b) Zigzag nanotubes correspond to $(n, 0)$ or $(0, m)$, armchair nanotubes have (n, n), and chiral nanotubes have general (n, m) values. Nanotubes can either be metallic (green circles) or semiconducting (blue circles). From Dresselhaus et al. 1998 [122].

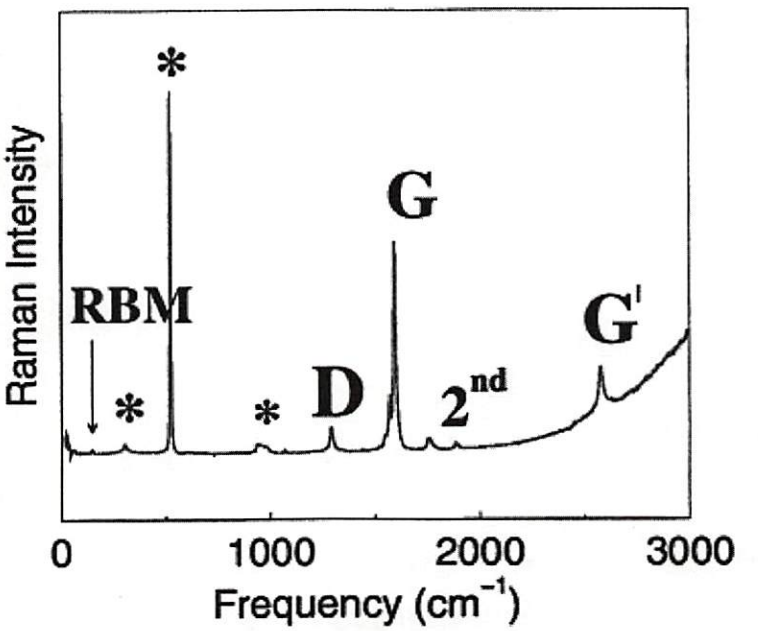

Figure 2.4: Raman spectrum from one nanotube taken over a broad frequency range using $E_{laser}(\lambda = 785 \text{ nm}) = 1.58$ eV excitation and showing the radial breathing mode (RBM), the D-band, the G-band, and the G'-band. The features marked with an asterisk (*) at 303, 521, and 963 cm^{-1} are from the Si/SiO_2 substrate and helped calibrate the nanotube Raman spectrum. From Dresselhaus et al. 2002 [123].

with respect to the zigzag axis. The integers can also fix the diameter

$$d_t = \frac{|C_h|}{\pi} = \frac{2.49\text{Å}}{\pi}\sqrt{n^2 + m^2 + nm} \tag{2.3}$$

and the conduction type of the SWNT. Zigzag and armchair nanotubes correspond to chiral angles of $\theta = 0°$ or ($n = 0$ or $m = 0$) and $\theta = 30°$ or ($n = m$). Other chiral angles or other n and m values correspond to chiral nanotubes. An (n, m) CNT is metallic when $n = m$, it has a small bandgap when $n - m = 3i$ [359] where i is an integer, and it is a true semiconductor for $n - m \neq 3i$ [125], [330].

Resonance Raman spectroscopy (see Figure 2.4) has characterized carbon nanotubes both in terms of the diameter distribution in bundles of singlewall nanotubes (SWNT)

and whether a nanotube is metallic or semiconducting [126]. Raman spectroscopy examines SWNT nondestructively [192], [126], [421] and can image them [196]. The technique became a structural characterization tool for SWNTs with the observation of single-nanotube Raman spectrum [123] that had the features of the SWNT-bundle Raman spectrum [126].

The observation of Raman spectra from just one nanotube is possible because of the very large density of electronic states close to the van Hove singularities of the nanotube's one dimensional structure [124]. A nanotube gives large Raman signals when the incident or scattered photons in the Raman process resonate with an electronic transition between van Hove singularities in the valence and conduction bands with energy states E_{ii} (see Figure 2.5) and produce strong coupling between the electrons and phonons of the nanotube [123].

The peak energies or van Hove singularities in the density of states (see Figure 2.5) are unique for each (n, m) value and so the interband transition energies E_{ii} are unique [123]. The interband transitions are strongly favored when the photon energy excites an electron from the ith peak in the valence band density of electronic states to the ith peak in the conduction band density of states [123].

The main technique for probing the phonon spectra has been Raman spectroscopy [124]. Nanotubes scatter light differently [238] depending on their diameter and chirality [266] [265] [390], doping [192] [126] [390], and deformation [298] [391]. Every possible nanotube denoted by (n, m) has a distinct electronic and vibrational spectrum, so that there is a one-to-one relation between (n, m) and the singularities in the 1D joint electronic density of states [124] [126].

All features of the Raman spectra (Figure 2.4) are sensitive to (n, m), including the radial breathing mode (in which all the carbon atoms are moving in-phase in the radial direction), the G-band (where neighboring atoms are moving in opposite directions

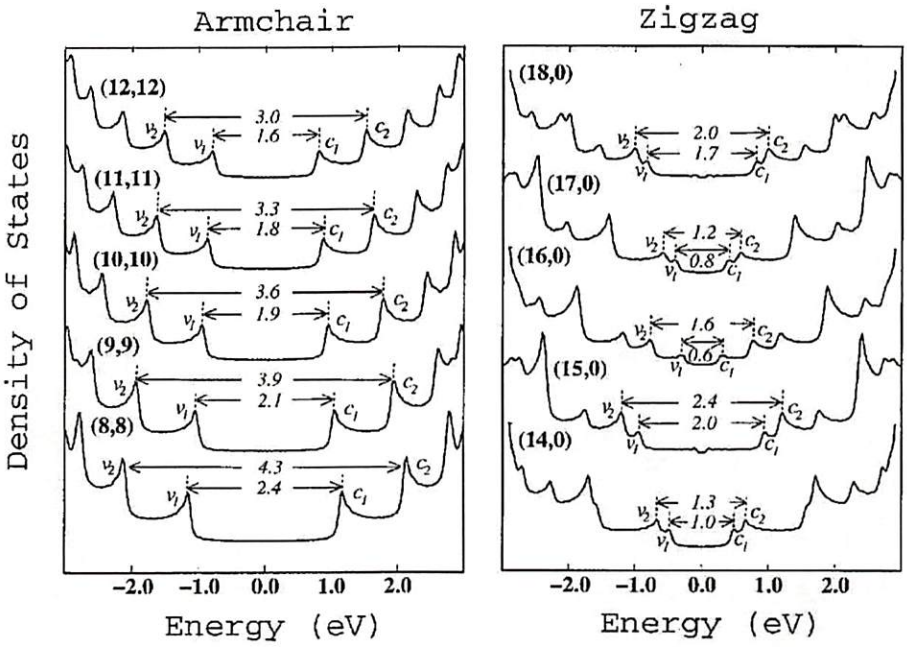

Figure 2.5: Electronic 1D density of states (DOS) calculated with a tight binding model for $(8,8)$, $(9,9)$, $(10,10)$, $(11,11)$, and $(12,12)$ armchair nanotubes and for $(14,0)$, $(15,0)$, $(16,0)$, $(17,0)$, and $(18,0)$ zigzag nanotubes and assuming a nearest neighbor carbon-carbon interaction energy $\gamma_0 = 3.0$ eV. The zero eV energy corresponds to the Fermi level. The valence band energies are on the left and the conduction band energies are on the right of the Fermi level. The peaks v_i and c_i are the van Hove singularities [124]. Wave-vector conserving optical transitions can occur between mirror image singularities in the 1D density of states, i.e. $v_1 \rightarrow c_1$ and $v_2 \rightarrow c_2$, etc. and these optical transitions are given in the figure in units of eV. These interband transitions are responsible for the resonant Raman effect. From Dresselhaus et al. 2000 [126].

along the surface of the tube as in 2D graphite), the dispersive disorder-induced D-band, and its second-order related harmonic G'-band [124] [126]. The radial breathing mode (RBM) is most sensitive to (n,m) and its frequency ω_{RBM} is inversely proportional to nanotube diameter d_t [126]:

$$\omega_{RBM} \propto 1/d_t \tag{2.4}$$

Researchers study Raman spectra to identify the structure (n,m) of a carbon nanotube and so identify whether it is metallic or semiconducting [465] [407] [29].

Metallic nanotubes have low predicted quantum resistance and conduct ballistically with long mean-free path of at least 1 μm at room temperature [227] [281] [164]. The nanotube's cylindrical shape avoids surface effects of three-dimensional conductors and edge effects of two-dimensional conductors. Narrow nanotubes are one-dimensional conductors. Landauer's equation

$$G = (2c^2/h) \sum_{i=1}^{N} T_i \tag{2.5}$$

gives their two-terminal conductance G [221] [108] where $2c^2/h$ is the quantum of conductance, T_i is the transmission of a contributing conduction channel or subband, and h is the Planck's constant. The sum involves two channels ($N = 2$) because the band structure of a metallic nanotube is approximately two sets for low energies or a few hundred milli electron-volts (meV) from the Fermi energy E_F.

A metallic SWNT has a low predicted resistance of

$$R = \frac{1}{G} = \frac{h}{4c^2} \approx 6 \text{ k}\Omega \tag{2.6}$$

according to Landauer's equation (2.5) for low energies and in the absence of any scattering or when all $T_i = 1$. This contact resistance is quantum mechanical and is due to the mismatching conduction channels in the nanotube and the metal contacts.

Metallic SWNT conduct ballistically [321] [466] [251] [23] because the charge carriers encounter little scattering due to the one-dimensional confinement, energy requirements, and momentum conservation. The large mean-free path corresponds to a room temperature resistivity of $\rho \approx 10^{-6} \Omega$/cm and equals or exceeds the conductivity of the best metal at room temperature [321]. The one-dimensional conduction also allows reduced power dissipation. The narrow tips allow field emission that can activate phosphors at 1–3 volts for electrodes that are one micrometer (1 μm) apart.

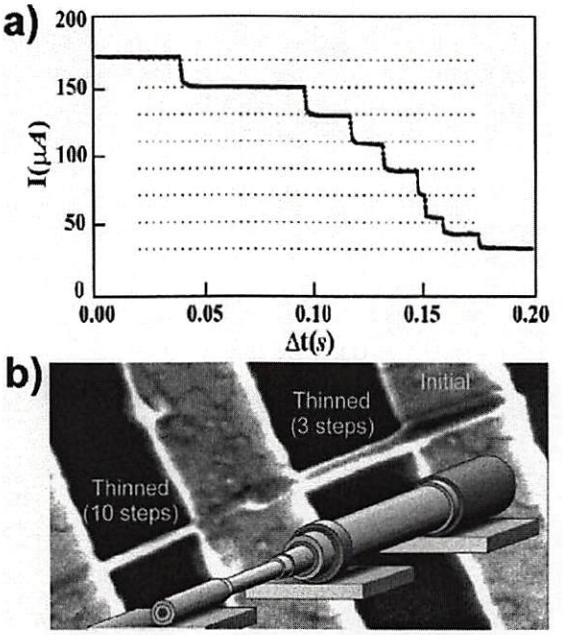

Figure 2.6: Multiwall carbon nanotubes consist of many layers. (a) Stepwise decrease of the current during the breakdown of an MWNT. (b) Images of an MWNT showing part of the initial tube, as well as segments of the same MWNT from which three and ten carbon atom shells have been removed. Avouris et al. 2003 [27].

A MWNT has a more complex structure because each of its shells can have different electronic character and chirality and the shells can interact [90] [91]. Researchers observed that a MWNT's bandgap inversely relates to its diameter. The variable size gives MWNT one-dimensional or two-dimensional characteristics. The outer-shell conduction can dominate the carrier transport at low bias and temperatures if the MWNT side-bonds to metal electrodes.

The semiconductor SWNT can change its conductivity in response to an external electric field in a gate effect [21] [436] [191], the presence of some chemicals in adsorption doping, the presence of photons [412] [239] [241], the presence of a magnetic

field [32], or a mechanical deformation in carbon-carbon bond change. The pristine semiconductor nanotube has a predicted diameter-dependent bandgap [125] [330]:

$$E_{GAP} = \frac{4hv_F}{3d} \tag{2.7}$$

where d is nanotube diameter and v_F is the Fermi velocity. Experiments confirmed the diameter dependence [471] [354]. Light also alters the conductivity of semiconductor nanotubes [239]. Researchers predict that doping with alkali metal can change semiconductor SWNT to metallic [131]

The conductivity of a SWNT changes in response to implanted dopant atoms [494] and to adsorption of water, oxygen, methane, or other molecules [247] [249] [157] that alters the energies of charge carriers. Nanotube sensitivity to water and oxygen [230] may be an interaction with impurities that the production process left behind [181]. This is an example of nanotube sensitivity to the interaction between nearby molecules and otherwise undetectable molecules. Nanotube conductivity becomes sensitive to carbon monoxide only after doping [373] or deformation [106].

Nanotube conductivity also changes when functional groups attach. This includes fluorination [327], substitution reaction of fluorinated SWNTs in solutions [326] [53], noncovalent functionalization of aromatic organic molecules [430] [491], and direct functionalization to the sidewall of SWNTs by various chemical groups such as atomic hydrogen [372], [240], nitrene [34], aryl groups [33], nitrenes, carbenes, radicals [209], COOH, NH_2 [83], 1,3-dipolar cyclo-additions [173], N-alkylidene amino groups [425], alkyl groups [480], and aniline [135]. The state of the functional groups can also modify nanotube conductivity. This enables DNA and protein sensitivity [460] [78] [457].

Mechanical deformation also affects electrical properties. The conductance of a SWNT decreases as the tip of an atomic force microscope (AFM) bends the nanotube

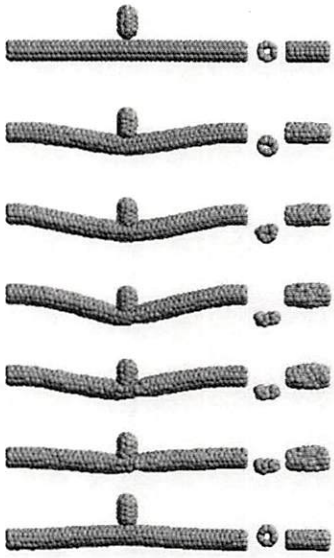

Figure 2.7: Bending a nanotube. Simulations of the deformation under the manipulation of an AFM tip. The top four figures show the equilibrium configurations corresponding to $\theta = 0°, 7°, 11°$, and $15°$, respectively, during the downward motion of the tip while the bottom three figures show the equilibrium configurations corresponding to $\theta = 11°, 7°$, and $0°$, respectively, as the tip is being withdrawn. The accompanying figures in each case give the side view and the top view, respectively, of the bending region. θ is calculated by $\theta = \tan^{-1}(2\delta/l)$ where δ is the maximum deflection and l is the suspended length of the SWNT. Liu et al. 2000 [286].

[441] [286]. Experimental and theoretical work found that sp^3 carbon-carbon bonds began to replace the sp^2 bonds in a SWNT at large bending angles $\theta \geq 15°$. This reduces conductance because it reduces the available free electrons.

A metallic carbon nanotube can act as a quantum dot that traps electrons in three dimensions and produce Coulomb oscillations when a new electron enters the tube [257]. This allows precise control of electron flow. The Coulomb oscillations or the Coulomb blockade effect occurs when electrons oppose attempts to insert more than one electron at a time onto a nanotube. This can occur at low temperatures when the total

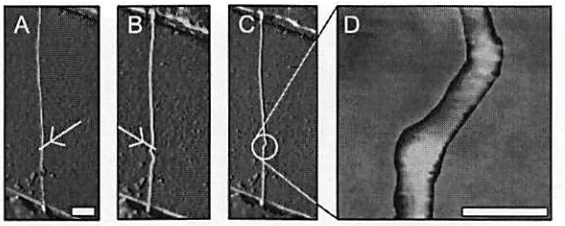

Figure 2.8: Fabrication of a room-temperature single-electron transistor within an individual metallic carbon nanotube by manipulation with an AFM. (A) Nanotube between Au electrodes on top of a Si/SiO_2 substrate with a gate-independent resistance of 50 kΩ. An AFM tip pressed down onto the substrate and moved along the path indicated by the arrow, thus dragging the nanotube into a new configuration. Bar, 200 nm. (B) Nanotube after creation of a buckle. The dragging action has resulted in a tube that has buckled. A second dragging action is performed as indicated by the arrow. (C) Double-buckle nanotube device. (D) Enlarged image of the double-buckle device. The image shows a height increase at the buckling points, as expected. The final device resistance at room temperature is one order of magnitude larger ($\approx$ 0.5MΩ). Bar, 20 nm. Postma et al. 2001 [380].

capacitance C of a conducting island is so small that adding a single electron requires an electrostatic energy

$$E_c = \frac{e^2}{2C} \tag{2.8}$$

larger than the thermal energy k_BT where k_B is the Boltzman's constant and temperature T is in Kelvin [121].

The Coulomb blockade effect can also occur at room temperature. Two strong bends within a metallic carbon nanotube act as nanometer-sized tunnel barriers for electron transport and sandwich an island within the nanotube [379], [350]. Coulomb blockade blocks single-electron tunneling for temperatures and bias voltages that are low relative to a characteristic energy:

$$E_{additional} = eV^+ = \frac{e^2}{C} + \Delta E \tag{2.9}$$

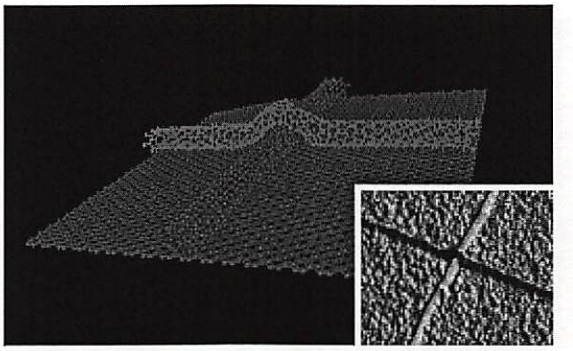

Figure 2.9: Two crossing (8, 0) singlewall nanotubes on a graphene plane. The mechanical structure was determined numerically using Tersoff-Brenner molecular dynamics. Twenty unit cells of each nanotube are shown in the image. Inset: AFM image of two crossing nanotubes on a silicon dioxide substrate. The nanotubes were grown using a CVD process. Nojeh et al. 2003 [350].

for adding an electron to the nanotube island. The symbol V^+ denotes the bias voltage needed to add an electron to the island at room temperature, C is the sum of all capacitances to the island, and ΔE is the energy difference between consecutive quantum energy levels [380].

Bulk productions of SWNT can use arc discharge, laser ablation, or chemical vapor deposition (CVD). Arc-discharge and laser ablation in addition to CVD can produce carbon nanotubes in quantity [142] [44] [439]. The CVD method can combine with silicon-wafer technique such as electron-beam lithography to control the position and orientation while growing a SWNT [250] [102] [193]. Arc-discharge produced multiwall carbon nanotubes at the gram level in 1992 using a combination of inert gas pressure and arcing current [142]. A metal catalyst such as cobalt in the carbon anode in the arc-discharge system produced singlewall carbon nanotubes in 1993 [44]. Laser ablation with metal catalyst such as nickel and cobalt in the carbon target produced singlewall carbon nanotubes at the 1–10 gram level in 1996 [439]. The two methods produced singlewall nanotubes in ropes of tens of individual nanotubes in close-packed hexagonal crystals due to van der Waals attraction. The two methods

also made fullerenes, graphitic polyhedrons with metal particles, and amorphous carbon that coated the nanotube walls. The chemical stability of nanotubes allows nitric acid to remove the amorphous carbon species and some of the metal catalyst species. CVD with methane can grow singlewall carbon nanotubes with structural perfection [250], [102]. CVD with ethylene also grows singlewall carbon nanotubes [193].

Researchers have increasing control of CNT and NW [456], [479], [469] growth and can separate different types of CNT. The CVD process allows controlled nanotube growth on pre-patterned wafers [165]. The catalyst's location [250], [74] and shape [464] and substrate crystal direction [115] all control the location and direction of the growth. Gas flow [212], shaped catalyst [464], and electric fields [490] also control the direction of the growth. Selective shell-by-shell breakdown of MWNT allows the fabrication of CNFETs with a specific bandgap $E_{GAP} \approx \frac{1}{d}$ [90]. Post-synthesis alignment of CNT [490] can be very effective if it combines with selectively removed [15], selectively disabled [35], or bulk-separated [260], [261] metallic and semiconductor CNT.

2.2 Nanotubes Can Benefit Nonlinear Devices

Nanotubes have electrical and mechanical properties that can benefit nonlinear devices that include transistors, single-electron transistors, and array antennas. Nanotube-based transistors can be smaller [398], faster [132], and stronger [486] [27] than silicon transistors. This section focuses on nanotube-based nonlinear devices because carbon nanotubes can conduct better than poly-crystal metallic nanowires, most semiconductor nanowires, and most non-carbon nanotubes. Nanotube conductivity can improve array antennas that interface with nanoscale devices.

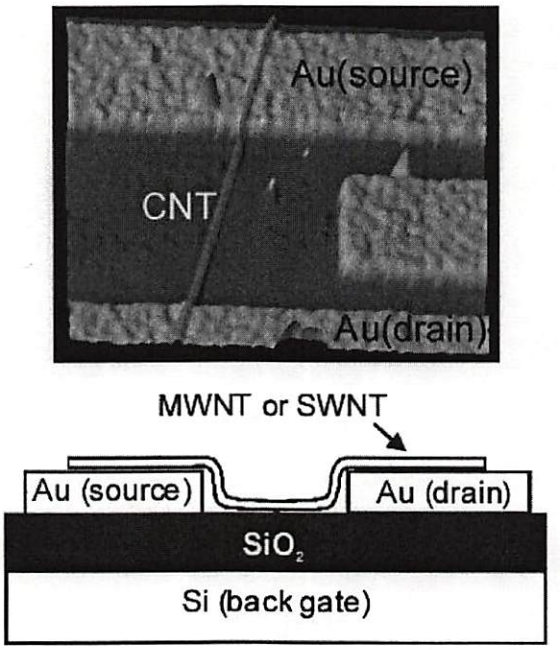

Figure 2.10: Top: AFM image of an early carbon nanotube field effect transistor design that draped a nanotube over electrodes. Bottom: Schematic cross section of the CNFET. Martel et al. 1998 [316].

2.2.1 Nanotube Transistors and Diodes

Semiconductor SWNT can conduct current in field-effect transistors (FET). The nanotube FET consist of two end-electrodes that bias the nanotube and for an adjacent gate that controls the transistor conductivity. This section reviews several nanotube FET architectures.

The first nanotube FETs "draped" the SWNT over gold electrodes in 1998 [436] [316]. They were p-type FETs and had an on/off current ratio of $\approx 10^5$. The van der Waals force-based contact with the electrodes were poor and caused high parasitic contact resistance $R \geq 1M\Omega$, low drive currents, low transconductance $g_m \approx 1$ nS, and high inverse subthreshold slopes S ≈1–2V/decade. These early FETs had back-gates with thick oxide layers $t_{OX} \approx$ 100–150 nm that contributed to the low performance.

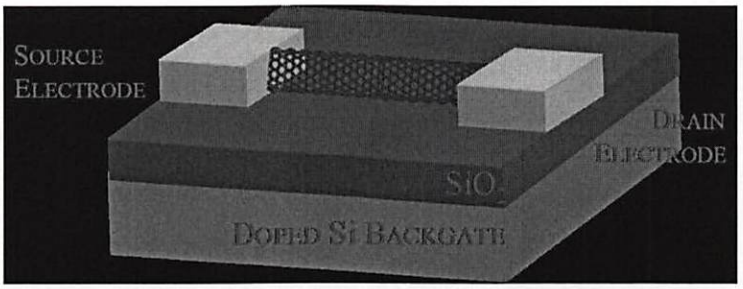

Figure 2.11: The schematic of a CVD-grown carbon nanotube field effect transistor. The overdoped substrate is a backgate.

The typical current-voltage (I–V) characteristics indicate that the pristine (undoped) semiconductor nanotubes act as hole-doped semiconductors at room temperature and that the nanotube devices are p-type FET's [492] [316] [19]. A transistor's output current is the scaled difference between the input and the threshold voltages $V - V_T$ with a gain g_m for suprathreshold voltages and is zero for subthreshold voltages:

$$I = g_m(V - V_T) \tag{2.10}$$

where g_m is negative and a suprathreshold voltage V is more negative than the threshold voltage V_T for a p-type FET.

An insulating oxide layer capacitively couples the gate and the nanotube. The thickness of the oxide t_{OX} layer affects the transistor performance. The early FETs had backgates with thick oxide layers $t_{OX} \approx$ 100–150 nm. Silicon MOSFETs have a planar capacitor and so have a gate capacitance that is inversely proportional to the thickness t_{OX}:

$$C \approx \frac{1}{t_{OX}} \tag{2.11}$$

while CNFETs have a predicted gate capacitance [316]

$$C \approx \frac{1}{ln(at_{OX} + b)} \tag{2.12}$$

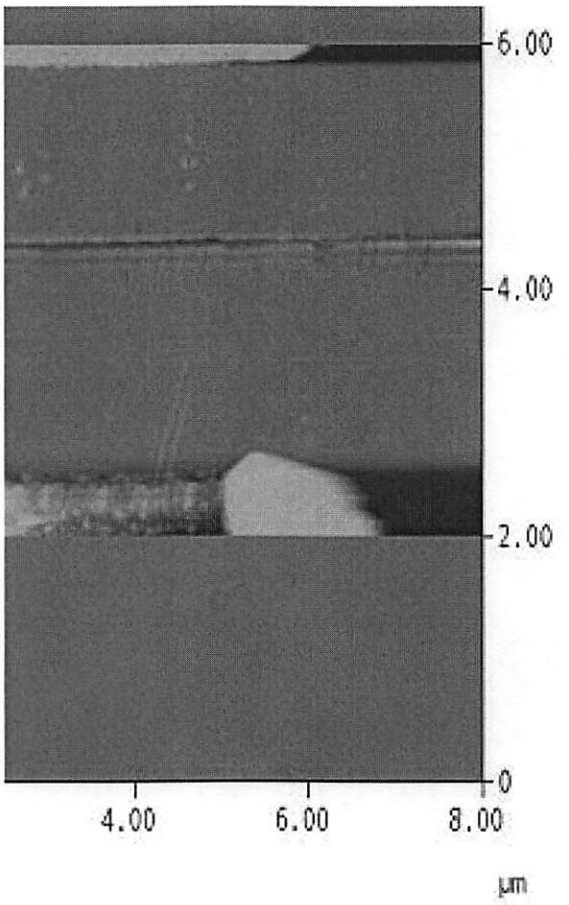

Figure 2.12: AFM image of a singlewall carbon nanotube FET with ohmic contacts. The titanium-gold metal contacts are on the top and the bottom of the image.

The nanotube-metal contact affects transistor performance. A semiconductor SWNT forms a Schottky diode at the interface with metal. The valence band edge of the semiconductor nanotube matches the Fermi energy of the metal and forms a Schottky barrier, and the metal's high work function strips electrons from the nanotube in hole-doping [22] [28] [202] [471]. The thinness of the barrier permits one-dimensional tunneling that can dominate carrier transport. [273].

Titanium and nickel electrodes can ohmically contact metallic and semiconductor nanotubes and have low contact resistance [308] [315] [493]. The FETs with ohmic

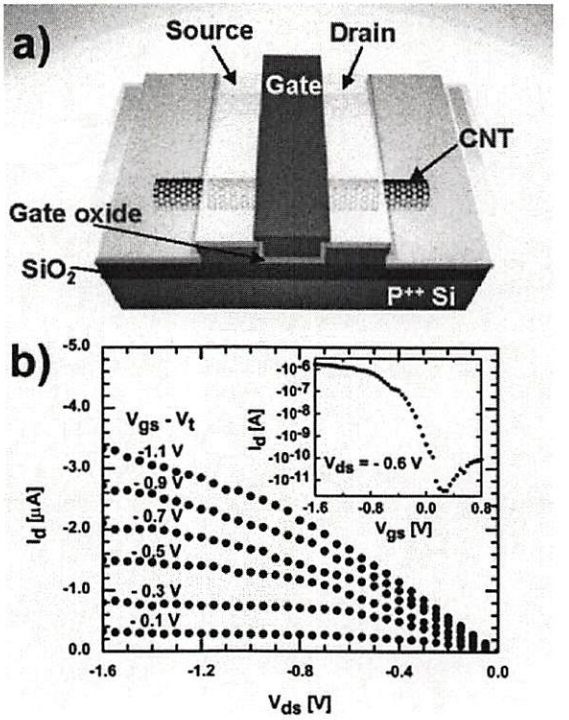

Figure 2.13: Top-gated carbon nanotube field effect transistor. (a) Schematic representation of a top-gated CNFET with Ti source, drain, and gate electrodes. A 15-nm SiO_2 film was used as the gate oxide. (b) The $I - V$ characteristics of the device. Avouris et al. 2003 [27].

contacts were p-type and had a high on/off ratio of $\approx 10^6$, a contact resistance of $\approx$ 30kΩ, a drive current of microamps (μA), and a transconductance $g_m = 0.34\mu$S [317] [315]. Thermal annealing of the titanium or cobalt contacts reduces contact resistance by producing a stronger coupling between the metal and the nanotube. The titanium electrodes form titanium carbide (TiC) during annealing.

The gate configuration also affects transistor performance. A top gate of 15–20 nm-thick dielectric film made FETs that were superior to back-gated FETs [472]. Each top-gated transistor could respond to a different gate voltage, had a lower threshold voltage of –0.5V, high drive currents, and a high transconductance of $g_m = 3.3\mu$S. Saline or electrolytes can also gate CNFETs [399] and give a high transconductance of $g_m \approx$

20μS. Researchers made CNFET with polymer electrolytes as the gate medium after observing that saline solutions can gate CNFET [399] [259]. The polymer electrolyte-gated CNFET exhibit no hysteresis and have high gate-efficiency,

The nanotube FETs are competitive with silicon devices. The prototype CNFETs can deliver three to four times higher drive currents than silicon MOSFETs for 15-nm gate length bulk silicon processes [487] and 50-nm gate length SOI processes [77]. Their transconductance is about four times higher.

Nanotube FETs can be very small. Singlewall nanotubes are very narrow and their predicted minimal gate length is about 5 nm [398]. The nanotube transistors can be very fast because they have high carrier mobility [132] [168]. Researchers have demonstrated reliable operation up to 580 MHz [20] and predicted terahertz (THz) cutoff frequencies [67].

CNT-based FETs operate as p-type or n-type transistors. Several ways can change the mode of operation from the pristine p-type to n-type that include adding electron donor atoms (n-doping), removing adsorbed oxygen by annealing the contacts in vacuum [113], and changing the polymer gate. Other CNT-based diodes require no doping [269].

The so-called "oxygen doping" differs from other doping because the oxygen interacts with the nanotube-metal junction and causes the p-type characteristic for FETs in air by pinning the metal's Fermi level near the nanotube's valence band maximum [93]. Polymer-gated FETs can also tune their modes of operation: A change in the chemical group of the polymer changes the FET from p-type to n-type [414], [296].

A split-gate electrode over a semiconductor carbon nanotube produces a near-ideal diode if half of the split gate applies a positive voltage and the other applies a negative voltage [269]. This creates a p-n junction in the nanotube without chemical doping.

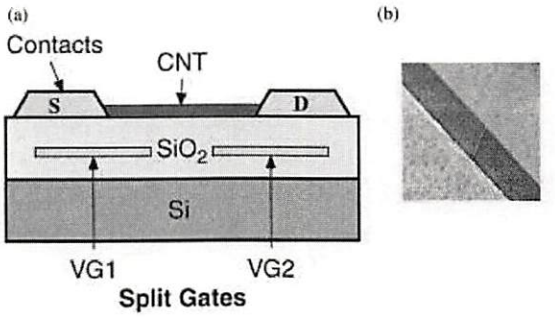

Figure 2.14: Singlewall carbon nanotube p-n junction diode with split gate (a) Schematic cross section of SWNT p-n junction diode. The split gates V_{G1} and V_{G2} are used to electrostatically dope a SWNT. For example, a p-n junction with respect to the source contact S can be formed by biasing $V_{G1} < 0$ and $V_{G2} > 0$; (b) SEM of a SWNT over a 1 μm split gate. Lee et al. 2004 [269].

Doping creates both p-type and n-type FETs on the same substrate and so creates CMOS-like logic gates. Complementary metal on semiconductor (CMOS) combines both types of transistors in one logic gate such as the nanotube inverter [114] and reduces power dissipation by reducing current flow. A positive input gate voltage turns the n-type CNFET on and the p-type CNFET off. This causes the output voltage to approximate the negative voltage and allows no current to flow between the positive and the negative voltages. A negative input gate voltage turns on the p-type FET and turns off the n-type FET to produce a positive output. Graduated doping produces a p-type section next to a n-type section on the same nanotube to produce a single and potentially many logic gates in one nanotube [494].

Nanotube-based transistors have applications as sensors because the transistor conductivity changes in the presence of adsorbed molecules or radiation. Nanotube sensors are sensitive and can detect and distinguish different chemicals [423]. The changed conductivity measurably alters the transistor thresholds and so changes the transistor outputs for the same bias and gate voltages. Nanotube sensors can detect

inorganic and organic molecules including DNA and proteins with modifications such as the attachment of functional groups.

Nano-structured transistors can also consist of materials other than carbon nanotubes. These materials include non-carbon nanotubes and nanowires of various compositions. Some transistors use as few as single nanowires or non-carbon nanotubes to pass current. Others (such as silicon (Si) and cadmium sulfide (CdS) in thin film transistors [128]) use aggregates of the nanowires or non-carbon nanotubes. Examples of non-carbon or inorganic nanotube transistors include gallium nitride (GaN) nanotubes [179] and boron nitride (BN) nanotubes [387]. Examples of nanowire transistors include indium phosphide (InP) [127], platinum (Pt) [400], indium oxide (In_2O_3) [278], germanium (Ge) [459], and gallium nitride (GaN) nanowires [244]. Examples of nanofiber transistors include polymer nanofiber [376] and vanadium pentoxide (V_2O_5) nanofiber [243]. Examples of nanowire single electron transistors (SET) include indium phosphide (InP), indium arsenide (InAs) [438], and silicon (Si) [342]. The smallest inorganic or non-carbon nanotubes are molybdinum sulfide (MoS_2) nanotubes that are semiconductors and have sub-nanometer diameters [495].

2.2.2 Nanotube Transistors Can Improve SETs and Quantum Dots

Nanotube-based field-effect transistors can improve single-electron transistors and quantum dots by taking advantage of nanotube conductivity. Nanotubes can conduct ballistically so nanotube transistors has little scattering. Nanotubes form very narrow conduction channels in transistors so bent nanotubes can form SETs. And nanotube FET-based SETs allow electrons to pass only if both a gate voltage permits nanotube conduction and an input voltage has a required value.

A carbon nanotube forms a quantum dot when a short segment of the one-dimensional conductor approximates a zero-dimensional confined region. A nanotube

quantum dot can operate as a single-electron transistor (SET) because Coulomb blockade quantizes the conduction so the SET admits one electron at a time. The metallic nanotube-based SET requires certain voltage values to admit one electron: It turns on and off again every time an electron enters [237]. The semiconductor nanotube-based SET has the additional requirement that the gate voltage must permit current flow. This is analogous to a field-effect transistor that allows a current to flow when the gate voltage turns it on.

A nanotube quantum dot can be a short nanotube [60] [61] [82] [86] [225] [353], a fullerene molecule [9] [366] [447], or a segment of a nanotube. One design draped and deformed the top nanotube in a nanotube cross junction [350]. The deformed or bent regions were conduction barriers and sandwiched the conductive quantum dot. Another design pinched off a section of a nanotube to form a Coulomb island [380]. The Coulomb island is the conductive region that the pinched low-conduction regions sandwiched.

Another SET design dopes a nanotube to form a PNP junction [248]. This is the low-dimensional limit of a planar sandwiched PNP junction that forms a two-dimensional electron-trap or a quantum well. A PNP junction confines electrons because each component PN junction permits electrons to flow to the thin N-layer in the center. Doping a nanotube creates a nanometer-width N-layer for a quantum dot.

Nanotube-based room-temperature SETs have applications for electron-based spintronics [473] because they allow single-electron manipulation. Spintronics compute with the quantum states of electrons or photons [473]. The applications are promising if the SETs could combine with room-temperature nanotube ballistic conduction [164] [227] [281] that can preserve an electron's spin [445].

SETs and quantum dots also have applications for artificial atoms. The quantum confinement of electrons can approximate an atom because the trapped electrons form

orbital-like patterns. These artificial orbitals can interact with light and other atoms similar to the electron orbitals in natural atoms [319]. Cadmium selenide quantum dots are an example of artificial atoms [268], [338]. Different size dots emit photons at different fixed frequencies after absorbing energetic photons. The size affects the pattern of the trapped electrons: The semiconductor quantum dots have size-dependent bandgaps. The fixed-frequency photon emission resembles a dye's optical properties. Incident photons excites the trapped electrons and then the excited electrons emit photons at a specific frequency that depends on the electron patterns or electronic density of states.

2.2.3 Nanotubes Can Directly Detect Electromagnetic Signals in Array Antennas

Metallic SWNT and multiwall CNT can directly detect electromagnetic radiation and apply array designs. A new nanotube-impedance theorem in Chapter 4 supports this nanotube-antenna prediction. And researchers have demonstrated optical frequency antenna-length effects with a carbon nanotube array [458].

Nanotubes have estimated impedances that suggest narrow bandwidth due to large aspect ratios. The estimated impedances also predict that nanotubes resonate similar to observed dipole effect [234].

Researchers can grow singlewall nanotubes up to two millimeters in length [212] and can make metal-dipole antennas on a silicon substrate for communications [283]. These findings suggest that nanotubes can work as antennas and can apply to wireless communications, interchip connections, and sensor networks.

Nanotube dipole-array antennas can gain sensitivity from having numerous elements [48] [145] [176] [279] [455]. The impedance analysis in Chapter 4 supports this array application because the analysis predicts a similarity between nanotube dipoles and

thin-wire metal dipoles and so supports the use of similar array design techniques. A nanotube-dipole array [190] can also operate in a wide range of frequencies for frequency-independent designs [145] that vary the dipole lengths and spacing [68].

Nanotube antennas can be attractive in an all-nanotube architecture. Nanotubes can help reduce the size of wireless sensors for networks such as the smart dust project [432] both by using miniature nanotube circuits and by using nanotube antennas that interface with those circuits. Nanotube dipoles should be more sensitive than nanometer-size metal dipoles because nanotubes can resist oxidation, electromigration [27], and grain-boundary effects [46] that can increase impedance in nanometer-size metal wires.

A junction between two nanotubes has electrical properties that promise an all-nanotube architecture and hence vast arrays of nanometer-sized electronic devices [485]. Yao et al. predicted that metal-to-semiconductor nanotube junctions would behave as rectifying diodes [485]. And that metal-metal nanotube junctions would have high conductivity [485] and so can apply to circuit interconnection and antenna impedance matching [68].

A nanotube array can also modify electromagnetic signals as a diode array [416] or as an artificial nonlinear composite [26] [24]. Sjogren et al. have predicted a diode-array waveguide that controlled the amplitude of transmitted millimeter waves at gigahertz frequencies [416]. The array elements were Schottky diodes. These monolithic diode arrays could shift the phase of a GHz signal and double or triple the signal frequencies. Other array elements can consist of amplifiers, mixers, and oscillators [416]. Nanotubes can make the dipole antennas, the Schottky diodes [202], amplifiers, mixers, and oscillators [410] to implement the diode arrays.

Nanotubes can implement artificial composites. Arnaut et al. have predicted that an artificial composite or a frequency-selective surface can create any harmonics and sub-harmonics from a single-frequency input signal [24]. The composite consists of an array

of electric molecules or nonlinearly-loaded electrically-small dipole antennas. Feedback control of the load transistors allows the system to adaptively cancel interference, minimize output power, or compensate antenna impedance. Nanotube antennas and nanotube transistors can implement these artificial composites on the nanoscale.

2.3 Nanoparticles Can Make Adaptive and Programmable Materials

Nanoparticles can make adaptive or programmable materials that can alter the materials' properties in response to stimuli [319]. Suspended nanoparticles can form shear thickening fluids that increase viscosity in response to a large shear stress [38] [207]. The particles in the fluids inhibit each other's movement [52] [75]. And iron nanoparticles can form magnetorheologic fluids that increase viscosity in the presence of a magnetic field [231] and can programmably stiffen treated fabric [451].

Nanoparticles can enhance armor by making fabrics that stiffen on impact or in the presence of programmed stimuli. Suspended silica nanoparticles can form shear thickening fluids whereas suspended iron nanoparticles can reversibly solidify a liquid.

Shear thickening is a non-Newtonian flow of concentrated colloidal dispersions (or suspensions of very small particles) [312] [313] [314] that has a large and sometimes discontinuous increase in viscosity with increasing shear stress [38] [207]. Hydrodynamic lubrication forces between the colloidal particles form jamming clusters or hydroclusters that reversibly thicken the colloidal suspension [52] [75], [152] [162]. Researchers can predict the onset of shear thickening in steady shear for colloidal hard sphere suspensions (see Figure 2.15) and electrostatically stabilized dispersions.

A shear thickening fluid that consists of suspended silica nanoparticles hardens on impact and prevents fibers from slipping in a fabric [272] similar to powdered fabrics

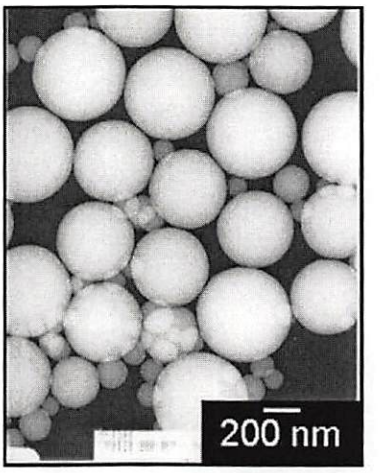

Figure 2.15: Scanning electron micrograph of silica nanoparticles in a shear thickening fluid. Wetzel et al. 2004 [143].

[117]. This helps the fibers distribute the force of the impact similar to the polymer resin in a hardened fiber composite [429] but allows the fabric to be flexible.

Magnetorheologic (MR) fluids are suspensions of magnetic particles in a carrier fluid. The rheologic properties of MR fluids undergo changes on application of a magnetic field [231]. Colloidal iron suspension mixes iron nanoparticles in heavy oil and switches from fluid-like to solid-like in a magnetic field [274]. The size of the nanoparticles help the suspension resist settlement [231].

Researchers combined MR fluids with silica nanoparticles and found that the nano-additives gave the fluid large complex viscosity for high additive concentrations [451]. This can have applications for programmable fabrics that turns stiff when a magnetic-field generator turns on and retains shear thickening characteristics when the generator is off.

Chapter 3

Signal Processing with Nanotube Stochastic Resonance

Nanotube-SR effects and nanotube transistors can enhance signal processing. Nanotube transistors exhibited noise-enhanced detection of weak signals in electrical experiments that we conducted. The observed nanotube-SR effect suggests that noise can enhance signal processing. This prediction is reasonable because researchers have reported SR effects in sensors and in electrical systems that include signal processing circuits.

Nanotubes can enhance transistors and so can improve both digital and analog signal processing. Nanotubes can also enhance electromechanical systems [409] and surface acoustic wave devices [307] to improve signal processing.

Section 3.1 discusses how nanotubes can enhance signal processing. Section 3.2 reports experimental results with nanotubes that show noise-enhanced detection.

3.1 Nanotube Transistors Can Enhance Signal Processing

Nanotube-based transistors can enhance both analog and digital signal processing circuits. The nanotube field-effect transistors (FET) can improve integrated circuits with higher device density due to smaller sizes [398], higher speed operations due to higher carrier mobility [132], flexible substrates [54] due to nanotube-enhanced conductive

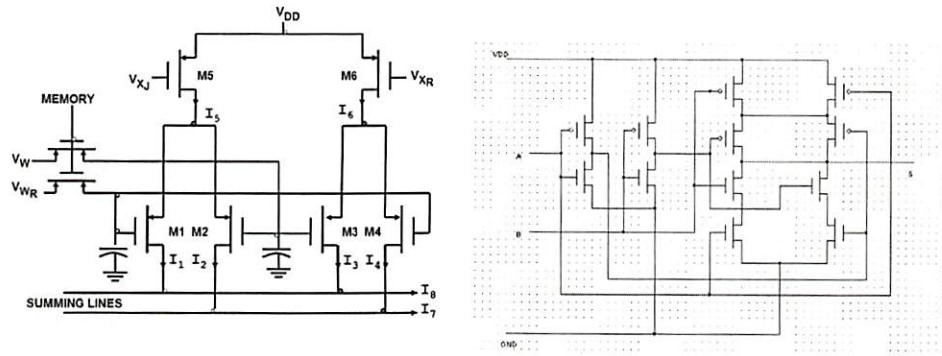

(a) Analog Gilbert Multiplier (b) Digital Half Adder (XOR)

Figure 3.1: Nanotube transistors can enhance both analog and digital circuits. (a) Analog Gilbert multiplier. The product of the change in input voltages $\Delta V_W = V_W - V_{W_R}$ and $\Delta V_X = V_{X_J} - V_{X_R}$ is proportional to the difference of the currents: $I_7 - I_8 \propto \Delta V_W \Delta V_X$. Redrawn from [262]. (b) Digital half adder in complementary logic. The sum bit S of two single binary bits A and B resembles the truth table for XOR(A,B). A separate carry-logic computes the carry bit of the sum.

polymers, and lower thermal noise if ballistic conduction [227] [281] [164] reduces resistive conduction. So nanotube transistors can improve signal processing circuits.

Nanotubes can enhance digital signal processing (DSP) because nanotube-enhanced logic gates can add and multiply [467]. Researchers have demonstrated nanotube transistor-based logic circuits [31] [228] [288]. The nanotube-enhanced logic gates can apply to both digital adders and multipliers [467] (see Figure 3.1).

An exclusive OR (XOR) gate adds two binary bits and produces a sum bit [467]. A carry logic computes the carry bit. An array of adders can multiply: A shift-and-add circuit can multiply two binary sequences X and Y. The multiplication consists of computing partial products and summing the bit-shifted partial products. Binary multiplication is equivalent to a logical AND so the partial products are (X AND $Y(k)$) where $Y(k)$ is the k^{th} bit. Nanotubes can also enhance memory [388] [402] elements so that an all-nanotube architecture can enhance a digital signal processor.

Nanotubes can enhance analog signal processing in different types of filter circuits. Nanotube-enhanced transistors can build multipliers and amplifiers for transversal filters and active filters. Nanotube-enhanced electromechanical devices can build variable inductors or capacitors for resistor-inductance-capacitance (RLC) filters and can build surface-acoustic-wave (SAW) filters.

Nanotubes can enhance multipliers (see Figure 3.1(a)) that implement mixers [331] [184], phase-locked loops [184], differentiators [184], and neural networks [200]. And nanotubes can enhance operational amplifiers that implement adders, feedback amplifiers [183], integrators [183], differentiators [183], and rectifiers [184].

Analog multipliers (or mixers) and low noise amplifiers are essential to wireless communications for modulation/demodulation and frequency downconversion [331] [155]. Nanotubes can improve signal modulation because nanotube multipliers can have higher speed due to high carrier-mobility [132] and have larger dynamic range due to large transconductance and current carrying-capacity [27].

Nanotube transistors can improve amplifier performance by approximating ideal operational amplifiers (op-amps) in a single architecture. An ideal operational amplifier (op-amp) is a differential input, single-ended output amplifier with infinite gain, infinite input resistance, and zero output resistance [183]. Silicon technology approximates this ideal by combining two different processes: Bipolar complementary metal on silicon (BiCMOS) transistors have large transconductance. And bipolar field effect transistors (BiFET) have the infinite input resistance and current gain of field effect transistors [182]. Nanotube amplifiers can have large transconductance [27] and the infinite input resistance and current gain of a FET [182] and so can approximate the ideal op-amp.

Nanotubes can improve low-noise amplifiers if the nanotube-amplifier designs can combine near-ideal op-amps with ballistic conduction [27]: Charge carriers travel without scattering over micron lengths. This ballistic conduction differs from the

resistive conduction channel of a silicon FET. The resistive or thermal noise is the major source of noise in FETs [182]. Nanotube amplifiers can further reduce carrier-scattering noise or resistive noise in nearly ideal amplifiers.

Nanotube multipliers can enhance discrete-time transversal filters. The transversal filter or tapped-delay line filter requires only analog adders, multipliers, and delay elements (or memory). The filter output $y(n)$ has the form of a finite convolution sum [199] for a finite-impulse response (FIR) filter with a length-M filter impulse response $h(n) = w(n)$:

$$y(n) = \sum_{k=0}^{M-1} w(k)x(n-k) \tag{3.1}$$

that adds the inner product between the k^{th} delayed or tap input $x(n-k)$ and the k^{th} tap weight $w(k)$. The convolution sum in (3.1) can use nanotube transversal filter architecture to implement any discrete-time linear time-invariant (LTI) FIR filters with a real impulse response.

The tapped-delay line can also implement an infinite-impulse response (IIR) filter if it uses feedback and realizes the difference equation [356] [384]

$$y(n) = \sum_{k=1}^{N} a_k y(n-k) + \sum_{k=0}^{M} b_k x(n-k) \tag{3.2}$$

where a transfer function $H(z)$ or the z-transform [381] of the impulse response $h(n)$ gives the tap weights or feedback coefficients a_k and b_k

$$H(z) = \sum_{k=-\infty}^{\infty} h(k)z^{-k} = \frac{\sum_{k=0}^{M} b_k z^{-k}}{1 - \sum_{k=1}^{N} a_k z^{-k}} \tag{3.3}$$

and assuming that the z-transform converges. The transfer function has zeros b_k in the numerator and poles a_k in the denominator. The zeros are associated with forward paths and the poles with feedback paths [200].

The transversal filter has applications for adaptive filtering. Nanotube adaptive filters can compute the optimal impulse response or tap weights $w(k)$ for a FIR transversal filter by applying the Yule-Walker algorithm, the least-mean-square algorithm, the recursive least-squares algorithm, or the fast transversal filters algorithm [200]. The Yule-Walker algorithm uses estimates of the autocorrelation sequence of the input signal.

The adaptive IIR filters compute the optimal transfer function coefficients a_k and b_k by applying an equation error method or an output-error method to minimize a cost function based on the estimation error [200]. The equation error method applies the adaptive FIR technique to update the feedback coefficients in an all-zero nonrecursive form and then copy the coefficients to an all-pole nonrecursive form for another update. The output-error method directly updates the feedback coefficients in a pole-zero recursive fashion [200].

Nanotube can also enhance RLC networks and tunable filters. Nanotube oscillators [410] and electromechanical switches [233] can programmably vary capacitance and impedance in RLC networks and tunable filters. The FET structure of the nanotube oscillators [410] suggests that nanotube electromechanical systems can integrate with nanotube transistors. And nanotube and silicon transistors are compatible [444] [27]. So nanotubes can further enhance signal processing by combining nanotube and silicon transistors with nanotube electromechanical systems on the same chip.

Nanotubes have physical strength and stability that can enhance electromechanical devices that switch, mix, and filter signals. Nanotube stability can overcome the limitations that find mechanical or acoustic devices harder to miniaturize due to dangling chemical bonds at the etched surfaces that reduce performance [483]. Nanotubes are small, strong, and chemically non-reactive and so resist surface losses [483] that worsen in nanoscale structures. This is because the surface to volume ratio scales up with

$1/r$ where r is device dimension. Surface losses are also susceptible to the ambient conditions [483].

Electromechanical switches or relays [133] [299] control signal and power flows. These switches can also modulate signal phase by routing a signal through different transmission paths and can use their length to delay or phase-shift the signal [133] [299]. Researchers predict that nanotube-based electromechanical switches can carry large currents, have low impedance, and turn on and off rapidly. [271] [277]

Nanotubes can mechanically oscillate [476] with high resonant frequencies and high Q-values (or ratio of center frequency to bandwidth). These nano electromechanical oscillators can mix and filter signals similar to MEMS oscillators [36] [284] [324] [347] [435] [474]. A nanotube electromechanical oscillator has a predicted gigahertz oscillation frequency for a multiwall nanotube with a 30-nm diameter, 500-nm length, and Young's modulus [443] as high as 1.8TPa [476]. Researchers have reported that μm-long ropes of single-wall carbon nanotubes have a high Q-factor of over 1,000 at an oscillating frequency over 2 GHz [394] and that μm-long single or double-wall carbon nanotubes have a Q-factor of 40–200 for tunable resonant frequencies from 3–200 MHz [410].

Nanotubes can also improve tunable RLC filters that use MEMS variable capacitors [5] [51] [163] [351] or tunable impedance [242] [297] in a resistor-inductor-capacitor (RLC) network design. This is because stronger and more stable cantilever nanotubes [277] can improve the switched MEMS variable capacitors [271] that use cantilever geometry to tune capacitance. Researchers predict that a multiwall nanotube nanorelay has over 1 GHz resonance frequency [233] and have demonstrated a nanorelay that has 0.1 GHz estimated resonance frequency and carry over 100 μA of current [271].

A mechanical resonator or oscillator can have a higher Q-factor than an electronic resonator [483] because a mechanical resonator has high energy storage capacity, low

internal loss, and low parasitic coupling to the surrounds while an electronic resonator suffers from the resistance in the RLC circuitry [483].

Nanotubes can enhance the acoustic transduction in SAW devices. Nanotube tips concentrate electric fields [80] and so a nanotube film should stimulate a piezoelectric layer better than metal [309]. This can reduce the size of the transducers [307]. SAW devices contribute to wireless communications [337] with high Q-factor low-noise tunable oscillators [156] [336] [477], and high frequency filters [362] with high bandwidth-selectivity.

SAW filters include transverse filters [337] that implement finite impulse response (FIR) filters, resonator filters [477], and programmable filters that correlate [208] (can apply to matched filters [357]) and convolve [206]. SAW devices can also sense temperature, humidity, and pressure [119] and can operate passively and wirelessly [119] for remote wireless sensor applications.

Nanotubes can also directly process electromagnetic (EM) signals. A new nanotube-impedance theorem predicts that nanotubes can be narrowband resonant dipole antennas in Chapter 4. The nanotube-antenna prediction is reasonable because researchers have reported that nanotube dipole radiators [99] [234] use their lengths to tune for a wide range of frequencies [68] up to optical frequencies [458].

Nanotube antennas can be attractive because multiwall nanotubes and single-crystal nanowires can be better than nanometer-thin poly-crystal wires: They can carry large currents [94] [463], conduct electrons with little scattering [227] [281] [164], and are compatible with nanotube signal processing circuits. Nanotube antennas will soon become testable because researchers have grown straight nanotubes to many millimeters [280] [488] [212] with precise control over nanotube length [72]. This can apply to millimeter wavelength RF antennas that lie on silicon substrates [283].

Nanotubes can detect photons. Researchers have reported infrared detection with nanotubes: The multiwall nanotubes have diameter-dependent bandgaps that respond to infrared over a broad wavelength range from 1–15 μm [29] [289] [413] [475] [484]. The MWNT diameter tunes the spectral range and the length tunes the absorption efficiency. The wavelength-response range may be broader than both nanotube and semiconductor quantum well and quantum dots that have tunable peak-wavelength response [484]. Nanotube photodetectors can help free-space interconnection between chips [160] [153] because they can be sensitive and because they can be compact and so can increase data channels.

Nanotubes can generate EM signals. They can emit photons as light-emitting diodes [166] [332], emit radio waves as resonant dipole radiators [68] [458], or emit electrons [112] that then stimulate microwave [194] [229] [468], visible [211], ultraviolet [349], or x-ray radiations [80]. Nanotube field emitters have a lower emission threshold and a higher current capacity than conventional electric field emitters [80]. Researchers are exploring nanotube field emission for microwave radar and communications in traveling wave tubes [229] [468].

3.2 Noise Helped Nanotubes Detect Signals

Electrical noise can help pulse-train signal detection at the nanolevel. Experiments on a singlewall carbon nanotube transistor confirmed that a threshold exhibited stochastic resonance (SR) for finite-variance and infinite-variance noise: Small amounts of noise enhanced the nanotube detector's performance.

The experiments used a carbon nanotube field effect transistor to detect noisy subthreshold electrical signals. Two new SR hypothesis tests also confirmed the SR effect in the nanotube transistor. Three measures of detector performance showed the

SR effect: Shannon's mutual information, the normalized correlation measure, and an inverted bit error rate compared the input and output discrete-time random sequences.

The nanotube detector had a threshold-like input-output characteristic in its gate effect. It produced little current for subthreshold digital input voltages that fed the transistor's gate. Three types of *synchronized* white noise corrupted the subthreshold Bernoulli sequences that fed the detector. The Gaussian, the uniform, and the impulsive Cauchy noise combined with the random input voltage sequences to help the detector produce random output current sequences.

The experiments observed the SR effect by measuring how well an output sequence matched its input sequence. Shannon's mutual information used histograms to estimate the probability densities and computed the entropies. The correlation measure was a scalar inner product of the input and output sequences. The inverted bit error rate computed how often the bits matched between the input and output sequences.

The observed nanotube SR effect was robust: It persisted even when infinite-variance Cauchy noise corrupted the signal stream. Such noise-enhanced signal processing at the nano-level promises applications to signal detection in wideband communication systems and biological and artificial neural networks.

Noise can sometimes help neurons and other nonlinear systems detect signals. Figure 3.2 shows how additive white uniform pixel noise can improve the quality of the degraded image of a carbon nanotube. Several researchers have demonstrated the SR effect for various types of threshold units or neurons [253] [254] [255] [222] [171] [64] [174] [470] [341]. Figure 3.3 illustrates a simulated SR effect in the mutual information of a simple threshold neuron for Bernoulli signals and for white Gaussian noise.

The new SR theorems in [254] give broad sufficient conditions for SR to occur in any threshold system for all possible finite-variance noise types and for most infinite-variance noise types. We restate these SR theorems below.

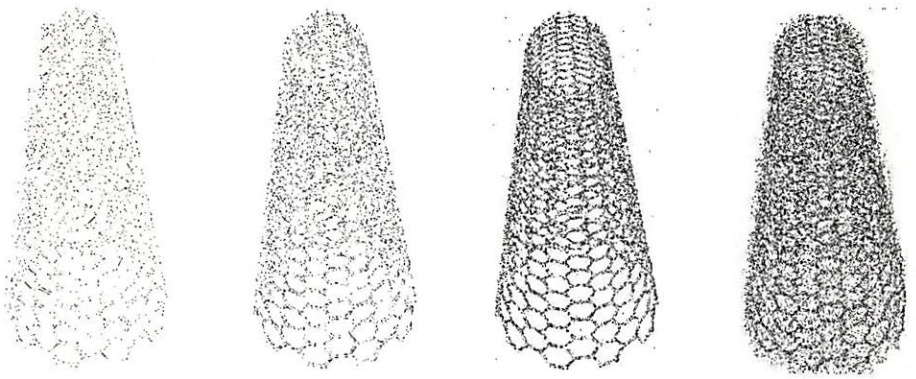

(a) $A = 0$ (b) $A = 0.6$ (c) $A_{opt} = 0.85$ (d) $A = 1.1$

Figure 3.2: Uniform pixel noise can improve the quality of an image through a stochastic-resonance effect. A small amount of noise sharpens the image features while too much noise degrades them. We produced these noisy images by applying a pixel-level threshold to an artistic rendering of a carbon nanotube. The threshold gives a white pixel $y = 1$ as output if the input grayscale pixel $x \in [0, 1]$ equals or exceeds a threshold θ: $y = g(x + n - \theta) = 1$ for $(x + n - \theta) \geq 0$ and $y = 0$ for $(x + n - \theta) < 0$. The threshold is $\theta = 0.001$. (a) The faint image results when we apply the threshold to the original image: $g(x - \theta) = 1$ for $(x - \theta) \geq 0$ and 0 otherwise. Figures (b) through (d) show the effect of increasing additive noise: The noise interval grows from b to d: $A = 0.6$ in (b), $A_{opt} = 0.85$ in (c), and $A = 1.1$ in (d). The additive noise is uniformly distributed over a symmetric interval around zero ($\sim$U$(-A, A)$) so it is zero mean.

Simulations show that these SR theorems apply to a threshold-like ramp function that often models a transistor's current-voltage characteristics: A transistor's output current $I = G(V - V_T)$ equals the scaled difference between the input and the threshold voltages $V - V_T$ with a gain G for suprathreshold voltages and is zero for subthreshold voltages. We note that the threshold neuron model lacks the internal state dynamics of the FitzHugh-Nagumo (FHN) and the Hodgkin-Huxley (HH) neuron models [368], [369].

Computer simulations produced the signature nonmonotonic SR curve in Figure 3.4(a) for noisy Bernoulli sequences that fed a transistor with parameters $G = -1$ nA/V and $V_T = -2$ V and for Shannon's mutual information, the correlation measure, and the inverted bit error rate. The three measures produced similar SR curves: The

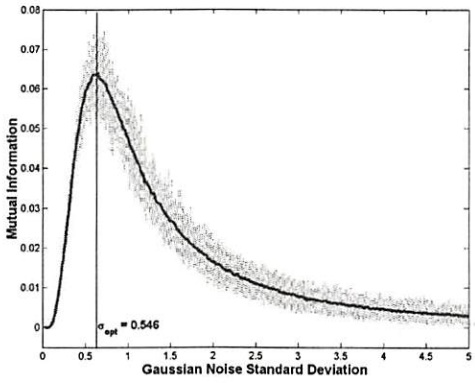

Figure 3.3: Simulated SR for white Gaussian noise. The plot shows the smoothed input-output mutual information of the simple threshold as a function of the standard deviation of additive white Gaussian noise. Each vertical dashed line shows the maximal and minimal range in one sample of 100 trials. The simple threshold gives a binary output y depending on the magnitude of the input x relative to a threshold value θ. It has the form $y = g(x-\theta) = 1$ if $x \geq \theta$ and $y = 0$ otherwise. The threshold has a nonzero noise optimum at $\sigma_{opt} \approx 0.546$ and shows the SR effect. The threshold value is $\theta = 1$. The input Bernoulli signal b_i has an amplitude A = 0.8 and equally likely symbols that have success probability $p = 1/2$. The Gaussian noise n_i adds to the bipolar input Bernoulli signal b_i. The input sequence S consists of noisy symbols $s_i = b_i + n_i$ and the output sequence Y consists of $y_i = g(s_i - \theta)$. Each trial uses 10,000 input-output sample pairs (s_i, y_i) to estimate theprobability densities and to compute the mutual information.

SR curves have similar optimal noise standard deviations σ_{opt} in the interval $(0.3, 0.5)$. The SR curves also correlated. The correlation coefficient R measured the strength of the correlation: $R = 0.9367$ for the mutual information and the correlation measure, $R = 0.8265$ for the mutual information and the inverted bit error rate, and $R = 0.9541$ for the correlation measure and the inverted bit error rate with p-value< 0.001 for all. These simulations led to the natural prediction that an actual nanotube transistor would exhibit the SR effect.

Experiments confirmed the SR prediction using a pristine (undoped) nanotube threshold detector: A transistor whose conduction channel was a nanometer-width semiconductor singlewall carbon nanotube [436] [492] [316] [81] [290] [405]. The

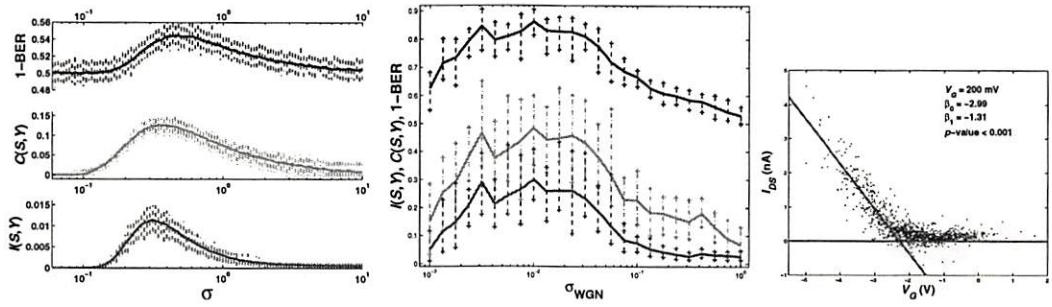

(a) Simulated SR (b) Nanotube SR (c) Threshold Detector

Figure 3.4: Performance for both (a) simulated and (b) nanotube transistor experiments gave the nonmonotonic stochastic-resonance (SR) signature with similar modes for additive white Gaussian noise. The three performance measures were the bottom red mutual-information curve $I(S,Y)$, the middle green correlation-measure curve $C(S,Y)$, and the top blue inverted bit-error-rate curve 1–BER that varied with the standard deviation σ of the Gaussian noise. (c) The stochastic I-V_G curve shows a threshold-like gate effect of the p-type nanotube detector. Linear regression of the random input-output pair (s_i, y_i) estimated the threshold gate voltage $V_T = -2.3$ V.

experiments applied different Bernoulli input sequences that used different combinations of subthreshold gate voltages as their ON/OFF symbols. *Synchronized* Gaussian, uniform, and infinite-variance Cauchy noise added to the input sequences and produced the SR effect: They helped the nanotube transistor detect the subthreshold input. Shannon's mutual information, an input-output correlation, and an inverted bit error rate measured the detector performance.

Figure 3.4(b) shows the nonmonotonic signature of SR for white Gaussian noise and Figure 3.4(c) shows the threshold-like nonlinearity of the nanotube transistor. The modes of the three SR curves occurred for nonzero noise strength with a standard deviation of at least 0.01. The three SR curves correlated with each other and the correlation coefficients were $R = 0.9830$ for the information and the correlation curves, $R = 0.9774$ for the information and the bit-error-rate curves, and $R = 0.9877$ for the correlation and the bit-error-rate curves with p-value< 0.001 for each. Nonlinear

stochastic experiments can have extreme variations as the simulated SR in Figure 3.4(a) shows.

We observed the nanotube SR effect (Figure 3.4(b)) despite the nanotube instabilities that caused fluctuations in the stochastic I-V_G curve in Figure 3.4(c). Both the simulated and experimental SR curves have similar variations (vertical bars) that are as much as half the height of the SR modes.

The nanotube experiments produced the SR effect for Shannon's mutual information [427] [37], the input-output correlation measure [87] [88], and the inverted bit error rate that measured how well the output sequences matched the input Bernoulli sequences. We note that the three measures correlate well and have similar SR modes or optimal noise levels in the simulations (Figure 3.4(a)) and that they show strong correlation and have the same optimal noise level in the experiments (Figure 3.4(b)).

The mutual information $I(S, Y)$ subtracts the noisy channel's (the transistor's) output conditional entropy $H(Y|S)$ from its unconditional entropy $H(Y)$ [95]: $I(S, Y) = H(Y) - H(Y|S)$. The input signal S was a sequence of random binary voltages that produced a random output sequence Y in the form of a transistor current. The correlation measure $C(S, Y)$ normalized the zero-lag value of the cross-correlation sequence

$$r_{SY}(l) = \sum_{k=1}^{N} s(k)y(k-l) \tag{3.4}$$

of the two sequences with subtracted means.

These two measures did not assume that the nanotube detector had a special structure and did not impose a threshold scheme on the experiment. But the inverted bit error rate (1–BER) decided whether each output y_i was a '0' or '1' by applying a threshold scheme: A Bayes discriminant function in a two-class minimum-distance classifier [130] that used complete knowledge of the input. The 1–BER measured how often

the input and output bits agreed: 1–BER = $1 - (N_{error}/N) = N_{correct}/N$ where N_{error} counted the number of bits that differed between the length-N input and out sequences and $N_{correct}$ counted the number of bits that agreed.

The nanotube transistor had a threshold-like nonlinearity that produced the SR effect. Figure 3.4(c) gives the transistor's current-voltage characteristics I-V_G in response to the noisy input signal by plotting the experiments' input-output pairs (s_i, y_i). The nanotube detector's input S is the transistor gate voltage V, and the output Y is the current I. The transconductance G related the output drain-to-source current I to the suprathreshold input gate voltage V with respect to the threshold voltage V_T:

$$Y = I = \begin{cases} G(V - V_T) \text{ for } S = V \leq V_T \\ 0 \text{ else} \end{cases} \tag{3.5}$$

The transconductance G was negative because the pristine nanotube transistors exhibited current-voltage characteristics that were consistent with p-type transistors. Linear regression fit the data to the transistor equation (3.5), extrapolated the nonlinearity in Figure 3.4(c), and estimated the threshold voltage $\hat{V_T} \approx -2.3$ V.

3.2.1 Stochastic Resonance Theory

Stochastic resonance (SR) occurs when noise enhances the performance of a nonlinear system [256]. The SR effect occurs in nature, in electrical systems, in neuron models, and in climate [42] [41] [43] but no report of SR in carbon nanotubes. Examples from nature include crayfish [363] [370] [118] and crickets [276] [328] [329] that elude predators and sharks [55] and paddlefish [403] that find prey. SR occurs in neural studies of a rat's brain [175] and mechanoreceptors [89]. Examples of electrical systems that exhibit SR include ring lasers [322] [449], Chua's circuit [18], [17], comparators [178], coupled diode resonators [291], tunnel diodes [311] [310], Schmitt triggers [323], Ising

systems [344] [415] [56], bistable magnetic systems [172] [187], electron paramagnetic resonance [172], magnetoelastic ribbons [422], superconducting quantum interference devices (SQUIDs) [401] [470] [204], Josephson junctions [205] [59], optical systems [39], [136], chemical systems [137] [258] [275] [161] [188], and quantum-mechanical systems [292] [306] [365] [364] [186]. Some bistable systems [141] [62] can exhibit the SR effect. The single-well Duffing oscillator [138] [140] [139] and van der Waals interaction (unpublished manuscript) can both exhibit the SR effect without a potential barrier. The SR effect can also exhibit more than one mode [420] [285] [318] [452]. Examples of neuronal models that exhibit the SR effect include dynamical models —- the bistable potential neuron [65], the Hodgkin-Huxley neuron [368], [87], [293], [378], the FitzHugh-Nagumo neuron [88], [294] [340] [375], and the integrate-fire neuron [63] [76] [377] [424] —- and threshold units or neurons [427] [87] [88], [118], [66] [170] [177] for finite-variance noise types and using mutual information or cross-correlation to measure the performance.

A Simple Threshold Neuron Stochastically Resonates

Reference [254] shows that a simple threshold is a sufficient condition for the SR effect and for all finite-variance noise and for all major infinite-variance noise. We review two theorems from [254]: They show that small amounts of independent additive noise can increase the mutual information of threshold neurons if the neurons detect subthreshold noisy Bernoulli input signals. The first theorem shows that the SR effect occurs for all finite-variance noise probability density functions (pdf) that obey a simple mean constraint. The second theorem shows that the SR effect holds for all infinite-variance noise types in the broad family of stable distributions.

The theorems use the standard discrete-time threshold neuron model [256] (and references therein).

$$y = \mathrm{Sgn}\,(s + n - \theta) = \begin{cases} 1 \text{ if } s + n \geq \theta \\ 0 \text{ if } s + n < \theta \end{cases} \tag{3.6}$$

where $\theta > 0$ is the neuron's threshold, s is the bipolar input Bernoulli signal with arbitrary success probability p such that $0 < p < 1$ and with amplitude $A > 0$, and n is the additive white noise with probability density $p(n)$.

The threshold neuron study uses binary signals that have subthreshold symbols. The symbol '0' denotes the input signal $s = -A$ and output signal $y = 0$. The symbol '1' denotes input signal $s = A$ and output signal $y = 1$. We assume subthreshold input signals: $A < \theta$. Then the conditional probabilities $P_{Y|S}(y|s)$ are

$$\begin{aligned} P_{Y|S}\,(0|0) &= \Pr\{s + n < \theta\}\,|_{s=-A} = \Pr\{n < \theta + A\} \\ &= \int_{-\infty}^{\theta+A} p(n)dn \qquad (3.7) \\ P_{Y|S}\,(1|0) &= 1 - P_{Y|S}\,(0|0) \qquad (3.8) \\ P_{Y|S}\,(0|1) &= \Pr\{s + n < \theta\}\,|_{s=A} = \Pr\{n < \theta - A\} \\ &= \int_{-\infty}^{\theta-A} p(n)dn \qquad (3.9) \\ P_{Y|S}\,(1|1) &= 1 - P_{Y|S}\,(0|1) \qquad (3.10) \end{aligned}$$

and the marginal density is

$$P_Y\,(y) = \sum_S P_{Y|S}\,(y|s)\,P_S\,(s) \tag{3.11}$$

The performance measure is Shannon's mutual information. The discrete mutual information of the input S and output Y is the difference between the output unconditional entropy $H(Y)$ and the output conditional entropy $H(Y|S)$ conditioned on the input:

$$
\begin{aligned}
I(S,Y) &= H(Y) - H(Y|S) && (3.12)\\
&= -\sum_{y} P_Y(y) \log P_Y(y) \\
&\quad + \sum_{s}\sum_{y} P_{SY}(s,y) \log P_{Y|S}(y|s) && (3.13)\\
&= -\sum_{y} P_Y(y) \log P_Y(y) \\
&\quad + \sum_{s} P_S(s) \sum_{y} P_{Y|S}(y|s) \log P_{Y|S}(y|s) && (3.14)\\
&= \sum_{s}\sum_{y} P_{SY}(s,y) \log \frac{P_{SY}(s,y)}{P_S(s)\,P_Y(y)} && (3.15)
\end{aligned}
$$

So the mutual information is the expectation of the random variable $\log\left[P_{SY}(s,y)/P_S(s)\,P_Y(y)\right]$:

$$
I(S,Y) = E\left[\log \frac{P_{SY}(s,y)}{P_S(s)\,P_Y(y)}\right] \tag{3.16}
$$

Here $P_S(s)$ is the probability density of the input S, $P_Y(y)$ is the probability density of the output Y, $P_{Y|S}(y|s)$ is the conditional density of the output Y given the input S, and $P_{SY}(s,y)$ is the joint density of the input S and the output Y. Simple bipolar histograms of samples can estimate these densities in practice. The mutual information is the relative entropy between the joint density P_{SY} $(s,\ y)$ and the product density $P_S(s)P_Y(y)$. We note that the mutual information is zero if S and Y are independent and give log(1) = 0: The joint density is the product of the marginal densities: $P_{SY}(s,y) = P_S(s)P_Y(y)$. Jensen's inequality [95] implies that the mutual information is nonnegative: $I(S,Y) \geq 0$.

The proof of the theorem shows that if $I(S,Y) > 0$ then eventually the mutual information $I(S,\ Y)$ tends toward zero as the noise variance tends toward zero for subthreshold signals. So the mutual information $I(S,\ Y)$ must increase as the noise variance increases from zero. The proof uses the fact that $I(S,\ Y) = 0$ if and only if S and Y are statistically independent. This reduces the proof to showing that S and Y are asymptotically independent: $I(\sigma) \rightarrow 0$ as $\sigma \rightarrow 0$ or equivalently that $P_{SY}(s,y) = P_S(s)P_Y(y)$ or that $P_{Y|S}(y|s) = P_Y(y)$ as $\sigma \rightarrow 0$.

Theorem 1. Suppose that the threshold neuron Equation (3.6) has noise probability density function $p(n)$ and that the input signal S is subthreshold ($A < \theta$). Suppose that there is some statistical dependence between input random variable S and output random variable Y (so that $I(S;Y) > 0$). Suppose that the noise mean $E[n]$ does not lie in the signal-threshold interval $(\theta - A, \theta + A)$ if $p(n)$ has finite variance. Then the threshold neuron (3.6) exhibits the nonmonotone SR effect in the sense that $I(S,Y) \rightarrow 0$ as $\sigma \rightarrow 0$.

Theorem 2. Suppose $I(S,Y) > 0$ and the threshold neuron Equation (3.6) uses α-stable noise with location parameter $a \notin (\theta - A, \theta + A)$ Then the neuron (3.6) exhibits the nonmonotone SR effect if the input signal is subthreshold.

3.2.2 Noise-Enhanced Nanotube Detector Experiments

The nanotube experiments confirmed the SR prediction for nanometer-wide transistors detecting weak Bernoulli signals in noise and for both finite-variance and infinite-variance noise. The nanotube detector exhibited the SR effect by comparing the random Bernoulli input signal to the random output and computing Shannon's mutual information, the normalized correlation measure, and the inverted bit error rate.

Each of the nanotube experiments applied 32 independent trials of 1,000-symbol input sequences for 25 noise levels per type and over a range of gate voltages. The

25 sampled noise levels ranged from 0.001 to 1 standard deviation σ (dispersion γ for infinite-variance Cauchy) linearly in logarithmic scale. The noisy input S was a *synchronized* Bernoulli sequence $s_i = b_i + n_i$ of the sum of random subthreshold binary values b_i and additive white noise n_i of three types. So there was no *timing* noise in the pulse train as in the FHN neuron model [368], [369]. Synchronization allows the nanotube systems to implement a variety of algorithms from signal processing and communications.

The gate voltages in Figure 3.4 were ON= -1.6 V and OFF= -1.4 V for the two equally likely symbols. The experiments updated the noisy input symbols s_i about once every 10 ms. A 200 mV drain-source voltage biased the nanotube at room temperature in vacuum. The experiment measured and averaged 10 samples of the detector output at 100 kilo-samples per second near the end of each symbol interval to estimate the output symbols y_i.

Setup for the Nanotube Detector Experiments

The experiment tested a carbon nanotube field effect transistor (FET) as a threshold detector with subthreshold signal plus noise. The detector consisted of a singlewall semiconductor carbon nanotube bridging two electrodes in Figure3.5. Reference [250] contains details of the fabrication. A voltage is subthreshold if it is more positive than a p-type FET's threshold voltage and produces picoamp current in an OFF state. The experiments tested whether noise could enhance subthreshold signals to produce measurable currents.

The detector had titanium-gold electrodes for the source and the drain terminals and used the p-doped silicon substrate as a backgate. The nanotube was pristine (undoped) and was in ohmic contact with the electrodes that consisted of 20 nm Ti and 60 nm Au

on top of the ends of the nanotube. A thin layer of silicon dioxide (500 nm) insulated the nanotube from the p-doped backgate.

The CVD technique combined with e-beam lithography to grow a singlewall nanotube that was less than 2 nm in diameter and 3-5 micrometers (μm) long between the two electrodes for our nanotube detector. The gap between the electrodes was approximately 3 μm wide but the singlewall nanotube was not straight as it spanned the gap. Atomic force microscopy produced the image of the detector in Figure 3.5 and showed that the nanotube had a diameter $d < 2$ nm that was consistent with a singlewall nanotube.

Four steps prepared the nanotube detector that started from a piece of wafer to a chip carrier in a cryostat: transistor screening, wafer cutting, wire bonding, and vacuum pumping. The screening step measured the current-voltage I-V_D characteristics of every metal contact pairs on the wafer to identify the conducting devices, measured the I-V_G of those conducting pairs to identify the semiconductors, and applied atomic force microscopy to verify that the semiconductors were nanotubes.

The cutting step broke the silicon wafer into smaller chips that would fit in a chip carrier while a polymer coating protected the detector from any debris. The bonding step gave a detector the electrical connection to a test equipment from inside a chip carrier and a vacuum. A wire-bonding machine applied pressure and short bursts of ultrasound to fuse gold wires to the chip carrier's bonding posts on the one end and to the silicon chip's contact pads on the other end. The pumping step held a detector and its carrier in a cryostat at room temperature while a vacuum pump evacuated air and contaminants such as water.

A Hewlett Packard 4156B Semiconductor Parameter Analyzer characterized the transistor behavior in the current-voltage plots in Figure 3.6. The analyzer produced a current-drain voltage (I-V_D) curve by sweeping the drain-source voltage while holding

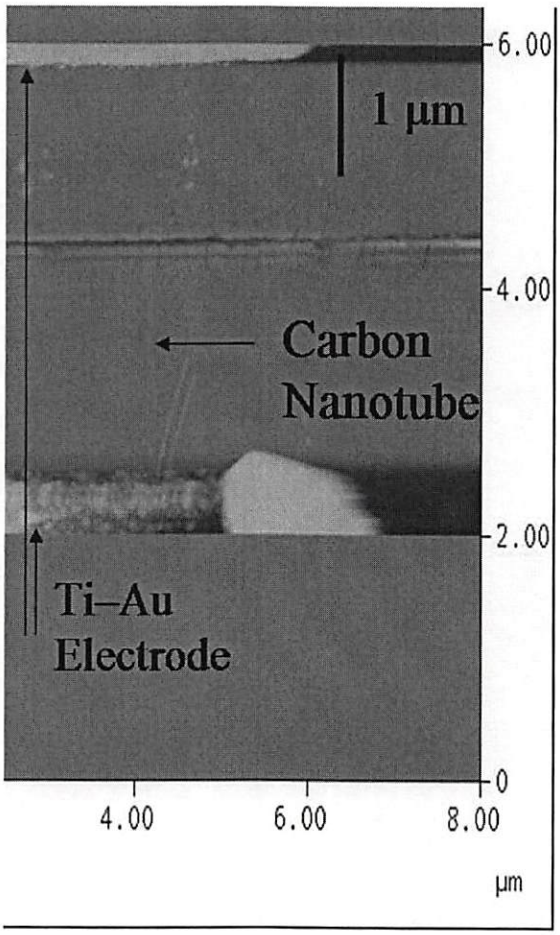

Figure 3.5: Micrograph of a nanotube bridging two electrodes. Atomic force microscope (AFM) captured an image of the detector. The nanotube was three to five μm long between the Ti-Au electrodes at the top and bottom of the image and less than 2 nm in diameter according to the AFM.

the gate voltage constant. The analyzer produced a current-gate voltage (I-V_G) curve by sweeping the gate voltage while holding the drain-source voltage constant at small voltages to avoid channel pinch off.

Figure 3.4(c) plotted the detector's output current Y against the input voltage S and showed the p-type transistor behavior of the detector with little hysteresis. Linear regression estimated the transconductance and the threshold voltage. The estimated threshold voltage is where the regression line intersects the bottom axis. These estimated

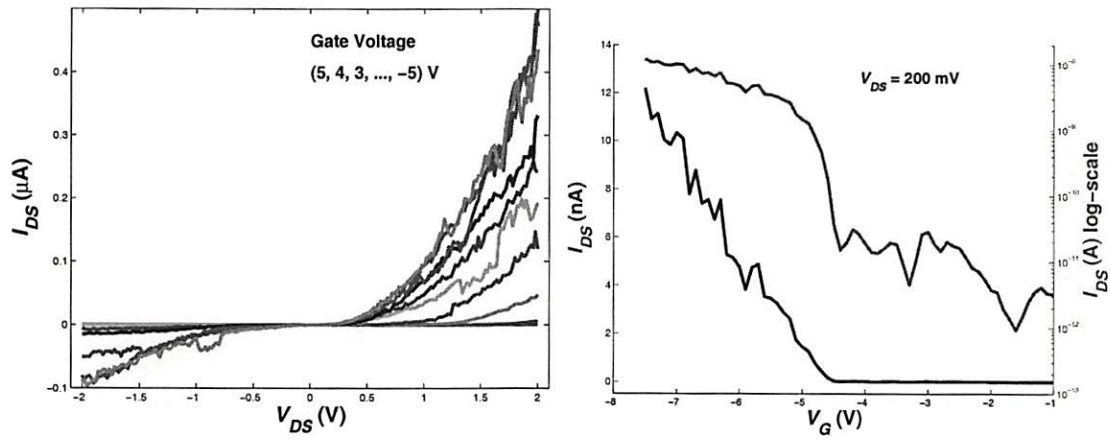

(a) I-V_{DS} (b) I-V_G

Figure 3.6: Nanotube transistor gate effect. A Hewlett Packard 4156B Semiconductor Parameter Analyzer showed the nonlinearity as the transistor's current I varied with its gate voltage V_G. (a) I-V_D: The HP4156B varied the drain-source voltage V_D from -2 V to 2 V while keeping V_G constant. Each curve corresponds to a different $V_G \in \{-5, -4, -3, \ldots, 4, 5\}$ V. (b) I-V_G: The V_D was constant at 200 mV while the V_G stepped from -7.5 V to 7.5 V in a single sweep.

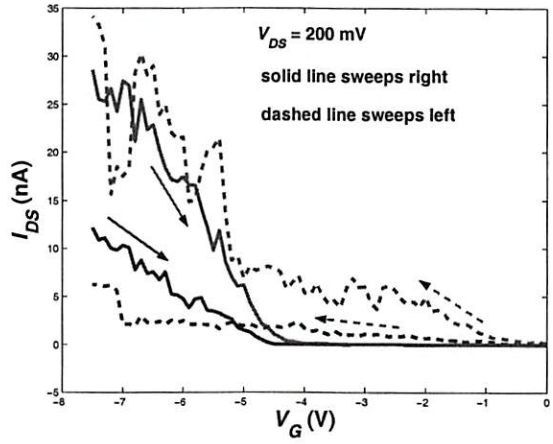

Figure 3.7: Nanotube transistor hysteresis. The HP 4156B performed a double sweep of the gate voltage: V_G stepped up from -7.5 V to 7.5 V then stepped down to -7.5 V. The arrows in the plot show the directions of the voltage sweeps. The drain-source voltage was 200 mV. Exposure to vacuum changed the hysteretic loop (blue). Solid line is for sweeps to the right. Dashed line is for sweeps to the left. We note that researchers have reduced hysteresis by coating the nanotube devices with a layer of PMMA polymer and heating the coated devices [247].

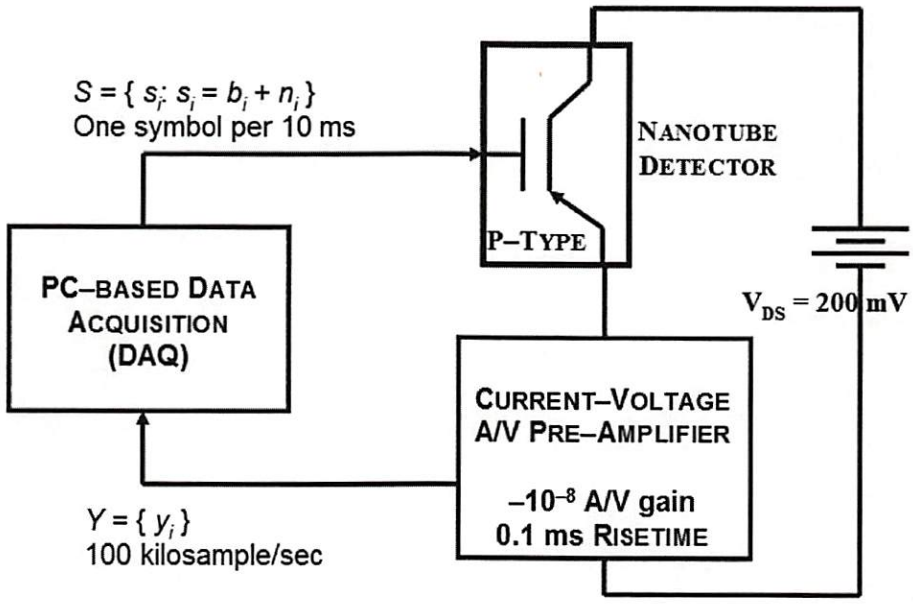

Figure 3.8: Equipment for the nanotube noise experiments. The threshold detector was a p-type carbon nanotube field effect transistor. The input was the gate voltage and the output was the current of the nanotube detector. The DAQ updated the input symbols about once every 10 ms to allow the data acquisition and the amplifier hardware to reach steady state. Each output symbol was the average of 10 DAQ measurements near the end of the symbol interval. Each of the nanotube experiments applied 32 independent trials of 1,000-symbol input sequences for 25 noise levels per type and over a range of gate voltages. The 25 sampled noise levels ranged from 0.001 to 1 standard deviation σ (dispersion γ for infinite-variance Cauchy) linearly in logarithmic scale. A cryostat provided the electrical connection between the detector and the laboratory and kept the detector in a vacuum and at room temperatures.

parameters differed from those of the $I - V_G$ curve that the semiconductor analyzer produced in Figure 3.6(b). The hysteretic effect could account for the differences: Different parts of the hysteretic loop gave different parameters for the gate effect. The experiments used input voltages that changed magnitudes at random and produced data in Figure 3.4(c) that averaged the hysteretic effect.

Figure 3.8 shows the equipment setup for the experiments. A PC-based National Instruments PCI-MI0-16XE-10 data acquisition (DAQ) board converted the noise-corrupted signal S from digital to analog (DA) and converted the conditioned noisy output Y from analog to digital (AD). The AD-DA conversion has a 16-bit resolution and a 10 microsecond (μs) rise time. The DAQ board has a selected input voltage range in the interval $[-5, 5]$V for AD conversion and a fixed output voltage range in the interval $[-10, 10]$V for DA conversion. A voltage divider divided the smallest output voltage increment by two. This improved the resolution of the DAQ's analog output voltage but reduced the dynamic range of the DA conversion to the interval $[-5, 5]$V.

A DL 1211 current-voltage preamplifier conditioned the detector output current$Y$ before data acquisition sampled it as a voltage. The amplifier converts a small current (10 nA) into a large voltage (1 V) with the 10^{-8} A/V gain setting. The analog voltage has a maximal time delay of 0.1 ms with the 0.1 ms rise-time setting.

A software driver in LabView produced the random signal S and the additive noise, timed the update of the noisy signal sequence, and supervised the DA and AD conversions. The LabView program provided the uniform random number generator. The driver converted the uniform random number into zero mean white Gaussian sequences, zero mean white uniform sequences, zero-location white Cauchy sequences, and independent Bernoulli sequences with equal symbol probabilities ($p = q = 1/2$).

Nanotube field effect transistor technology produced detectors that could exhibit hysteresis [247], [168], [388] or react to adsorbed molecules [355] [93] [249]. The detector was not ideal because its conductance, gate effect, and hysteresis changed over time. The detector exhibited some hysteresis but not enough to prevent the SR effect. A current-voltage I-V_G curve showed the hysteretic loop in Figure 3.7. The threshold voltage and the transconductance changed with a direction change of the gate voltage

sweep. Charge trapping by water molecules on the silicon dioxide surface could cause hysteresis [247].

We designed the experiments to prevent the non-ideal detector properties from confounding the results. The experiments treated the nanotube detector as a *memoryless* discrete-time threshold. So the experiments did not treat the hysteretic detector as a bistable dynamical device such as the optical bistable system in [333]. We kept the detector in vacuum to reduce the hysteretic effect but some effect persisted even after 72 hours in vacuum. The experiments applied subthreshold symbols that were at least two standard deviations away from the far left leg of the deterministic hysteretic loop.

Plotting the detector's random output Y as a function of its noisy input S gave a *stochastic* I-V_G curve that showed the non-ideal but threshold-like gate effect of a transistor in Figure 3.4(c). The input signals had short hold times, small voltage ranges, and rapid voltage transitions. This differed from the *deterministic* voltage sweeps that had longer hold times, large voltage ranges, and slow transitions that gave the I-V_G curve in Figure 3.6(b) and the hysteretic curves in Figure 3.7. Again the hysteresis did not prevent the observation of the SR effect.

Nanotubes Stochastically Resonate in Experiments

The experiment found the SR effect for mutual information, normalized correlation, and inverted bit error rate for Gaussian (Figure 3.9) and uniform (Figure 3.10) noise and for four combinations of binary symbols (a)$(-2.0, -1.8)$ V, (b)$(-1.8, -1.6)$ V, (c)$(-1.6, -1.4)$ V, and (d)$(-1.4, -1.2)$ V. Each pair had a 0.2-volt separation because sensitivity analysis showed that the separation gave complete SR modes within the range of noise levels. A linear regression of the transistor's gate effect estimated the threshold voltage and aided the selection of the subthreshold ON/OFF symbols. Figure 3.4(b) enlarges Figure 3.9(c) and shows the SR effect for additive white Gaussian noise and

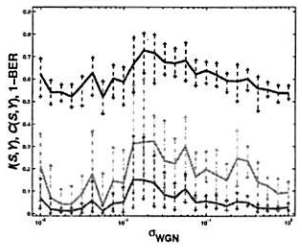

(a) ON = −2.0V and OFF = −1.8V

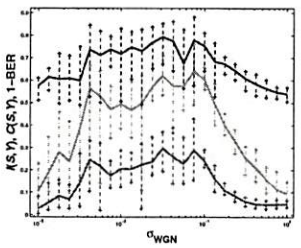

(b) ON = −1.8V and OFF = −1.6V

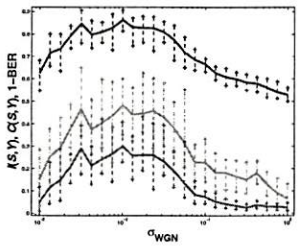

(c) ON = −1.6V and OFF = −1.4V

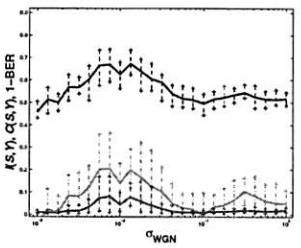

(d) ON = −1.4V and OFF = −1.2V

Figure 3.9: SR for additive white Gaussian noise. The detector performance exhibited SR for four combinations of gate voltages: The inverted bit error rate 1–BER (top blue), correlation measure $C(S, Y)$ (middle green), and mutual information $I(S, Y)$ (bottom red) increase for small amounts of noise and then decrease for larger amounts. The SR mode or optimal noise level σ_{opt} was the same standard deviation value between 0.01 and 0.1 for (a) and (b) and about 0.01 for (c) and (d). Each vertical dashed bar shows the maximal and minimal range of 32 averaged experimental trials. The solid polygonal line connects the means of 25 sets of experiments that sampled the range of noise levels between 0.001 and 1 standard deviations. The SR experiments used four combinations of input gate voltages to test the nanotube detector. (a) ON = −2.0V and OFF = −1.8V. (b) ON = −1.8V and OFF = −1.6V. (c) ON = −1.6V and OFF = −1.4V. (d) ON = −1.4V and OFF = −1.2V.

for the subthreshold signal pair ON = −1.6 V and OFF = −1.4 V. The SR mode of the mutual-information curve is six times the value at minimal noise. The SR mode of the correlation-measure curve is three times the value at minimal noise. The SR mode of the inverted bit-error-rate curve shows a forty percent improvement over the value at minimal noise.

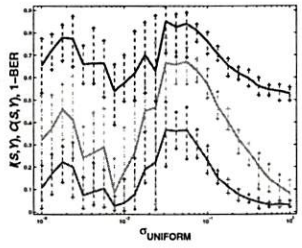

(a) ON = -2.0V and OFF = -1.8V

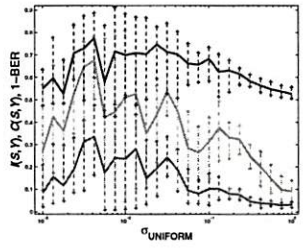

(b) ON = -1.8V and OFF = -1.6V

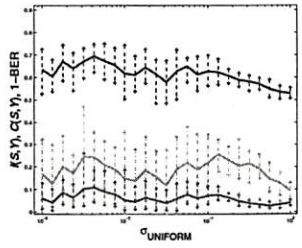

(c) ON = -1.6V and OFF = -1.4V

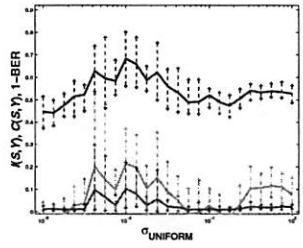

(d) ON = -1.4V and OFF = -1.2V

Figure 3.10: SR for additive white uniform noise. The SR effect occurred for four combinations of gate voltages and for three performance measures: Top blue for the inverted bit error rate, middle green for the input-output correlation, and bottom red for the mutual information. Two of the four plots appear to have multimodal SR curves. Each plot used one of four combinations of input gate voltages. (a) ON = -2.0V and OFF = -1.8V. (b) ON = -1.8V and OFF = -1.6V. (c) ON = -1.6V and OFF = -1.4V. (d) ON = -1.4V and OFF = -1.2V.

We also passed impulsive or infinite-variance white noise through the nanotube detector to test whether it was robust to occasional large noise spikes. We chose the highly impulsive Cauchy noise [256] for this task. This infinite-variance noise had the probability density function

$$p(n) = \frac{1}{\pi}\left(\frac{\gamma}{n^2 + \gamma^2}\right) \tag{3.17}$$

for zero location and finite dispersion γ. Not all Cauchy experiments produced a measurable SR effect: Figure 3.11(a) shows that a diminished SR effect still persists for Cauchy noise with subthreshold signal pair ON = -2.0 V and OFF = -1.8 V.

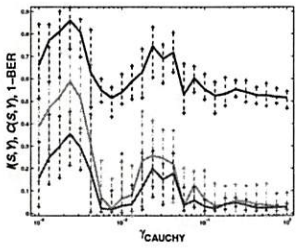

(a) ON = -2.0V and OFF = -1.8V

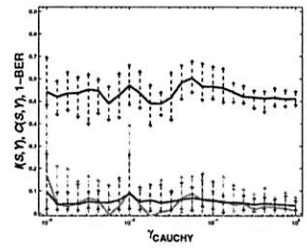

(b) ON = -1.8V and OFF = -1.6V

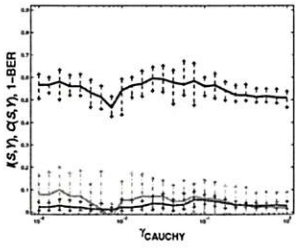

(c) ON = -1.6V and OFF = -1.4V

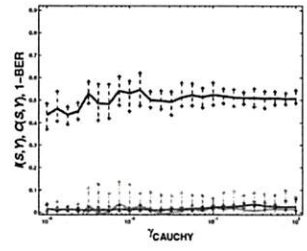

(d) ON = -1.4V and OFF = -1.2V

Figure 3.11: Robust SR for additive white Cauchy noise. The Cauchy-noise experiments produced a measurable SR effect for at least one combination of gate voltages and for three performance measures: the bottom red mutual information, the middle green cross correlation, and the top blue inverted bit error rate. This highly impulsive noise has infinite variance and infinite higher-order moments. The plot in (a) shows clear SR effect with more than one mode. The large SR mode lies at dispersion $\gamma \approx 0.003$. A second SR mode lies at dispersion $\gamma \in (0.3, 0.4)$. The plots in (b) and (c) show an approximate SR effect for the SR mode occurring for dispersion of at least $\gamma = 0.05$ in (b) and $\gamma \approx 0.02$ in (c). Each plot used one of four combinations of input gate voltages. (a) ON = -2.0V and OFF = -1.8V. (b) ON = -1.8V and OFF = -1.6V. (c) ON = -1.6V and OFF = -1.4V. (d) ON = -1.4V and OFF = -1.2V.

The experiments detected an SR effect if a performance measure had at least one nonmonotonic "bump" or mode. Two statistical tests rejected the null hypothesis $\mathbf{H}_0$ that noise decreased the detector performance monotonically and so confirmed the nanotube-SR prediction. The hypothesis tests treated three averaged performance measures as probability density functions (pdf) and compared them to a monotonically decreasing β-pdf. The tests rejected the null hypothesis because three performance measures all exhibited one or more statistically significant modes for three types of additive noise.

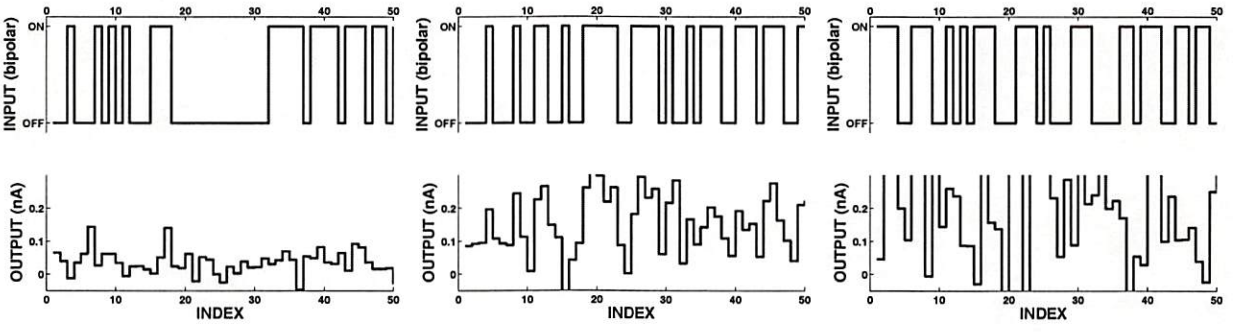

(a) $\sigma = 0.001$ (b) $\sigma = 0.01$ (c) $\sigma = 1.0$

Figure 3.12: Bernoulli input and detector output for Gaussian noise shows a SR effect. Three pairs of input and output sequences (column-wise) show that noise can help signal detection in a SR effect. The top row shows the random binary (Bernoulli) input where the symbol '$+1$' stands for ON and '-1' for OFF. The bottom row shows the detector output for three noise levels. (a) The detector output is small and not similar to the input for a low noise standard deviation $\sigma = 0.001$. (b) The detector output is similar to the input for the optimal noise standard deviation $\sigma_{opt} = 0.01$. (c) The detector output is large and not similar to the input for a large noise level ($\sigma = 1.0$). The output exceeds the scale in this plot. The transistor gate voltages were -1.6 V for the ON symbol and -1.4 V for the OFF symbol.

Some of the SR plots show more than one mode. Several researchers reported multimodal SR [285] [318] [452] in the plot of system performance against noise. The apparent multiple SR modes in the uniform experiments may be due to fluctuations. But the clear second mode for the Cauchy experiments may involve clipping: The limited dynamic range $[-5, 5]$ V of the data acquisition equipment may have produced the second peak in the graph as a truncation artifact because it clipped large spikes when it converted the infinite-variance Cauchy noise to voltage.

Plotting the input-output sequences S and Y also shows the stochastic resonance effect. Figure 3.12 shows three sample pairs of input and output sequences for different Gaussian noise standard deviations. A segment of the output sequence matches the input sequence better for near-optimal noise levels in Figure 3.12(b) than for too little noise in (a) or too much in (c).

The experiments measured the detector's performance with the mutual information, the normalized correlation measure, and the inverted bit error rate. They measured how well the output sequence matched the input. The performance measures were discrete-time functions. Shannon's mutual information used probability densities of the input and the output sequences.

A histogram of the output sequence Y gave the discrete probability density function

$$P(Y = Y_i) = p_i \tag{3.18}$$

that computed the unconditional Shannon entropy $H(Y) = -\sum_{i=1}^{N} p_i \ln p_i$ for mutual information without converting the detector output into a binary sequence with a threshold scheme. The histogram applied 120 equal-sized bins to the output sequence. Sorting the output sequence based on the binary input symbols and then applying the histogram gave the conditional output discrete probability density function

$$P_{Y|S}(Y = Y_i|S = S_j) = \frac{p_{ji}}{p_j} \tag{3.19}$$

conditioned on the input symbols that computed the conditional entropy $H(Y|S) = -\sum_{i=1}^{N}\sum_{j=1}^{N} p_{ji} \ln\left(\frac{p_{ji}}{p_j}\right)$. The mutual information measure was the difference between the unconditional and the conditional output entropies (3.12).

The correlation measure was the scalar inner product of the input and output sequences. A cross-correlation sequence compared the input and output symbol sequences and gave a measure of their match for different lag values:

$$r_{SY}(l) = \sum_{k=1}^{N} s(k)y(k-l) \tag{3.20}$$

where the capital letters S and Y denoted the length-N random sequences and the lower case letters $s(k)$ and $y(k)$ denoted values at some index k. The zero-lag ($l = 0$) value of the cross correlation sequence (3.21) gave the scalar performance measure that compared the input and output random sequences. Subtracting the sample mean from the output sequence improved the match between similar input and output sequences. The input Bernoulli sequence was approximately zero mean. The computation used $+1$ for the equally likely ON symbol and -1 for OFF so equal numbers of $+1$'s and -1's gave exactly zero mean.

A normalization scheme divided the zero-lag cross correlation $r_{SY}(0)$ by the square root of the energy of the input and output sequences and gave the normalized correlation measure [427], [356]:

$$\begin{aligned} C(S,Y) &= \frac{r_{SY}(0)}{\sqrt{|S|}\sqrt{|Y|}} \\ &= \frac{\sum_{k=1}^{N} s(k)y(k)}{\sqrt{\sum_{k=1}^{N} s(k)s(k)}\sqrt{\sum_{k=1}^{N} y(k)y(k)}} \end{aligned} \tag{3.21}$$

where the energy of a sequence is the same as the zero-lag value of its autocorrelation:

$$|x| = \sum_{k=1}^{N} x^2(k) = \sum_{k=1}^{N} x(k)x(k-l)|_{l=0} = r_{XX}(0) \tag{3.22}$$

The bit error rate measures how often a received bit or detector output y_i differs from the transmitted bit or input s_i. The experiments used complete information of the transmitted signal s_i and computed a threshold or discriminant function to classify the received bit y_i. Sorting by the input bit divided the output sequence into two clusters:

one for each input binary symbol. Optimal two-class discrimination [130] was the midpoint between the two cluster means:

$$g(\sigma) = \frac{1}{2}\left[\frac{1}{N_{ON}}\sum_{i=1}^{N_{ON}}(y_i|s_i = ON) + \frac{1}{N_{OFF}}\sum_{i=1}^{N_{OFF}}(y_i|s_i = OFF)\right] \tag{3.23}$$

based on the sequences for each sampled noise standard deviation σ (dispersion γ for Cauchy noise). The threshold scheme converted an output Y to a binary sequence

$$Y_{binary}(y_i, g) = \begin{cases} 1 \text{ for } y_i \geq g \\ 0 \text{ for } y_i < g \end{cases} . \tag{3.24}$$

to compute the frequency of mismatch between the input and output binary sequences: BER = N_{error}/N where N_{error} is the number of mismatching bits in a length-N sequence.

An increase in the bit-error-rate measure (BER) denotes a decrease in performance. So we inverted the BER by subtracting it from unity: 1–BER = $N_{correct}/N$ by counting the number of matching bits $N_{correct}$ and created a convex (cup down) SR curve. We note that the BER measure has values in the range $[0, 0.5]$ and that the 1–BER measure has values in the range $[0.5, 1]$. The apparent offset is due to the threshold detection of binary signals with two equally likely and subthreshold symbols. Both subthreshold symbols appear as OFF or '0' to the nanotube detector. So the maximal value of the BER measure (or 1–BER) denotes that half of the subthreshold symbols are wrong (or correct).

The nanotube experiments confirmed the SR prediction [256] after simulations extended the sign threshold (3.6) result to the transistor nonlinearity. The nanotube detector exhibited a threshold-like gate effect: It had negligible conductance or gave picoamp current for subthreshold gate voltages ($V > V_T$). The current varied linearly

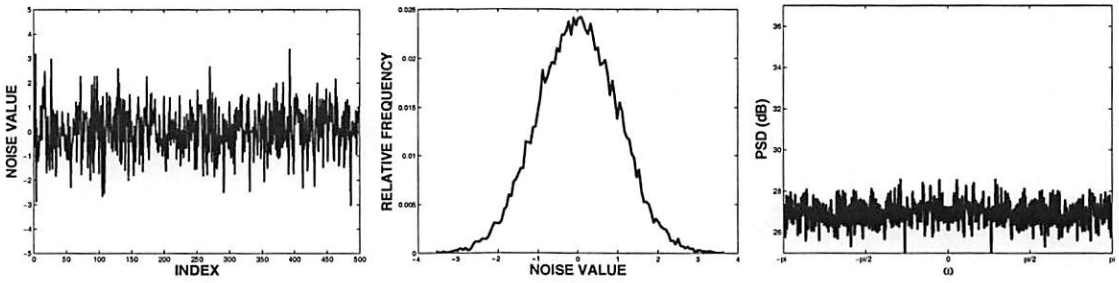

(a) Gaussian Noise Sample (b) Histogram pdf (c) Power Spectral Density

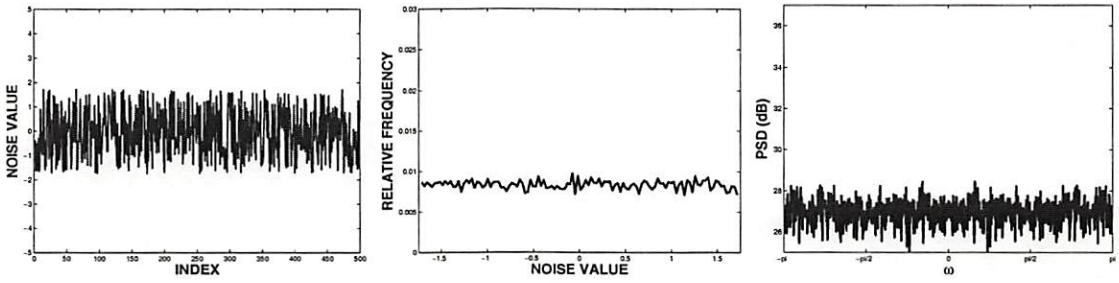

(d) Uniform Noise Sample (e) Histogram pdf (f) Power Spectral Density

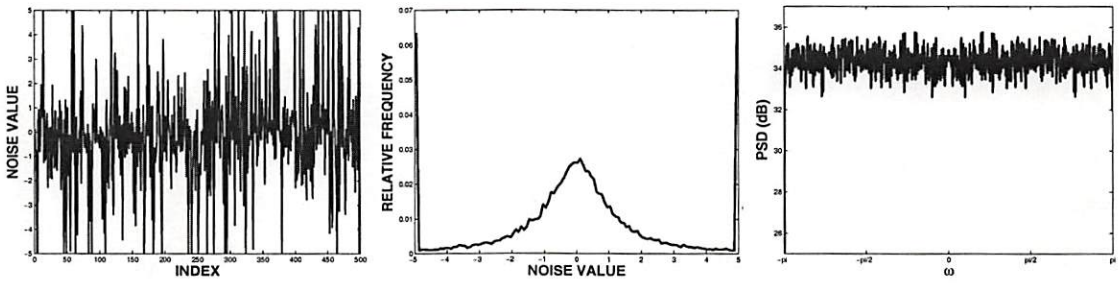

(g) Cauchy Noise Sample (h) Histogram pdf (i) Power Spectral Density

Figure 3.13: Gaussian, uniform, and Cauchy noise samples. Additive white (a) Gaussian, (d) uniform, and (g) clipped Cauchy noise samples. The noise samples had unit standard deviation $\sigma = 1.0$ ($\gamma = 1.0$ for Cauchy). (b), (e), and (h) show the histograms of the noise samples and estimate the discrete probability density function of the noise. (c), (f), and (i) show the discrete noise power spectral density. Cauchy bell curves have fatter tails than do Gaussian bell curves: The impulsive Cauchy noise produces outliers more frequently. Clipping large values to ± 5 removed the occasional large spikes and produced the two peaks on either side of the Cauchy bell curve in (h). The discrete power spectrum is flat over the $[-\pi, \pi]$ interval in (c), (f), and (i). The noise samples were uncorrelated in time.

with suprathreshold gate voltages ($V \leq V_T$) where the transconductance was the slope or gain.

The experiments applied discrete-time white noise of three types: Gaussian, uniform, and infinite-variance Cauchy noise. Figure 3.13 shows samples of the three noise types in (a), (d), and (g), their histograms in (b), (e), and (h), and their power spectra in (c), (f), and (i). A power spectral density of the discrete-time zero-mean noise $n(k)$ is a discrete-time Fourier transformation of its autocorrelation sequence

$$R_n\left(e^{j\omega}\right) = \sum_{l=-\infty}^{\infty} r_n\left(l\right) e^{-j\omega l} \tag{3.25}$$

where the autocorrelation sequence is $r_n\left(l\right) = \sum_{k=-\infty}^{\infty} n\left(k\right) n\left(k-l\right)$.

Hypothesis Tests for SR

Two statistical tests confirmed that the SR-curves were nonmonotonic. A goodness-of-fit test measures how well a candidate probability density function (pdf) matches a benchmark pdf given a set of data from the candidate pdf. The null hypothesis H_0 states that the two pdfs are the same. The test rejects the null hypothesis if a test statistic exceeds a critical value for a given significance level α. The significance level α denotes the probability of a Type-I error—-the probability of rejecting the null hypothesis when it is true. The p-value measures the credibility of the null hypothesis H_0 given the data. A statistical test rejects the null hypothesis H_0 at the significance level α if the p-value is less than the significance level: Reject H_0 if p-value $< \alpha$.

The popular β-pdf family has two shape parameters (α and θ) that give continuous pdfs over a finite-length interval such as the unit interval $[0, 1]$. Some of these β-pdf decrease monotonically. These include the β-pdf in Figure 3.14(a) with parameters $\alpha = 0.5$ and $\theta = 5$ among many others that we tested. Two types of goodness-of-fit tests

rejected the match between the candidate (normalized) SR curves and the monotonically decreasing β-pdf $\beta(0.5, 5)$. A β-pdf has the form

$$f_{\alpha,\theta}(x) = \frac{x^{\alpha-1}(1-x)^{\theta-1}}{B(\alpha,\theta)} \tag{3.26}$$

for $x \in [0, 1]$ and positive parameters $\alpha > 0$ and $\theta > 0$. The denominator term $B(\alpha, \theta)$ is

$$B(\alpha,\theta) = \int_0^1 x^{\alpha-1}(1-x)^{\theta-1}dx = \frac{\Gamma(\alpha)\Gamma(\theta)}{\Gamma(\alpha+\theta)} \tag{3.27}$$

with Γ function

$$\Gamma(n+1) = \int_0^\infty u^n e^{-u}du = n\Gamma(n) \tag{3.28}$$

for $n > 0$ ($\Gamma(1) = 1$ and $\Gamma(n+1) = n!$ if n is a positive integer). The β-pdf contrasts with the SR-curves because it is nonzero only for $x \in [0, 1]$ and because it decreases monotonically to zero as x increases to 1 for the parameters $\alpha = 0.5$ and $\theta = 5$.

The goodness-of-fit tests converted each averaged SR-curve to its equivalent pdf $f_{SR}(k)$. The conversion interpolated 25 averaged values so that the SR-curves had a uniform increment of $\Delta x = 0.001$ and were nonzero only in the interval $[0, 1]$. The conversion integrated (via discrete approximation) and normalized the SR-curves so that they integrated to one:

$$\int_{-\infty}^{\infty} f_{SR}(x)\,dx = \int_0^1 f_{SR}(x)\,dx \approx \sum_{k=1}^{N} f_{SR}(k)\,\Delta x = 1 \tag{3.29}$$

where f_{SR} is the normalized SR curve.

The χ^2-test compared the SR-pdfs (mutual information, correlation measure, and inverted bit-error-rate) to the β-pdf in Figure 3.14(a). We converted the pdf $f(k)$ to the

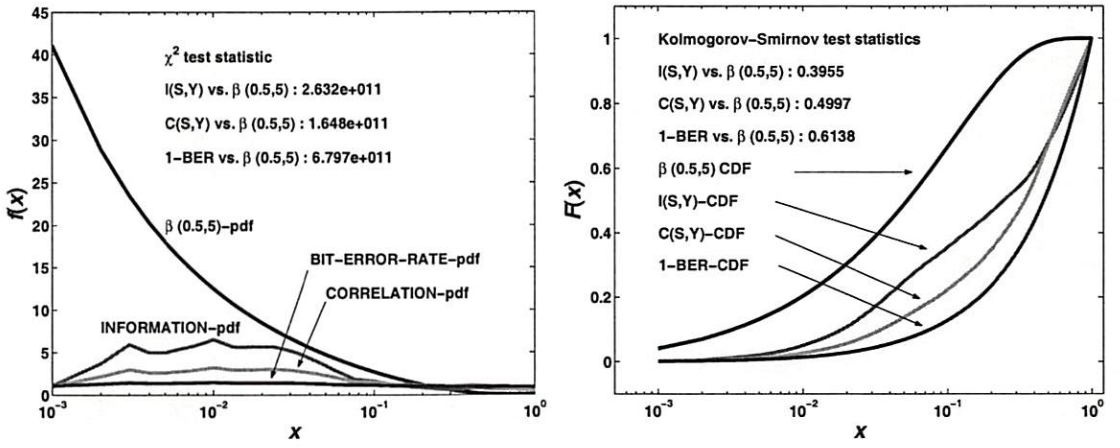

(a) pdf (b) CDF

Figure 3.14: The SR probability density functions and cumulative density functions. (a) The β-probability density function (pdf) and the SR-pdfs. The reference pdf (top black curve) had a β distribution with the parameters $\alpha = 0.5$ and $\theta = 5$ ($\sim \beta(0.5, 5)$) and decreased monotonically. A normalization scheme converted the SR-curves in Figure 3.4 (b) into their equivalent pdf f_{SR} (red for information, green for correlation, and blue for 1–BER). A test statistic that exceeded a critical value rejected the null hypothesis H_0: SR-pdfs $\sim \beta(0.5, 5)$ and so confirmed that the SR-curves were nonmonotonic. (b) The β-cumulative distribution function (CDF) and the SR-CDFs. Integrating the pdfs gave the CDFs. The $\beta(0.5, 5)$ pdf gave the top black CDF. The SR-pdfs gave the red (information), green (correlation), and blue (1–BER) CDFs. The CDF-based statistical tests removed a potential defect in the pdf-based test: The tail of the pdf could skew the test statistic if it gave near-zero values in the denominator of the test statistic. Rejecting the hypothesis H_0: SR-CDFs $\sim \beta(0.5, 5)$ confirmed that the SR-curves were nonmonotonic.

cumulative distribution function (CDF) $F(k)$ by integration (via discrete approximation):

$$F(x) = \int_{-\infty}^{x} f(u)\, du = \int_{0}^{x} f(u) du \approx \sum_{j=1}^{k} f(j)\, \Delta x = F(k) \tag{3.30}$$

The CDF appeared in both a χ^2-test and a Kolmogorov-Smirnov (KS) test: The tests compared the SR-generated CDFs to the β-CDF in Figure 3.14(b).

The goodness-of-fit test applied the χ^2-test with the null hypothesis H_0: SR-pdfs $\sim \beta(0.5, 5)$ and the alternate hypothesis H_a: SR-pdfs $\nsim \beta(0.5, 5)$ at the smallest level

of significance $\alpha = 0.001$. The test rejected the null hypothesis if the test statistic exceeded the critical value. The test statistic had the form

$$\chi^2_{test} = \sum_i \frac{(O_i - E_i)^2}{E_i} \tag{3.31}$$

where O_i was an observed value in the SR-pdfs and E_i was an expected value in the reference β-pdf. The critical value was $\chi^2_{critical} = 48.2679$ for the smallest level of significance $\alpha = 0.001$ and for degree of freedom $\nu = (k-1-m) = (25-1-2) = 22$ where k was the number of data and m was the number of parameters in the test. The test statistic was $\chi^2_{pdftest} = 2.632 \times 10^{11}$ for the mutual-information pdf, $\chi^2_{pdftest} = 1.648 \times 10^{11}$ for the correlation-measure pdf, and $\chi^2_{pdftest} = 6.797 \times 10^{11}$ for the inverted bit-error-rate pdf. So the χ^2-test showed that the monotonically decreasing β-pdf differed substantially from any of the SR-pdfs with p-value < 0.001.

A second χ^2-test based on the CDF removed a potential confounding factor in the pdf-based test: The small values in the tail of the pdf might skew the test statistic if it gave near-zero values in its denominator. The CDF-based goodness-of-fit test applied the null hypothesis H_0: SR-CDFs $\sim \beta(0.5, 5)$ and the alternate hypothesis H_a: SR-CDFs $\nsim \beta(0.5, 5)$. The test statistic was $\chi^2_{CDFtest} = 89.2559$ for the mutual information CDF, $\chi^2_{CDFtest} = 129.1207$ for the correlation measure CDF, and $\chi^2_{CDFtest} = 212.8394$ for the inverted bit-error-rate CDF. The test statistics greatly exceeded the critical value $\chi^2_{critical} = 48.2679$. The χ^2-test showed that the β-CDF differed substantially from the SR-CDFs with p-value < 0.001.

The Kolmogorov-Smirnov (KS) test for goodness-of-fit also tested how well the SR-CDFs matched a β-CDF for the null hypothesis H_0: SR-CDFs $\sim \beta(0.5, 5)$ and the alternate hypothesis H_a: SR-CDFs $\nsim \beta(0.5, 5)$. by comparing the CDF-based test statistic to the critical value $KS_{critical} = 0.32$ for the smallest significance level $\alpha =$

0.01 and for $n = 25$ (number of data). The test statistic equaled the largest difference between the observed and the expected CDF values:

$$KS_{test} = \max_i (|O_i - E_i|) \tag{3.32}$$

where O_i was an observed value in the SR-CDF and E_i was an expected value in the reference β-CDF. All three test statistics exceeded the critical value: $KS_{test} = 0.3955$ for the mutual-information CDF, $KS_{test} = 0.4997$ for the correlation-measure CDF and $KS_{test} = 0.6138$ for the bit-error-rate CDF. So the KS-test rejected the null hypothesis and showed that the monotonic decreasing β-CDF differed from the SR-CDFs with p-value < 0.001.

We performed control experiments to verify that the SR effect occurred for the nanotube. The control experiments had no nanotube bridging the source and drain electrodes and applied only additive Gaussian noise. The transistor had no gate effect in the absence of a nanotube: it gave sub-nano amp current for any gate voltage. The control showed no SR-effect: the performance curves were flat for any noise level and for any gate voltage.

The SR-detection results should hold for different nanoscale transistors because the SR prediction applied to transistor and other threshold-like nonlinearities. These results suggest that noise can improve nanosensor sensitivity if the devices adapt to the available noise by changing thresholds. The threshold modification can be field programmable with the addition of select chemicals or electric fields for ambient noise that is greater than the optimal noise. The detection system can also adaptively add noise to improve sensitivity for less-than-optimal ambient noise.

Chapter 4

Nanotube Antennas Can Directly Detect Electromagnetic Signals

Nanotube-dipole antennas can detect narrowband electromagnetic (EM) signals. We present a new nanotube-antenna theorem in this chapter. The theorem predicts that multiwall nanotube (MWNT) dipole antennas should resemble thin-wire dipole antennas for nanotube EM-wave propagation at or near the free-space velocity of light. Nanotube antennas can resonate, have diameter-dependent narrow bandwidths, and can apply to array designs similar to thin-wire dipoles. The antenna prediction can apply to quantum conductors that satisfy a central assumption on wave propagation and antenna current distribution.

Multiwall nanotubes and single-crystal nanowires can act as resonant dipole antennas that can integrate with nanoscale electronics if technology can reduce their intrinsic resistance. Both multiwall-nanotube and single-crystal nanowire-based dipole antennas can be highly-selective narrowband detectors because they have high length to diameter ratios [431] [386] [212] [478]. Both MWNT and single-crystal NW can conduct better than similar-sized poly-crystal metal wires that can suffer from grain-boundary effects [46] or can fail due to electromigration [201] [446].

MWNT antennas in an all nanotube architecture can have another advantage over nanoscale metal wires: Nanotube (NT) wires can connect NT devices and NT antennas without metal-NT junctions. The junction between metal and a nanotube can produce high impedance Schottky diodes [202]. Researchers are studying nanotube

interconnections [103], [367] and could one day produce an all-nanotube architecture with low junction impedance.

Section 4.1 presents the nanotube-antenna analysis and prediction. Section 4.2 discusses how nanotubes can directly process electromagnetic signals in a cochlear-model spectral processing.

4.1 Nanotubes Can Detect Narrowband Electromagnetic Signals Because They Are Narrow Resonant Dipole Antennas

Quantum-conductor dipole analysis predicts that nanotubes can be dipole antennas similar to thin-wire dipoles. This prediction applies if the velocity of EM wave propagation v_p in nanotubes is at or near the free-space speed of light c. Antenna analysis estimated the complex self impedance $Z_{in} = R_{in} + jX_{in}$ of a lossless nanotube dipole and found that nanotube impedance is similar to that of thin-wire dipoles for $v_p \approx c$. So nanotube antennas can resonate and have narrow bandwidth similar to thin-wire dipoles.

Nanotube dipoles have thin-wire-like resonant length and radiation resistance for small quantum-induced changes in EM-wave propagation. Figure 4.1 plots nanotube self impedance versus normalized nanotube length and compares the perfect-conductor case $k_p = k_0$ and a limited quantum-conductor case $k_p \approx k_0$. The free-space wave number k_0 is a function of free-space wavelength λ that is a function of c: $k_0 = 2\pi/\lambda$ and $\lambda = \omega/c$. The quantum-limited wave number k_p is a function of quantum-compressed wavelength λ_p. Nanotube dipoles can have a fundamental resonant length that is approximately half free-space wavelength $l \approx \lambda/2$ for small changes in the velocity of EM-wave propagation $v_p \approx c$ that lead to $k_p \approx k_0$.

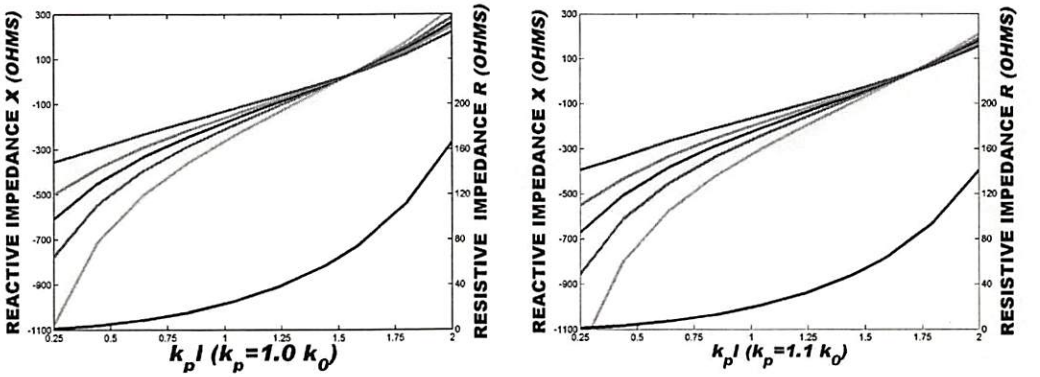

(a) $k_p = k_0$ (b) $k_p \approx k_0$

Figure 4.1: Similarity between nanotube and thin-wire dipole impedance for $k_p \approx k_0$. The figures plot the real and imaginary parts of impedance versus a normalized dipole length $k_p l$. (a) $k_p = k_0$ corresponds to the perfect-conductor case. (b) $k_p = 1.1 \cdot k_0$ corresponds to a weak quantum-conductor case. The top five color curves are nanotube input reactance for five different dipole diameters as a function of compressed wavelength. The five diameters a/λ_p are 0.009525 (red), 0.006350 (green), 0.004763 (blue), 0.003175 (magenta), and 0.001588 (cyan) from top to bottom. The bottom-most black curve is the nanotube input reactance.

The estimated nanotube impedance predicts resonance for approximately half-wave dipole lengths because the estimated half-wave impedance has zero reactance (or imaginary part of impedance). Resonant dipoles have zero reactance according to antenna theory [382]. Wang et al. have demonstrated optical-frequency antenna length effect for arrays of multiwall nanotubes [458]. The observed nanotube-antenna length effect has free-space wavelengths and so supports the predicted thin-wire-like resonant lengths for nanotube antennas.

Nanotube dipoles can have narrower bandwidths than thin-wire dipoles due to smaller diameter-to-length ratios. Nanotubes have smaller ratios because they are nanometers in diameter [431] and can be many micrometers [492] to millimeters [212] in length. Dipole-reactance curves have slopes that steepen with decreasing dipole diameter-to-length ratios (Figure 4.1). Steeper slopes correspond to narrower

bandwidths because small changes in frequency cause large changes in reactance. So nanotube dipoles have narrower bandwidth than thin-wire dipoles.

The estimated impedance has resistance (or real part of impedance) that resembles free-space resistance for the fundamental resonant-dipole length. So nanotube dipoles have thin-wire like radiation efficiency for $k_p \approx k_0$.

The estimated resistance is the nanotube radiation resistance because the analysis has a low-resistive loss assumption (lossless case). An efficient antenna radiates most or all of its input signal power if its radiation resistance matches free-space resistance because the matched-load case produces little or no wave reflection [382]. The lossless case gives a kind of best case estimate in the sense that non-zero intrinsic ohmic losses in the conductor reduces antenna radiation.

The similarity between nanotube impedance and thin-wire impedance also suggests that thin-wire based uniform-linear-array designs [147] can apply to nanotubes. The array design can increase nanotube-antenna sensitivity because nanotube-dipole arrays can gain sensitivity by adding array elements. A corollary to the nanotube-antenna theorem shows that nanotubes have thin-wire-like mutual impedances. This mutual impedance similarity directly supports array designs using nanotubes.

Nanotube dipoles can fail to resonate for large reductions in the velocity of EM wave propagation $k_p >> k_0$. Figure 4.2(a) plots nanotube reactance as a function of normalized dipole length for $k_p = 1.45 \cdot k_0$. The estimated nanotube reactance becomes more negative with small increases in k_p (Figure 4.1) and eventually becomes all negative (Figure 4.2(a)). Nanotube dipoles do not resonate for $k_p >> k_0$ due to nonzero estimated reactance.

Figure 4.2(b) plots nanotube resonant resistance as a function of k_p. The radiation resistance falls rapidly as k_p increases. Nanotube dipoles can become very inefficient

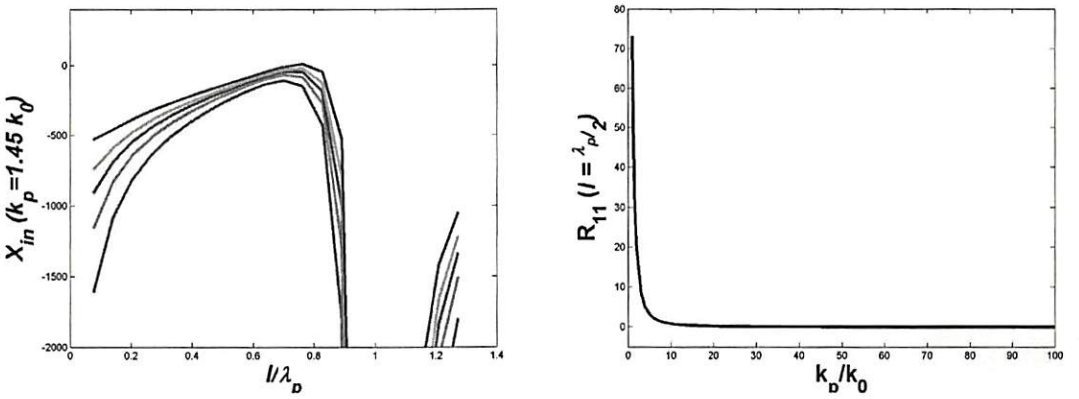

(a) No Resonance for $k_p = 1.45 \cdot k_0$ (b) Radiation Resistance

Figure 4.2: Nanotube antenna input impedance for $k_p >> k_0$. (a) Nanotube reactance is all negative and so the nanotube antenna does not resonate for larger k_p. (b) Nanotube input resistance falls rapidly with increasing k_p. The input resistance is the nanotube radiation resistance for the lossless case.

for large k_p because the estimated resistance becomes many orders of magnitude smaller than free-space resistance.

Nanotube antennas can be an attractive design choice for small reductions in EM-wave propagation. Multiwall nanotube and single-crystal nanowire antennas can be better than nanometer-size thin wires because poly-crystal metal wires can have high intrinsic resistive-losses and act as poor antennas: Oxidation [335], heating and electromigration [201] [446], and grain-boundary effects [46] can reduce conductivity for nm-diameter poly-crystal metal wires. The nanotube (or nanowire) antennas are also better than poly-crystal wires because they can interface with nanotube (or nanowire) circuits without high-impedance junctions. The antenna prediction applies to quantum conductors in general and so can apply to single-crystal metallic nanowires such as in [478].

The antenna analysis assumes a low-resistive loss in the nanotubes and gives a kind of best-case estimate in the sense that additional ohmic losses in the conductor reduces

antenna radiation. The lossless case is where the resistive self impedance R_{in} equals the radiation resistance because R_{in} is the only resistance in the radiator's equivalent circuit by assumption [382]. The ideal antenna resistance equals or matches the free-space radiation resistance and would minimize signal reflection [382]. The conductor's intrinsic resistance dissipates as heat a portion of the otherwise-radiated power [382].

We note that nanotubes have high measured resistance but should replace poly-crystal thin-wires as antennas for two reasons [68] [132] [462]. The first reason is that nanotubes are stronger and have fewer defects. Increasingly narrow poly-crystal thin-wires have high resistance due to grain-boundary scattering [46] and oxidation [335] or fail due to heating and electromigration [201] [446].

The second reason is that nanotube resistance should reduce as technology improves. Multiwall-nanotube resistance should reduce below the predicted minimum of about 6.5 $k\Omega$ for a singlewall nanotube due to parallel conduction in multiple shells [241] [411]. Ballistic-nanotube resistance should also reduce [227] [281] [164]. They have a low predicted resistivity of $\rho \approx 10^{-6}$ Ω/cm that equals or exceeds the conductivity of the best metal at room temperature for a μm-length mean free path [321]. Such a μm-length nanotube dipole should resonate near THz frequencies.

4.1.1 Nanotube Antenna Theorem: Nanotube dipoles are resonant and narrowband

We present a new theorem for nanotube-dipole antennas: It shows that nanotube antennas are resonant and narrowband based on derived formulas for nanotube-dipole self and mutual impedances. The theorem modified the thin-wire dipole model to estimate nanotube-dipole self impedance and mutual impedance. And the theorem predicts that a nanotube dipole resembles a thin-wire dipole if electromagnetic waves propagate in the nanotube at or near the free-space velocity of light.

The theorem modifies the perfect-conductor thin-wire dipole model (such as in [382]) to fit quantum conductors. It alters only one assumption in the thin-wire dipole model: Quantum conductance limits the velocity of charge and wave propagation in the nanotube [7] [10] [107] [149] [418] [497]. The slow-wave assumption alters the wavelength and the propagation constant or wave number $k_p \neq k_0$ of EM waves in the quantum conductor [374]. So we model the quantum-conductor dipole by replacing k_0 with k_p in nanotube current distribution.

The theorem uses the slow-wave assumption to compress the wavelength in an assumed sinusoidal current distribution in the dipole antenna. The compressed sinusoidal current assumption is in two parts. The first part is that current distribution is sinusoidal or wave-like in a quantum conductor. This is reasonable because researchers report wave-like current excitations in one-dimensional quantum systems [69] [70] [49] [100] [154] [236] [235] [270] [358] [437]. Lee et al. have reported periodic standing waves due to defects in nanotube quantum wires [270]. Fechner et al. estimated that "the harmonics of the total current oscillate in space with some periodicity" in a one-dimensional conductor [154]. Burke set up "standing-wave resonances in SWNT of finite length" to analyze the one-dimensional conduction and to calculate wave velocity [69].

The second part is that quantum effects can reduce wave velocity in quantum conductors. Researchers model the slow-wave effect by using plasmons that have limited velocity at or near the Fermi velocity [7] [10] [107] [149] [418] [497]. Aligia et al. estimated that the plasmon velocity in a quantum wire can be 10–30 times the Bohr velocity or one order of magnitude slower than c [10]. Burke estimated that the plasmon velocity in a nanotube can approximate the Fermi velocity of graphite $v_p \approx v_F \approx 8 \times 10^5$ or two orders of magnitude slower than c [68] [69]. The reduced

velocity corresponds to a wave number $k_p \approx 100 \cdot k_0$ in a quantum transmission-line model [68] [197] [198] [419] [437]. So $k_p \neq k_0$.

The nanotube-antenna theorem modifies the wave number k_p to summarize the effects of quantum charging on nanotube current distribution that is central to the nanotube antenna effect. We focus on quantum charging because it strongly influences electron transport in quantum wires [245] and because electron transport directly influences current distribution that is central to antenna radiation [382].

Nanotubes exhibit quantum charging either as quantum wires [197] [419] [437] or as quantum dots [14] [71] [379]. The proof of the nanotube-antenna theorem focuses on long nanotubes that can exhibit quantum charging [122] [411]: Bezryadin et al. observed single-electron Coublomb charging in singlewall nanotubes at low temperatures [45]. Quantum charging causes the slow-wave effects or wavelength compression of EM propagation in quantum conductors [10] [149] [418] [497]. Quantum transmission lines model this wave compression with an additional quantum capacitance that alters the wave number k_p [69] [70].

The proof of the theorem modifies a perfect-conductor model to fit a quantum conductor by altering the wave number in the antenna current distribution. The perfect-conductor thin-wire dipole model assumes a current distribution that uses the free-space wave number k_0:

$$I(z) = I_0 \sin[k_0(|l| - z)] \tag{4.1}$$

where $2l$ is the dipole length [145] [382].

The nanotube current distribution is sinusoidal in shape similar to the thin-wire dipole model [144] [382]. But the sinusoidal period shortens due to a quantum-induced

reduction in the velocity of EM-wave propagation in the conductor [68]. The modified nanotube current distribution has $k_p \neq k_0$:

$$I(z) = I_0 \sin\left[\underline{k_p}(|l| - z)\right] \tag{4.2}$$

A lossless assumption neglects intrinsic resistive losses in the quantum conductor and leads to a sinusoidal current distribution with a periodicity proportional to the wave velocity [68] [69]. So the reduced wave velocity gives a shorter wavelength in the quantum conductor than in free space. The lossless assumption also reduces the wave vector k to a scalar wave number or propagation constant k_0 [68].

Other model assumptions include [145]: The dipole is in free space. The dipole diameter is much less than either the dipole length or the wavelength of the EM signal. The current lies on the surface of the cylindrical dipole: This is reasonable for a quantum-limited nanotube where most or all of the current flows on the surface of the outermost shell. The end effects are negligible: This is reasonable for a nanotube that has a very small diameter relative to its length. The feed-region effects are negligible: A half-dipole over a reflecting ground plane can approximate a full-dipole in free space that has an infinitesimal voltage source at the input.

The derivation of the impedance formulas equates the radiated power of a lossless dipole antenna P_{rad} to its dissipated power P_{dis} and solves for the input impedance z_in. Poynting's theorem gives the radiated power as a function of an induced electric field and an antenna current distribution [145]:

$$\overline{P}_{rad} = \frac{1}{2}\mathfrak{Re}\int_V \mathbf{E}\cdot\mathbf{J}^{r\star}dV + \frac{1}{2}\mathfrak{Re}\oint_S \mathbf{E}\times\mathbf{H}^{\star}dS \tag{4.3}$$

where the second term in (4.3) gives the radiated power of the energy flow across a surface S. A circuit with input current I_{in} and input impedance Z_{in} dissipates an average power

$$\overline{P}_{dis} = \frac{1}{2} I_{in} I_{in}^{\star} Z_{in} \tag{4.4}$$

And an induced electromagnetic field (EMF) method calculates the radiated electric field in the Fresnel (or near) zone around the antenna.

The proof of the theorem derives nanotube-impedance formulas by equating the dissipated power (4.4) and the radiated-power term in (4.3)

$$\frac{1}{2} I_{in} I_{in}^{\star} Z_{in} = \frac{1}{2} \int_S (\overline{\mathbf{E}} \times \overline{\mathbf{H}^{\star}}) \cdot dS \tag{4.5}$$

The total radiated power is the integration of the Poynting vector over a cylindrical surface around the dipole antenna for an arbitrary current distribution [382]:

$$|I_{in}^2| Z_{in} = - \int_{-l}^{l} E_z(a, z') I^{\star}(z') dz' \tag{4.6}$$

where a is the diameter of the cylindrical surface and where the limits of the integration spans the length of the cylinder $2l$. The formula uses only the z-directed electric field because only E_z in the Poynting vector has a nonzero dot product with dS in (4.3).

The proof then uses the induced EMF method and substitutes a modified current distribution. The modified current distribution changes the form of the electric field and so changes the form of the self and mutual impedances.

Theorem: (*Self Impedance*) Suppose that a nanotube dipole has a compressed current distribution $I(z)$ with a wave number k_p that differs from the free-space wave number k_0 due to quantum-charging effects.

Then nanotube-dipole self impedance Z_{in} or Z_{11} has the form:

$$
\begin{aligned}
Z_{in} &= \left(\frac{k_p}{k_0}\right)\frac{j\eta_0}{4\pi\sin^2 k_p l} \\
&\int_{-l}^{l}\left\{-2\cos(k_p l)\frac{e^{-jk_0R_0}}{R_0}+\frac{e^{-jk_0R_1}}{R_1}+\frac{e^{-jk_0R_2}}{R_2}\right\}\sin k_p(l-|z|)dz \\
&- k_0\left(\frac{k_p^2}{k_0^2}-1\right)\frac{j\eta_0}{4\pi\sin^2 k_p l} \\
&\int_{-l}^{l}\int_{-l}^{l}\sin(k_p(l-|z'|))\sin(k_p(l-|z|))\frac{e^{-jk_0r}}{r}dz'dz
\end{aligned}
\tag{4.7}
$$

where $R_0 = \sqrt{a^2+z^2}$ is the distance between an observe point $\mathbf{P} = (x,y,z)$ on a cylindrical surface around the dipole and the center of the dipole $(0,0,0)$, $R_1 = \sqrt{a^2+(z-l)^2}$ is the distance between $\mathbf{P}$ and the top of the dipole $(0,0,-l)$, $R_2 = \sqrt{a^2+(z+l)^2}$ is the distance between $\mathbf{P}$ and the bottom of the dipole $(0,0,l)$ and $r = \sqrt{a^2+(z-z')^2}$ is the distance between $\mathbf{P}$ and an arbitrary point on the dipole axis $(0,0,z')$ and where $a^2 = x^2+y^2$.

We briefly state the corollary to the theorem before the proof.

Corollary (*Mutual Impedance*) Suppose that two nanotube dipoles lie on the yz-plane and have the same wave number k_p. And suppose that dipole 1 has length $2l_1$ and centers at the origin and that dipole 2 has length $2l_2$ and centers at $(0,Y,Z)$.

Then the formula for the mutual impedance Z_{12} between the two nanotube dipoles has a similar form as the self-impedance formula (4.8) except for different distances R_0, R_1, R_2, and r and different limits of integration $\pm l_1$ and $\pm l_2$. The modified distances $R_0 = \sqrt{Y^2+(z+Z)^2}$ is the distance between an observe point $\mathbf{Q} = (0,Y,z+Z)$ on dipole 2 and the center of dipole 1 $(0,0,0)$, $R_1 = \sqrt{Y^2+(z+Z-l)^2}$ is the distance between $\mathbf{Q}$ and the top of dipole 1 $(0,0,+l)$, $R_2 = \sqrt{Y^2+(z+Z+l)^2}$ is the distance

between $\mathbf{Q}$ and the bottom of dipole 1 $(0, 0, -l)$, and $r = \sqrt{Y^2 + (z + Z - z')^2}$ is the distance between $\mathbf{Q}$ and an arbitrary point along the axis of dipole 2 $(0, 0, z')$.

Proof: The proof of the theorem follows from the power relation between the maximal dissipated power and the total radiated power of a lossless antenna. The radiated power is due to Poynting's theorem. We compute the Fresnel-zone electric field using a cylindrical surface around the nanotube dipole. Then the radiated power depends only on the z-directed electric field E_z due to the dot product between the electric field $\mathbf{E}$ and the cylindrical surface vector dS.

The proof models a nanotube as a quantum conductor. The quantum-conductor model has a compressed sinusoidal current distribution $I(z)$ that induces an electric field that differs from the perfect-conductor thin-wire model. We calculate the required electric field E_z by substituting the compressed $I(z)$ into the induced EMF method. We then substitute the calculated E_z into the Poynting vector (4.6) and solve for the impedance.

The induced EMF method calculates the electric field due to a current distribution in the nanotube antenna. The Fresnel-zone (or near-zone) solution of Maxwell's equations for the radiated field has the form [382]:

$$\overline{E}_z(a, z) = \frac{-j\omega\mu_0}{4\pi} \int \left[\hat{z} + \frac{1}{k_0^2} (\hat{z} \cdot \nabla') \nabla' \right] I(z') \Psi dz' \tag{4.8}$$

where a line integral along z' replaces the surface integral for the slender-dipole model and where the operator ∇' differentiates with respect to the source-dipole coordinates z'.

We solve for the induced electric field E_z due to an assumed sinusoidal current $I(z)$. The nanotube current distribution has the form

$$I(z) = I_0 \sin k_p (l - |z|) \tag{4.9}$$

and uses a wave-propagation constant k_p that differs from the free-space propagation constant k_0. Equation (4.9) modifies the thin-wire current distribution

$$I(z) = I_0 \sin k_0 (l - |z|) \tag{4.10}$$

and differs only in the propagation constant $k_p \neq k_0$. This modified current distribution is central to the derivation of the nanotube impedance formula.

The induced electric field has the form

$$E_z(a, z) = \frac{-j\omega\mu_0}{4\pi} \int_{-l}^{l} \left[1 + \frac{1}{k_0^2} \frac{\delta^2}{\delta z'^2}\right] I(z')\Psi dz' \tag{4.11}$$

The derivation uses integration by parts to solve the near-zone electric field [382]:

$$E_z(a, z) = \frac{-j\omega\mu_0}{4\pi} \int_{-l}^{l} \left[I(z') + \frac{1}{k_0^2} \frac{d^2}{dz'^2} I(z')\right] \Psi dz' \tag{4.12}$$

$$+ \frac{-j\omega\mu_0}{4\pi k_0^2} \left[I(z') \frac{d\Psi}{dz'} - \Psi \frac{dI(z')}{dz'}\right]_{-l}^{l} \tag{4.13}$$

where z' is the coordinate of the source dipole and z is the coordinate of the receive dipole.

An alternate form of the current distribution rewrites the absolute value function $|z'|$ in $I(z')$ to simplify the differentiation [382]:

$$I(z') = I_0 \left[\sin k_p l \cos k_p z' - \cos k_p l \sin k_p z' \mathrm{Sgn}(z')\right] \tag{4.14}$$

where $\mathrm{Sgn}(z')$ is the sign function and equals one for $z' > 0$, zero for $z' = 0$, and minus one for $z' < 0$. This begins the Prata solution for the impedance formula [382].

The derivation requires the first and second derivative of the current distribution with respect to z' . They have the forms below for compressed current distribution $I(z')$:

$$\begin{aligned} \frac{dI(z')}{dz'} &= \frac{d}{dz'} I_0 \left(\sin k_p l \cos k_p z' - \cos k_p l \sin k_p z' \mathrm{Sgn}(z')\right) \\ &= I_0\{ - k_p \sin k_p l \sin k_p z' - 2\delta(z') \cos k_p l \sin k_p z' \\ &- k_p \cos k_p l \cos k_p z' \mathrm{Sgn}(z')\} \end{aligned} \tag{4.15}$$

and

$$\begin{aligned} \frac{d^2 I(z')}{dz'^2} &= -I_0\{k_p^2 \sin k_p l \cos k_p z' + 2\delta'(z') \cos k_p l \sin k_p z' \\ &+ k_p 2\delta(z') \cos k_p l \cos k_p z' + k_p 2\delta(z') \cos k_p l \cos k_p z' \\ &- k_p^2 \cos k_p l \sin k_p z' \mathrm{Sgn}(z')\} \end{aligned} \tag{4.16}$$

where the derivative of the sign function is a delta function

$$\frac{d}{dz'} \mathrm{Sgn}(z') = 2\delta(z') \tag{4.17}$$

The first term of the integration by parts (4.12) uses the second derivative of the current distribution so its integrand has the form

$$\mathrm{Integrand} = \left\{ I(z') + \frac{1}{k_0^2} \frac{d^2 I(z')}{dz'^2} \right\} \Psi \tag{4.18}$$

$$\begin{aligned} &= I_0 \left\{ \left(1 - \frac{k_p^2}{k_0^2}\right) \sin\left(k_p (l - |z'|)\right) \right. \\ &- \left. \frac{2}{k_0^2} \delta'(z') \cos k_p l \sin k_p z' \right. \end{aligned} \tag{4.19}$$

$$- \frac{k_p}{k_0^2}(2+2)\delta(z')\cos k_p l \cos k_p z' \Big\} \Psi$$

where

$$\delta'(z') = \frac{d}{dz'}\delta(z') \tag{4.20}$$

The delta functions $\delta(z')$ and $\delta'(z')$ reduce an integration into an evaluation [382]:

$$\int g(\xi)\delta(\xi)d\xi = g(\xi)|_{\xi=0} \tag{4.21}$$

and

$$\int g(\xi)\delta'(\xi)d\xi = -\frac{d}{d\xi}g(\xi)|_{\xi=0} \tag{4.22}$$

So the first term of the integration by parts gives

$$\begin{aligned} \text{First Term} &= \frac{-j\omega\mu_0}{4\pi k_0} I_0 \Big\{ -2\left(\frac{k_p}{k_0}\right)\cos k_p l \Psi|_{z'=0} \\ &+ k_0\left(1-\frac{k_p^2}{k_0^2}\right)\int_{-l}^{l} \sin(k_p(l-|z'|))\Psi(z,z')dz' \Big\} \end{aligned} \tag{4.23}$$

Note that Prata's solution keeps only the first half of the first term (4.23) because $k_p = k_0$ zeros out the second half of (4.23) in perfect-conductor thin-wire dipole models.

The second term of the integration by parts uses only the product of the wave function Ψ and the first derivative of the current distribution $\frac{dI(z')}{dz'}$ and has the form

$$\begin{aligned} \text{Second Term} &= \frac{-j\omega\mu_0}{4\pi k_0^2}\left[-\Psi\frac{dI(z')}{dz'}\right]_{-l}^{l} \\ &= \frac{-j\omega\mu_0}{4\pi k_0}\Psi(z,z')I_0\Big\{\frac{2}{k_0}\delta(z')\cos k_p l \sin k_p z' \\ &+ \frac{k_p}{k_0}\sin k_p l \sin k_p z' + \frac{k_p}{k_0}\cos k_p l \cos k_p z' \mathrm{Sgn}(z')\Big\}_{-l}^{l} \end{aligned} \tag{4.24}$$

because

$$\left[I(z')\frac{d\Psi}{dz'}\right]_{-l}^{l} \equiv 0 \tag{4.25}$$

where $\frac{d}{dz}\Psi(z)$ is bounded and multiplies $I(z' = +l)$ and $I(z' = -l)$ that are zero by assumption. The evaluation for $z' = l$ and $z' = -l$ gives

$$\text{Second Term} \;=\; \frac{-j\omega\mu_0 I_0}{4\pi k_0}\left(\frac{k_p}{k_0}\right)\left[\Psi|_{z'=l} + \Psi|_{z'=-l}\right] \tag{4.26}$$

The Fresnel-zone (or near-zone) electric field combines (4.23) and (4.26) and has the form

$$\begin{aligned} E_z = \frac{-j\eta_0 I_0}{4\pi}\Bigg\{ & \left(\tfrac{k_p}{k_0}\right)\left[-2\cos(k_p l)\tfrac{e^{-jk_0R_0}}{R_0} + \tfrac{e^{-jk_0R_1}}{R_1} + \tfrac{e^{-jk_0R_2}}{R_2}\right] \\ - \; & k_0\left(\tfrac{k_p^2}{k_0^2} - 1\right)\textstyle\int_{-l}^{l}\sin(k_p(l-|z'|))\Psi(z,z')dz'\Bigg\} \end{aligned} \tag{4.27}$$

where the integral is with respect to the source dipole coordinate z' and where $\eta_0 = \omega\mu_0/k_0 = 120\pi$. Note that the second half of E_z becomes zero for a perfect-conductor thin-wire model $k_p = k_0$.

We substitute the calculated electric field (4.28) into the power relation

$$Z_{in} = \frac{-1}{|I_{in}^2|}\int_{-l}^{l} E_z(a,z')I^*(z')dz' \tag{4.28}$$

and solve for the impedance. The self impedance Z_{11} or Z_{in} has the final form as in (4.8)

$$\begin{aligned} Z_{in} \;=\; & \left(\frac{k_p}{k_0}\right)\frac{j\eta_0}{4\pi\sin^2 k_p l} \\ & \int_{-l}^{l}\left\{-2\cos(k_p l)\frac{e^{-jk_0R_0}}{R_0} + \frac{e^{-jk_0R_1}}{R_1} + \frac{e^{-jk_0R_2}}{R_2}\right\}\sin k_p(l-|z|)dz \end{aligned} \tag{4.29}$$

$$- \quad k_0 \left(\frac{k_p^2}{k_0^2} - 1 \right) \frac{j\eta_0}{4\pi \sin^2 k_p l} \int_{-l}^{l} \int_{-l}^{l} \sin(k_p(l - |z'|)) \sin(k_p(l - |z|)) \Psi(z, z') dz' dz$$

where

$$R_0 = \sqrt{a^2 + (z)^2} \tag{4.30}$$

$$R_1 = \sqrt{a^2 + (z - l)^2} \tag{4.31}$$

$$R_2 = \sqrt{a^2 + (z + l)^2} \tag{4.32}$$

and

$$\Psi(z, z') = \frac{e^{-jk_0\sqrt{a^2+(z-z')^2}}}{\sqrt{a^2 + (z - z')^2}} \tag{4.33}$$

□

The mutual impedance Z_{12} has a similar derivation as Z_{in} and has a similar form. It generalizes for two distinct dipoles and so uses different distances R and different dipole lengths in the formula. The mutual impedance between two nanotube dipoles has the form:

$$\begin{aligned} Z_{12} \quad = \quad & \left(\frac{k_p}{k_0} \right) \frac{j\eta_0}{4\pi \sin k_p l_1 \sin k_p l_2} \int_{-l_2}^{l_2} \left\{ -2\cos(k_p l) \frac{e^{-jk_0 R_0}}{R_0} + \frac{e^{-jk_0 R_1}}{R_1} + \frac{e^{-jk_0 R_2}}{R_2} \right\} \sin k_p(l_2 - |z|) dz \\ - \quad & k_0 \left(\frac{k_p^2}{k_0^2} - 1 \right) \frac{j\eta_0}{4\pi \sin k_p l_1 \sin k_p l_2} \int_{-l_2}^{l_2} \int_{-l_1}^{l_1} \sin(k_p(l_1 - |z'|)) \sin(k_p(l_2 - |z|)) \Psi(z, z') dz' dz \end{aligned} \tag{4.34}$$

where

$$R_0 = \sqrt{Y^2 + (z + Z)^2} \tag{4.35}$$

$$R_1 = \sqrt{Y^2 + (z + Z - l)^2} \tag{4.36}$$

$$R_2 = \sqrt{Y^2 + (z + Z + l)^2} \tag{4.37}$$

and

$$\Psi(z, z') = \frac{e^{-jk_0\sqrt{Y^2+(z+Z-z')^2}}}{\sqrt{Y^2 + (z + Z - z')^2}} \tag{4.38}$$

The mutual-impedance formula generalizes the self-impedance formula: Self impedance is a special case where the source and the receive dipoles are physically the same.

The mutual-impedance formula follows a similar derivation as the self-impedance formula except that the source dipole (or dipole 1) is distinct from the receive dipole (or dipole 2). The center of the source dipole is at the origin and the center of the receive dipole is at the point $(0, Y, Z)$. Both dipoles lie on the yz-plane. The induced current at the length-l_2 receive dipole has the assumed sinusoidal distribution

$$I(z) = I_0 \sin k_p (l_2 - |z|) \tag{4.39}$$

And the length-l_1 source dipole has the assumed sinusoidal distribution

$$I(z') = I_0 \sin k_p (l_1 - |z'|) \tag{4.40}$$

The induced electric field has a similar form as (4.28)

$$\begin{aligned} E_z &= \left(\frac{k_p}{k_0}\right) \frac{-j\eta_0 I_0}{4\pi k_0} \left[-2\cos(k_p l)\frac{e^{-jk_0R_0}}{R_0} + \frac{e^{-jk_0R_1}}{R_1} + \frac{e^{-jk_0R_2}}{R_2}\right] \\ &+ k_0 \left(1 - \frac{k_p^2}{k_0^2}\right) \frac{-j\eta_0 I_0}{4\pi k_0} \left[\int_{-l_1}^{l_1} \sin(k_p(l_1 - |z'|)\Psi(z, z')dz'\right] \end{aligned} \tag{4.41}$$

where the distances R_0, R_1, and R_2 differ from (4.28):

$$R_0 = \sqrt{Y^2 + (z+Z)^2} \tag{4.42}$$

$$R_1 = \sqrt{Y^2 + (z+Z-l)^2} \tag{4.43}$$

$$R_2 = \sqrt{Y^2 + (z+Z+l)^2} \tag{4.44}$$

where the modified wave function is

$$\Psi(z,z') = \frac{e^{-jk_0\sqrt{Y^2+(z+Z-z')^2}}}{\sqrt{Y^2+(z+Z-z')^2}} \tag{4.45}$$

4.1.2 Quantum-Dipole Impedance Results Lead to Three Key Predictions

The nanotube-antenna theorem makes three key predictions. The first prediction is that nanotubes can approximate ideal dipoles for low resistive losses and for limited quantum effects. Nanotube-dipole antennas can resemble thin-wire antennas for a limited range of $k_p \approx k_0$: A nanotube dipole can have a resonant length of approximately half freespace-wavelength $\lambda/2$ and a radiation resistance of the same order of magnitude as the free-space radiation resistance (73 Ω).

The second prediction is that nanotubes can have narrower bandwidths than thin-wires because they are narrower. And the third prediction is that nanotubes can be poor radiators for strong quantum effects. Quantum-conductor dipoles can fail to resonate and have a low radiation resistance of the order 10^{-3} Ω for $k_p \approx 100 \cdot k_0$.

The proof of the theorem also suggests a testable hypothesis: The current distribution in a nanotube-dipole antenna has a sinusoidal shape and a compressed wavelength for

$k_p \neq k_0$. Observed nanotube antenna-length effect had free-space wavelengths [458]. This strengthens the sinusoidal-current assumption.

The nanotube-antenna theorem gives an impedance formula that can estimate self or input impedance $Z_{in} = R_{in} + jX_{in}$ that has a real or resistive part R_{in} and an imaginary or reactive part X_{in}. The reactive input impedance or input reactance predicts nanotube resonance, narrow bandwidth, and limits on quantum-induced wave compression k_p/k_0.

The resistive input impedance or input resistance predicts lower radiation efficiency for a nanotube-dipole antenna that has quantum-induced wave compression $k_p \neq k_0$. The nanotube input resistance estimates the radiation resistance for the lossless-case and reduces with increasing k_p.

Figure 4.3 plots the real and the imaginary parts of the input impedance Z_{in} as a function of $k_p l$ or as a function of the ratio of dipole length to the compressed wavelength l/λ_p and for four values of $k_p = 1.0 \cdot k_0$, $1.1 \cdot k_0$, $1.2 \cdot k_0$, and $1.3 \cdot k_0$. The estimated reactive self impedance (or self reactance) X_{in} shows a first resonance for approximately half wavelength dipoles, for most dipole diameters, and for quantum effects that give a wave-compressed $k_p \leq 1.3 \cdot k_0$ or $\frac{k_p}{k_0} \leq 1.3$.

The input reactance curves all cross zero (0 Ω) and so predict resonance for the dipole diameters shown. A dipole is resonant if its impedance has no capacitive or inductive components or that its self reactance equals zero [382].

We note that dipole resonant length is based on the longer free-space wavelength for small $k_p \approx k_0$ and that dipoles can fail to resonate for large $k_p >> k_0$. The nanotube-antenna resonant lengths appear to increase in Figure 4.3 from (a) to (d) because the resonant length is half the free-space wavelength $\lambda/2$ instead of half the compressed wavelength $\lambda_p/2$ [10] [69]. The apparent lengthening is due to a shrinking $k_p l$ relative to free-space kl for wave compression that increases k_p.

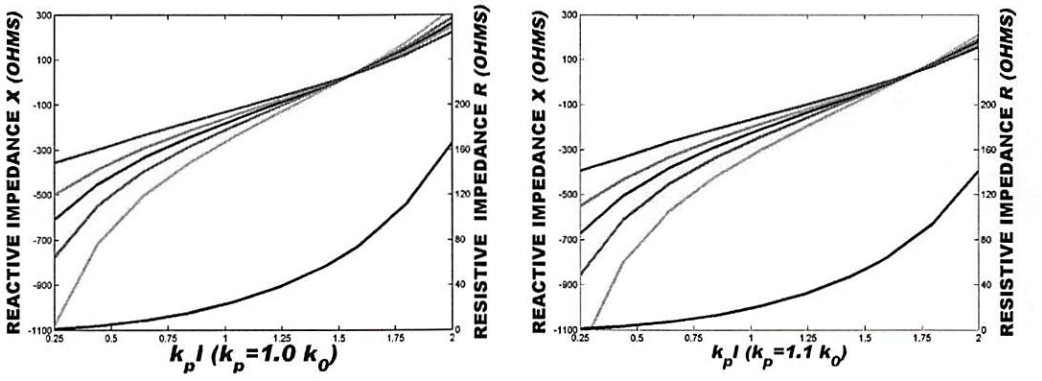

(a) $k_p = k_0$ (b) $k_p \neq k_0$

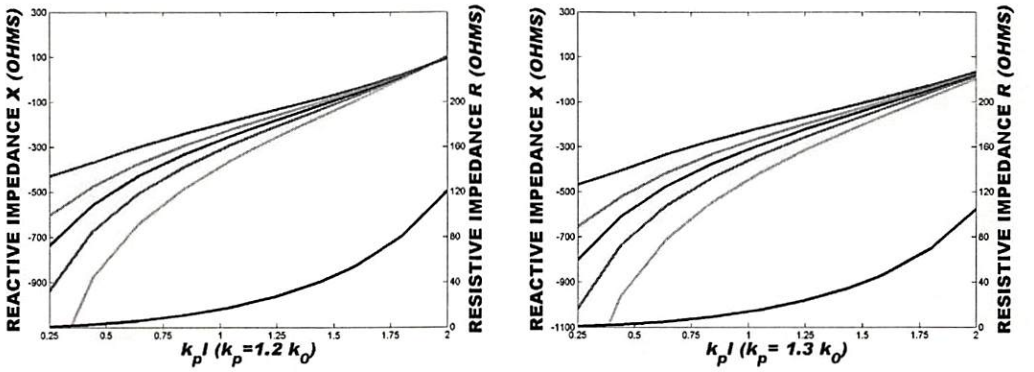

(c) $k_p \neq k_0$ (d) $k_p \neq k_0$

Figure 4.3: Nanotube antenna input impedance for different values of $k_p \approx k_0$. The figures plot the real and imaginary parts of impedance versus a normalized dipole length $k_p l$. (a) $k_p = k_0$ corresponds to the perfect-conductor case. (b)–(d) $k_p \approx k_0$ corresponds to four increasing but weak quantum-conductor cases. The top five color curves are nanotube input reactance for five different dipole diameters as a function of compressed wavelength. The five diameters a/λ_p are 0.009525 (red), 0.006350 (green), 0.004763 (blue), 0.003175 (magenta), and 0.001588 (cyan) from top to bottom. The bottom-most black curve is the nanotube input reactance.

The reactance curves have steeper slopes for smaller dipole diameters and so predict narrow bandwidths for increasingly narrower dipoles. The reactance curves also becomes more negative with increasing k_p and is a periodic function of dipole length. So the reactance curves will become all negative as k_p grows for stronger quantum effects.

The resistive self impedance R_{in} predicts increasing resistance with longer dipoles similar to classic thin-wire models but predicts a decreasing radiation efficiency with more quantum effects. The input resistance increases with dipole length as expected but the self-resistance curves fall for increasing k_p. Figure 4.2(b) shows that the radiation resistance of a resonant dipole falls rapidly with increasing k_p.

The self impedance plots show that the estimated self impedances for nanotubes and nanowires are similar to the self impedance for perfect conductors in thin-wire dipole models. So nanotubes and nanowires can work as well as thin-wires in dipole antennas for the lossless case ($k_p = k_0$). Nanotubes and nanowire dipoles can become more attractive than increasingly narrower thin-wire dipoles because thin-wire dipoles can become poor radiators with decreasing width. Nanotubes and nanowires can conduct better than poly-crystal thin wires that can lose conductance due to oxidation, electromigration, and grain-boundary effects. And nanotubes can be more flexible and resist oxidation better than single-crystal nanowires.

The reactance curves for nanometer diameters predict high quality (Q) factor for nanotube dipoles. The predicted high Q-factor or narrow bandwidth relative to center frequency [129] is based on the steep slopes of the nanotube reactance curves.

The reactance plots in Figure 4.4 show several curves that correspond to different dipole sizes. The curves that correspond to 2-nm and 50-nm diameters show rapid changes in X_{in} for relatively small changes in dipole length. This suggests that a resonant-length dipole has near-zero reactance (or nearly resonates) only for a narrow range of frequencies. The reasoning is that small changes in length l causes large changes in reactance X away from zero. So the reactance of a resonant-length dipole remains near zero for a narrow band of frequencies around the resonant frequency.

The estimated self reactance predicts no resonance (Figure 4.5) for any length dipoles, for nano and micro-scale dipole diameters, and for $k_p >> k_0$. Sensitivity

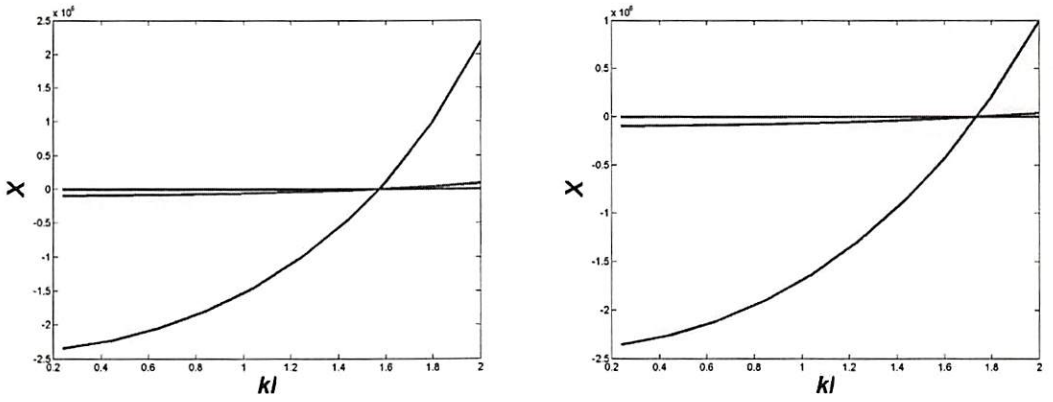

(a) $k_p/k_0 = 1.0$ (b) $k_p/k_0 = 1.1$

Figure 4.4: Input reactance has steep slope for small diameters and for $k_p \approx k_0$. The slope of the reactance curve and its magnitude vary wildly for nanometer-size diameters. The central black curve contains five overlapping curves for the five dipole diameters shown in Figure 4.3. The nearby green curve corresponds to a 50-nm wide dipole. The large blue curve corresponds to a 5-nm wide dipole. The estimated reactance neglects diameter-dependent quantum effects for this figure to illustrate the diameter dependence of dipole bandwidth. Smaller dipole diameter causes more variation in input reactance with small changes in dipole length. So a smaller range of frequencies can approximate a dipole's resonance frequency. (a) corresponds to the perfect conductor case $k_p = k_0$ and (b) corresponds to weak quantum effects $k_p \approx k_0$. Both exhibit the sharp slope in reactance that predicts narrow bandwidths. Note that smaller diameter dipoles will begin to lose resonance sooner than larger diameter dipoles because reactance becomes increasingly negative for larger k_p and combines with impedance periodicity to become entirely negative.

analysis shows that the reactance grows more negative with increasing ratio while the resistance falls rapidly. Sensitivity analysis also shows that the first resonance occurs for half free-space wavelength ($\approx \lambda/2$) for $k_p \approx k_0$ and that resonance fails to occur (all negative reactance) for small diameters.

Quantum conductors should make poor antennas if quantum effects reduced wave velocity to be much less than the free-space velocity of light [10] [69]. Resonance fails to occur for any dipole length and for all simulated diameters for $k_p \approx 100 \cdot k_0$ in sensitivity analysis. We note that a plasmon-limited quantum conductor has wave

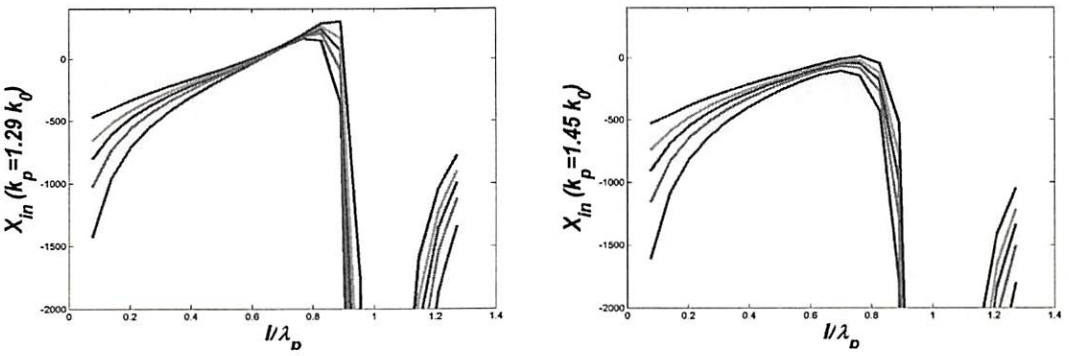

(a) Some Dipoles Fail to Resonate

(b) All Dipoles Fail to Resonate

Figure 4.5: Antenna reactance begins to lose resonance for some dipole diameters and small k_p: $k_p/k_0 = 1.29$ in (a) and becomes all negative for large k_p: $k_p/k_0 = 1.45$ in (b). This predicts no resonance for any dipole length. The five curves shown here have diameter to length ratios of $a/l = 0.009525$, 0.00635, 0.004763, 0.003175, and 0.001588 from top to bottom.

number $k_p \approx 100 \cdot k_0$ if nanotube Fermi velocity limits the plasmon velocity and so limits the velocity of electronic wave propagation in the nanotube [68] [374] [107]. Our near-field based nanotube-antenna theorem extends the analysis in [68] and predicts no resonance and a lower radiation resistance of the order 10^{-3} Ω for this plasmon-limited case.

4.1.3 Mutual Impedance Results: Nanotubes Should Employ Thin-Wire Based Array Designs

Nanotubes can employ thin-wire based array design techniques because nanotube dipoles and thin-wire dipoles have similar mutual impedances. The similarity holds for limited quantum effects $k_p \approx k_0$. And researchers have reported the excitation of arrays of nanotubes [190] and antenna effects in arrays of nanotubes [458].

Figure 4.6 plots the mutual impedance between two nanotube dipoles as a function of normalized separation and for different k_p. The two nanotube dipoles have resonant

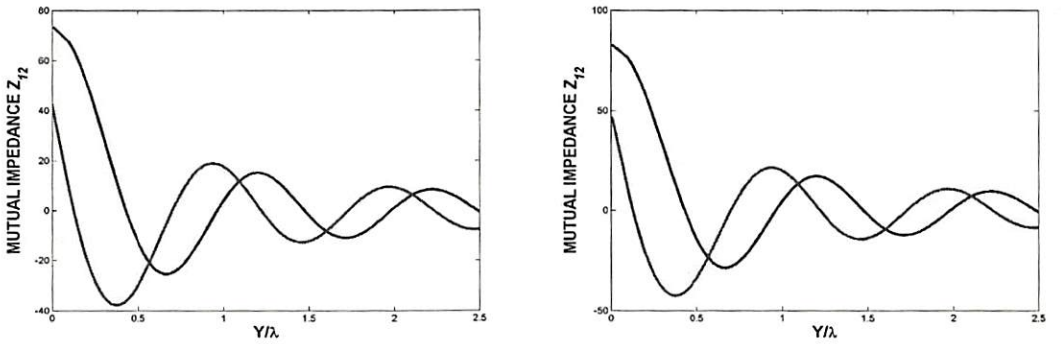

(a) $k_p = k_0$ (b) $k_p \approx k_0$

Figure 4.6: Mutual-impedance similarity between nanotube and thin-wire dipoles. (a) shows the mutual impedance for the perfect-conductor (or thin-wire dipole) case. (b) shows the mutual impedance for a limited quantum conductor (or nanotube) case for $k_p = 1.1 \cdot k_0$. The figures plot the mutual impedance between two parallel half-wavelength dipoles as a function of normalized dipole separation Y/l. The top blue curve is the real or resistive part of the mutual impedance. The bottom red curve is the imaginary or reactive part.

lengths $l = \lambda/2$. The mutual impedance plots are similar between the perfect-conductor case $k_p = k_0$ and the limited quantum conductor case $k_p \approx k_0$.

The mutual-impedance similarity suggests that nanotubes can employ uniform-linear-array (ULA) design and analysis. ULA design and analysis [11] factor antenna radiation into two terms: An element factor and an array factor [146]. The element factors involve only the current distribution in one of the elements [146].

The nanotube-thin-wire similarity suggests that the two types of resonant dipoles have similar element factors. The fine structure in the antenna pattern comes from the array factor for small elements that have broad patterns such as dipoles [146]. ULA designs based on nanotube half-wave dipoles could be identical to designs based on thin cylindrical dipoles because the designs would involve only the array factor and so involves only the spacing between the elements and the relative phase of the fed signals.

4.2 A Proposed Cochlear-Model Architecture Uses Nanotubes to Detect and Process Signals

A proposed cochlear-model architecture can sample and process the frequency spectra of electromagnetic signals by using banks of nanotube antennas. The narrowband nanotube antennas match different frequency components and can directly analyze the spectrum of an EM signal with high resolution.

4.2.1 Mammalian Cochlea Inspires Signal Processing that Uses Frequency Decomposition and Banks of Narrowband Detector

The mammalian cochlea of the inner ear excels at processing sound and has inspired many signal processing designs [50] [185] [263] [300] [348] [434] [442] [461]. Noca et al. have proposed nanotube acoustic sensors based on artificial cochlear stereocilia [348] and proposed radio frequency spectrum analyzers based on an array of nanotube mechanical oscillators [216]. They also demonstrated radio-signal coupling in an array of cantilever nanotubes [109] [210] [215]. Other researchers have proposed a silicon "fishbone" that spatially separates the frequency components of an acoustic signal and then feeds a bank of tuned cantilever oscillators [434].

Here a proposed nanotube cochlea-model architecture can directly process electromagnetic (EM) signals and does not require mechanical oscillators such as [348], [216], [410], and [434]. Applying nanotube antennas to a cochlear model suggests an architecture that uses nanotube-dipole antennas to sample an EM signal's frequency spectrum and perhaps uses a waveguide to separate the signal's frequency components. Figure 4.8 shows a schematic drawing that illustrates the proposed architecture. The rest of this section briefly reviews some relevant features of cochlear signal processing and then discusses the proposed architecture.

The cochlea separates the input acoustic signal into overlapping frequency bands and compresses the large acoustic intensity range into the much smaller mechanical and electrical dynamic range of the inner hair cell [12]. The cochlear structure processes or filters acoustic signals in a so-called "traveling wave" [453]: The cochlea resembles a dispersive transmission line where the different frequency components that make up the input signal travel at different speeds along the basilar membrane. This isolates each frequency component at a different place [203] along the basilar membrane (Figure 4.7(c)). The different frequency components attenuate and do not travel beyond their frequency-matched place in the basilar membrane. Mammalian cochlear processing includes frequency-domain sampling [12] [158], dynamic-range compression [395] [396], amplification [397], and noise enhancement (stochastic resonance) [224].

Hair bundles or stereocilia protrude from the apexes of hair cells (Figure 4.7(d)) along the reticular lamina [213] or the upper surface of the organ of Corti. Acoustic signals produce shearing between the tectorial membrane and the reticular lamina and displace the hair bundles. Each bundle consists of two to four rows of hair-like stereocilia. The hair cells transduce the mechanical displacements into a change in the receptor current flowing through the cell by mechanical gating of ion channels located in the hair bundle [13]. Auditory-nerve fibers attached to the hair cells produce action potentials in response to these voltages.

Auditory nerve fibers connect to the base of each of the two types of hair cell. The inner hair cells connect to the auditory nerve by afferent fibers that deliver neural signals to the brain. The outer hair cells connect by efferent nerve fibers that receive neural signals from the brain. The outer hair cells outnumber the inner hair cells about three to one but 95% of the auditory-nerve fibers innervate or connect to the inner hair cells. The outer hair cells can convert voltage across their cell membrane into length changes and influence cochlear micromechanics [58] and amplify the mechanical signal [346].

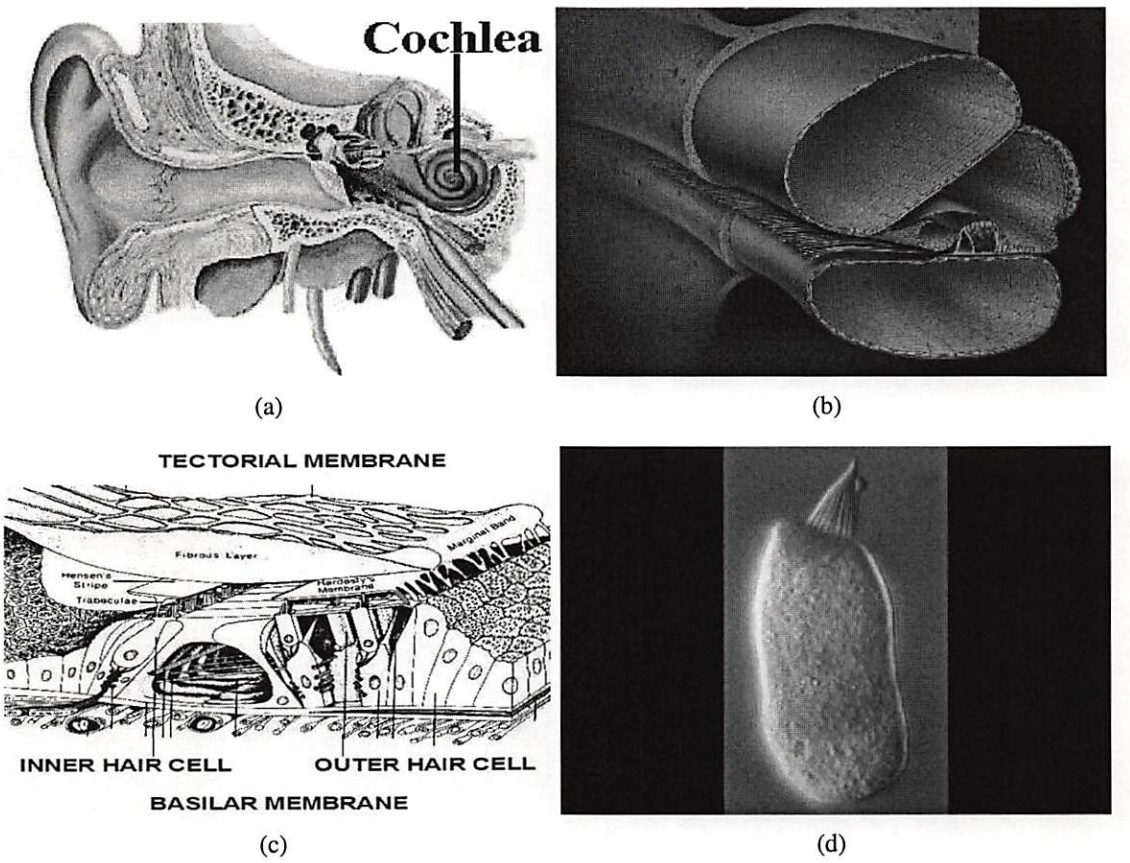

Figure 4.7: Cochlear anatomy. (a) The location of the human cochlea with respect to the external ear canal. The cochlea is shown here as the blue spiral structure, which resembles a snail. With permission from A. N. Salt [406]. (b) The interior of the cochlea has two membranes that span the length and width of the cochlea and sandwich the organ of Corti. The basilar membrane is on the bottom, and the tectorial membrane is on top of the organ of Corti. With permission from S. Neely [345]. (c) Enlarged image of the organ of Corti that is sensitive to acoustic signals. With permission from D. J. Lim [282]. The cochlear fluids have negligible damping effect on the cochlear transduction [158] [13]. (d) A light microscopic image of a hair cell that has been isolated from the tissues that normally surround it. Hair cells convert mechanical stimulations of the microscopic sensory hairs that project from their apical surface into an electrical signal. This hair cell is about 30 μm long and the hair bundle is about 5 μm wide. With permission from A. J. Hudspeth [213].

4.2.2 A Proposed Cochlear-Model Architecture Uses Nanotubes to Sample and Process EM Signals

The proposed nanotube-based cochlea-model processor (NCP) applies nanotube signal processing electronics and nanotube-dipole antennas to directly process electromagnetic (EM) signals. Nanotube antennas have narrow bandwidth that can increase the resolution of the spectral processing. Nanotube signal processing can make the spectral processing faster and more sensitive.

An array design can also increase detector sensitivity. The array of nanotube antennas tunes for each narrow frequency band. A bank of array antennas can help the NCP sample the signal spectrum.

An array of MWNT dipoles can gain antenna power by increasing array elements and so increases array cross-sectional area to intercept more EM energy similar to traditional dipole arrays [145]. This is because element spacing depends on the free-space wavelength of the frequency signal regardless of the width of the MWNT dipoles [382].

The advantage of the narrow dipole elements is their compatibility with nanotube (or nanowire) electronics. An all-nanotube architecture avoids high-impedance contacts between metal and nanotubes. And the nano-scale electronics can fit more function in the antenna area for sufficient shielding between the electronics and the nanotube (or nanowire)-based dipoles.

A reconfigurable array of nanotube dipoles can receive multiple frequency signals by connecting different number of dipole elements in a line to form longer dipoles [383]. The elements can interconnect with nanotube-based relays that have predicted high-speed switching [271] [233] and can integrate with nanotube dipoles.

The narrowband nanotube antennas should match spatially isolated frequency components because this can increase frequency selectivity. A waveguide or a bank

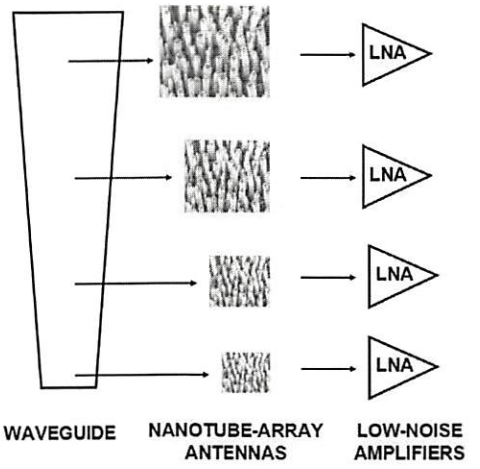

Figure 4.8: A sketch of the waveguide-fed nanotube-array antennas. The nanotube cochlear-model spectral processing architecture uses an optical frequency waveguide to separate different frequency components and to feed frequency-matched nanotube-array antennas. A nanotube-array antenna is more sensitive than a single nanotube. A bank of tunable bandwidth low-noise amplifiers can both filter the antenna output to increase frequency selectivity and amplify the antenna output. The nonlinear amplifier allows noise to enhance faint antenna outputs. The sample nanotube array is reproduced with permission from Kempa et al. [458].

of tunable filters can separate frequency components in space. Figure 4.8 shows a schematic waveguide that distributes different frequency signals to matching nanotube-array antennas. A modified waveguide can implement a dispersive transmission line by reducing waveguide dimensions over its length to restrict the wavelength of a transmitted signal [98] [217].

Researchers have demonstrated optical waveguides with hollow-core fibers [98], a dielectric coaxial waveguide [217], and nanowires [267]. Filtering can also model the cochlear "traveling wave". Researchers have demonstrated an array of antenna-resonator-antenna modules or a frequency-selective surface that directly bandpass-filters

a microwave frequency signal [4]. A NEMS-based tunable filter can also attenuate undesired frequency components in the antenna output to increase frequency selectivity.

The bank of nanotube antennas can estimate an electromagnetic signal's spectrum. The nanotubes sample each frequency component over some time period over a range of frequencies. This is similar to a wavelet decomposition that samples the frequency range with sinusoidal basis functions [381] such as the Gabor transform or the short-time Fourier transform [450].

The sampled spectrum can estimate a signal's spectrogram that has applications in speech, sonar, and radar processing. The estimated spectral density is also the Fourier transform of a signal's autocorrelation (3.25) [223]. This suggests that the proposed architecture can implement signal processing techniques that require an estimate of the autocorrelation of the input signal such as the Yule-Walker algorithm in adaptive signal processing and beamforming algorithms in array signal processing [200].

The frequency sampling suggests that the proposed architecture should be able to process signals in the frequency domain. This can apply to filtering, Doppler radar, matched-filter detection, and frequency-hop detection. Frequency-domain filtering suppresses, amplifies, or phase-shifts select frequency components for low-pass, band-pass, high-pass, comb, and arbitrary-impulse-response linear time-invariant filters. The proposed architecture can implement the frequency-domain multiplication of the signal with the filter transfer function [356] by processing the output of the nanotube antennas.

Doppler radar estimates velocity using a first and second order moment based on an estimate of the Doppler spectrum [57]. Matched filtering is an optimal detection that maximizes the signal to noise ratio [223] when the input signal matches the target signal. The frequency-domain filter weights are the Fourier transform of the time-reversed target signal. Frequency-hop detection is a special case of the matched-filter detection where the target signal is a sinusoid with time-varying frequencies. A frequency-hop

detector can apply to digital frequency modulation and to frequency-division multiple access where the signal changes frequency over time and the hop-pattern conveys information.

The nanotube cochlear-model processing (NCP) can benefit from an all-nanotube architecture that combines high-speed nanotube signal processing with nanotube-dipole antennas. The all-nanotube NCP can process optical frequency signals because nanotube devices can operate up to predicted THz speeds [67] and nanotube arrays have shown antenna length effect at optical frequencies [458]. And nanotube antennas have very narrow bandwidths that can increase the resolution of the cochlear-model spectral processing.

The proposed architecture may also apply noise-enhanced detection of weak signals. Experiments on nanotube stochastic resonance showed that electrical noise can help nanotubes detect faint voltage signals. And researchers have reported noise-enhanced detection in biological cochleae [224] and cochlear implants [339]. So noise-enhancement should benefit the proposed cochlear-model spectral processing.

Chapter 5

Nanotubes Should Enhance Body Armor

Nanotubes should enhance body-armor stealth and strength. This proposed research direction extrapolates applied and theoretical findings. We present a review of nanoenhanced materials, our experimental analysis of body-armor performance, and a proposed adaptive camouflage that support the informed extrapolation.

Researchers have demonstrated that nanotube additives strengthen fibers [264] [6] and toughen ceramics [371], [428], [482], [481], [489] and so can help body armor resist ballistic impacts. Researchers have also demonstrated that nanoparticle-treated fabric armor can adapt to stimuli [272] and can reduce physiological costs of wearing armor.

Nanotubes can reduce physiological costs such as bruising because strengthened materials can reduce body-armor deformation. Nanoparticle-enhanced armor stiffens on impact to reduce deformation [272] and so should reduce or eliminate the bruising effect of bullets that deform soft body armor. The enhanced materials may further reduce heat exhaustion because they can decrease body-armor stiffness, thickness, and weight as well as increase body-armor heat-carrying capacity.

We modeled body-armor bruising effects to study a physiological cost of wearing armor. Field experiments measured body-armor performance with a bruise profile. We modeled the bruising effect of nonpenetrating bullet impacts with statistical and fuzzy

methods and a baseball comparison. The analysis techniques can also model the bruising effects of nano-enhanced body armor.

Nanotube electronics should adapt camouflage patterns to disguise armor. A proposed adaptive camouflage uses nanotubes and nanoparticles to help conceal armor. The proposed camouflage uses octopus-model artificial color organs to display changing camouflage patterns and uses nanotube sensors and processors to coordinate the displayed patterns.

Section 5.1 discusses how nanomaterials can enhance body armor performance. Section 5.2 summarizes our study of soft body-armor performance in terms of a bruise profile. The Appendix presents the experimental results in detail. Section 5.3 proposes an octopus-model adaptive camouflage that uses nanotubes and nanoparticles to help disguise body armor.

5.1 Nanomaterials Can Enhance Body-Armor Strength and Adaptability

Nanotubes and nanoparticles can strengthen armor materials and make adaptive and programmable armor materials. Nanotubes can strengthen polymer fibers and ceramic composites in body armor whereas nanoparticles can help make armor fabric more flexible until external stimuli causes the armor to stiffen.

Body armor materials include textiles, fiber composites, ceramic composites, and metal. Military flak jackets are a compromise between mobility and protection and can consist of camouflaged flexible Kevlar fabrics that cover the torso and composite or metal-plate inserts that reinforce key areas. Mobility is important because it makes the armor user harder to target.

The flexible fabrics allow more mobility but do not stop rifle bullets [454]. The metal or composite plates stop rifle bullets but are heavy so protect only parts of the torso. The flak jackets optimize ballistic protection by covering the torso and shoulders with flexible fabric and reinforcing the front and back with ceramic or metal plates.

Flak jackets optimize mobility by exposing the limbs and joints. The joints are unprotected to retain mobility because thick fabric armor can be stiff and resists bending. An effective camouflage should enhance armor stealth and further improve armor performance.

Alumina ceramic-composite armor can be harder than bullets and can often fracture a bullet on impact without deforming. But ceramics are inflexible and heavy and inhibit movement and heat dissipation. Thin and flexible armor give the armor user more mobility and reduce physiological costs such as heat exhaustion [180]. Nanotube additives strengthen ceramics [371], [428], [482], [481], [489] and polymers [6]. The strengthened materials can make armor thinner and lighter and so reduce physiological costs.

Researchers have found that adding 0.1 wt % carbon nanotubes to alumina composite increases the fracture toughness from 3.7 to 4.9 $MPa{\cdot}m^{1/2}$ [428] and that adding 10 wt % nanotubes nearly triples the fracture toughness of nanocrystalline alumina (9.7 $MPa{\cdot}m^{1/2}$) [489]. Nanotube-enhanced alumina ceramics permit armor designs that use thinner and lighter ceramic plates to cover a larger area and so can add mobility and reduce physiological costs. Nanotubes might also toughen boron carbide that has a diamond-like hardness of about 30 GPa but that fails to resist high-velocity bullets [79].

The textile and fiber-composite soft body armor resist bullet penetration because the fibers distribute a bullet's crushing force over a large area when the bullet deforms the armor [302]. The two most common ballistic fabrics in the United States are Kevlar and Spectra Shield [454]. Kevlar is an aramid or poly-(*p*-phenylene terephthalamide)

(PPTA) fiber and its fabrics are woven [301]. Zylon or poly(p-phenylene benzobisoxazole) (PBO) fibers are stronger than Kevlar but Kevlar is the most popular armor fiber.

Spectra Shield consists of ultra high molecular weight polyethylene and its fibers are resin-bonded instead of woven and lie parallel in each criss-crossing sheet [454]. A ballistic fabric resists bullets better if its threads consist of numerous fine microfibers [301].

Nanotube additives strengthen polymers to make stronger fibers and fabrics. Ballistic fabrics absorb and disperse an impact's energy from the struck fibers to other fibers in the fabric [454]. This dissipation reduces the severity of the impact when the armor stops the bullet.

Nanotube-strengthened fibers can absorb more energy. Researchers have strengthened Zylon or PBO fibers with multiwall nanotubes: Adding 10 wt% MWNT increases PBO fiber's tensile strength by 50% [264].

Nanoparticle-treated fabrics recruit more fibers to disperse a bullet's impact energy. The silica nanoparticle-based shear thickening fluid (STF) hardens on impact and reduces sliding between fibers. This helps a struck fiber disperse the impact energy to neighboring fibers.

Researchers have shown that a STF-treated Kevlar armor resists ice pick thrusts that penetrate untreated armor [143] and have shown that the STF-treated armor deforms less on bullet impact than untreated armor [272] [232] (see Figure 5.1). STF-treated armor can be thinner and so can be more flexible. This should help armor designs that protect limbs and joints.

Magnetic rheologic (MR) fluids harden in magnetic fields so a MR-treated armor can have programmable toughness. The iron nanoparticles turn a MR fluid into a solid when magnetic fields cause the nanoparticles to agglomerate [1] [2].

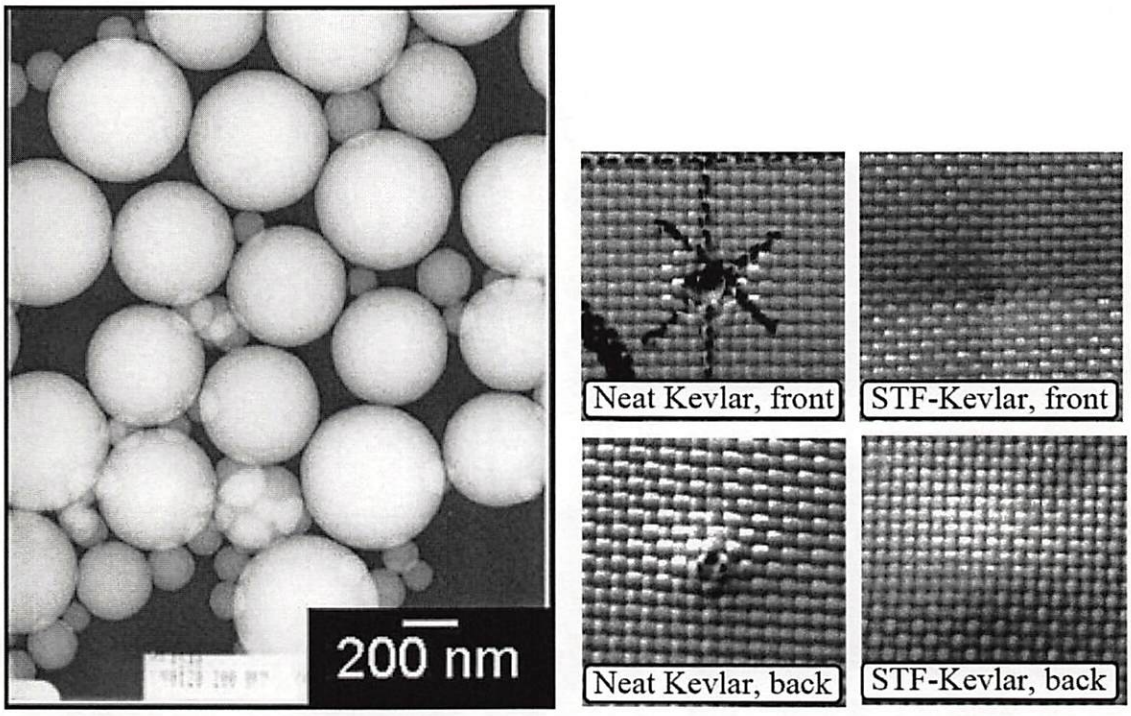

(a) Silica Nanoparticle

(b) Resist Spike Impact

(c) Plain Kevlar

(d) STR-treated Kevlar

Figure 5.1: Shear thickening fluid enhances Kevlar armor (a) Scanning electron micrograph of silica nanoparticles in a shear thickening fluid. (b) STF-treated Kevlar resists spike penetration. (c) Untreated Kevlar shows larger deformation than (d) STF-treated Kevlar. With permission from Wetzel et al. 2004 [143].

Deshmukh et al. have found that a MR-treated cellular solid can modulate total energy absorption by a factor of 50-fold for small volume fractions of the fluid ($\approx$15%) using magnetic fields varying from 0 to 0.2 Tesla [116]. MR fluid-impregnated armor fabric should recruit fibers to disperse impact energy similar to the STF-treated armor because the fabrics have interfiber spacing that resembles the experimental substance in [116]. These enhanced fabric armor might prevent a bullet impact from bruising the tissue beneath the armor.

5.2 A Bruise Profile Measures Soft Body Armor Performance

A bruise profile can measure the performance of nanoparticle-enhanced body armor. Field experiments used a bruise profile to model the blunt injury effects of a handgun bullet that deformed generic Kevlar fabric armor against a backing material that simulated tissue. The bruise profile measured armor performance in terms of a physiological cost. This section summarizes our experimental findings based on Kevlar-fabric armor. The Appendix contains the complete report.

Our analysis techniques can also model bruising effects in nanoenhanced armor. The analysis techniques can evaluate the performance of the enhanced armor that can reduce or eliminate bruising effects for nonpenetrating bullets.

We analyzed the experimental data statistically and found that impact deformation correlated with bullet weight and momentum better than it correlated with bullet kinetic energy. We applied a fuzzy system to predict the bruising effect of handgun bullets on body armor. This type of fuzzy analysis can learn to predict the bruising effect for nanoparticle-enhanced body armor.

We also compared handgun bullets and baseballs by shooting bullets at armor-clad Plumber's Putty targets and by pitching baseballs at bare Putty targets. The Plumber's Putty does not simulate tissue but records the impact deformation in a consistent medium.

Baseball impact depths were comparable to bullet-armor impact depths: Getting shot with a .22 caliber bullet when wearing soft body armor resembles getting hit in the bare chest with a 40-mph baseball. Getting shot with a .45 caliber bullet resembles getting hit with a 90-mph baseball.

What is the bruising effect of a bullet on soft body armor that deforms and permits the impact to affect tissue beneath the armor? Figure 5.2 shows the bruise beneath the armor after a .44 caliber bullet struck a police officer's upper left chest. The Kevlar-fabric armor stopped the bullet but the impact still injured soft tissue. Few researchers examine the bruising effect of soft body armor [226]. A national standard for armor testing [343] includes an evaluation of the so-called "backface signatures" that are the deformation in the armor's backing material after a gunshot. The standard uses modeling clay to back and record the armor deformation instead of gelatin blocks that can simulate tissue. So the backface deformation data correlate little with a bullet's bruising effect.

We examined the bruising effect with a fuzzy function approximator and a baseball analogy. Bullet impact experiments produced the bullet-armor bruise data that generated a quantitative bruise profile and a baseball-impact comparison. The bruise profile gave the depth and width of the deformation that a handgun bullet made on gelatin-backed armor (see Figure 5.3) for gelatin blocks that we made with Type 250A Ordnance Gelatin (from Kind & Knox Gelatin).

Experiments shot different caliber handgun bullets at gelatin-backed armor to produce armor deformations. The depths and widths of the deformations correlated with handgun-bullet weight, momentum, and kinetic energy. Deformation correlated the least

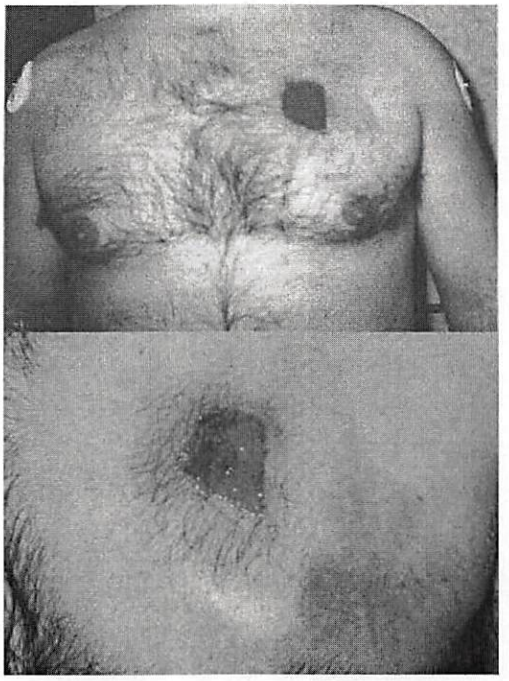

Figure 5.2: (a) Actual bruise from a police officer shot by a .44 caliber weapon in the line of duty while wearing soft body armor. (b) Close-up of the "backface signature" bruise in (a). Note that the bruise includes the discoloration around the wound. Photo reproduced with permission from the IACP/Du Pont Kevlar Survivors' Club.

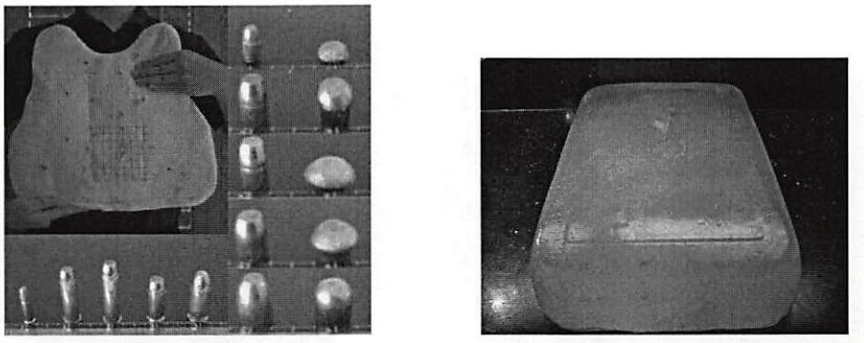

(a) Fabric Armor (b) Gelatin Block

Figure 5.3: Armor experiments used soft body armor and ordnance gelatin blocks. (a) A 14-ply Kevlar soft body armor panel (from a Superfeatherlite vest from Second Chance) and some sample cartridges (.22, .38, .357 magnum, .40, and .45 caliber). The right side of the image shows the pristine and armor-deformed bullets for the five calibers. (b) A sample 10% ordnance gelatin block. A target consisted of a generic armor-clad gelatin block. The gel block simulated tissue.

with bullet kinetic energy and did not correlate with bullet speed for experiments that varied both bullet weight and speed.

We applied a simple linear regression model

$$y = \beta_0 + \beta_1 x \tag{5.1}$$

to test whether bullet deformation y correlated with each of a bullet's properties: weight, momentum, kinetic energy, speed and distance to target. The null hypothesis $\mathbf{H}_0 : \beta_1 = 0$ stated that the slope β_1 of the regression line in (5.1) was zero and thus the impact deformation's depth and width (dependent variables) did not vary with a bullet's weight, momentum, kinetic energy, speed, or distance to target (independent variables). The p-value measures the credibility of $\mathbf{H}_0$. A statistical test rejects the null hypothesis $\mathbf{H}_0$ at a significance level α if the p-value is less than that significance level: Reject $\mathbf{H}_0$ if p-value $< \alpha$. A test would reject the null hypothesis $\mathbf{H}_0$ at the standard significance levels $\alpha = 0.05$ and $\alpha = 0.01$ if p-value < 0.001. Correlation coefficient R^2 measures the strength of the correlation.

Linear regression gave correlation coefficients R^2 between armor-deformation depth and bullet weight ($R^2 = 0.880$ and $p < 0.001$), momentum ($R^2 = 0.741$ and $p < 0.001$), kinetic energy ($R^2 = 0.474$ and $p < 0.001$), speed ($R^2 = 0.089$ and $p < 0.025$), and distance to target ($R^2 = 0.415$ and $p < 0.001$). This showed that the correlations for weight and momentum were statistically more significant than kinetic energy and that speed did not correlate with deformation depth.

We applied a multiple regression

$$y = \beta_0 + \beta_1 x_1 + \beta_2 x_2 \tag{5.2}$$

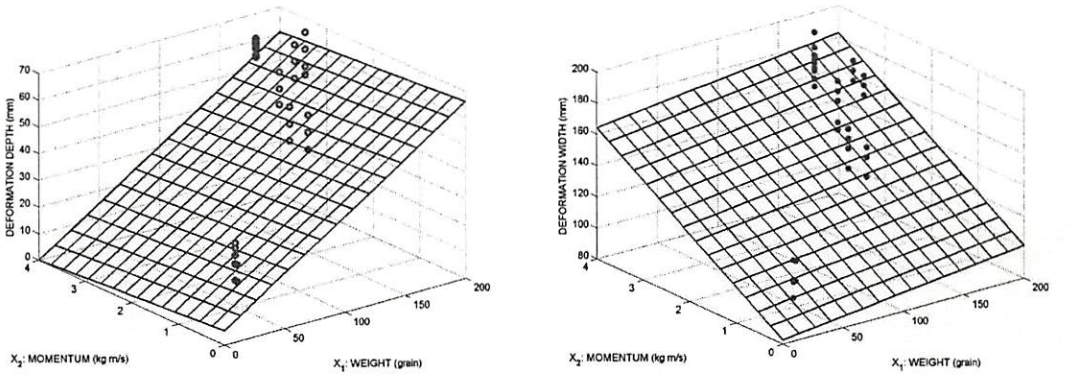

(a) DEPTH (b) WIDTH

Figure 5.4: The deformation data from gelatin-backed bullet-armor experiments that used generic Kevlar fabric armor. The figures show the complete set of experimental depth data in (a) and the width data in (b) and their fit to regression planes as functions of weight (X_1) and momentum (X_2). The regression planes consist of those points that satisfy the regression equations: $y_1 = 5.550 + 0.304x_1 - 1.361x_2$ for depth in (a) and $y_2 = 84.846 + 0.425x_1 - 0.240x_2$ for width in (b).

for combinations of a bullet's property such as weight and momentum and tested the null hypothesis $\mathbf{H}_0 : \beta_i = 0$ for $i = 0, 1, 2$ that all the parameters were statistically insignificant. This tested whether the deformation's depth and width varied with the combination of a bullet's weight and momentum. The multiple regression produced regression coefficients between deformation depth and the combination of weight and momentum ($\beta_1 = 0.304$, $p < 0.001$, $\beta_2 = -1.361$, and $p = 0.510$) and the combination of weight and kinetic energy($\beta_1 = 0.293$, $p < 0.001$, $\beta_2 = -0.006$, and $p = 0.427$). This showed that the coefficient for bullet weight was statistically more significant than for either momentum or kinetic energy. These regression tests helped guide our choice of weight and momentum as the inputs of a fuzzy system.

A fuzzy system learned from the bullet-armor experimental data to predict the bruise profile for range ammunition, generic fabric armor, and ordnance gelatin blocks. Figure 5.4 shows a set of data that tuned a fuzzy system. Impact experiments that test new

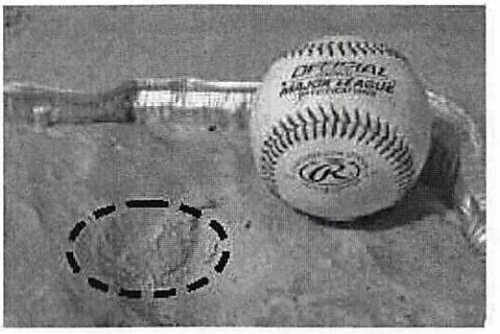

Figure 5.5: A regulation baseball and a crater of its impact. Pitching machines threw baseballs at tubs of Plumber's Putty. A chronograph measured the speed of each baseball. The baseball speeds were approximately 40, 50, 60, 70, 80, and 90 miles per hour.

armor designs would produce impact data that can tune the fuzzy system and update the bruise profiles for the new armor designs including nano-based enhancements.

Baseball experiments compared bullet-armor impacts to baseball impacts in two ways: Deformation depths in putty and the slopes of the fitted regression lines. The first way compared how the two types of projectile deformations differed. The experiments found that baseball impacts and bullet-armor impacts had similar depths in Oatey's Plumber's Putty (see Figure 5.5). The similarity of impact depths suggested that handgun shots on soft body armor would feel like baseball impacts without armor. Fast-baseball impact depths were comparable to bullet-armor impact depths: Getting shot with a .22 caliber bullet when wearing soft body armor resembles getting hit on the chest with a 40-mph baseball. Getting shot with a .45 caliber bullet resembles getting hit with a 90-mph baseball.

The second way compared the correlation and regression slopes of the two types of impacts. The experiments found that the mean depth of a baseball's impact and the depth of a bullet's armor-impact both correlated with projectile momentum (see Fig. 5.6). The baseball impacts had correlation $R^2 = 0.93$, regression equation $y = -6.155 + 5.188x$, and p-value < 0.001 where x was a baseball's momentum in kilograms meter per second

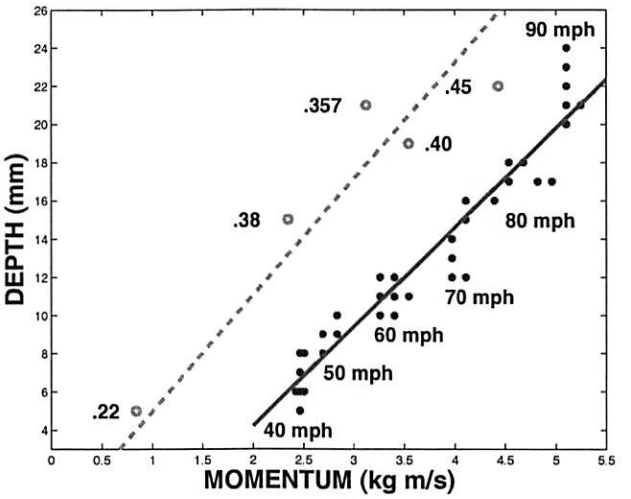

Figure 5.6: Baseball and bullet impact depths in Plumber's Putty versus momentum. The baseball impact depth correlated with baseball momentum $R^2 = 0.93$ and p-value < 0.001 for the null hypothesis: $\beta_1 = 0$. The solid line on the right is the regression line for the baseball impacts (blue dots) $y = -6.155 + 5.188x$ where x is baseball momentum and y is putty deformation depth. Only two data points fell outside of the 95% confidence bounds. Bullet-armor impact depths correlated with bullet momentum $R^2 = 0.97$. The green dashed line on the left is the regression line for the bullet-armor impacts (green circles) $y = 2.124 + 4.766x$ where x is bullet momentum and y is depth. The two regression lines have the similar slope $\beta_1 \approx 5$. A multiple regression analysis with dummy variables (Gujarati-Chow test) could not reject the null hypothesis $H_0 : \beta_1(\text{baseball}) = \beta_1(\text{armor})$ for the test statistics $t = 0.855$ and p-value $= 0.396$. So the test retained the null hypothesis that the two types of impacts had the same slope.

(kg m/s) and y was the putty deformation depth in millimeters (mm). The bullet-armor impacts had similar correlation $R^2 = 0.97$, regression equation $y = -2.12 + 4.76x$, and p-value < 0.001.

The putty-impact regression lines had similar slopes $\beta_1 \approx 5$ for the baseball impacts ($\beta_1 = 5.188$) and the bullet-armor impacts ($\beta_1 = 4.766$). Fig. 5.6 suggests that the two lines are parallel: Same slope with different intercepts. A modified Chow test (Gujarati-Chow test [189]) confirmed that the two putty-impact regression lines had statistically indistinguishable slopes for the slope-term test statistic $t = 0.855$ and p-value $= 0.396$.

The p-value implies that the identical-slope hypothesis must be retained at the standard significance levels $\alpha = 0.05$ and $\alpha = 0.01$.

5.3 A Proposed Octopus-Model Architecture Uses Nanotubes and Nanoparticles to Adapt Camouflage

Nanotubes can coordinate octopus-model artificial color organs to disguise body armor. The proposed adaptive camouflage models an octopus that changes skin patterns to avoid detection.

The adaptive camouflage can match a background by using nanotube signal processing to change displayed patterns. Nanotube optical sensors [484] can sample a background image. Nanotube processors can quickly [67] select a preset pattern or compose a custom pattern that optimally matches a background.

Nanotubes can interconnect the sensors, processors, and color organ by applying embedded wired connection in a flexible substrate [54] or by applying wireless connection in a distributed network (such as in [432]).

This section reviews how *Octopus vulgaris* and other cephalopods camouflage or disguise their bodies and proposes an octopus-model adaptive camouflage that uses nanotubes and nanoparticles.

5.3.1 Octopus Physiology for Camouflage

An octopus can abruptly change its appearance or mimic other animals by changing its color, texture, posture, and locomotion [325]. The octopus responds to visual input and selects an appropriate body pattern from a small set of patterns that are "hardwired" into the central nervous system [325]. The preset patterns either help the animal match its background or break up the outline of its body.

Researchers have further documented nine octopus specimen that mimic poisonous animals [352] (see Figure 5.7). These octopuses use posture and locomotion to mimic swimming fish and sea snake both in appearance and motion.

The octopus camouflage changes whole body patterns to either blend in with the background by matching the color, brightness, and texture (see Figure 5.8(a)) or break up the body outline by displaying disruptive patterns (Figure 5.8(b)). A whole body pattern consists of organized collections of skin patches or units (see Figures 5.8(c) and 5.8(d)).

Individual skin patches have chromatophores and iridophores that display different colors, leucophores that adjust brightness, and skin papillae musculature that change texture [325]. The chromatophores and the iridophores occur across the whole patch. The leucophores occur only in the central region of the patch and beneath the chromatophores and the iridophores. A skin papilla occurs exactly at the center of a patch. It contracts to stretch the patch into a spike.

The octopus camouflage is an orchestration between chromatophores, iridophores, leucophores and skin muscles [325]. *Octopus vulgaris* has up to 230 chromatophores per square millimeter of skin and devotes millions of neurons to control them [325]. Chromatophore motoneurons send pulses to expand specific sets of chromatophores in the skin. Banks of chromatophore motoneurons act in concert to produce the bars, bands, and lines in *Octopus vulgaris*' skin [325]. An octopus selects a stipple, mottle, or disruptive pattern if it sees discontinuities.

The octopuses match the background brightness by manipulating the chromatophores and the leucophores. Relaxing the dark-colored chromatophores reduces their size and uncovers the underlying leucophores that reflect the surrounding light and help match both the color and brightness of a low-light background (see Figure 5.9).

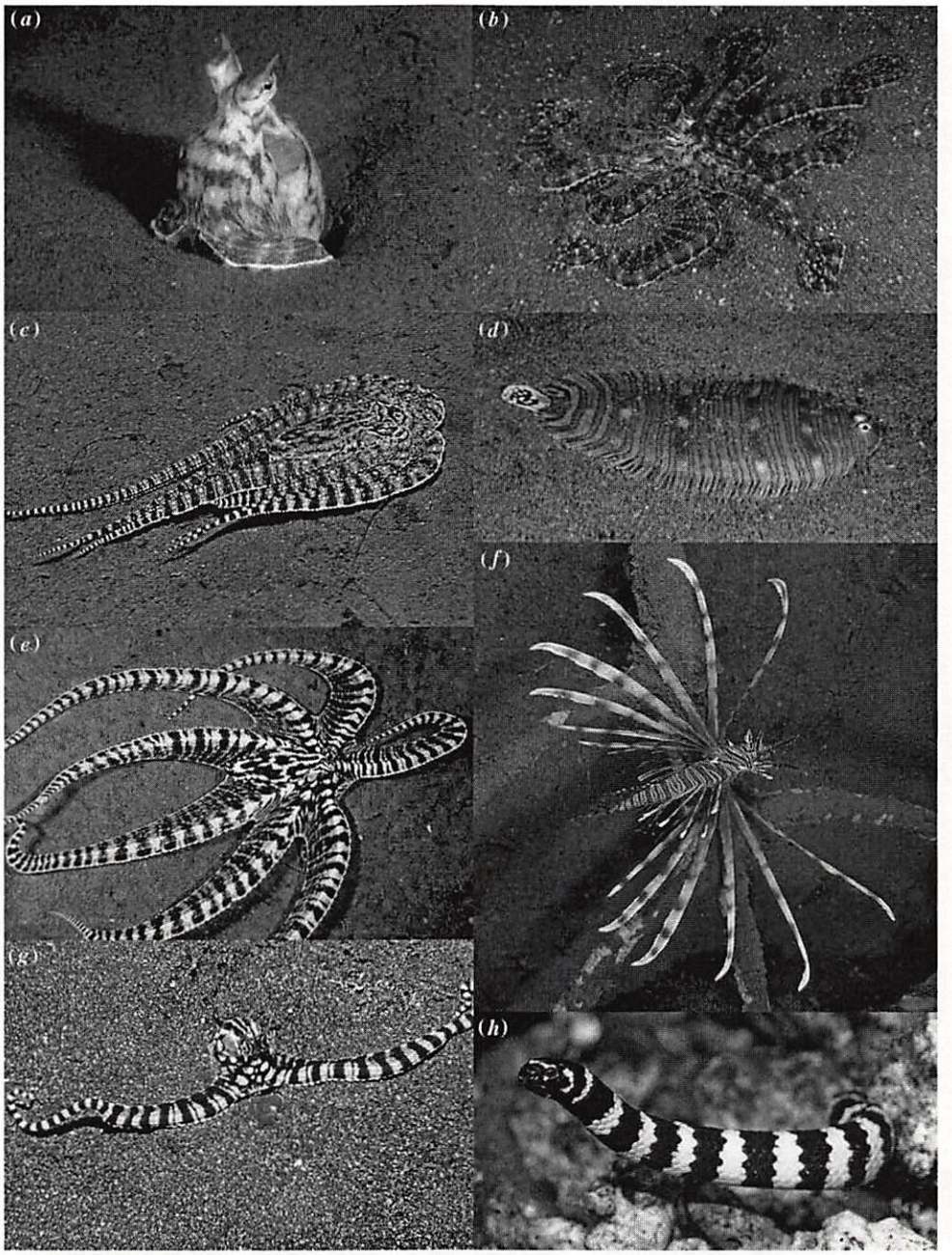

Figure 5.7: Mimic octopus (a) sentinel state in mouth of burrow; (b) normal foraging color pattern; (c) flatfish mimicry; (d) flatfish model, banded sole (Zebrias sp.); (e) lion-fish mimicry; (f) lion-fish model (Pterois sp.); (g) sea-snake mimicry; (h) sea-snake model, banded sea-snake (Laticauda sp.). Photographs by permission M. Norman et al. 2001 [352].

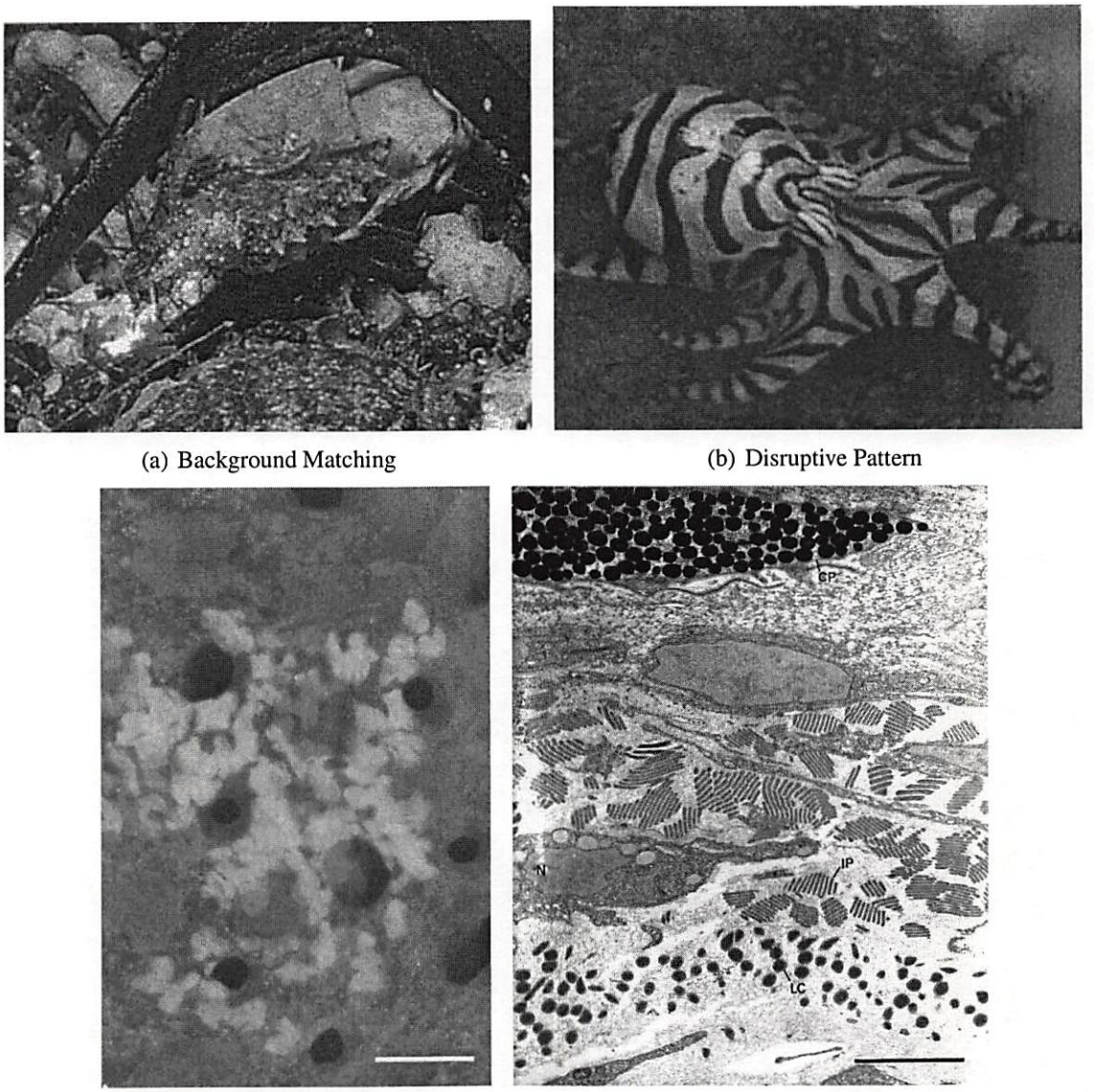

(a) Background Matching

(b) Disruptive Pattern

(c) Skin Patch

(d) Cross Section

Figure 5.8: Examples of cephalopod camouflage. (a) *S. officinalis* hatchling conceals itself with major lateral papillae and raised arms (mantle length 10 mm). Messenger 2001 [325]. (b) *Octopus zonatus* shows disruptive pattern (mantle length, 30 mm). Hanlon 1988 and Messenger 2001 [195]. (c) *Octopus vulgaris* chromatophore unit. Underlying leucophores reflect white and iridophores appear as small blue-green. Scale bar 50 μm. Froesch and Messenger, 1978 [167]. (d) Low-power electron micrograph of a vertical skin section of *Octopus vulgaris* shows a chromatophore (CP) above iridophores (IP) and leucophores. IP for iridosomal platelets, N for nucleus, and LC for leucophore clubs. Scale bar 5 μm. Froesch and Messenger, 1978 [167].

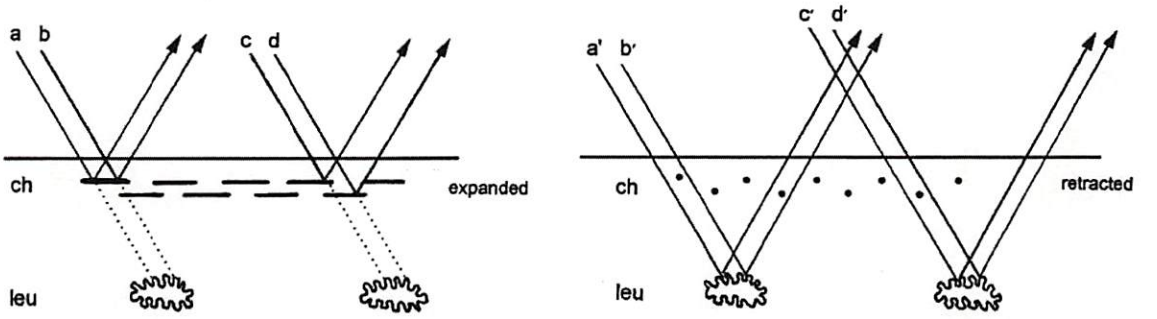

(a) Bright Background (b) Low-light Background

Figure 5.9: Schematics of background matching with chromatophores (ch) and leucophores (leu). (a) The chromatophores contract their muscle fibers and expand to absorb light and let their pigment color show for well-lit backgrounds. (b) The chromatophores relax and reduce their size for low-light backgrounds. This uncovers the leucophores that reflect the background light. Messenger 2001 [325].

The octopuses match the colors in a well-lit background by selectively contracting the chromatophore muscles that control the relative sizes of the differently colored chromatophores. *Octopus vulgaris* has yellow, orange, red, brown, and black chromatophores [360]. The iridophores refract light to give green, cyan, and blue colors. The uncovered leucophores reflect background light so can match the background color.

A single chromatophore receives multiple innervation so it can participate in different patterns [325]. The skin papilla muscles contract and turn a skin patch into a spike. This can match the smooth or rough texture of a background [360].

The chromatophores in an octopus and other cephalopods are neuromuscular organs [325]. A cephalopod uses neural control of the chromatophore organs to change its appearance almost instantaneously [325]. Each chromatophore consists of a pigment-containing elastic sacculus that attaches to a set of obliquely striated radial muscles. Each radial muscle has its own nerves and glia. The excited muscles contract to expand the chromatophore. The relaxed muscles allow the elastic sacculus to retract the chromatophore (see Figure 5.10).

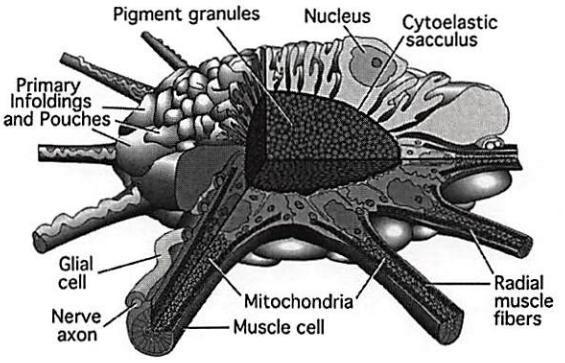

Figure 5.10: Cephalopod chromatophore organ. The figure is a retracted chromatophore from the squid, *Loligo opalescens*. Messenger 2001 [325].

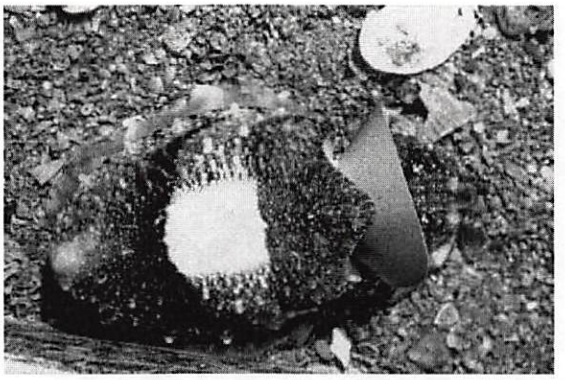

Figure 5.11: The cephalopod next to a white stone displays a white square. A plastic ruff placed around the "neck" of *Sepia officinalis* (mantle length 120 mm) prevents it from seeing its own mantle but does not prevent it from showing an appropriate disruptive pattern, which includes such distinctive components as the White square. Messenger 2001 [325].

Octopus vulgaris has more than a million neurons in the chromatophore lobes. Specific nerve fibers innervate groups of chromatophores within fixed morphological arrays and so produce visible chromatomotor fields [325]. Researchers believe that the skin patterns are hard-wired. But the mimic octopuses [352] suggest that at least a part of the camouflage behavior is learned. Figure 5.11 shows a cephalopod that adapts its gross disruptive patterns to mimic a nearby object.

5.3.2 A Proposed Adaptive Camouflage Models *Octopus vulgaris*

A proposed adaptive camouflage can help conceal armor by modeling octopuses to match camouflage patterns to backgrounds. The proposed architecture loosely follows the schematic in Figure 5.9. Artificial color organs can display programmable patterns. And nanotube detectors and processors can select a camouflage pattern that optimally matches a background.

A prototype adaptive camouflage may use available components. Researchers have developed a color-change gel in Figure 5.12(a) that models octopus chromatophore organs. Commercial cadmium selenide (CdSe) semiconductor quantum dots or q-dots in Figure 5.12(c) can be superior pigments in artificial chromatophores. Retro-reflective materials in Figure 5.12(d) can be efficient artificial leucophores. Nanotube-based actuators [192] can implement artificial papillae that alter surface textures.

Programmable MR-treated fabrics can help an armor user maintain a posture to remain hidden. The MR-treated armor can programmably stiffen [231] [116] to support joints and so can help with posture.

Nanotube signal processing should further help disguise armor by approximating invisibility. Researchers have demonstrated an "optical camouflage" [433] that approximates invisibility by duplicating the background image. The adaptive camouflage should approximate invisibility by simulating a transmissive medium at the pixel level.

Nanotubes and nanoparticles can model an artificial chromatophore organ or chromatomotor that consists of photoemitters, reflecter/scatterers, and photoabsorbers. Stimuli-responsive polymer particles [8] can combine with mature products such as CdSe q-dots [385] and retro-reflective beads and prisms [393] to produce prototype chromatomotors. A 20–60 μm diameter particle of N-isopropylacrylamide (NIPAM) polymer shrinks by a factor of ten for heating that increases the temperature to 34 °C

from room temperature [8]. Particles smaller than 20 μm in diameter absorb light poorly so the shrunken particles show little color [8].

Commercial CdSe q-dots should improve the pigments in [8] because q-dots are more stable than most dye and offer many more color choices. A 50 μm diameter bead rests on a reflective surface and reflects an incident light back to its source [433] with high reflective efficiency.

Commercial retro-reflective beads should improve the leucophores [393]. *Octopus vulgaris* chromatophores measure 300 μm in diameter (see Figure 5.9(a)) so an artificial chromatophore of a similar size would use tens of NIPAM particles and reflective beads.

One possible architecture resembles a modified liquid-crystal display (LCD) (see Figure 5.9(b)): The expanded polymer particles display color from the q-dots and cover the retro-reflective beads in each artificial chromatomotor pixel. Other possible architectures can use electromechanical switches to cover and uncover the q-dots and the reflectors or use switchable reflective substrates [295].

The artificial chromatophores can incorporate a light source to conceal an armor user in backlit conditions or when the armor user appears darker than the background (see Figure 5.13). An ultraviolet emitter can stimulate a cluster of artificial chromatophores and cause their q-dots to emit light [385] in low-light conditions. Nanotube field emitters can generate ultraviolet light [349] with an electron beam.

Effective camouflage requires only a fixed set of patterns that can match most backgrounds as the octopuses demonstrate. A central control architecture models the optic-lobe controlled camouflage in an octopus that selects an optimal pattern based on visual information.

A camouflage pattern can be hardwired for designed patterns (Figure 5.14) and can also be adapted for new or changing patterns. An adaptive camouflage can take

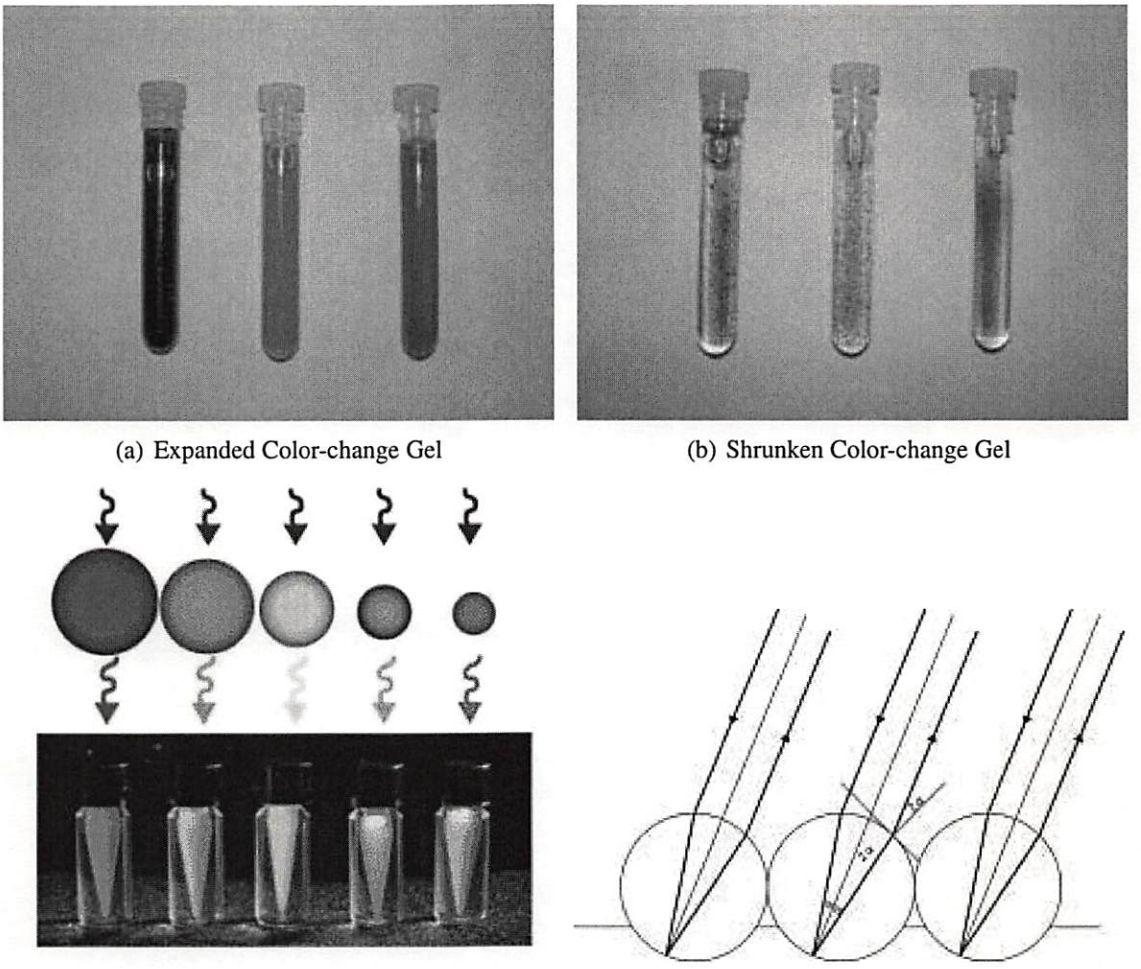

(a) Expanded Color-change Gel

(b) Shrunken Color-change Gel

(c) CdSe Quantum Dots

(d) Micron-scale Beads

Figure 5.12: Micro and nano scale materials for adaptive camouflage. (a) and (b) Dispersions of color change gel particles that contain black, magenta and blue dye. (a) Expanded state at 20 °C. (b) Shrunken state at 40 °C. With permission from R. Akashi [8]. (c) Vials of nano scale quantum dots under UV illumination. The colored spheres illustrate the relative sizes of the CdSe quantum dots in the vials. Quantum Dot Corporation, online http://www.qdots.com (d) Micron scale beads converts a reflective surface into a retro-reflective surface: Light reflects back toward the source. With permission from S. Tachi [433].

a snapshot of its surroundings, compare the image sample with stored patterns, and select the best hardwired pattern using little computation.

Figure 5.13: Matching background brightness and color improves camouflage. The center soldier appears brighter than the surroundings. The fourth soldier on the right appears darker than the immediate surroundings. This shows that brightness-matching and color-matching improves camouflage effectiveness. Photograph by permission G. Cramer [97].

Nanotube photodetectors can be compact and sensitive and fit in ultra-dense arrays. An all-nanotube architecture for signal processing and interconnection can operate at high speeds. This nanotube signal processing can process the visual information, assemble a combination of fixed patterns, and control an array of photoemitters such as the artificial chromatomotors.

Pure singlewall nanotube fibers [150] have strength and conductivity that suggest super-strong and conductive fabrics that can be part of the armor and can connect the detector array to the signal processing integrated circuits. The nanotube sensors and circuits can also integrate on a flexible conductive polymer substrate [479] that covers the armor.

Adaptive camouflage can approximate invisibility if it precisely duplicates the background. A so-called "optical camouflage" duplicates the background perfectly

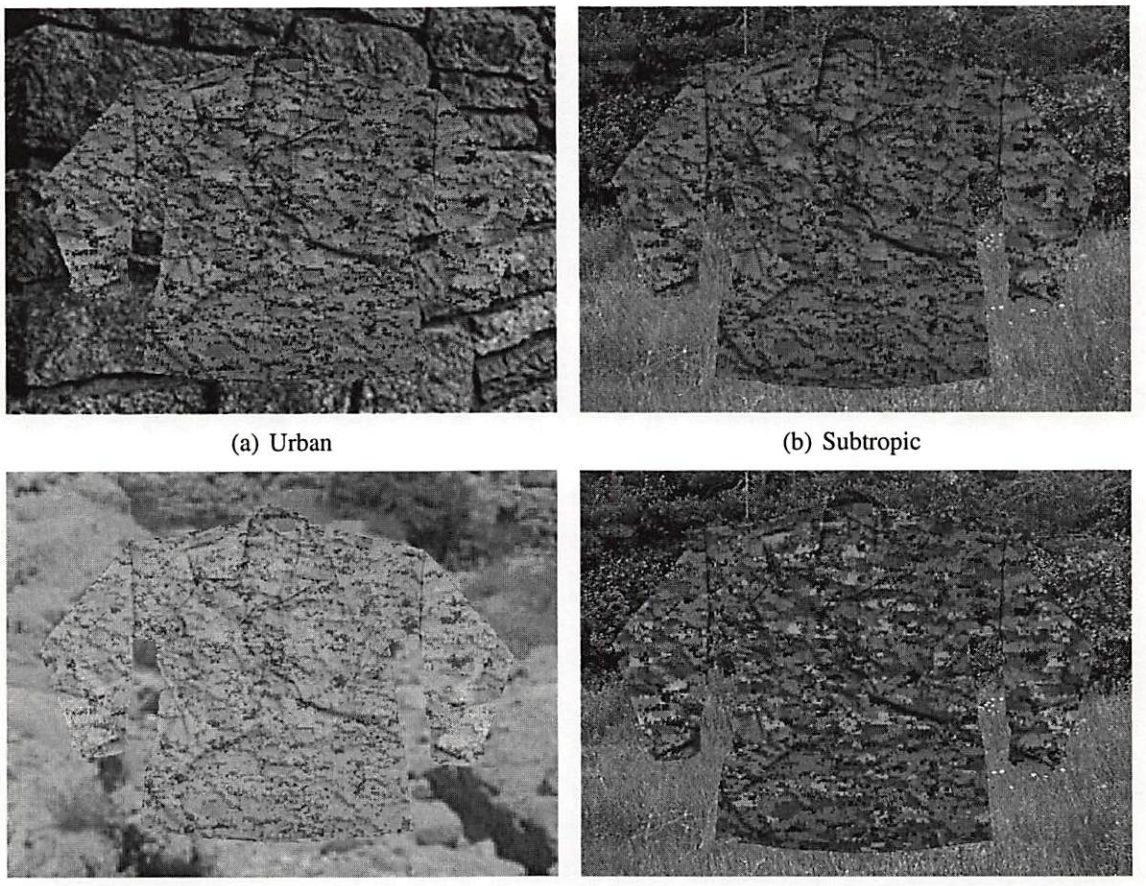

(a) Urban (b) Subtropic

(c) Desert (d) Woodland

Figure 5.14: Designed camouflage patterns. The designer developed these camouflage patterns using proprietary graphics techniques known as Camouflage Designated Enhanced Fractal Geometry. Photographs courtesy of G. Cramer [96].

but only from certain viewing positions (see Figure 5.15). True invisibility requires duplicating almost all incident light as if the light passed through air.

Nanotube signal processing may approach invisibility at the pixel level: A high-resolution wide-area array of photodetectors samples the incident light. A similarly distributed array of photoemitters displays the sampled image. A central or distributed signal processor extracts the frequency, phase, amplitude, and angle of arrival from the

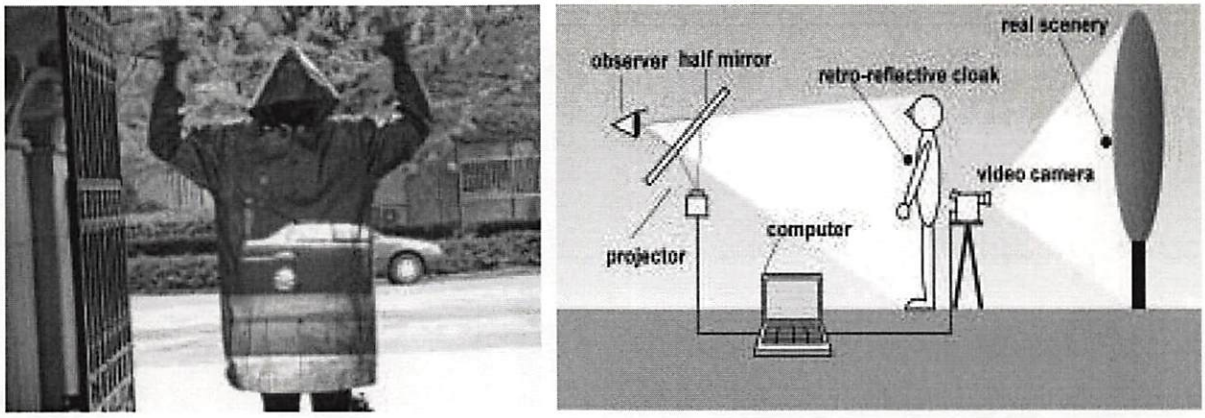

(a) Optical Camouflage (b) Video Projection

Figure 5.15: Video projection produces near invisibility. A camera behind the person records the background for projection onto the person's cloak. The cloak has a coating of retro-reflective material. S. Tachi 2003 [433].

sampled image and computes the weights for each emitter to duplicate the optical field for almost all viewing positions. This should resemble a holographic display.

Nanotube high-speed computation [67] may perform the image and array signal processing in real time with a reduced resolution. Nanotube interconnection, switches, sensors, and emitters can enable compact and low-power designs.

Single-electron transistor-based artificial molecules can improve on the octopus model. True hologram-like invisibility may be possible with large arrays of nanoscale photodetectors, emitters, and distributed signal processors. One such nanoscale emitter may be a CNT-SET-based artificial molecule that can tune its emission frequency.

The artificial molecules can emit light using the same principle as the semiconductor quantum dots [385]: Excited electrons emit photons with energy equal to or greater than the semiconductor bandgap to return to its ground state. Each semiconductor nanoscale dot has an electronic density of states with a size-dependent bandgap. So a SET-based artificial molecule can tune its emission frequency because it can alter the electronic density of states by adding single electrons [319].

Chapter 6

Conclusions

Nanotubes can process noisy signals in various contexts. We presented two central findings and a proposed research direction that support this general thesis.

Nanotubes can enhance signal processing by using noise-enhanced detection and by using nanotube-enhanced transistors. We presented experimental results based on a carbon nanotube transistor that showed noise-enhanced detection at the nanolevel. We also reviewed nanotube electrical and mechanical properties that can enhance transistors.

Nanotubes can further enhance signal processing by directly detecting electromagnetic (EM) signals as narrowband resonant dipole antennas. We presented a nanotube-antenna theorem based on a quantum-conductor model that showed a similarity between nanotube-dipole antennas and thin-wire dipole antennas for limited quantum effects. This nanotube detection of EM signals lead to a proposed cochlear-model signal processing architecture that could directly detect and filter EM signals.

Nanotubes can also enhance body-armor stealth and strength. We proposed a research direction for adaptive camouflage based on applied and theoretical analysis. We reviewed nanotube-enhanced armor materials and nanoparticle-enhanced body armor. We also presented experimental analysis of body-armor performance in terms of a physiological cost.

We next propose five areas for future research that are informed extrapolations of the presented work. The first area of research is the measurement of the current distribution in a nanotube-dipole antenna. The presented antenna analysis assumes a compressed

sinusoidal current distribution for quantum conductors and requires experimental data to verify the current-distribution assumption.

Experimental setup can be difficult. Nanotubes and nanowires have large contact resistance with micro-scale electrodes that can complicate impedance measurement and so affect current-distribution measurements. The size of nanotubes and nanowires can further complicate voltage and current measurements along nano-diameter dipole antennas.

A related research area is that noise should help our proposed architecture for direct cochlear-model spectral processing of EM signals using nanotube antennas. Noise enhancement should benefit the proposed architecture because noise helps nanotube transistors detect signals and because gated nanotubes can act as antennas. So noise should benefit gated nanotube-array antennas. Noise can also benefit the proposed architecture because programmable-threshold transistors should adapt to changing noise levels to optimize noise benefits and because amplifiers can exhibit noise-enhancement and so apply noise enhancement to the proposed architecture that amplifies the antenna output.

The second area of research is that noise should help tune a mechanical oscillator's resonance frequency or help it filter signals. Researchers have demonstrated stochastic resonance (SR) in bistable systems that include oscillators. Their results suggest noise-enhanced detection could benefit nanotube oscillators.

Thermal or acoustic noise might help an oscillator use less power. Oscillator SR effect could save power if thermal noise helps an oscillator maintain a frequency using a low-power reference signal or using a reduced power supply.

A related area of research is to use nanotube electromechanical oscillators in cochlear-model spectral processing. Nanotube oscillators resemble cochlear stereocilia in shape, variable-conductivity, frequency-tuning, and variable-length. An artificial

cochlea might use nanotube stereocilia to amplify, transduce, and process acoustic signals. Noise should help nanotube stereocilia detect faint signals because noise helps the mammalian cochlea detect faint sounds and because researchers showed that mechanical oscillators exhibit SR.

The third area of research is to develop a prototype artificial color organ using commercial products. The proposed adaptive camouflage can enhance concealment if it selects from a set of hardwired camouflage patterns and can switch between desert, woodland, and urban camouflage patterns for example. Nanoscale quantum dots can improve the pigments in a camouflage pattern. Microscale retroreflectors can help a camouflage match background light levels. And researchers have demonstrated a heat-activated polymer that can compress pigment sacs.

The fourth area of research is the manipulation of artificial molecules. The single-electron transistor (SET)-based artificial molecules may form programmable pseudo orbitals as each additional electron in the SET modifies the electron density of states. The proposed artificial molecule [319] may improve adaptive camouflage by programmably emitting light of different frequencies.

Artificial molecules might also help manipulate particles at the nanolevel. A programmable electron pattern can attract a particle but prevent it from forming van der Waals attachment with the substrate of the artificial molecule. So this manipulator might resemble a miniature crane that can programmably pick up and release nanoscale objects.

The fifth area of research might apply nanotube-based electronics to further enhance body armor by heating and melting copper-jacketed bullets similar to an electric armor for lightly armored vehicles. British researchers have developed an electric armor to defend against shaped-charge weapons [417] and protect lightly armored personnel carriers.

The electric armor defeats a shaped charge by disrupting the focus of the molten copper that a shaped charge produces to melt thin armor. The electric armor consists of two conductive armor plates that send a large electric current to a copper jet that completes the circuit. This generates intense heat that vaporizes the molten copper and disperses the copper jet.

Nanotubes may help body armor protect against bullets with a similar strategy. Banks of nanotube-based supercapacitors [287] can provide the electric charge with minimal size. Nanotube electronics can use Doppler radar to detect and locate an incoming bullet [218]. Two laser beams can track the bullet and create a plasma path [25] in the air to electrically heat the bullet in addition to the two parallel conductive armor plates in the electric armor. Melting the copper jacket and the lead core of a bullet can disrupt the bullet because the bullet's spin can disperse the melted metal.

Reference List

[1] "Army Selects MIT for $50 Million Institute to Use Nanomaterials to Clothe, Equip soldiers," MIT News Office, 13 March 2002. http://web.mit.edu/newsoffice/nr/2002/isn.html.

[2] "ISN Projects Include Armor Made of Nanoscopic Material," MIT News Office, 24 September 2003. http://web.mit.edu/newsoffice/tt/2003/sep24/isn.html.

[3] *Second Chance Saves*, pp. 7 and 16. Second Chance Inc., Central Lakes, Michigan, 1999.

[4] A. Abbaspour-Tamijani, K. Sarabandi, G. M. Rebeiz, "Antenna-filter-antenna arrays as a class of bandpass frequency-selective surfaces," *IEEE Transactions on Microwave Theory and Techniques*, vol. 52, no. 8, pp. 1781–1789, August 2004.

[5] A. Abbaspour-Tamijani, L. Dussopt, G. M. Rebeiz, "Miniature and Tunable Filters Using MEMS Capacitors," *IEEE Transactions on Microwave Theory and Techniques*, vol. 51, no. 7, pp. 1878-1885, July 2003.

[6] M. Abdelkader, J. C. Withers, R. O. Loutfy, A. Moravsky, M. Sennett, "The investigation of carbon nanotubes for lightweight armor materials," *The 23rd Army Science Conference*, 2003.

[7] G. R. Aizin, N. J. M. Horing, L. G. Mourokh, V. M. Kovalev, "Current driven electromagnetic wave amplification by double quantum wire superlattice," *Journal of Applied Physics*, vol. 96, no. 8, pp. 4225–4232, October 2004.

[8] R. Akashi, H. Tsutsui, A. Komura, "Polymer gel light-modulation materials imitating pigment cells," *Advanced Materials*, vol. 14, no. 24, pp. 18081811, December 2002.

[9] A. S. Alexandrov, A. M. Bratkovsky, R. Stanley Williams, "Bistable tunneling current through a molecular quantum dot," *Physical Review B*, vol. 67, pp. 075301–075304, 2003.

[10] A. A. Aligia, J. L. Gervasoni, N. R. Arista, "Stopping force on point charges in cylindrical wires," *Physical Review B*, vol. 70, pp. 235331–235335, 2004.

[11] J. Allen, "Gain and impedance variation in scanned dipole arrays," *IEEE Transactions on Antennas and Propagation*, vol. 10, no. 5, pp. 566–572, September 1962.

[12] J. B. Allen, "Nonlinear cochlear signal processing," *Physiology of the Ear, Second Edition*, A. F. Jahn, J. Santos-Sacchi, Editors, chapter 19, pp. 393–442, Singular Thompson, 2001.

[13] J. B. Allen, "Cochlear micromechanics: A physical model of transduction," *Journal of the Acoustical Society of America*, vol. 68, no. 6, pp. 1660–1670, 1980.

[14] I. Amlani, R. Zhang, J. Tresek, R. K. Tsui, "Room-temperature single-electron charging effects in an ambipolar single-walled carbon nanotube grown by chemical vapor deposition," *Journal of Vacuum Science and Technology B*, vol. 21, pp. 2848, 2003.

[15] L. An, Q. Fu, C. Lu, J. Liu, "A Simple Chemical Route To Selectively Eliminate Metallic Carbon Nanotubes in Nanotube Network Devices," *Journal of the American Chemical Society*, vol.126, no.34, pp.10520–10521, 2004.

[16] M. C. Andrews, R. J. Young, "Fragmentation Of Aramid Fibers In Single-Fiber Model Composites," *Journal Of Materials Science*, vol. 30, Issue 22, pp. 5607–5616, 15 November 1995.

[17] V. S. Anishchenko, M. A. Safonova, L. O. Chua, "Stochastic resonance in Chua's circuit driven by amplitude or frequency modulated signals," *International Journal of Bifurcation and Chaos*, vol. 4, no. 2, pp. 441-446, 1994.

[18] V. S. Anishchenko, M. A. Safonova, L. O. Chua, "Stochastic resonance in Chua's circuit," *International Journal of Bifurcation and Chaos*, vol. 2, no. 2, pp. 397-401, 1992.

[19] R. D. Antonov, A. T. Johnson, "Subband population in a single-wall carbon nanotube diode," *Physical Review Letters*, vol. 83, pp. 3274–3276, 1999.

[20] J. Appenzeller and D. J. Frank, "Frequency dependent characterization of transport properties in carbon nanotube transistors," *Applied Physics Letters*, vol. 84, pp. 1771, 2004.

[21] J. Appenzeller, J. Knoch, V. Derycke, R. Martel, S. Wind, P. Avouris, "Field-modulated carrier transport in carbon nanotube transistors," *Physical Review Letters*, vol. 89, pp. 126801–126804, 2002.

[22] J. Appenzeller, J. Knoch, V. Derycke, R. Martel, S. Wind, P. Avouris, "Short-channel like effects in Schottky barrier carbon nanotube field-effect transistors," in *Proceedings of the IEDM 2002*, pp. 285–288, 2002.

[23] J. Appenzeller, R. Martel, P. Avouris, H. Stahl, B. Lengeler, "Optimized contact configuration for the study of transport phenomena in ropes of single-wall carbon nanotubes," *Applied Physics Letters*, vol. 78, pp. 3313–3315, 2001.

[24] L. R. Arnaut, "Adaptive control and optimization of electromagnetic radiation, attenuation, and scattering using self-adaptive material systems," *IEEE Transactions on Antennas and Propagation*, vol. 51, no. 7, pp. 1530–1548, July 2003.

[25] A. Aston, Editor, "Welding with laser-beam precision," *Businessweek*, 11 June 2001.

[26] F. Auzanneau, R. W. Ziolkowski, "Artificial composite materials consisting of nonlinearly loaded electrically small antennas: operational-amplifier-based circuits with applications to smart skins," *IEEE Transactions on Antennas and Propagation*, vol. 47, no. 8, pp. 1330–1339, August 1999.

[27] Ph. Avouris, J. Appenzeller, R. Martel, S. J. Wind, "Carbon nanotube electronics," *Proceedings of the IEEE*, vol. 91, no. 11, pp. 1772-1784, November 2003.

[28] Ph. Avouris, R. Martel, S. Heinze, M. Radosavljevic, S. Wind, V. Derycke, J. Appenzeller, J. Terso, "The role of Schottky barriers on the behavior of carbon nanotube field-effect transistors," *AIP Conference Proceedings*, vol. 633, no. 1, pp. 508–512, 14 October 2002.

[29] S. M. Bachilo, M. S. Strano, C. Kittrell, R. H. Hauge, R. E. Smalley, R. B. Weisman, "Structure-Assigned Optical Spectra of Single-Walled Carbon Nanotubes ," *Science*, vol. 298, no. 5602, pp. 2361–2366, 20 December 2002.

[30] T. E. Bachner, Jr. "The V-50 Ballistic Limit: A Reliable Test for Body Armor," *IWBA Wound Ballistics Review*, vol. 1, no. 4, pp. 20–25, 1996.

[31] A. Bachtold, P. Hadley, T. Nakanishi, C. Dekker, "Logic circuits with carbon nanotube transistors," *Science*, vol. 294, pp. 1317–1320, 2001.

[32] A. Bachtold, C. Strunk, J.-P. Salvetat, J.-M. Bonard, L. Forr, T. Nussbaumer, C. Schnenberger, "Aharonov Bohm oscillations in carbon nanotubes", *Nature*, vol. 397, pp. 673–675, 1999.

[33] J. L. Bahr, J. M. Tour, "Highly Functionalized Carbon Nanotubes Using in Situ Generated Diazonium Compounds," *Chemical Materials*, vol. 13, no. 11, pp. 3823–3824, 2001.

[34] J. L. Bahr, J. Yang, D. V. Kosynkin, M. J. Bronikowski, R. E. Smalley, J. M. Tour, "Functionalization of Carbon Nanotubes by Electrochemical Reduction of Aryl Diazonium Salts: A Bucky Paper Electrode," *Journal of the American Chemical Society*,vol. 123, no. 27, pp. 6536–6542,2001.

[35] K. Balasubramanian, R. Sordan, M. Burghard, K. Kern, "A Selective Electrochemical Approach to Carbon Nanotube Field-Effect Transistors, " *Nano Letters*, vol. 4, no. 5, pp. 827–830, 2004.

[36] F. D. Bannon, III, J. R. Clark, C. T.-C. Nguyen, "High-Q HF microelectromechanical filters," *IEEE Journal of Solid-state Circuits*, vol. 35, no. 4, pp. 512–526, April 2000.

[37] S. Barbay, G. Giacomelli, F. Marin, "Noise-assisted transmission of binary information: theory and experiment," *Physical Review E*, vol. 63, pp. 051110–051118, 2000.

[38] H. A. Barnes, "Shear-Thickening ("Dilatancy") in Suspensions of Nonaggregating Solid Particles Dispersed in Newtonian Liquids," *Journal of Rheology*, vol. 33, pp. 329, 1989.

[39] R. Bartussek, P. Hänggi, P. Jung, "Stochastic resonance in optical bistable systems," *Physical Review E*, vol. 49, no. 5, pp. 3930–3939, May 1994.

[40] M. Bartz, "Large-scale dithering enhances ADC dynamic range," *Microwave & RF*, vol. 32, pp. 192 194+, May 1993.

[41] R. Benzi, G. Parisi, A. Sutera, A. Vulpiani, "A theory of stochastic resonance in climatic change," SIAM *Journal of Applied Mathematics*, vol. 43, no. 3, pp. 565–578, June 1983.

[42] R. Benzi, G. Parisi, A. Sutera, A. Vulpiani, "Stochastic resonance in climatic change," *Tellus*, vol. 34, pp. 10–16, 1982.

[43] R. Benzi, A. Sutera, A. Vulpiani, "The mechanism of stochastic resonance," *Journal of Physics A*, vol. 14, pp. L453–L457, 1981.

[44] D. S. Bethune, C. H. Kiang, M. DeVries, G. Gorman, R. Savoy, J. Vazquez, R. Beyers, "Cobalt-Catalyzed Growth of Carbon Nanotubes with Single-Atomic-Layer Walls," *Nature*, vol. 363, pp. 605–607, 1993.

[45] A. Bezryadin, A. R. M. Verschueren, S. J. Tans, C. Dekker, "Multiprobe transport experiments on individual single-wall carbon nanotubes," *Physical Review Letters*, vol. 80, no. 18, pp. 4036–4039, May 1998.

[46] A. Bietsch, B Michel, "Size and grain-boundary effects of a gold nanowire measured by conducting atomic force microscopy," *Applied Physics Letters*, vol. 80, no. 18, pp. 3346–3348, 2002

[47] M. Blaber, online image of sp^2 hybrid orbital, http://wine1.sb.fsu.edu/chm1045/notes/Geometry/Hybrid/Geom05.htm

[48] L. V. Blake, *Antennas*, pp. 69-70 "Open-circuited and short-circuited lines can also behave like resonant circuits. This behavior occurs when the length of the line is an integral multiple of a quarter wavelength," Artech House Inc., Dedham, MA, 1984.

[49] Ya. M. Blanter, F. W. J. Hekking, M. Buttiker, "Interaction constants and dynamic conductance of a gated wire," *Physical Review Letters*, vol. 81, no. 9, pp. 1925–1928, 31 August 1998.

[50] J.-C. Bor, C.-Y. Wu, "Analog electronic cochlea design using multiplexing switched-capacitor circuits," *IEEE Transactions on Neural Networks*, vol. 7, no. 1, pp. 155–166, January 1996.

[51] R. L. Borwick, III, P. A. Stupar, J. F. DeNatale, R. Anderson, R. Erlandson, "Variable MEMS Capacitors Implemented Into RF Filter Systems," *IEEE Transactions on Microwave Theory and Techniques*, vol. 51, no. 1, pp. 315–319, January 2003.

[52] G. Bossis, J. F. Brady, "The rheology of Brownian suspensions," *Journal of Chemical Physics*, vol. 91, pp. 1866, 1989.

[53] P. J. Boul, J. Liu, E. T. Mickelson, C. B. Huffman, L. M. Ericson, I. W. Chiang, K. A. Smith, D. T. Colbert, R. H. Hauge, J. L. Margrave, R. E. Smalley, R. E. "Reversible sidewall functionalization of buckytubes," *Chemical Physics Letters*, vol. 310, no. (3,4), pp. 367–372, 1999.

[54] K. Bradley, J.-C. P. Gabriel, G. Gruner, "Flexible nanotube electronics," *Nano Letters*, vol. 3, no. 10, pp. 1353–1355, October 2003.

[55] H. A. Braun, H. Wissing, K. Schäfer, M. C. Hirsch, "Oscillation and noise determine signal transduction in Shark multimodal sensory cells," *Nature*, vol. 367, pp. 270–273, January 1994.

[56] J. J. Brey and A. Prados, "Stochastic resonance in a one dimension Ising model," *Physics Letters A*, vol. 216, pp. 240–246, June 1996.

[57] V. N. Bringi, V. Chandrasekar, pp. 287 *Polarimetric Doppler weather radar: principles and applications*, Cambridge University Press, Cambridge, New York, 2001.

[58] W.E. Brownell, C.R. Bader, D. Bertran, Y. de Rabaupierre, "Evoked mechanical responses of isolated cochlear outer hair cells," *Science*, vol. 227, pp.194–196, 1985.

[59] P. Bryant, K. Wiesenfeld, B. McNamara, "The nonlinear effects of noise on parametric amplification: an analysis of noise rise in Josephson junctions and other systems," *Journal of Applied Physics*, vol. 62, pp. 2898-2913, 1987.

[60] M. R. Buitelaar, W. Belzig, T. Nussbaumer, B. Babi, C. Bruder, C. Schnenberger, "Multiple Andreev Reflections in a Carbon Nanotube Quantum Dot," *Physical Review Letterws*, vol. 91, pp. 057005, 2003.

[61] M. R. Buitelaar, A. Bachtold, T. Nussbaumer, M. Iqbal, C. Schnenberger, "Multiwall Carbon Nanotubes as Quantum Dots," *Physical Review Letters*, vol. 88, pp. 156801, 2002.

[62] A. R. Bulsara, R. D. Boss, E. W. Jacobs, "Noise effects in an electronic model of a single neuron," *Biological Cybernetics*, vol. 61, pp. 211-222, 1989.

[63] A. R. Bulsara, T. C. Elston, C. R. Doering, S. B. Lowen, K. Lindenberg, "Cooperative behavior in periodically driven noisy integrate-fire models of neuronal dynamics," *Physical Review E*, vol. 53, no. 4, pp. 3958-3969, April 1996.

[64] A. R. Bulsara, L. Gammaitoni, "Tuning in to noise," *Physics Today*, pp. 39-45, March 1996.

[65] A. R. Bulsara, E. W. Jacobs, T. Zhou, F. Moss, L. Kiss, "Stochastic resonance in a single neuron model: Theory and analog simulation," *Journal of Theoretical Biology*, vol. 152, pp. 531-555, 1991.

[66] A. R. Bulsara, A. Zador, "Threshold Detection of Wideband Signals: A Noise-Induced Maximum in the Mutual Information," *Physical Review E*, vol. 54, pp. R2185, 1996.

[67] P. J. Burke, "Carbon nanotube devices for GHz and THz applications," *Proceedings of the 2003 International Semiconductor Device Research Symposium*, pp. 314–315, 2003.

[68] P. J. Burke, S. Li, Z. Yu, "Quantitative Theory of Nanowire and Nanotube Antenna Performance," *Submitted*, Preprint accessed 19 August 2004.

[69] P. Burke, "Luttinger liquid theory as a model of the gigahertz electrical properties of carbon nanotubes," *IEEE Transactions on Nnaotechnology*, vol. 1, no. 3, pp. 129–144, September 2002.

[70] P. J. Burke, I. B. Spielman, J. P. Eisenstein, "High frequency conductivity of the high-mobility two-dimensional electron gas," *Applied Physics Letters*, vol. 76, no. 6, pp. 745–747, 7 February 2000.

[71] M. R. Buitelaar, A. Bachtold, T. Nussbaumer, M. Iqbal, and C. Schönenberger, "Multiwall carbon nanotubes as quantum dots," *Physics Review Letters*, vol. 88, pp. 156801, 2002.

[72] A. Cao, R. Baskaran, M. J. Frederick, K. Turner, M. Ajayan, G. Ramanath, "Direction-selective and length-tunable in-plane growth of carbon nanotubes," *Advanced Materials*, vol. 15, no. 13, 4 July 2003.

[73] A. W. Carroll, C. A. Soderstrom, "A New Nonpenetrating Ballistic Injury," *Annals of Surgery*, vol. 188, no. 6, pp. 753–757, December 1978.

[74] A. Cassel, N. Franklin, T. Tombler, E. Chan, J. Han, H. Dai, "Current directed growth of free-standing single-walled carbon nanotubes," *Journal of the American Chemical Society*, vol. 121, pp. 7975–7976, 1999.

[75] A. A. Catherall, J. R. Melrose, R. C. Ball, "Shear thickening and order–disorder effects in concentrated colloids at high shear rates," *Journal of Rheology*, vol. 44, pp. 1, 2000.

[76] F. Chapeau-Blondeau and X. Godivier, "Stochastic resonance in nonlinear transmission of Spike signals: An exact model and an application to the neuron," *International Journal of Bifurcation and Chaos*, vol. 6, no. 11, pp. 2069-2076, 1996.

[77] R. Chau, et al., "A 50 nm depleted-substrate CMOS transistor," *Proceedings of the IEDM 2001*, pp. 45–48, 2001.

[78] R. J. Chen, S. Bangsaruntip, K. A. Drouvalakis, N. W. S Kam, M. Shim, Y. Li, W. Kim, P. J. Utz, H. Dai, "Noncovalent functionalization of carbon nanotubes for highly specific electronic biosensors," *Proceedings of the National Academy of Sciences of the United States of America*, vol. 100, no. 9, pp. 4984–4989, 29 April 2003.

[79] M. Chen, J. W. McCauley, K. J. Hemker, "Shock-induced localized amorphization in boron carbide," *Science*, vol. 299, pp. 1563–1566, March 2003.

[80] Y. Cheng, J. Zhang, Y. Z. Lee, B. Gao, S. Dike, W. Lin, J. P. Lu, and O. Zhou, "Dynamic radiography using a carbon-nanotube-based field-emission x-ray source," *Review of Scientific Instruments*, vol. 75, pp. 3264–3267, 2004.

[81] C. L. Cheung, A. Kurtz, H. Park, C. M. Lieber, "Diameter controlled synthesis of carbon nanotubes," *Journal of Physical Chemistry B* vol. 106, pp. 2429, 2002.

[82] L. Chico, W. Jasklski, "Localized states and conductance gaps in metallic carbon nanotubes," *Physical Review B*, vol. 69, pp. 085406-085410, 2004.

[83] P. W. Chiu, G. S. Duesberg, U. Dettlaff-Weglikowska, S. Roth, "Interconnection of carbon nanotubes by chemical functionalization," *Applied Physics Letters*, vol. 80, no. 20, pp. 3811–3813, 2002.

[84] I. S. Chocronbenloulo, J. Rodriguez, A. Sanchezgalvez, "A Simple Analytical Model To Simulate Textile Fabric Ballistic Impact Behavior," *Textile Research Journal*, vol. 67, no. 7, pp. 520–528, July 1997.

[85] Gregory Chow, "Tests of Equality between Sets of Coefficients in Two Linear Regressions", *Econometrica*, vol. 28, no. 3, pp. 591–605, 1960.

[86] F. Cleri, P. Keblinski, I. Jang, S. B. Sinnott, "Localization and quantization in covalently bonded carbon nanotube junctions," *Physics Review B*, vol. 69, pp. 121412–121415, 2004.

[87] J. J. Collins, C. C. Chow, A. C. Capela, T. T. Imhoff, "Aperiodic stochastic resonance," *Physical Review E*, vol. 54, pp. 5575, 1996.

[88] J. J. Collins, C. C. Chow, T. T. Imhoff, "Aperiodic stochastic resonance in excitable systems," *Physical Review E*, vol. 52, no. 4, pp. R3321-R3324, October 1995.

[89] J. J. Collins, T. T. Imhoff, P. Grigg, "Noise-Enhanced Information Transmission in Rat SA1 Cutaneous Mechanoreceptors via Aperiodic Stochastic Resonance," *Journal of Neurophysiology*, vol. 76, pp. 642-645, 1996.

[90] P. G. Collins, M. S. Arnold, P. Avouris, "Engineering carbon nanotubes using electrical breakdown," *Science*, vol. 292, pp. 706–709, 2001.

[91] P. G. Collins and P. Avouris, "Multishell conduction in multiwalled carbon nanotubes," *Applied Physics A*, vol. 74, pp. 329–332, 2002.

[92] P. G. Collins, Ph. Avouris, "Nanotubes for Electronics," *Scientific American*, pp. 62–69, December 2000.

[93] P. G. Collins, K. Bradley, M. Ishigami, A. Zettl, "Extreme oxygen sensitivity of electronic properties of carbon nanotubes," *Science*, vol. 287, pp. 1801, 2000.

[94] P. G. Collins, M. Hersam, M. Arnold, R. Martel, P. Avouris, "Current saturation and electrical breakdown in multi-walled carbon nanotubes," *Physcial Review Letters*, vol. 86, pp. 3128–3131, 2001.

[95] T. M. Cover, J. A. Thomas, *Elements of Information Theory*. New York, Wiley, 1991.

[96] G. Cramer and T. R. O'Neill, Designed camouflage patterns, Online photos http://www.hyperstealth.com/ miltex/

[97] G. Cramer and T. R. O'Neill, Photo illustrates that camouflage can still reveal human form due to mismatches with the background, Online photo http://www.hyperstealth.com/ pixelpat/ 9007.jpg

[98] R. F. Cregan, B. J. Mangan, J. C. Knight, T. A. Birks, P. St. J. Russell, P. J. Roberts, D. C. Allan, "Single-Mode Photonic Band Gap Guidance of Light in Air," *Science*, vol. 285, pp. 1537–1539, September 1999.

[99] R. J. Crowley, U. S. Patent No. 6,258,401, 10 July 1997.

[100] G. Cuniberti, M. Sassetti, B. Kramer, "AC conductance of a quantum wire with electron-electron interactions," *Physical Review B*, vol. 57, no. 3, pp. 1515–1526, 1998.

[101] P. M. Cunniff, "A Semiempirical Model for the Ballistic Impact Performance of Textile-based Personnel Armor," *Textile Research Journal*, vol. 66, no. 1, pp. 45–59, January 1996.

[102] H. Dai, J. Kong, C. Zhou, N. Franklin, T. Tombler, A. Cassell, S. Fan, M. Chapline, "Controlled chemical routes to nanotube architectures, physics, and devices," *Journal of Physical Chemistry*, vol. 103, pp. 11246, 1999.

[103] S. Dag, R. T. Senger, S. Ciraci, "Theoretical study of crossed and parallel carbon nanotube junctions and three-dimensional grid structures," *Physical Review B*, vol. 70, pp. 205407–205415, 2004.

[104] A. B. Dalton, S. Collins, E. Munoz, J. M. Razal, V. H. Ebron, J. P. Ferraris, J. N. Coleman, B. G. Kim, R. H. Baughman, "Super-tough carbon-nanotube fibres," *Nature*, vol. 423, pp. 703, 12 June 2003.

[105] A. B. Dalton, S. Collins, J. Razal, E. Munoz, V. H. Ebron, B. G. Kim, J. N. Coleman, J. P. Ferraris, R. H. Baughman, "Continuous carbon nanotube composite fibers: properties, potential applications, and problems," *Journal of Material Chemistry*, vol. 14, no. 1, pp. 1–3, 2004

[106] L. B. da Silva, S. B. Fagan, R. Mota, "Ab Initio Study of Deformed Carbon Nanotube Sensors for Carbon Monoxide Molecules," *Nano Letters*, vol. 4, no. 1, pp. 65-67, 2004.

[107] S. Das Sarma, E. H. Hwang, "Dynamical response of a one-dimensional quantum-wire electron system," *Physical Review B*, vol. 54, no. 3, pp. 1936–1946, July 1996.

[108] S. Data, *Electronic Transport in Mesoscopic Systems Cambridge*, U.K., Cambridge University Press, 1995.

[109] J. F. Davis, M. Bronikowski, D. Choi, L. Epp, M. Hoenk, D. Hope, B. Kowalczyk, F. Noca, E. Wong, B. Hunt, B. Chang, M. Jouzi, M. Tzolov, A. yin, J. Xu, J. D. Adam, R. M. Young, J. Adams, B. Rogers, "High-Q mechanical resonator arrays based on carbon nanotubes," *Third IEEE Conference on Nanotechnology*, IEEE-NANO 2003, vol. 2, pp. 635–638, August 2003.

[110] W. de Heer, P. Poncharal, C. Berger, J. Gezo, Z. Song, J. Bettini, D. Ugarte, "Liquid Carbon, Carbon-Glass Beads, and the Crystallization of Carbon Nanotubes," *Science*, vol. 307, pp. 907–910, 11 February 2005.

[111] C. Dekker, "Carbon nanotubes as molecular quantum wires," *Physics Today*, pp. 22–28, May 1999.

[112] N. de Jonge, M. Allioux, M. Doytcheva, M. Kaiser, K. B. K. Teo, R. G. Lacerda, W. I. Milne, "Characterization of the field emission properties of individual thin carbon nanotubes," *Applied Physics Letters*, vol. 85, pp. 1607, 2004.

[113] V. Derycke, R. Martel, J. Appenzeller, Ph. Avouris, "Controlling doping and carrier injection in carbon nanotube transistors," *Applied Physics Letters*, vol. 80, no. 15,pp. 2773–2775, 2002.

[114] V. Derycke, R. Martel, J. Appenzeller, P. Avouris, "Carbon nanotube inter- and intra-molecular logic gates," *Nano Letters*, vol. 1, pp. 453–456, 2001.

[115] V. Derycke, R. Martel, M. Radosavljevic, F. M. Ross, P. Avouris, "Catalyst-free growth of ordered single-walled carbon nanotube networks," *Nano Letters*, vol. 2, pp. 1043–1046, 2002.

[116] S. S. Deshmukh, G. H. McKinley, "Adaptive energy-absorbing materials using field-responsive fluid-impregnated cellular solids," *Advanced Functional Materials*, submitted 2004.

[117] L. Dischler, T. T. Moyer, J. B. Hensen, *US Patent*, no. 5776839, 1998.

[118] J. K. Douglass, L. Wilkens, E. Pantazelou, F. Moss, "Noise enhancement of information transfer in crayfish mechanoreceptors by stochastic resonance," *Nature*, vol. 365, 337-340, 1993.

[119] B. Drafts, "Acoustic wave technology sensors," *IEEE Transactions on Microwave Theory and Techniques*, vol. 49, no. 4, pp. 795–802, April 2001.

[120] M. S. Dresselhaus, G. Dresselhaus, P. Avouris, Editors, *Carbon Nanotubes: Synthesis, Structure Properties and Applications*, Berlin, Germany, Springer-Verlag, 2001.

[121] M. S. Dresselhaus, G. Dresselhaus, Ph. Avouris (Eds.), "Carbon nanotubes," *Topics in Applied Physics*, vol. 80, pp. 147–171, 2001.

[122] M. S. Dresselhaus, G. Dresselhaus, P. Eklund, R. Saito, "Carbon nanotubes," *Physics World*, January 1998.

[123] M. S. Dresselhaus, G. Dresselhaus, A. Jorio, A. G. Souza Filho, M. A. Pimenta, R. Saito, "Single nanotube Raman spectroscopy," *Accounts of Chemical Research*, vol. 35, no. 12, 2002.

[124] M. S. Dresselhaus, G. Dresselhaus, A. Jorio, A. G. Souza Filho, R. Saito, "Raman spectroscopy on isolated single wall carbon nanotubes," *Carbon*, vol. 40, pp. 2043-2061, 2002.

[125] M. S. Dresselhaus, G. Dresselhaus, R. Saito, "Carbon fibers based on C_60 and their symmetry," *Physical Review B*, vol. 45, pp. 6234–6242, 1992.

[126] M. S. Dresselhaus, P. C. Eklund, "Phonons in carbon nanotubes," *Advances in Physics*, vol.49, no.6, pp. 705–814, September-October 2000.

[127] X. Duan, Y. Huang, Y. Cui, J. Wang, C. M. Lieber, "Indium phosphide nanowires as building blocks for nanoscale electronic and optoelectronic devices," *Nature*, vol. 409, pp. 66–69, 04 January 2001.

[128] X. Duan, C. Niu, V. Sahi, J. Chen, J. W. Parce, S. Empedocles, J. L. Goldman, "High-performance thin-film transistors using semiconductor nanowires and nanoribbons," *Nature*, vol. 425, no. 6955, pp. 274–278, 18 September 2003.

[129] R. O. Duda, "Footnote on auditory filters," online http://www-engr.sjsu.edu/ ̃duda/Duda.R.GSLM.3f1.html accessed 21 October 2004.

[130] R. O. Duda and P. E. Hart, *Pattern Classification and scene analysis*. Wiley, New York, Chichester, Brisbane, Toronto, Singapore 1973.

[131] E. Durgun, S. Dag, S. ciraci, O.Gulseren, "Energetics and Electronic Structures of Individual Atoms Adsorbed on Carbon Nanotubes," *Journal of Physical Chemistry B*, vol. 108, no. 2, pp. 575–582, 2004.

[132] T. Dürkop, S. A. Getty, E. Cobas, M. S. Fuhrer, "Extraordinary Mobility in Semiconducting Carbon Nanotubes", *Nano Letters*, vol. 4, no. 1, pp. 35–39, January 2004.

[133] L. Dussopt, G. M. Rebeiz, "Intermodulation Distortion and Power Handling in RF MEMS Switches, varactors, and Tunable Filters," *IEEE Transactions on Microwave Theory and Techniques*, vol. 51, no. 4, pp. 1247-1256, April 2003.

[134] A. K. Dutta, D. Penumadu, B. Files, "Nanoindentation testing for evaluating modulus and hardness of single-walled carbon nanotube-reinforced epoxy composites," *Journal of Materials Research*, vol. 19, no. 1, pp. 158–164, January 2004.

[135] C. A. Dyke, J. M. Tour, "Solvent-Free Functionalization of Carbon Nanotubes," *Journal of the American Chemical Society*, vol. 125, no. 5, pp. 1156–1157, 2003.

[136] M. I. Dykman, G. P. Golubev, I. K. Kaufman, D. G. Luchinsky, P. V. E. McClintock, E. A. Zhukov, "Noise-enhanced optical heterodyning in an all-optical bistable system," *Applied Physics Letters*, vol. 67, no. 3, pp. 308-310, July 1995.

[137] M. I. Dykman, T. Horita, J. Ross, "Statistical distribution and stochastic resonance in a periodically driven chemical system," *Journal of Chemical Physics*, vol. 103, no. 3, pp. 966-972, July 1995.

[138] M. I. Dykman, D. G. Luchinsky, R. Mannella, P. V. E. McClintock, S. M. Soskin, N. D. Stein, "Resonant subharmonic absorption and second-harmonic generation by a fluctuating nonlinear oscillator," *Physical Review E*, vol. 54, no. 3, pp. 2366-2377, September 1996.

[139] M. I. Dykman, D. G. Luchinsky, R. Mannella, P. V. E. McClintock, N. D. Stein, N. G. Stocks, "Supernarrow spectral peaks and high-frequency stochastic resonance in systems with coexisting periodic attractors," *Physical Review E*, vol. 49, no. 2, pp. 1198-1215, February 1994.

[140] M. I. Dykman, D. G. Luchinsky, R. Mannella, P. V. E. McClintock, N. D. Stein, N. G. Stocks, "Nonconventional stochastic resonance," *Journal of Statistical Physics*, vol. 70, nos. 1/2, pp. 479-499, January 1993.

[141] M. I. Dykman, P. V. E. McClintock, "Power spectra of noise driven nonlinear systems and stochastic resonance," *Physica D*, vol. 58, 10, 1992.

[142] T. W. Ebbesen, P. M. Ajayan, "Large-scale synthesis of carbon nanotubes," *Nature*, vol. 358, pp. 220, 1992.

[143] R. G. Egres Jr., Y. S. Lee, J. E. Kirkwood, K. M. Kirkwood, E. D. Wetzel, N. J. Wagner, "Protective fabrics utilizing shear thickening fluids," *Proceedings of the Industrial Fabrics Association International (IFAI) 4th International Conference on Safety and Protective Fabrics*, 27–29 October 2004, to appear.

[144] R. S. Elliott, Section 1.7, *Antenna Theory and Design, Revised Ediction*, John Wiley & Sons, Hoboken, New Jersey, 2003.

[145] R. S. Elliott, *Antenna Theory and Design*, Prentice-Hall, New Jersey, 1981.

[146] R. S. Elliott, Chapter 4, *Antenna Theory and Design*, Prentice-Hall, New Jersey, 1981.

[147] R. S. Elliott, Chapter 8, *Antenna Theory and Design*, Prentice-Hall, New Jersey, 1981.

[148] R. L. Ellis, F. Lalande, H. Y. Jia, C. A. Rogers, "Ballistic Impact Resistance of SMA and Spectra Hybrid Graphite Composites," *Journal Of Reinforced Plastics And Composites*, vol. 17, no. 2, pp. 147–164, 1998.

[149] R. Egger, H. Grabert, "Charging effects in quantum wires," *Physical Review B*, vol. 55, no. 15, pp. 9929–9934, April 1997.

[150] L. M. Ericson, H. Fan, H. Peng, V. A. Davis, W. Zhou, J. Sulpizio, Y. Want, R. Booker, J. Vavro, C. Guthy, A. N. G. Parra-Vasquez, M. J. Kim, S. Ramesh, R. K. Saini, C. Kittrell, G. Lavin, H. Schmidt, W. W. Adams, W. E. Billups, M. Pasquali, W.-F. Hwang, R. H. Hauge, J. E. Fischer, R. E. Smalley, "Macroscopic, neat, single-walled carbon nanotube fibers," *Science*, vol. 305, pp. 1447–1450, 3 September 2004.

[151] M. L. Fackler, J. A. Malinowski, "The Wound Profile: A Visual Method for Quantifying Gunshot Wound Components," *Journal of Trauma*, vol. 25, no. 6, pp. 522–9, 1985.

[152] R. S. Farr, J. R. Melrose, R. C. Ball, "Kinetic theory of jamming in hard-sphere startup flows," *Physical Review E*, vol. 55, pp. 7203, 1997.

[153] M. Fatehi, J. Ford, "Free-Space Optical Signal Switch Arrangement" *United States Patent* no. 6,002,818

[154] A. Fechner, M. Sassetti, B. Kramer, E. Galleani d'Agliano, "Nonlinear ac transport and local fields in quantum wires," *Physical Review B*, vol. 64, pp. 195315–195329, 2001.

[155] K. Feher, H. Mehdi, "Modulation/microwave integrated digital wireless developments," *IEEE Transactions on Microwave Theory and Techniques*, vol. 43, no. 7, pp. 1715–1732, July 1995.

[156] M. Feldmann, J. Henaff, pages *xiii–xix*, *Surface acoustic waves for signal processing*, English translation by Artech House,Norwood, MA, 1989.

[157] K. A. S. Fernando, Y. Lin, W. Want, S. Kumar, B. Zhou, S.-Y. Xie, L. T. Cureton, Y.-P. Sun, "Diminished Band-Gap Transitions of Single-Walled Carbon Nanotubes in Complexation with Aromatic Molecules," *Journal of the American Chemical Society*, vol. 126, no. 33, pp. 10234–10235, 2004.

[158] H. Fletcher, "On the dynamics of the cochlea," *Journal of the Acoustical Society of America*, vol. 23, pp. 637–645, November 1951.

[159] P. N. Fletcher, M. Dean, A. R. Nix, "Mutual coupling in multi-element array antennas and its influence on MIMO channel capacity," *Electronics Letters*, vol. 39, no. 4, pp. 342–344, February 2003.

[160] J. E. Ford, Y. Fainman, and S. H. Lee, "Array interconnection by phase coded optical correlation," *Optics Letters*, vol. 15, pp. 1088–1090, 1990.

[161] A. Förster, M. Merget, F. W. Schneider, "Stochastic resonance in chemistry 2: The peroxidase-oxidase reaction," *Journal of Physical Chemistry*, vol. 100, pp. 4442-4447, 1996.

[162] D. R. Foss, J. F. Brady, *Journal of Fluid Mechanics*, vol. 407, pp. 167, 2000.

[163] E. Fourn, A. Pothier, C. Champeaux, P. Tristant, A. Catherinot, P. Blondy, G. Tann, E. Rius, C. Person, F. Huret, "MEMS Switchable Interdigital Coplanar Filter," *IEEE Transactions on Microwave Theory and Techniques*, vol. 51, no. 1, pp. 320-324, January 2003.

[164] S. Frank, P. Poncharal, Z. L. Wang, W. A. de Heer, "Carbon Nanotube Quantum Resistors," *Science*, vol. 280, pp. 1744–1746, 12 June 1998.

[165] N. Franklin and H. Dai, "An enhanced CVD approach to extensive nanotube networks with directionality," *Advanced Materials*, vol. 12, pp. 890–894, 2000.

[166] M. Freitag, J. Chen, J. Tersoff, J. C. Tsang, Q. Fu, J. Liu, Ph. Avouris, "Mobile Ambipolar Domain in Carbon-Nanotube Infrared Emitters," *Physical Review Letters*, vol. 93, pp. 076803, 2004.

[167] D. Froesch, J. B. Messenger, "On leucophores and the chromatic unit of *Octopus vulgaris*," *London Journal of Zoology*, vol. 186, pp. 163–173, 1978.

[168] M. S. Fuhrer, B. M. Kim, T. Drkop, T. Brintlinger, "High-Mobility Nanotube Transistor Memory," *Nano Letters*, vol. 2, no. 7, pp. 755–759, July 2002.

[169] G. A. Galanti, *Caring for Patients from Different Cultures (2nd ed.)*, University of Pennsylvania Press, Pennsylvania, Philadelphia, 1997.

[170] L. Gammaitoni, "Stochastic resonance in multi-threshold systems," *Physics Letters A*, vol. 208, pp. 315-322, December 1995.

[171] L. Gammaitoni, A. R. Bulsara, "Noise activated nonlinear dynamic sensors," *Physical Review Letters*, vol. 88, pp. 230601, 2002.

[172] L. Gammaitoni, M. Martinelli, L. Pardi, S. Santucci, "Observation of stochastic resonance in bistable electro-paramagnetic- resonance systems," *Physical Review Letters*, vol. 67, no. 13, pp. 1799-1802, September 1991.

[173] V. Georgakilas, K. Kordatos, M. Prato, D. M. Guldi, M. Holzinger, A. Hirsch, "Organic Functionalization of Carbon Nanotubes," *Journal of the American Chemical Society*, vol. 124, no. 5, pp. 760–761, 2002.

[174] Z. Gingl, L. Kiss, and F. Moss, "Non-dynamical stochastic resonance: theory and experiments with white and arbitrarily coloured noises," *Europhysics Letters*, vol. 29, pp. 191, 1995.

[175] B. J. Gluckman, T. I. Netoff, E. J. Neel, W. L. Ditto, M. L. Spano, S. J. Schiff, "Stochastic resonance in a neuronal network from mammalian brain," *Physical Review Letters*, vol. 77, no. 19, pp. 4098–4101, November 1996.

[176] L. C. Godara, "Applications of antenna arrays to mobile communications. I. Performance improvement, feasibility, and system considerations," *Proceedings of the IEEE*, vol. 85, no. 7, pp. 1031–1060, July 1997.

[177] X. Godivier, F. Chapeau-Blondeau, "Stochastic resonance in the information capacity of a nonlinear dynamic system," *International Journal of Bifurcation and Chaos*, vol. 8 no. 3, pp. 581–589, 1998.

[178] X. Godivier, F. Chapeau-Blondeau, "Noise-assisted signal transmission in a nonlinear electronic comparator: Experiment and theory," *Signal Processing*, vol. 56, pp. 293–303, 1997.

[179] J. Goldberger, R. He, Y. Zhang, S. Lee, H. Yan, H.-J. Choi, P. Yang, "Single-crystal gallium nitride nanotubes," *Nature*, vol. 422, pp. 599–602, 10 April 2003.

[180] R. F. Goldman, "Physiological costs of body armor," *Military Medicine*, vol. 134, no. 3, pp. 204–210, 1969.

[181] A. Goldoni, R. Larciprete, L. Petaccia, S. Lizzit, "Single-Wall Carbon Nanotube Interaction with Gases: Sample Contaminants and Environmental Monitoring," *Journal of the American Chemical Society*, vol. 125, no. 37, pp. 11329–11333, 2003.

[182] P. R. Gray, R. G. Meyer, chapter 3, *Analysis and design of analog integrated circuits* third edition, John Wiley and Sons, New York 1993.

[183] P. R. Gray, R. G. Meyer, chapter 6, *Analysis and design of analog integrated circuits* third edition, John Wiley and Sons, New York 1993.

[184] P. R. Gray, R. G. Meyer, chapter 10, *Analysis and design of analog integrated circuits* third edition, John Wiley and Sons, New York 1993.

[185] I. Grech, J. Micallef, T. Vladimirova, "Silicon cochlea and its adaptation to spatial localisation," *IEE Proceedings on Circuits, Devices, and Systems*, vol. 146, no. 2, pp. 70–76, April 1999.

[186] M. Grifoni and P. Hänggi, "Nonlinear quantum stochastic resonance," *Physical Review E*, vol. 54, no. 2, pp. 1390–1401, August 1996.

[187] A. N. Grigorenko and P. I. Nikitin, "Stochastic resonance in a bistable magnetic system," *IEEE Transactions on Magnetism*, vol. 31, pp. 2491–2493, September 1995.

[188] A. Guderian, G. Dechert, K.-P. Zeyer, F. W. Schneider, "Stochastic resonance in chemistry. 1. The Belousov- Zhabitinsku reaction," *Journal of Physical Chemistry*, vol. 100, pp. 4437–4441, 1996.

[189] D. Gujarati, "Use of Dummy Variables in Testing for Equality between Sets of Coefficients in Two Linear Regressions: A Note," *American Statistician*, vol. 24, no. 1, pp. 50–52, 1970.

[190] G. Gumbs, G. A. Aizin, "Collective excitations in a linear periodic array of cylindrical nanotubes," *Physical Review B*, vol. 65, pp. 195407–195412, 2002.

[191] J. Guo, S. Goasquen, M. Lundstrom, S. Datta, "Metal-insulator-semiconductor electrostatics of carbon nanotubes," *Applied Physics Letters*, vol. 81, pp. 1486–1488, 2002.

[192] S. Gupta, M. Hughes, A. H. Windle, J. Robertson, "Charge transfer in carbon nanotube actuators investigated using in situ Raman spectroscopy," *Journal of Applied Physics*, vol. 95, no. 4, pp. 2038–2048, 15 February 2004.

[193] J. Hafner, M. Bronikowski, B. Azamian, P. Nikolaev, D. Colbert, R. Smalley, "Catalytic growth of single wall carbon nanotubes from metal particles," *Chemical Physics Letters*, vol. 296, pp. 195–202, 1998.

[194] J.-H. Han, T. Y. Lee, D. Y. Kim, J.-B. Yoo, C.-Y. Park, J. J. Choi, T. Jung, I. T. Han, J. E. Jung, J. M. Kim, "High field-emission current of carbon nanotubes grown on TiN-coated Ta substrate for electron emitters in a microwave power amplifier," *Journal of Vacuum Science and Technology B*, vol. 22, no. 4, pp. 1636–1642, July 2004.

[195] R. T. Hanlon, "Behavioral and body patterning characters useful in taxonomy of field identification of cephalopods," *Malacologia*, vol. 29, pp. 247–265, 1988.

[196] A. Hartschuh, E. J. Snchez, X. S. Xie, L. Novotny, "High-Resolution Near-Field Raman Microscopy of Single-Walled Carbon Nanotubes," *Physical Review Letters*, vol. 90, pp. 095503, 7 March 2003.

[197] J. Haruyama, I. Takesue, Y. Sato, "Coulomb blockade in a single tunnel junction directly connected to a multiwalled carbon nanotube," *Applied Physics Letters*, vol. 77, no. 18, pp. 2891–2893, October 2000.

[198] J. Haruyama, K. Hijioka, M. Tako, Y. Sato, "Coulomb blockade related to mutual Coulomb interaction in an external environment in an array of single tunnel junctions connected to Ni nanowires," *Physical Review B*, vol. 62, no. 12, pp. 8420–8429, September 2000.

[199] S. S. Haykin, chapter 1, *Adaptive Filter Theory* second edition, Prentice-Hall, Englewood Cliffs, New Jersey.

[200] S. S. Haykin, chapter 21, *Adaptive Filter Theory* second edition, Prentice-Hall, Englewood Cliffs, New Jersey.

[201] J. He, Z. Suo, T. N. Marieb, J. A. Maiz, "Electromigration lifetime and critical void volume," *Applied Physics Letters*, vol. 85, no. 20, pp. 4639–4641, 15 November 2004

[202] S. Heinze, J. Tersoff, R. Martel, V. Derycke, J. Appenzeller, P. Avouris, "Carbon nanotubes as Schottky barrier transistors," *Physics Review Letters*, vol. 89, pp. 106801–106804, 2002.

[203] H. L. F. Helmholtz, pp. 22–58, *Helmholtz's popular scientific lectures*, Dover, New York, 1962.

[204] A. D. Hibbs, E. W. Jacobs, J. J. Bekkedahl, A. R. Bulsara, F. Moss, "Signal enhancement in a r.f. SQUID using stochastic resonance," *Il Nuovo Cimento, Luglio-Agosto*, vol. 17 D, nos. 7–8, pp. 811–817, 1995.

[205] A. D. Hibbs, A. L. Singsaas, E. W. Jacobs, A. R. Bulsara, J. J. Bekkedahl, F. Moss, "Stochastic resonance in a superconducting loop with Josephson junction," *Journal of Applied Physics*, vol. 77, no. 6, pp. 2582–2590, March 1995.

[206] M. Hikita, C. Takubo, K. Asai, "New SAW-convolver demodulation technique using Costas-loop synchronization for high-speed spread-spectrum signal," *IEEE Transactions on Microwave Theory and Techniques*, vol. 49, no. 4, pp. 749–953, April 2001.

[207] R. L. Hoffman, "Discontinuous and dilatant viscosity behavior in concentrated suspensions. II. Theory and experimental tests," *Journal of Colloid Interface Sciences*, vol. 46, pp. 491, 1974.

[208] K. Hohkawa, T. Suda, Y. Aoki, C. Hong, C. Kaneshiro, K. Koh, "Design on semiconductor coupled SAW convolver," *IEEE Transactions on Ultrasonics, Ferroelectrics and Frequency Control*, vol. 49, no. 4, pp. 466–474, April 2002

[209] M. Holzinger, O. Vostrowsky, A. Hirsch, F. Hennrich, M. Kappes,R. Weiss, F. Jellen, Frank "Sidewall functionalization of carbon nanotubes," *Angewandte Chemie, International Edition*,vol. 40,no. 21, pp. 4002–4005, 2001.

[210] D. Hoppe, B. Hunt, M. Hoenk, F. Noca, J.M. Xu, "Carbon Nanotube Arrays Enable Ultra-Miniature RF Circuits," *NASA Tech Breifs*, 30207, 2003

[211] Y. Hori, T. Shibata, M. Tanaka, O. Oda, "Light-emitting element," *United States Patent Application* 20020167271, 14 November 2002.

[212] S. Huang, X. Cai, J. Liu, "Growth of Millimeter-Long and Horizontally Aligned Single–Walled Carbon Nanotubes on Flat Substrates," *Journal of the American Chemical Society*, vol. 125 no. 19, pp. 5636–5637, 2003.

[213] A. J. Hudspeth, "Cochlea," *Science*, vol. 230, pp. 745–752, 1985.

[214] A. Hunt, G. Dorshimer, J. Kissick, S. Ryan, "IsolatedJejunal Rupture After Blunt Trauma," *The Physician and Sportsmedicine*, vol. 9, no.11, November 2001.

[215] B. Hunt, M. Honek, F. Noca, J.M. Xu, "Waveguide-Embedded Carbon Nanotube Array RF Filter and RF Filter Bank," *NASA Tech Brief Journal*, 2003

[216] B. Hunt, F. Noca, M. Hoenk, "Carbon Nanotubes as Resonators for RF Spectrum Analyzers," *NASA Tech Brief Journal*, NPO-30206, April 2003.

[217] M. Ibanescu, Y. Fink, S. Fan, E. L. Thomas, and J. D. Joannopoulos, "An All-Dielectric Coaxial Waveguide," *Science*, vol. 289, pp. 415–419, July 2000.

[218] "Dopler radar in personnel ballistic protection," IBIS Technologies, LLC. Online ttp://www.ibistek.com/pdf/ipps.pdf

[219] S. Iijima, T. Ichihashi, "Single-shell carbon nanotubes of 1-nm diameter," *Nature*, vol. 363, pp. 603, 1993.

[220] S. Iijima, "Helical microtubules of graphitic carbon," *Nature*, vol. 354, pp. 56, 1991.

[221] Y. Imry and R. Landauer, "Conductance viewed as transmission," *Review of Modern Physics*, vol. 71, pp. S306–S312, 1999.

[222] M. E. Inchiosa, J. W. C. Robinson, A. R. Bulsara, "Information-theoretic stochastic resonance in noise-floor limited systems: the case for adding noise," *Physical Review Letters*, vol. 85, pp. 3369-3372, 2000.

[223] V. K. Ingle, D. G. Manolakis, S. Kogon, *Statistical and Adaptive Signal Processing: Spectral Estimation, Signal Modeling, Adaptive Filtering and Array Processing*; McGraw-Hill Companies: New York, NY, 1999.

[224] F. Jaramillo, K. Wiesenfeld, "Mechanoelectrical transduction assisted by Brownian motion: a role for noise in the auditory system," *Nature Neuroscience*, vol. 1, no. 5, pp. 384–388, September 1998.

[225] P. Jarillo-Herrero, S. Sapmaz, C. Dekker, L. P. Kouwenhoven, H. S. J. van der Zant, "Electron-hole symmetry in a semiconducting carbon nanotube quantum dot ," *Nature*, vol. 429, pp. 389–392, 2002.

[226] A. Jason, M. L. Fackler, "Body Armor Standards: A Review and Analysis," *IWBA Wound Ballistics Review*, vol. 1, no. 1, pp. 14–37, 1992.

[227] A. Javey, J. Guo, Q. Wang, M. Lundstrom, H. Dai, "Ballistic carbon nanotube field-effect transistors," *Nature*,vol. 424, pp. 654–657, 07 Aug 2003.

[228] A. Javey, Q. Wang, A. Urai, Y. Li, H. Dai, "Carbon nanotube transistor arrays for multi-stage complementary logic and ring oscillators," *Nano Letters*, vol. 2, pp. 929–932, 2002.

[229] K. L. Jensen, "Field emitter arrays for plasma and microwave source applications," *Physics of Plasmas*, vol. 6, no. 5, pp. 2241–2253, 1999.

[230] S.-H. Jhi, S. G. Louie, M. L. Cohen, "Electronic properties of oxidized carbon nanotubes," *Physical Review Letters*, vol. 85, pp. 1710–1713, 2000.

[231] S. John, J.-H. Yoo, N. M. Wereley, R. Radhakrishnan, T. S. Sudarshan, "Magnetorheological fluids exploiting nanometer-sized particles," *Proceedings of the SPIE International Society of Optical Engineers*, vol. 4699, pp. 473, 2002.

[232] T. Johnson, "Army scientists, engineers develop liquid body armor," *Army News Service*, 21 April 2004. Online http://www4.army.mil/ ocpa/ read.php?story_id_key=5872

[233] L. M. Jonsson, T. Nord, J. M. Kinaret, S. Viefers, "Effects of surface forces and phonon dissipation in a three-terminal nanorelay," *Journal of Applied Physics*, vol. 96, pp. 629, 2004.

[234] A. Jorio, A. G. Souza Filho, V. W. Brar, A. K. Swan, M. S. Unlu, B. B. Goldberg, A. Righi, J. H. Hafner, C. M. Lieber, R. Saito, G. Dresselhaus, M. S. Dresselhaus, "Polarized resonant Raman study of isolated single-wall carbon nanotubes: Symmetry selection rules, dipolar and multipolar antenna effects," *Physical Review B*, vol. 65, pp. 121402–121405, 2002.

[235] C. Kane, L. Balents, M. P. A. Fisher, "Coulomb interactions and mesoscopic effects in carbon nanotubes," *Physical Review Letters*, vol. 79, no. 25, p. 5086–5089, 22 December 1997.

[236] S. Kang, P. J. Burke, L. N. Pfeiffer, K. W. West, "Ballistic transport at GHz frequencies in ungated HEMT structures," *Solid-State Electronics*, vol. 48, pp. 2013–2017, 2004.

[237] M. A. Kastner, "The single electron transistor and artificial atoms," *Annals of Physics*, vol. 9, no. 11-12, pp. 885–894, 2000.

[238] H. Kataura, Y. Kumazawa, Y. Maniwa, I. Umezu, S. Suzuki, Y. Ohtsuka and Y. Achiba, "Optical properties of single-wall carbon nanotubes," *Synthetic Metals*, vol. 103, no. 1–3, pp. 2555–2558, June 1999.

[239] R. F. Khairutdinov, M. E. Itkis, R. C. Haddon, "Light Modulation of Electronic Transitions in Semiconducting Single Wall Carbon Nanotubes," *Nano Letters*, vol. 4, no. 8, pp. 1529-1533, 2004.

[240] B. N. Khare, M. Meyyappan, A. M. Cassell, C. V. Nguyen, J. Han, "Functionalization of Carbon Nanotubes Using Atomic Hydrogen from aGlow Discharge," *Nano Letters*, vol. 2, no.1, pp. 73–77, 2002.

[241] J. Kim, H.-M. So, N. Kim, J.-J. Kim, K. Kang, "Microwave response of individual multiwall carbon nanotubes," *Physical Review B*, vol. 70, pp. 153402–1535, 2004.

[242] H.-K. Kim, S. Jung, K. Kang, J.-H. Park, Y.-K. Kim, "Low-loss analog and digital micromachined impedance tuners at the Ka-band," *IEEE Transactions on Microwave Theory and Technique*, vol. 49, no. 12, pp.2394–2400, 2001.

[243] G. T. Kim, J. Muster, V. Krstic, J. G. Park, Y. W. Park, S. Roth, M. Burghard, "Field-effect transistor made of individual V_2O_5 nanofibers," *Applied Physics Letters*, vol. 76, no. 14, pp. 1875–1877, 3 April 2000.

[244] J.-R. Kim, H. M. So, J. W. Park, J.-J. Kim, J. Kim, C. J. Lee, S. C. Lyu, "Electrical transport properties of individual gallium nitride nanowires synthesized by chemical-vapor-deposition," *Applied Physics Letters*, vol. 80, no. 19, pp. 3548–3550, 13 May 2002.

[245] J. U. Kim, I. V. Krive, J. M. kinaret, "Nonequillibrium plasmons in a quantum wire single-electron transistor," *Physical Review Letters*, vol. 90, no. 17, pp. 176401–176404, May 2003.

[246] P. Kim, L. Shi, A. Majumdar, P. L. McEuen, "Thermal Transport Measurements of Individual Multiwalled Nanotubes," *Physics Review Letters*, vol. 87, pp. 215502, 2001.

[247] W. Kim, A. Javey, O. Vermesh, Q. Wang, Y. Li, H. Dai, "Hysteresis caused by water molecules in carbon nanotube field-effect transistors," *Nano Letters*, vol. 3, pp. 193, 2003.

[248] J. Kong, J. Cao, H. Dai, E. Anderson, "Chemical profiling of single nanotubes: Intramolecular p-n-p junctions and on-tube single-electron transistors," *Applied Physics Letters*, vol. 80, no. 1, pp.73–75, 2002.

[249] J. Kong, N. R. Franklin, C. Zhou, M. G. Chapline, S. Peng, K. Cho, H. Dai, "Nanotube molecular wires as chemical sensors," *Science*, vol. 287, pp. 622–625, 2000.

[250] J. Kong, H. Soh, A. Cassell, C. F. Quate, H. Dai, "Synthesis of individual single-walled carbon nanotubes on patterned silicon wafers," *Nature*, vol. 395, pp. 878, 1998.

[251] J. Kong, E. Yenilmez, T. W. Tombler, W. Kim, H. Dai, R. B. Laughlin, L. Liu, C. S. Jayanthi, S. Y. Wu, "Quantum interference and ballistic transmission in nanotube electron waveguides," *Physical Review Letters*, vol. 87, pp. 106801–106894, 2001.

[252] B. Kosko, *Fuzzy Engineering*, Prentice Hall, New Jersey, 1996.

[253] B. Kosko, S. Mitaim, "Robust Stochastic Resonance for Simple Threshold Neurons," *Physical Review E*, vol. 70, pp. 031911–031920, 27 September 2004.

[254] B. Kosko, S. Mitaim, "Stochastic resonance in noisy threshold neurons," *Neural Networks*, vol. 16, pp. 755, 2003.

[255] B. Kosko S. Mitaim, "Adaptive stochastic resonance for noisy threshold neurons based on mutual information," IJCNN'02 *IEEE Proceedings of the International Joint Conference on Neural Networks*, vol. 2, pp. 1980, May 2002.

[256] B. Kosko, S. Mitaim, "Robust stochastic resonance: Signal detection and adaptation in impulsive noise," *Physical Review E*, vol. 64, pp. 051110, November 2001.

[257] L. Kouwenhoven, C. Marcus, "Quantum dots," *Physics World*, June, pp. 35, 1998.

[258] H. A. Kramers, "Brownian motion in a field of force and the diffusion model of chemical reactions," *Physica*, vol. 7, no. 4, pp. 284-304, April 1940.

[259] M. Krger, M. R. Buitelaar, T. Nussbaumer, C. Schnenberger, L. Forr, "Electrochemical carbon nanotube field-effect transistor," *Applied Physics Letters*, vol. 78, pp. 1291–1293, 2001.

[260] R. Krupke, F. Hennrich, M. M. kappes, H. v. Lohneysen, "Surface Conductance Induced Dielectrophoresis of Semiconducting Single-Walled Carbon Nanotubes," *Nano Letters*, vol. 4, no. 8, pp. 1395–1399, August 2004.

[261] R. Krupke, F. Hennrich, H. v. Lohneysen, M. M. Kappes, "Separation of Metallic from Semiconducting Single-Walled Carbon Nanotubes," *Science*, vol. 301, pp. 344–347, 18 July 2003

[262] F. J. Kub, K. K. Moon, I. A. Mack, F. M. Long, "Programmable analog vector-matrix multipliers," *IEEE Journal of Solid-state Circuits*, vol.25, no. 1, pp. 207–214, January 1990.

[263] N. Kumar, G. Cauwenberghs, A. G. Andreou, "Auditory Feature Extraction Using Self-Timed, Continuous-Time Discrete-Signal Processing Circuits," *IEEE Transactions on Circuits and Systems II: Analog and Digital Signal Processing*,vol. 44, no. 9, pp. 723–728, September 1997.

[264] S. Kumar, T. D. Dang, F. E. Arnold, A. R. Bhattacharyya, B. G. Min, X. Zhang, R. A. Vaia, C. Park, W. W. Adams, R. H. Hauge, R. E. Smalley, S. Ramesh, P. A. Willis, "Synthesis, Structure, and Properties of PBO/SWNT Composites," *Macromolecules*, vol. 35, pp. 9039–9043, 2002.

[265] J. Krti, G. Kresse, H. Kuzmany,"First-principles calculations of the radial breathing mode of single-wall carbon nanotubes," *Physical Review B*, vol. 58, no. 14, pp. R8869–R8872, 1 October 1998.

[266] H. Kuzmany, W. Plank, M. Hulman, Ch. Kramberger, A. Grneis, Th. Pichler, H. Peterlik, H. Kataura, Y. Achiba, "Determination of SWCNT diameters from the

Raman response of the radial breathing mode," *European Physical Journal B*, vol. 22, pp. 307–320, 2001

[267] M. Law, D. J. Sirbuly, J. C. Johnson, J. Goldberger, R. J. Saykally, P. Yang, "Nanoribbon Waveguides for Subwavelength Photonics Integration," *Science*, vol. 305, pp. 1269–1273, August 2004.

[268] C. A. Leatherdale, C. R. Kagan, N. Y. Morgan, S. A. Empedocles, M. A. Kastner, M. G. Bawendi, "Photoconductivity in CdSe quantum dot solids," *Pysical Review B*, vol. 62, pp. 2669–2680, 15 July 2000.

[269] J. U. Lee, P. P. Gipp, C. M. Heller, "Carbon nanotube p-n junction diodes," *Applied Physics Letters*, vol. 85, pp. 145–147, 2004.

[270] J. Lee, S. Eggert, H. Kim, S.-J. Kahng, H. Shinohara, Y. Kuk, "Real space imaging of one-dimensional standing waves: Direct evidence for a Luttinger Liquid," *Physical Review Letters*, vol. 93, no. 16, pp. 166403–166406, 15 October 2004.

[271] S. W. Lee, D. S. Lee, R. E. Morjan, S. H. Jhang, M. Sveningsson, O. A. Nerushev, Y. W. Park, E. E. B. Campbell, "A three-terminal carbon nanorelay," *Nano Letters*, vol. 4, no. 10, pp. 2027–2030, 2004.

[272] Y. S. Lee, E. D. Wetzel, N. J. Wagner, "The ballistic impact characteristics of Kevlar woven fabrics impregnated with a colloidal shear thickening fluid," *Journal of Materials Science*, vol. 38, no. 13, pp.2825-2833, 2002.

[273] F. Leonard and J. Tersoff, "Novel length scales in nanotube devices," *Physical Review Letters*, vol. 84, pp. 4693–4696, 2000.

[274] E. Lemaire and G. Bossis, "Yield stress and wall effects in magnetic colloidal suspensions," *Journal of Physics D: Applied Physics* vol. 24 pp. 1473–1477, 14 August 1991.

[275] D. S. Leonard and L. E. Reichl, "Stochastic resonance in a chemical reaction," *Physical Review E*, vol. 49, no. 2, pp. 1734-1737, February 1994.

[276] J. E. Levin, J. P. Miller, "Broadband neural encoding in the cricket cercal sensory system enhanced by stochastic resonance," *Nature*, vol. 380, 165-168, 1996.

[277] C. Li, T.-W. Chou, "Single-walled carbon nanotubes as ultrahigh frequency nanomechanical resonators," *Physical Review B*, vol. 68, pp. 073405–073407, 2003.

[278] C. Li, B. Lei, D. Zhang, X. Liu, S. Han, T. Tang, M. Rouhanizadeh, T. Hsiai, C. Zhou, "Chemical gating of In_2O_3 nanowires by organic and biomolecules," *Applied Physics Letters*, vol. 83 pp. 4014-4016, 10 November 2003.

[279] J. Li, "Direction and polarization estimation using arrays with small loops and short dipoles," *IEEE Transactions on Antennas and Propagation*, vol. 41, no. 3, pp. 379-387, March 1993.

[280] S. Li, Z. Yu, C. Rutherglen, P. J. Burke, "Electrical Properties of 0.4 cm Long Single-Walled Carbon Nanotubes," *Nano Letters*, vol. 4, no. 10, pp. 2003–2007, October 2004.

[281] W. Liang, M. Bockrath, D. Bozovic, J. H. Hafner, M. Tinkham, H. Park, "Fabry-Perot interference in a nanotube electron waveguide," *Nature*, vol. 411, pp. 665–669, 2001.

[282] Reprinted with permission from David J. Lim, The Journal of the Acoustical Society of America, 67, 1686 (1980). Copyright 1980, Acoustical Society of America.

[283] J. Lin, L. Gao, A. Sugavanam, X. Guo, R. Li, J. E. Brewer, K. O. Kenneth, "Integrated Antennas on Silicon Substrates for Communication Over Free Space," *IEEE Electron Device Letters*, vol. 25, no. 4, pp. 196–198, April 2004.

[284] L. Lin, R. T. Howe, A. P. Pisano, "Micoelectromechanical filters for signal processing," *Journal of Microelectromechanical Systems*, vol. 7, no. 3, pp. 286–294, September 1998.

[285] J. F. Lindner, B. J. Breen, M. E. Wills, A. R. Bulsara, W. L. Ditto, "Monostable array-enhanced stochastic resonance," *Physical Review E*, vol. 63, pp. 051107, 2001.

[286] L. Liu, C. Jayanthi, M. Tang, S. Y. Wu, T. Tombler, C. Zhou, L. Alexeyev, J. Kong, H. Dai, "Controllable reversibility of an sp^2 to sp^3 transition of a single wall nanotube under the manipulation of an AFM tip: a nanoscale electromechanical switch?" *Physical Review Letters*, vol. 84, pp. 4950–4953, 2000.

[287] T. Liu, T.V. Sreekumar, S. Kumar, R.H. Hauge, R.E. Smalley, "SWNT/PAN Composite Film-based Supercapacitor," *Carbon*, vol. 41, pp. 2440–2442, 2003.

[288] X. Liu, C. Lee, C. Zhou, "Carbon nanotube field-effect inverters," *Applied Physics Letters*, vol. 79, no. 20, pp. 3329–3331, November 2001.

[289] X. Liu, T. Pichler, M. Knupfer, M. S. Golden, J. Fink, H. Kataura, and Y. Achiba, "Detailed analysis of the mean diameter and diameter distribution of single-wall carbon nanotubes from their optical response," *Physical Review B*, vol. 66, pp. 045411–045418, 2002.

[290] J. Liu, A. G. Rinzler, H. Dai, J. H. Hafner, R. K. Bradley, P. J. Boul, A. Lu, T. Iverson, K. Shelimov, C. B. Huffman, F. Rodriguez-Macias, Y.-S. Shon, T. R. Lee, D. T. Colbert, R. E. Smalley, "Fullerene pipes," *Science*, vol. 280, pp. 1253–1256, 1998.

[291] M. Löcher, G. A. Johnson, E. R. Hunt, "Spatiotemporal stochastic resonance in a system of coupled diode resonators," *Physical Review Letters*, vol. 77, no. 23, pp. 4698–4701, December 1996.

[292] R. Löfstedt and S. N. Coppersmith, "Quantum stochastic resonance," *Physical Review Letters*, vol. 72, no. 13, pp. 1947–1950, March 1994.

[293] A. Longtin, "Autonomous stochastic resonance in bursting neurons," *Physical Review E*, vol. 55, no. 1, pp. 868–876, January 1997.

[294] A. Longtin, "Synchronization of the stochastic FitzHugh-Nagumo equations to periodic forcing," *Il Nuovo Cimento, Luglio-Agosto*, vol. 17 D, no. 7-8, pp. 835–846, 1995.

[295] R. Lopez, L. A. Boatner, T. E. Haynes, R. F. Haglund, Jr., L. C. Feldman, "Switchable reflectivity on silicon from a composite VO_2-SiO_2 protecting layer," *Applied Physics Letters*, vol. 85, pp. 1410, 2004.

[296] C. Lu, Q. Fu, S. Huang, J. Liu, J. "Polymer Electrolyte-Gated Carbon Nanotube Field-Effect Transistor," *Nano Letters*, vol. 4,no. 4, pp. 623–627, 2004.

[297] V. M. Lubecke, W. R. McGrath, P. A. Stimson, D. B. Rutledge, "Micromechanical tuning elements in a 620-GHz monolithic integrated circuit," *IEEE Transactions on Microwave Theory and Technique*, vol. 46, no 12, pp.2098–2103, 1998.

[298] M. Lucas and R. J. Young, "Effect of uniaxial strain deformation upon the Raman radial breathing modes of single-wall carbon nanotubes in composites," *Physical Review B*, vol. 69, pp. 085405–085413, 2004.

[299] S. Lucyszyn, "Review of radio frequency microelectromechanical systems technology," *IEE Proceedings on Scientific Measurements and Technologies*, vol. 151, no. 2, pp. 93–103, March 2004

[300] R. F. Lyon, C. Mead, "An analog electronic cochlea," *IEEE Transactoins on Acoustics, Speech, and Signal Processing*, vol. 36, no. 7, pp. 1119–1134, July 1988.

[301] N. N. Machalaba, G. A. Bundnitskii, A. M. Shchetinin, G. G. Frenkel, "Trends in the development of synthetic fibers for armor material," *Fibre Chemistry'*, vol. 33, no. 2, pp. 117–126, 2001.

[302] D. MacPherson, "Dynamic Projectile Interactions and Associated Body Armor Effects," *IWBA Wound Ballistics Review*, vol. 1, no. 4, pp. 29–31, 1994.

[303] D. MacPherson, Lt. Ed Fincel Miloskovich, J. Nicholas "Body Armor Penetration Dynamics," *IWBA Wound Ballistics Review*, vol. 3, no. 2 pp. 16–24, 1997.

[304] D. MacPherson, pp. 67–85, *Bullet Penetration: Modeling the Dynamics and the Incapacitation Resulting from Wound Trauma*, Ballistic Publications1994.

[305] D. MacPherson, "The Dynamics of Tissue Simulation," *IWBA Wound Ballistics Review*, vol. 3, no. 1, pp. 21–23, 1997.

[306] D. E. Makarov and N. Makri, "Stochastic resonance and nonlinear response in double-quantum-well structures," *Physical Review B*, vol. 52, no. 4, pp. R2257-R2260, July 1995.

[307] A. V. Mamishev, K. Sundara-Rajan, F. Yang, Y. Du, M. Zahn, "Interdigital sensors and transducers," *Proceedings of the IEEE*, vol. 92, no. 5, pp. 808–845, May 2004.

[308] D. Mann, A. Javey, J. Kong, Q. Wang, H. Dai, "Ballistic transport in metallic nanotubes with reliable Pd ohmic contacts," *Nano Letters*,vol. 3, no. 11, pp. 1541–1544, 2003.

[309] G. D. Mansfeld, Yu. V. Gulyaev, Z. Ya. Kosakovskaya, S. G. Alekseev, V. V. Saraykin, "Acoustic and Acoustoelectronic Properties of Carbon Nanotube Films," *Physics of the Solid State*, vol. 44, no. 4, pp. 674–676, April 2002.

[310] R. N. Mantegna and B. Spagnolo, "Stochastic resonance in a tunnel diode in the presence of white or colored noise," *Il Nuovo Cimento, Luglio-Agosto*, vol. 17 D, nos. 7-8, pp. 873-881, 1995.

[311] R. N. Mantegna and B. Spagnolo, "Stochastic resonance in a tunnel diode," *Physical Review E*, vol. 49, no. 3, pp. R1792-R1795, March 1994.

[312] B. J. Maranzano and N. J. Wagner, "Flow-small angle neutron scattering measurements of colloidal dispersion microstructure evolution through the shear thickening transition," *Journal of Chemical Physics*, vol. 117, pp. 10291, 2002.

[313] B. J. Maranzano, N. J. Wagner, "The effects of particle size on reversible shear thickening of concentrated colloidal dispersions," *Journal of Chemical Physics*, vol. 114, pp. 10514, 2001.

[314] B. J. Maranzano, N. J. Wagner, "The effects of interparticle interactions and particle size on reversible shear thickening: Hard-sphere colloidal dispersions," *Journal of Rheology*, vol. 45, pp. 1205, 2001.

[315] R. Martel, V. Derycke, C. Lavoie, J. Appenzeller, K. K. Chan,J. Tersoff, Ph. Avouris, "Ambipolar Electrical Transport in Semiconducting Single-Wall Carbon Nanotubes," *Physical Review Letters*, vol. no. 87, pp. 256805, December 2001.

[316] R. Martel, T. Schmidt, H.R. Shea, T. Hertel, Ph. Avouris "Single and multi-wall carbon nanotube field-effect transistors," *Applied Physics Letters*, vol. 73, pp. 2447, 1998.

[317] R. Martel, H.-S. P. Wong, K. Chan, P. Avouris, "Carbon nanotube field-effect transistors for logic applications," in *Proceedings of the IEDM 2001*, pp. 159–161, 2001.

[318] S. Matyjaskiewicz, A. Krawiecki, J. A. Holyst, K. Kacperski, W. Ebeling, "Stochastic multiresonance in a chaotic map with fractal basins of attraction," *Physical Review E*, vol. 63, pp. 026215, 2001.

[319] W. McCarthy, *Hacking Matter: Levitating Chairs, Quantum Mirages, and the Infinite Weirdness of Programmable Atoms*, BasicBooks, New York, New York, 2003.

[320] P. L. McEuen, M. S. Fuhrer, H. Park, "Single-walled carbon nanotube electronics," *IEEE Transactions on Nanotechnology*, vol. 1, pp. 78–85, March 2002.

[321] P. L. McEuen, M. Bockrath, D. H. Cobden, Y.-G. Yoon, S. G. Louie, "Disorder, pseudospins, and backscattering in carbon nanotubes," *Physical Review Letters*, vol. 83, pp. 5098–5101, 1999.

[322] B. McNamara, K. Wiesenfeld, R. Roy, "Observation of Stochastic Resonance in a Ring Laser," *Physical Review Letters*, vol. 60, pp. 2626-2629, 1988.

[323] V. I. Melnikov, "Schmitt trigger: A solvable model of stochastic resonance," *Physical Review E*, vol. 48, no. 4, pp. 2481-2489, October 1993.

[324] D. Mercier, J.-C. Orlianges, T. Delage, C. Champeaux, A. Catherinot, D. Cross, P. Blondy, "Millimeter-wave tune-all bandpass filters," *IEEE Transactions on Microwave Theory and Techniques*, vol. 52, no. 4, pp. 1175–1181, April 2004.

[325] J. B. Messenger, "Cephalopod chromatophores: neurobiology and natural history," *Biological Review*, vol. 76, pp. 473–528, 2001.

[326] E. T. Mickelson, I. W. Chiang, J. L. Zimmerman, P. J. Boul, J. Lozano,J. Liu, R. E. Smalley, R. H. Hauge, J. L. Margrave, "Solvation of Fluorinated Single-Wall Carbon Nanotubes in Alcohol Solvents," *Journal of Physical Chemistry B*, vol. 103, no. 21 pp. 4318–4322, 1999.

[327] E. T. Mickelson, C. B. Huffman, A. G. Rinzler, R. E. Smalley,R. H. Hauge, J. L. Margrave, "Fluorination of single-wall carbon nanotubes," *Chemical Physics Letters* vol. 296, no. 1,2,pp. 188–194, 1998.

[328] J. P. Miller, G. A. Jacobs, F. E. Theunissen, "Representation of sensory information in the cricket cercal sensory system. I. Response properties of the primary interneurons," *Journal of Neurophysiology*, vol. 66, no. 5, pp. 1680–1689, November 1991.

[329] J. P. Miller, G. A. Jacobs, F. E. Theunissen, "Representation of sensory information in the cricket cercal sensory system. II. Information theoretic calculation of system accuracy and optimal tuning-curve widths of four primary interneurons," *Journal of Neurophysiology*, vol. 66, no. 5, pp. 1690–1703, November 1991.

[330] J. W. Mintmire, B. I. Dunlap, C. T. White, "Are fullerene tubules metallic?" *Physical Review Letters*, vol. 68, pp. 631–634, 1992.

[331] S. Mirabbasi, K. Martin, "Classical and Modern Receiver Architectures," *IEEE Communications Magazine*, pp. 132–139, November 2000.

[332] J. A. Misewich, R. Martel, Ph. Avouris, J. C. Tsang, S. Heinze, J. Tersoff, "Electrically Induced Optical Emission from a Carbon Nanotube FET," *Science*, vol. 300, pp. 783–786, 2 May 2003.

[333] M. Misono, T. Kohmoto, M. Kunitomo, Y. Fukuda, "Information gain in an optical bistable system by stochastic resonance," *Physical Review E*, vol. 67, pp. 061102-061105, June 2003.

[334] S. Mitaim, B. Kosko, "The Shape of Fuzzy Sets in Adaptive Function Approximation," *IEEE Transactions on Fuzzy Systems*, vol. 9, no. 4, pp. 637–656, August 2001.

[335] M. E. Toimil Molares, E. M. Hohberger, Ch. Schaeflein, R. H. Blick, R. Neumann, C. Trautmann, "Electrical characterization of electrochemically grown single copper nanowires," *Applied Physics Letters*, vol. 82, no. 13, pp. 2139–2141, 13 March 2003.

[336] G. K. Montress, T. E. Parker, D. Andres, "Review of SAW oscillator performance," *IEEE Ultrasonics Symposium*, pp. 43–54, 1994

[337] D. P. Morgan, "History of SAW devices," *IEEE International Frequency Control Symposium*, pp. 439–460, 1998.

[338] N. Y. Morgan, C. A. Leatherdale, M. Drndic, M. V. Jarosz, M. A. Kastner, M. Bawendi, "Electronic transport in films of colloidal CdSe nanocrystals," *Physical Review B*, vol. 66, pp. 075339, 2002.

[339] R. P. Morse, E. F. Evans, "Enhancement of vowel coding for cochlear implants by addition of noise," *Nature Medicine*, vol. 2, no. 8, pp. 928–932, August 1996.

[340] F. Moss, J. K. Douglass, L. Wilkens, D. Pierson, E. Pantazelou, "Stochastic resonance in an electronic FitzHugh-Nagumo model," *Annals of the New York Academy of Sciences: Stochastic Processes in Astrophysics*, J. R. Buchler and H. E. Kandrup, Editors, vol. 706, pp. 26–41, 1993.

[341] F, Moss, D. Pierson, D. O'Gorman, "Stochastic resonance: Tutorial and update," *International Journal of Bifurcation and Chaos*, vol. 6, pp. 1383–1397, 1994.

[342] H. Namatsu, Y. Watanabe, K. Yamazaki, T. Yamaguchi, M. Nagase, Y. Ono, A. Fujiwara, S. Horiguchi, "Fabrication of Si single-electron transistors with precise dimensions by electron-beam nanolithography," *Journal of Vacuum Science & Technology B: Microelectronics and Nanometer Structures*, vol. 21, no. 1, pp. 1–5 January 2003.

[343] National Institute of Justice (NIJ) Standards for *Ballistic Resistance of Personal BodyArmor and Stab Resistance of Personal Body Armor*, NIJ Standard-0101.04, 2004.

[344] Z. N'eda, "Stochastic resonance in Ising systems," *Physical Review E*, vol. 51, no. 6, pp. 5315-5317, June 1995.

[345] S. Neely, "Inside the cochlea," *Introduction to Cochlear Mechanics*, Boys Town National Research Hospital, Omaha, Nebraska, http://www.boystownhospital.org/ BasicClinic/neuro/cel/ Inside_Cochlea.asp

[346] S. T. Neely and D. O. Kim, "An active cochlear model showing sharp tuning and high sensitivity," *Hearing Research*, vol. 9, pp. 123–130, 1983.

[347] C. T.-C. Nguyen, "Frequency-selective MEMS for miniaturized low-power communication devices," *IEEE Transactions on Microwave Theory and Techniques*, vol. 47, pp. 1486–1503, 1999.

[348] F. Noca, M. Hoenk, B. Hunt, P. Koumoutsakos, J. Walther, T. Werder, "Bio-inspired acoustic sensors based on artificial stereocilia," *Journal of the Acoustic Society of America*, vol. 108, pp. 2494, 2000.

[349] D. Nicolaescu, V. Filip, F. Okuyama, "Proposal for a new UV-light generating device based on cold electron emission," *Journal of Vacuum Science and Technology A*, vol. 16, no. 5, pp. 2885–2889, September 1998.

[350] A. Nojeh, G. W. Lakatos, S. Peng, K. Cho, R. F. W. Pease, "A Carbon Nanotube Cross Structure as a Nanoscale Quantum Device," *Nano Letters*, vol. 3, no. 9, pp. 1187–1190, 2003.

[351] C. D. Nordquist, A. Muyshondt, M. V. Pack, P. S. Finnegan, C. W. Dyck, I. C. Reines, G. M. Kraus, T. A. Plut, G. R. Sloan, C. L. Goldsmith, C. T. Sullivan, "An X-band to Ku-band RF MEMS switched coplanar strip filter," *IEEE Microwave and Wireless Components Letters*, vol. 14, no. 9, pp. 425–427, September 2004.

[352] M. D. Norman, J. Finn, T. Tregenza, "Dynamic mimicry in an Indo-Malayan octopus," *Proceedings of the Royal Society of London B*, vol. 268, pp. 1755–1758, 2001.

[353] T. W. Odom, J.-L. Huang, P. Kim, C. M. Lieber, "Structure and Electronic Properties of Carbon Nanotubes," *Journal of Physical Chemistry B*, vol. 104, no. 13, pp. 2794–2809, 2000.

[354] T. W. Odom, J. L. Huang, P. Kim, C. M. Lieber, "Atomic structure and electronic properties of single-walled nanotubes," *Nature*, vol. 391, pp. 62-64, 1998.

[355] K. G. Ong, K. Zeng, C. A. Grimes, "A wireless, passive carbon nanotube-based gas sensor," *IEEE Sensors Journal*, vol. 2, pp. 82, 2002.

[356] A.V. Oppenheim, R.W. Schafer, J.R. Buck, *Discrete-Time Signal Processing, Second Edition*; Prentice-Hall, Inc., Upper Saddle River, NJ, 1999.

[357] G. Ostermayer, "On the noise behavior of a SAW convolver used as a matched filter," *IEEE Transactions on Microwave Theory and Techniques*, vol. 49, no. 4, pp. 779–786, April 2001.

[358] M. Ouyang, J.-L. Huang, C. M. Lieber, "One-dimensional energy dispersion of single-walled carbon nanotubes by resonant electron scattering," *Physical Review Letters*, vol. 88, no. 6, pp. 066804–066807, 2002.

[359] M. Ouyang, J.-L. Huang, C. L. Cheung, C. M. Lieber, "Energy gaps in 'metallic' single-walled carbon nanotubes," *Science*, vol. 292, pp. 702–705, 2001.

[360] A. Packard, F. G. Hochberg, "Skin patterning in Octopus and other genera," *Symposia of the Zoological Society of London*, vol. 38, pp. 191–231, 1977.

[361] V. B. Pai, M. W. Kelly, "Bruising Associated with the Use of Fluoxetine," *Annals of Pharmacotherapy*, vol. 30, No. 7–8, pp. 786–788, 1996.

[362] T. Palacios, F. Calle, J. Grajal, E. Monroy, M. Eickhoff, O. Ambacher, F. Omnes, "High frequency SAW devices on AlGaN: Fabrication, characterization and integration with optoelectronics," *IEEE Ultrasonics Symposium*, pp. 57–60, 2002.

[363] E. Pantazelou, C. Dames, F. Moss, J. Douglass, L. Wilkens, "Temperature dependence and the role of internal noise in signal transduction efficiency of Crayfish mechanoreceptors," *International Journal of Bifurcation and Chaos*, vol. 5, no. 1, pp. 101–108, 1995.

[364] T. P. Pareek, M. C. Mahato, A. M. Jayannavar, "Stochastic resonance and nonlinear response in a dissipative quantum two-state system," *Physical Review B*, vol. 55, no. 15, pp. 9318–9321, April 1997.

[365] T. P. Pareek, M. C. Mahato, A. M. M. Thorwart and P. Jung, "Dynamical hysteresis in bistable quantum systems," *Physical Review Letters*, vol. 78, no. 13, pp. 2503–2506, March 1997.

[366] H. Park, J. Park, A. K. Lim, E. H. Anderson, A. P. Allvisator, P. L. McEuen, "Nanomechanical oscillations in a single-C_{60} transistor," *Nature*, vol. 407, pp. 57, 2000.

[367] J. W. Park, J. Kim, K.-H. Yoo, "Electrical transport through crossed carbon nanotube junctions," *Journal of Applied Physics*, vol. 93, no. 7, pp. 2191–4193, 1 April 2003.

[368] X. Pei, L. Wilkens, F. Moss, "Noise-mediated spike timing precision from aperiodic stimuli in an array of Hodgkin-Huxley type neurons," *Physical Review Letters*, vol. 77, no. 22, pp. 4679–4682, November 1996.

[369] X. Pei, K. Bachmann, F. Moss, "The detection threshold, noise and stochastic resonance in the Fitzhugh-Nagumo neuron model," *Physics Letters A*, vol. 206, pp. 61–65, October 1995.

[370] X. Pei, L. Wilkens, F. Moss, "Light enhances hydrodynamic signaling in the multimodal caudal photoreceptor interneurons of the Crayfish," *Journal of Neurophysiology*, vol. 76, no. 5, pp. 3002–3011, November 1996.

[371] A. Peigney, Ch. Laurent, E. Flahaut, A. Rousset, "Carbon nanotubes in novel ceramic matrix nanocomposites," *Ceramics International*, vol.26, pp. 677–683, 2000.

[372] S. Pekker, J. -P. Salvetat, E. Jakab, J. -M. Bonard, L. Forro, "Hydrogenation of Carbon Nanotubes and Graphite in Liquid Ammonia," *Journal of Physical Chemistry B*, vol. 105, no. 33, pp. 7938–7943, 2001.

[373] S. Peng, K. Cho, "Ab Initio Study of Doped Carbon Nanotube Sensors ," *Nano Letters*, vol 3, no. 4, pp. 513, 2003.

[374] F. Perez, B. Jusserand, "Plasmons and the quantum limit in semiconductor wires," *Physical Review B*, vol. 60, no. 19, pp. 13310–13313, November 1999.

[375] D. Pierson, J. K. Douglass, E. Pantazelou, F. Moss, "Using an electronic FitzHugh-Nagumo simulator to mimic noisy electrophysiological data from stimulated Crayfish mechanoreceptor cells," *AIP Conference Proceedings: Noise in Physical Systems and 1/f Fluctuations*, P. H. Hanel and A. L. Chung, Editors., vol. 285, pp. 731–734, 1993.

[376] N. J. Pinto, A. T. Johnson, Jr., A. G. MacDiarmid, C. H. Mueller, N. Theofylaktos, D. C. Robinson, F. A. Miranda, "Electrospun polyaniline/polyethylene oxide nanofiber field-effect transistor," *Applied Physics Letters*, vol. 83, no. 20 pp. 4244–4246, 17 November 2003.

[377] H. E. Plesser and S. Tanaka, "Stochastic resonance in a model neuron with reset," *Physics Letters A*, vol. 225, pp. 228–234, February 1997.

[378] R. Plonsey and R. C. Barr, *Bioelectricity: A quantitative Approach*, Plenum Press, New York, 1988.

[379] H. W. Ch. Postma, M. de Jonge, Z. Yao, C. Dekker, "Electrical transport through carbon nanotube junctions created by mechanical manipulation," *Physical Review B*, vol. 62, pp. R10653–R10656, 2000.

[380] H. W. Ch. Postma, T. Teepen, Z. Yao, M. Grifoni, C. Dekker, "Carbon nanotube single-electron transistors at room temperature," *Science*, vol. 293, pp. 76, 2001.

[381] A. D. Poularikas, S. Seely, chapter 9, *Signals and Systems, Second Edition, Reprint*, Krieger Publishing Company, Malabar, Florida, 1994.

[382] A. Prata, Jr. "Notes on the graduate course EE573a, Antenna Analysis," University of Southern California, Department of Electrical Engineering-Electrophysics, Spring 2005.

[383] L. N. Pringle, P. H. Harms, S. P. Blalock, G. N. Kiesel, E. J. Kuster, P. G. Friederich, R. J. Prado, J. M. Morris, G. S. Smith, "A Reconfigurable Aperture Antenna Based on Switched Links Between Electrically Small Metallic Patches," *IEEE Transactions on Antennas and Propagation*, vol. 52, no. 6, pp. 1434–1445, June 2004

[384] J. G. Proakis, D. G. Manolakis, *Intorduction to Digital Signal Processing*, MacMillan, New York, New York, 1988.

[385] Semiconductor quantum dots, online http://www.qdots.com

[386] L. C. Qin, X. Zhao, K. Hirahara, Y. Miyamoto, Y. Ando, S. Iijima, "The smallest carbon nanotube," *Nature*, vol. 408, pp. 50, 2000.

[387] M. Radosavljevi, J. Appenzeller, V. Derycke, R. Martel, Ph. Avouris, A. Loiseau, J.-L. Cochon, D. Pigache, "Electrical properties and transport in boron nitride nanotubes," *Applied Physics Letters*, vol. 82, no. 23, pp. 4131–4133, 9 June 2003.

[388] M. Radosavljevic, M. Freitag, K. V. Thadani, A. T. Johnson, "Nonvolatile molecular memory elements based on ambipolar nanotube field effect transistors," *Nano Letters*, vol. 2, pp. 761, 2002.

[389] Ramu Ramanathan, *Introductory Econometrics with Applications*, fourth edition. Dryden Press, Fort Worth, Texas, 1998.

[390] A. M. Rao, E. Richter, S. Bandow, B. Chase, P. C. Eklund, K. A. Williams, S. Fang, K. R. Subbaswamy, M. Menon, A. Thess, R. E. Smalley, "Diameter-selective Raman scattering from vibrational modes in carbon nanotubes," *Science*, vol. 275, no. 5297, pp. 187–191, 10 Jan. 1997.

[391] S. Reich, H. Jantoljak, C. Thomsen, "Shear strain in carbon nanotubes under hydrostatic pressure," *Physical Review B*, vol. 61, pp. R13389–R13392, 15 May 2000.

[392] A. C. Rencher, *Linear Models in Statistics*, Wiley, New York, New York 2000.

[393] Retro-reflective material. Online http://www.reflexiteamericas.com/ micro-prism_technology.htm

[394] B. Reulet, A. Yu. Kasumov, M. Kociak, R. Deblock, I. I. Khodos, Yu. B. Gorbatov, V. T. Volkov, C. Journet, H. Bouchiat, "Acoustoelectric Effects in Carbon Nanotubes," *Physical Review Letters*, vol. 85, pp. 2829–2832, 2000.

[395] W. S. Rhode, "Some observations on cochlear mechanics," *Journal of the Acoustical Society of America*, vol. 64, pp. 158–176, June 1978.

[396] W. S. Rhode, "Observations of the vibration of the basilar membrane in squirrel monkeys using the Mössbauer technique," *Journal of the Acoustical Society of America*, vol. 49, pp. 1218–1231, 1971.

[397] L. Robles, M. A. Ruggero, "Mechanics of the Mammalian Cochlea," *Physiological Reviews*, vol. 81, pp. 1305–1352, 2001

[398] A. Rochefort, M. D. Ventra, Ph. Avouris, "Switching behaviour of semiconducting carbon nanotubes under an external electric field," *Applied Physics Letters*, vol. 78, pp. 2521, 2001.

[399] S. Rosenblatt, Y. Yaish, J. Park, J. Gore, V. Sazonova, P. L. McEuen, "High Performance Electrolyte Gated Carbon Nanotube Transistors," *Nano Letters*, vol. 2, pp. 869–872, 2002.

[400] L. Rotkina, J.-F. Lin and J. P. Bird, "Nonlinear current-voltage characteristics of Pt nanowires and nanowire transistors fabricated by electron-beam deposition," *Applied Physics Letters*, vol. 83, no. 21, pp. 4426–4428, 24 November 2003.

[401] R. Rouse, S. Han, J. E. Lukens, "Flux amplification using stochastic superconducting quantum interference devices," *Applied Physics Letters*, vol. 66, no. 1, pp. 108-110, January 1995.

[402] T. Rueckes, K. Kim, E. Joselevich, G. Y. Tseng, C.-L. Cheung, C. M. Lieber, "Carbon Nanotube-Based Nonvolatile Random Access Memory for Molecular Computing," *Science*, vol. 289, pp. 94-97, July 2000.

[403] D. F. Russel, Lon. A. Wilkens, F. Moss, "Use of behavioural stochastic resonance by paddlefish for feeding," *Nature*, vol. 402, pp. 291, 1999.

[404] A. J. Ryan MD, "Traumatic Injuries: Office Treatment of Deep Bruises," *Postgraduate Medicine*, vol. 59, no. 6, pp. 195–197, 1976.

[405] R. Saito, M. Fujita, G. Dresselhaus, M. S. Dresselhaus, "Electronic structure of chiral graphene tubules," *Applied Physics Letters*, vol. 60, pp. 2204, 1992.

[406] A. N. Salt, "A pictorial guide to the cochlear fluids," Cochlear Fluids Lab, Washington University, online, http://oto.wustl.edu/ cochlea/intro1.htm

[407] Ge. G. Samsonidze, S. G. Chou, A. P. Santos, V. W. Brar, G. Dresselhaus, M. S. Dresselhaus, A. Selbst, A. K. Swan, M. S. nl, B. B. Goldberg, D. Chattopadhyay, S. N. Kim, F. Papadimitrakopoulos, "Quantitative evaluation of the octadecylamine-assisted bulk separation of semiconducting and metallic single-wall carbon nanotubes by resonance Raman spectroscopy," *Applied Physics Letters*, vol. 85, no. 6, pp. 1006–1008, 2004.

[408] R. A. Santucci, Y.-J. Chang, "Ballistics for physicians: Myths about wound ballistics and gunshot injuries," *Journal of Urology*, vol. 171, pp. 1408–1414, April 2004.

[409] S. Sapmaz, Y. M. B.anter, L. Gurevich, H. S. J. van der Zant, "Carbon nanotubes as nanoelectromechanical systems," *Physical Review B*, vol. 67, no. 23, pp. 235414–235420, 2003.

[410] V. Sazonova, Y. Yaish, H. stnel, D. Roundy, T. A. Arias, P. L. McEuen, "A tunable carbon nanotube electromechanical oscillator," *Nature*, vol. 431, pp. 284, 2004.

[411] C. Schönenberger, L. Forró, "Multiwall carbon nanotubes," *Physics World*, June 2000.

[412] M. Shim, G. P. Siddons, "Photoinduced conductivity changes in carbon nanotube transistors," *Applied Physics Letters*,vol. 83, no. 17, pp. 3564–3566, October 2003.

[413] F. L. Shyu, C. P. Chang, R. B. Chen, C. W. Chiu, M. F. Lin, "Magnetoelectronic and optical properties of carbon nanotubes," *Physical Review B*, vol. 67, pp. 045405–045413, 2003.

[414] G. P. Siddons, D. Merchin, J. H. Back, J. K. Jeong, M. Shim, "Highly efficient gating and doping of carbon nanotubes with polymer electrolytes", *Nano Letters*, vol. 4, no. 5, pp. 927–931, 2004.

[415] S. W. Sides, R. A. Ramos, P. A. Rikvold, M. A. Novotny, "Kinetic Ising system in an oscillating external field: Stochastic resonance and residence-time distributions," *Journal of Applied Physics*, vol. 81, no. 8, pp. 5597–5599, April 1997.

[416] L. B. Sjogren, H.-X. L. Liu, F. Wang, T. Liu, X.-H. Qin, W. Wu, E. Chung, C. W. Domier, N. C. Luhmann, Jr., "A monolithic diode array millimeter-wave beam transmittance controller," *IEEE Transactions on Microwave Theory and Techniques*, vol. 41, no. 10, pp. 1782–1790, October 1993.

[417] M. Smith, "British develop electric force field to protect tanks," *The Daily Telegraph - London*, 21 August 2002.

[418] I. I. Smolyaninov, "Electron-plasmon interaction in a cylindrical mesoscopic system: Important similarities with Kaluza-Klein theories," *Physical Review B*, vol. 67, pp. 165406–165413, April 2003.

[419] E. B. Sonin, "Tunneling into 1D and quasi-1D conductors and Luttinger-liquid behavior," *Journal of Low Temperature Physics*, vol. 124, nos. 1-2, pp. 321–334, 2001.

[420] S. M. Soskin and P. V. E. McClintock, Comment on "Monostable array-enhanced stochastic resonance" *Physical Review E*, vol. 66, pp. 013101, 2002.

[421] A. G. Souza Filho, S. G. Chou, Ge. G. Samsonidze, G. Dresselhaus, M. S. Dresselhaus, Lei An, J. Liu, A. Jorio, A. Gruneis, R. Saito, "Stokes and anti-Stokes Raman spectra of small-diameter isolated carbon nanotubes," *Physical Review B*, vol. 69, pp. 115428–115435, 2004.

[422] M. L. Spano, M. Wun-Fogle, W. L. Ditto, "Experimental observation of stochastic resonance in a magnetoelastic ribbon," *Physical Review A*, vol. 46, no. 8, pp. 5253-5256, October 1992.

[423] A. Star, T.-R Han, J.-C. P. Gabriel, K. Bradley, G. Gruner, "Interaction of Aromatic Compounds with Carbon Nanotubes: Correlation to the Hammett Parameter of the Substituent and Measured Carbon Nanotube FET Response," *Nano Letters*, vol. 3, no. 10, pp. 1421-1423, 2003.

[424] M. Stemmler, "A single Spike suffices: The simplest form of stochastic resonance in model neurons," *Network: Computation in Neural Systems*, vol. 7, pp. 687-716, 1996.

[425] J. L. Stevens, A. Y. Huang, H. Peng, I. W. Chiang, V. N. Khabashesku, J. L. Margrave, "Sidewall Amino-Functionalization of Single-Walled Carbon Nanotubes through Fluorination and Subsequent Reactions with Terminal Diamines," *Nano Letters*, vol. 3, no. 3, pp. 331–336, 2003.

[426] T. Stephenson, Y. Bialas, "Estimation of the Age of Bruising," *Archives of Disease in Childhood*, vol. 74, no. 1, pp. 53–5, January 1996.

[427] N. G. Stocks, "Information transmission in parallel threshold arrays: suprathreshold stochastic resonance," *Physical Review E*, vol. 63, pp. 041114-041122, 2001.

[428] J. Sun, L. Gao, W. Li, "Colloidal Processing of Carbon Nanotube/Alumina Composites," *Chemical Materials*, vol. 14, no. 12, pp. 5169–5172 2002.

[429] S. R. Swanson, *Introduction to Design and Analysis with Advanced Composite Materials*, Prentice-Hall, 1997.

[430] G. U. Sumanasekera, B. K. Pradhan, H. E. Romero, K. W. Adu,P. C. Eklund, "Giant thermopower effects from molecular physisorption on carbon nanotubes," *Physical review letters*, vol. 89,no. 16, pp. 166801, 14 October 2002.

[431] L. F. Sun, S. S. Xie, W. Liu, W. Y. Zhou, Z. Q. Liu, D. S. Tsang, G. Wang, L. X. Qian, "Creating the narrowest carbon nanotubes," *Nature*, vol. 403, pp. 384, 2000.

[432] R. Szewczyk, J. Polastre, A. Mainwaring, D. Culler, "Lessons from a Sensor Network Expedition," *The First European Workshop on Wireless Sensor Networks* (EWSN '04), Berlin, Germany, January 19-21, 2004.

[433] S. Tachi, "Telexistence and retro-reflective projection technology," *Proceedings of the Fifth Virtual Reality International Conference* VRIC2003, pp. 69–77, May 2003.

[434] K. Tanaka, M. Abe, S. Ando, "A novel mechanical cochlea "fishbone" with dual sensor-actuator characteristics," *IEEE/ASME Transactions on Mechatronics*, vol. 3, no. 2, pp. 98–105, June 1998.

[435] W. C. Tang, T.-C. H. Nguyen, R. T. Howe, "Laterally driven polysilicon resonant microstructures," *SensorS and Actuators*, vol. 20, pp. 25–32, 1989.

[436] S. J. Tans, R. M. Verschueren, C. Dekker, "Room-temperature transistor based on a single carbon nanotube," *Nature*, vol. 393, pp. 49, 1998.

[437] R. Tarkiainen, M. Ahlskog, J. Penttilä, L. Roschier, P. Hakonen, M. Paalanen, E. Sonin, "Multiwalled carbon nanotube: Luttinger versus Fermi liquid," *Physical Review B*, vol. 64, pp. 195412–195415, 2001.

[438] C. Thelander, T. Mårtensson, M. T. Björk, B. J. Ohlsson, M. W. Larsson, L. R. Wallenberg, L. Samuelson, "Single-electron transistors in heterostructure nanowires," *Applied Physics Letters*, vol. 83, no. 10, pp. 2052–2054, 8 September 2003.

[439] A. Thess, R. Lee, P. Nikolaev, H. H. Dai, P. Petit, J. Robert, C. H. Xu, Y. H. Lee, S. G. Kim, A. G. Rinzler, D. T. Colbert, G. E. Scuseria, D. Tomanek, J. E. Fischer, R. E. Smalley, "Crystalline ropes of metallic carbon nanotubes," *Science*, vol. 273, pp. 483, 1996.

[440] D. Tománek, "Electrical and thermal transport in carbon nanotubes," *AIP Conference Proceedings*, vol. 544, no. 1, pp. 338–343, 21 November 2000.

[441] T. Tombler, C. Zhou, L. Alexeyev, J. Kong, H. Dai, L. Liu, C. Jayanthi, M. Tang, S. Y. Wu, "Reversible electromechanical characteristics of carbon nanotubes under local-probe manipulation," *Nature*, vol. 405, pp. 769, 2000.

[442] C. Toumazou, J. Ngarmnil, T. S. Lande, "Micropower log-domain filter for electronic cochlea," *IEEE Electronics Letters*, vol. 30, no. 22, pp. 1839–1841, 27 October 1994.

[443] M. M. Treacy, T. W. Ebbesen, J. M. Gibson, "Exceptionally high Young's modulus observed for individual carbon nanotubes," *Nature*, vol. 38, pp. 678–680, 1996.

[444] Y.-C. Tseng, P. Xuan, A. Javey, R. Malloy, Q. Wang, J. Bokor, H. Dai, "Monolithic Integration of Carbon Nanotube Devices with Silicon MOS Technology," *Nano Letters*, vol. 4 no. 1, pp. 123 -127, 2004.

[445] K. Tsukagoshi, B. W. Alphenaar, H. Ago, "Coherent transport of electron spin in a ferromagnetically contacted carbon nanotube," *Nature*, vol. 401, pp. 572–574, 07 Oct 1999.

[446] K. N. Tu, "Recent advances on electromigration in very-large-scale-integration of interconnects," *Journal of Applied Physics*, vol. 94, no. 9, pp. 5451–5473, 1 November 2003

[447] D. W. Utami, H.-S. Goan, G. J. Milburn, "Charge transport in a quantum electromechanical system," *Physical Review B*, vol. 70, pp. 075303–075312, 2004.

[448] G. C. Velmahos, R. Tatevossian, D. Demetriades, "The Seat Belt Mark Sign: A Call for Increased Vigilance Among Physicians Treating Victims of Motor Vehicle Accidents," *American Surgeon*, vol. 65, no. 2, pp. 181–185, 1999.

[449] G. Vemuri and R. Roy, "Stochastic resonance in a bistable ring laser," *Physical Review A*, vol. 39, no. 9, pp. 4668-4674, May 1989.

[450] M. Vetterli, J. Kovacevic, section 2.6.3, *Wavelets and Subband Coding*, Prentice Hall, Englewood Cliffs, New Jersey, 1995.

[451] J. de Vicente, M. T. Lpez-Lpez, F. Gonzlez-Caballero, J. D. G. Durn, "Rheological study of the stabilization of magnetizable colloidal suspensions by addition of silica nanoparticles," *Journal of Rheology*, vol. 47, pp. 1093, 2003.

[452] J. M. G. Vilar and J. M. Rubí, "Stochastic Multiresonance," *Physical Review Letters*, vol. 78, pp. 2882-2885, 1997.

[453] G. von Bksy, chapter 12, *Experiments in Hearing*, Translated and edited by E.G. Wever, New York, McGraw-Hill, 1960.

[454] D. W. Walsh, J. Hagen, "Body Armor: What It Is and What It Does," *Journal of Emergency Medical Services*, pp. 66–67, September 1994.

[455] Y. Wang, J. R. Cruz, "Performance enhancement of CDMA cellular systems with augmented antenna arrays," *IEEE Journal on Selected Areas in Communications*, vol. 19, no. 6, pp. 1052–1060, June 2001.

[456] D. Wang, F. Qian, C. Yang, Z. Zhong, C. M. Lieber, "Rational Growth of Branched and Hyperbranched Nanowire Structures," *Nano Letters*, vol. 4, no. 5, pp. 871–874, 2004.

[457] J. Wang, G. Liu, M. R. Jan, "Ultrasensitive Electrical Biosensing of Proteins and DNA: Carbon-Nanotube Derived Amplification of the Recognition and Transduction Events," *Journal of the American Chemical Society*, vol. 126, no. 10, pp. 3010–3011, 2004.

[458] Y. Wang, K. Kempa, B. Kimball, J. B. Carlson, G. Benham, W. Z. Li, T. Kempa, J. Rybczynski, A. Herczynski, Z. F. Ren, "Receiving and transmitting light-like radio waves: Antenna effect in arrays of aligned carbon nanotubes," *Applied Physics Letters*, vol. 85, pp. 2607, 2004.

[459] D. Wang, Q. Wang, A. Javey, R. Tu, H. Dai, H. Kim, P. C. McIntyre, T. Krishnamohan, K. C. Saraswat, "Germanium nanowire field-effect transistors with SiO2 and high- HfO2 gate dielectrics," *Applied Physics Letters*, vol. 83, no. 12, pp. 2432–2434, 22 September 2003.

[460] J. Wang, G. Liu, M. R. Jan, "Ultrasensitive Electrical Biosensing of Proteins and DNA: Carbon-Nanotube Derived Amplification of the Recognition and Transduction Events," *Journal of the American Chemical Society*, vol. 126, no. 10, pp.3010–3011, 2004.

[461] L. Watts, D. A. Kerns, R. F. Lyon, C. Mead, "Improved implementation of the silicon cochlea," *IEEE Journal of Solid-State Circuits*, vol. 27, no. 5, pp. 692–670, May 1992.

[462] B. Wei, R. Spolenak, P. Kohler-Redlich, M. Ruhle, E. Arzt, "Electrical transport in pure and boron-doped carbon nanotubes," *Applied Physics Letters*, vol. 74, no. 21, p. 3149–3151, May 1999.

[463] B. Q. Wei, R. Vajtai, P. M. Ajayan, ",Reliability and current carrying capacity of carbon nanotubes" *Applied Physics Letters*, vol. 79, no. 8, pp. 1172–1174, 2001

[464] B. Q. Wei, R. Vajtai, Y. Jung, J. Ward, R. Zhang, G. Ramanath, P. M. Ajayan, "Assembly of Highly Organized Carbon Nanotube Architectures by Chemical Vapor Deposition," *Chemical Materials*, vol. 15, no. 8, pp. 1598–1606, 2003.

[465] R. B. Weisman, "Simplifying carbon nanotube identification," *Industrial Physicist*, pp. 24–27, February/March 2004.

[466] L. Wenjie, M. Bockrath, D. Bozovic, J. H. Hafner, M. Tinkman, P. Hongkum, "Fabry-Perot interference in a nanotube electron waveguide," *Nature*, vol. 411, pp. 665-669, 2001.

[467] N. Weste, K. Eshraghian, *Principles of CMOS VLSI Design: A Systems Perspective, Second Edition, Reprint with Corrections*, Addison-Wesley, Menlo Park, California, 1994.

[468] D. R. Whaley, B. M. Gannon, C. R. Smith, C. M. Armstrong, C. A. Spindt, "Application of field emitter arrays to microwave power amplifiers," *IEEE Transactions on Plasma Science*, vol. 28, no. 3, pp. 727–747, June 2000.

[469] D. Whang, S. Jin, Y. Wu, C. M. Lieber, "Large-Scale Hierarchical Organization of Nanowire Arrays for Integrated Nanosystems," *Nano Letters*, vol. 3, no. 9, pp. 1255–1259, 2003.

[470] K. Wiesenfeld and F. Moss, "Stochastic resonance and the benefits of noise: From ice ages to Crayfish and SQUID's," *Nature*, vol. 373, pp. 33-36, January 1995.

[471] J. W. G. Wildoer, L. C. Venema, A. G. Rinzler, R. E. Smalley, C. Dekker, "Electronic structure of atomically resolved carbon nanotubes," *Nature*, vol. 391, pp. 59–62, 1998.

[472] S. Wind, J. Appenzeller, R. Martel, V. Derycke, P. Avouris, "Vertical scaling of single-wall carbon nanotubes transistors using top gate electrodes," *Applied Physics Letters*, vol. 80, pp. 3817, 2002.

[473] S. A. Wolf, D. D. Awschalom, R. A. Buhrman, J. M. Daughton, S. von Molnar, M. L. Roukes, A. Y. Chtchelkanova, D. M. Treger, "Spintronics: A Spin-Based Electronics Vision for the Future," *Science*, vol. 294, pp. 1488–1495, 16 November 2001.

[474] A.-C. Wong, C. T.-C. Nguyen, "Micromechanical mixer-filters ("Mixlers")," *Journal of Microelectromechanical Systems*, vol. 13, no. 1, pp. 100–112, February 2004.

[475] S. S. Wong, E. Joselevich, A. T. Woolley, C. L. Cheung, C. M. Lieber, "Covalently functionalized nanotubes as nanometre- sized probes in chemistry and biology," *Nature*, vol. 394, pp. 52–55, July 1998.

[476] E. W. Wong, P. E. Sheehan, C. M. Lieber, "Nanobeam mechanisms: elasticity, strength, toughness of nanorods and nanotubes," *Science*, vol. 277, pp. 1971–1975, 1997.

[477] P. V. Wright, "A review of SAW resonator filter technology," *IEEE Ultrasonics Symposium*, pp. 29–38, 1992.

[478] Y. Wu, J. Xiang, C. Yang, W. Lu, C. M. Lieber, "Single-crystal metallic nanowires and metal/semiconductor nanowire heterostructures," *Nature*, vol. 430, pp. 61–65, 2004.

[479] Y. Wu, Y. Cui, L. Huynh, C. J. Barrelet, D. C. Bell, C. M. Lieber, "Controlled Growth and Structures of Molecular-Scale Silicon Nanowires," *Nano Letters*, vol. 4, no. 3, pp. 433–436, 2004.

[480] Z. Wu, N. Tjandra, A. Bax, "^{31}P Chemical Shift Anisotropy as an Aid in Determining Nucleic Acid Structure in Liquid Crystals," *Journal of the American Chemical Society*, vol. 123, no. 15, pp. 3617–3618, 2001.

[481] Z. Xia, W. A. Curtin, B. W. Sheldon, "Fracture Toughness of Highly Ordered Carbon Nanotube/Alumina Nanocomposites," *Journal of Engineering Materials and Technology*, vol. 126, No. 3, pp. 238–244, July 2004.

[482] Z. Xia, L. Riester, W. A. Curtin, H. Li, B. W. Sheldon, J. Liang, B. Chang, J. M. Xu, "Direct observation of toughening mechanisms in carbon nanotube ceramic matrix composites," *Acta Materialia*, vol. 52, no. 4, pp. 931–944, 23 February 2004.

[483] J. Xu, "Nanotube electronics: non-CMOS routes," *Proceedings of the IEEE*, vol. 91, no. 11, pp. 1819–1829, November 2003.

[484] J. M. Xu, "Highly ordered carbon nanotube arrays and IR detection," *Infrared Physics and Technology*, vol. 42, pp. 485–491, 2001.

[485] Z. Yao, H. W. Ch. Postma, L. Balents, C. Dekker, "Carbon nanotube intramolecular junctions," *Nature*, vol. 402, pp. 273–276, 1999.

[486] M.-F. Yu, "Fundamental Mechanical Properties of Carbon Nanotubes: Current Understanding and the Related Experimental Studies," *Journal of Engineering Materials and Technology*, vol. 126, no. 3, pp. 271–278, July 2004.

[487] B. Yu, H. Wang, A. Joshi, Q. Xiang, E. Ibok, M.-R. Lin, "15 nm gate length planar CMOS transistor," in *Proceedings of the IEDM 2001*, pp. 937–939, 2001.

[488] Z. Yu, S. Li, P. J. Burke, "Synthesis of Aligned Arrays of Millimeter Long, Straight Single-Walled Carbon Nanotubes," *Chemical Materials*, vol. 16, no. 18, pp. 3414–3416, August 2004.

[489] G.-D. Zhan, J. D. Kuntz, J. Wan, A. K. Mukherjee, "Single-wall carbon nanotubes as attractive toughening agents in alumina-based nanocomposites," *Nature Materials*, vol. 2, no. 1, pp. 38–42, January 2003.

[490] Y. Zhang, A. Chang, J. Cao, Q. Wang, W. Kim, Y. Li, N. Morris, E. Yenilmez, J. Kong, H. Dai, "Electric-field-directed growth of aligned single-walled carbon nanotubes," *Applied Physics Letters*, vol. 79, pp. 3155–3157, 2001.

[491] J. Zhao, J. P. Lu, J. Han, C-K Yang, "Noncovalent functionalization of carbon nanotubes by aromatic organic molecules," *Applied Physics Letters*, vol. 82, no. 21, pp. 3746–3748, 2003.

[492] C. Zhou, J. Kong, H. Dai, "Transport measurements of individual semiconducting singled-walled carbon nanotubes of various diameters," *Applied Physics Letters*, vol. 76, pp. 1597, 2000.

[493] C. Zhou, J. Kong, H. Dai, "Intrinsic electrical properties of individual single-walled carbon nanotubes with small band gaps," *Physical Review Letters*, vol. 84, no. 24, pp. 5604–5607, 12 June 2000.

[494] C. Zhou, J. Kong, E. Yenilmez, H. Dai, "Modulated chemical doping of individual carbon nanotubes," *Science*, vol. 290, no. 5496, pp. 1552–1555, 2000.

[495] A. Zimina, S. Eisebitt, M. Freiwald, S. Cramm, W. Eberhardt, A. Mrzel,D. Mihailovic, "Electronic Structure of Subnanometer Diameter MoS2-Ix Nanotubes," *Nano Letters*, September 2004.

[496] A. M. Zoubir, B. Boashash, "The Bootstrap and Its Application in Signal Processing," *IEEE Signal Processing Magazine*, pp. 56–76, January 1998.

[497] U. Zülicke, A. H. MacDonald, "Plasmon modes and correlation functions in quantum wires and Hall bars," *Physical Review B*, vol. 54, no. 23, pp. 16813–16819, December 1996.

Appendix I

Modeling Gunshot Bruises in Soft-Body Armor with An Adaptive Fuzzy System

Abstract —- Gunshots produce bruise patterns on persons who wear soft body armor when shot even though the armor stops the bullets. An adaptive fuzzy system modeled these bruise patterns based on the depth and width of the deformed armor given a projectile's mass and momentum. The fuzzy system used rules with sinc-shaped if-part fuzzy sets and was robust against random rule pruning: Median and mean test errors remained low even after removing up to one fifth of the rules. Handguns shot different caliber bullets at armor that had a 10%-ordnance gelatin backing. The gelatin blocks were tissue simulants. The gunshot data tuned the additive fuzzy function approximator. The fuzzy system's conditional variance $V[Y|X = x]$ described the second-order uncertainty of the function approximation. Handguns with different barrel

lengths shot bullets over a fixed distance at armor-clad gelatin blocks that we made with Type 250A Ordnance Gelatin. The bullet-armor experiments found that a bullet's weight and momentum correlated with the depth of its impact on armor-clad gelatin ($R^2 = 0.881$ and p-value < 0.001 for the null hypothesis that the regression line had zero slope). Related experiments on Plumber's Putty showed that highspeed baseball impacts compared well to bullet-armor impacts for large-caliber handguns. A baseball's momentum correlated with its impact depth in putty ($R^2 = 0.93$ and p-value < 0.001). A bullet's momentum similarly correlated with its armor-impact in putty ($R^2 = 0.97$ and p-value < 0.001). A Gujarati-Chow test showed that the two putty-impact regression lines had statistically indistinguishable slopes for p-value $= 0.396$. Baseball impact depths were comparable to bullet-armor impact depths: Getting shot with a .22 caliber bullet when wearing soft body armor resembles getting hit in the chest with a 40-mph baseball. Getting shot with a .45 caliber bullet resembles getting hit with a 90-mph baseball.

I.1 Modeling Bullet-Armor Bruise Impacts

How does it feel to get shot while wearing soft body armor? One police officer described it as a sting while another officer described it as a "hard blow" [3]. Fig. 7.1 shows the bruise beneath the armor after a .44 caliber bullet struck a police officer's upper left chest. The armor stopped the bullet but the impact still injured soft tissue.

We examined the bruising effect with a fuzzy function approximator and a baseball analogy. Bullet impact experiments produced the bullet-armor bruise data that generated a quantitative bruise profile and a baseball-impact comparison. The bruise profile gave the depth and width of the deformation that a handgun bullet made on gelatin-backed armor for gelatin blocks that we made with Type 250A Ordnance Gelatin (from Kind & Knox Gelatin).

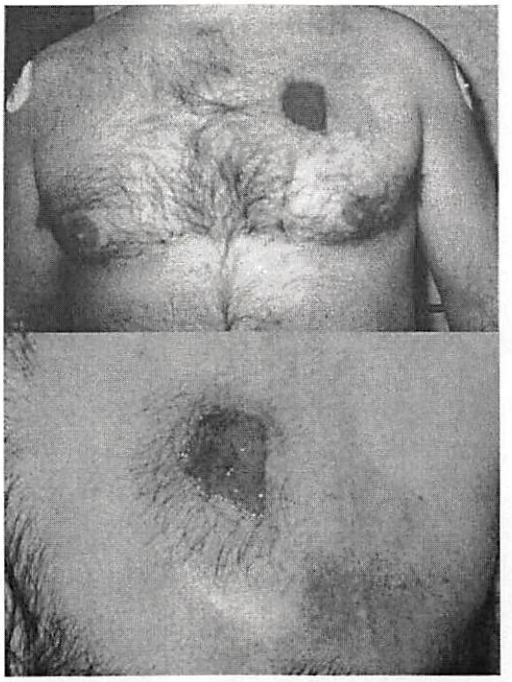

Figure 7.1: (a) Actual bruise from a police officer shot by a .44 caliber weapon in the line of duty while wearing soft body armor. (b) Close-up of the "backface signature" bruise in (a). Note that the bruise includes the discoloration around the wound. Photo reproduced with permission from the IACP/Du Pont Kevlar Survivors' Club.

Few researchers have studied the relationship between the bruising effect and the so-called *backface signature* or the deformation in the armor's backing material after a gunshot [226], [343]. Our bruise profile modeled the bullet-armor bruise with the depth and width of the deformation as a blunt object that could injure soft tissue. We quantified the bullet-armor impacts and baseball impacts on a common backing material–Plumber's Putty. The baseball analogy helped estimate gunshot impacts on armor. We found that a fast baseball could hit as hard as a large caliber handgun bullet on armor. The baseball and bullet impacts in putty had similar depths and statistically indistinguishable regression slopes.

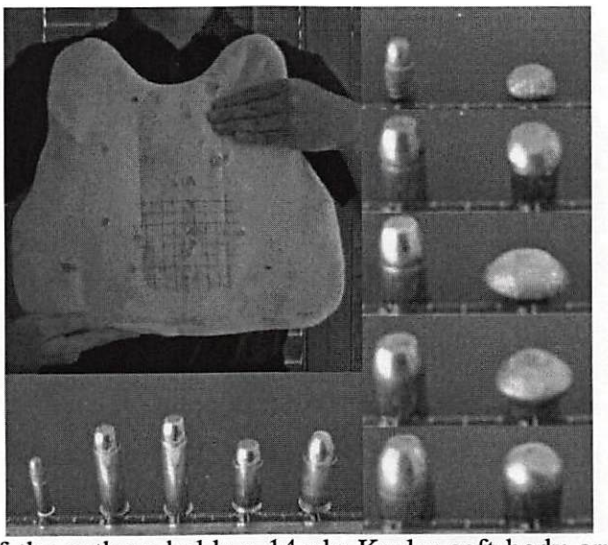

Figure 7.2: One of the authors holds a 14-ply Kevlar soft body armor panel (from a Superfeatherlite vest from Second Chance) and some sample cartridges (.22, .38, .357 magnum, .40, and .45 caliber). The right side of the image shows the pristine and armor-deformed bullets for the five calibers.

Soft Body Armor

An adaptive fuzzy system learned to model the depth and width of bruise profiles from the bullet-armor impact experiments. Two armor-impact experimental setups used gelatin blocks to simulate human tissue. A third armor-impact experimental setup used Plumber's Putty to record the bullet-armor deformation that compared with baseball impacts. The experiments confirmed the expectation that a bullet made a larger impact if it had a larger caliber or a larger momentum (see Table 7.1). But a larger and slower handgun bullet hit harder than a smaller and faster one in the experiments. Impact depth correlated better with momentum than with kinetic energy. This corroborated the finding that kinetic energy was not a good predictor of bullet penetration wounds [408].

We picked the initial rules based on our ballistic judgment and experience. The experimental data tuned the rules of an adaptive standard-additive-model (SAM) fuzzy system [252]. The SAM system used two scalar subsystems to model the depth and width of a bullet-armor impact in parallel given the bullet's weight and momentum. We

tested the robustness of the fuzzy system by removing rules in a random rule pruning. The median, mean, and maximal test errors resembled the initial approximation error for pruning that randomly removed up to 20% of the rules.

The next two sections review soft body armor and bullet-impact bruises. Section II reviews rule-based fuzzy function approximation. Section III reviews the standard additive model. Section IV provides the setup and results of the bullet-armor experiments. Section V provides the setup and results of the baseball impact experiments. Section VI provides the experimental setup and the results of the fuzzy function approximation.

Soft body armor prevents most handgun bullets from penetrating a user's body [454]. Our armor experiments used a generic armor that we made by combining many layers of fabric that wove together Kevlar fibers. Thinner armor is softer than thicker armor. Another type of armor material laminated together many layers of parallel fibers. Both types of armor deform under a bullet's impact and spread the impact's force over a wider area. Bullets penetrate by crushing [302]. So soft body armor arrests a handgun bullet by reducing its crushing force below a material-failure threshold [302].

Failure analysis does not consider the physiological effects as the armor stops a bullet. Some researchers define armor failure as material failure such as broken fibers or breached fabric layers [16], [303], [101], [84], [148]. Others require complete bullet passages [30]. Such definitions do not address the interactions that flexible armor permits with the underlying material.

These interactions have two effects. The first is that a bullet-armor impact can injure soft tissue even though the bullet does not penetrate the armor (see Fig. 7.1). The second effect is that soft body armor's performance can differ for different backing material that supports the armor [302]. We found that a hammer strike breached several layers of concrete-backed armor fabric but at least one handgun bullet bounced off gelatin-backed armor fabric.

DEPTH REGRESSION	R^2	β_0	β_1	$\mathbf{H}_0 : \beta_1 = 0$ t (p-value)
WEIGHT	0.880	5.385	0.280	19.892 ($p < 0.001$)
MOMENTUM	0.741	9.443	13.718	12.415 ($p < 0.001$)
KINETIC ENERGY	0.474	20.225	0.066	6.972 ($p < 0.001$)
SPEED	0.089	79.885	−0.124	−2.298 ($p = 0.025$)
TARGET DISTANCE	0.415	29.328	−1.203	−4.453 ($p < 0.001$)
WIDTH REGRESSION	R^2	β_0	β_1	$\mathbf{H}_0 : \beta_1 = 0$ t (p-value)
WEIGHT	0.865	84.816	0.421	18.580 ($p < 0.001$)
MOMENTUM	0.745	90.295	20.870	12.566 ($p < 0.001$)
KINETIC ENERGY	0.482	106.478	0.101	7.094 ($p < 0.001$)
SPEED	0.079	194.170	−0.177	−2.153 ($p = 0.036$)
TARGET DISTANCE	0.004	58.162	0.1082	0.340 ($p < 0.001$)

Table 7.1: Summary of linear regression statistics for the gelatin-backed bullet-armor impact experiments and for the simple linear model $y = \beta_0 + \beta_1 x$. Momentum mv and weight m correlated with an impact's depth and width while kinetic energy $\frac{1}{2}mv^2$ correlated the least. Target distance d correlated with an impact's depth while speed v and distance d correlated little with the impact's width. The R^2 measures the strength of the correlation between the input and output variables. The t statistic tested the parameter significance of a single regression coefficient β_1 between deformation (mm) and one of a bullet's mean weight (grain), momentum (kg m/s), kinetic energy (kg m^2/s^2), target distance (yard), and speed (m/s). The p-value measured the credibility of the null hypothesis $\mathbf{H}_0$ that the regression line had zero slope $\beta_1 = 0$ or that a dependent variable did not vary with the independent variable. A statistical test rejects the null hypothesis $\mathbf{H}_0$ at a significance level α if the p-value is less than that significance level. So the regression rejects the null hypothesis $\mathbf{H}_0$ for the customary significance levels $\alpha = 0.05$ and $\alpha = 0.01$ because p-value < 0.001.

The backface signature is the deformation in the backing material after a bullet strikes armor [343]. Studies of backface signatures [226] give little information about the impact as a bruising force if the backing material differs from soft tissue. One industry standard [343] measures the backface signature on a clay backing material. The clay records the impact in a plastic or permanent backface deformation but its properties differ from soft tissue.

Gelatin tissue simulant is elastic and responds to a bullet's crushing force similar to how soft tissue responds in bullet penetration tests [304], [305], [151]. So testing gelatin-backed soft body armor can help study the performance of the armor on a user's body. We performed the bullet-armor impact experiments on tissue simulant and defined a simple two-parameter bruise profile to describe the impact.

Bruising and the Bruise Profile

Bruising implies injury but need not indicate the severity of the injury. A bruise is escaped blood in the intercellular space after a blunt impact injures soft tissue [404]. The visible part of a bruise is the part of the escaped blood that is close to the skin surface. Scraping with a coin or a spoon can leave extensive but superficial bruises or welts that resemble bruises from abuse [169]. The visible bruise can change over time [426] at different rates based on sex, age, body fat [404], and medication [361]. So a bruise shows that a blunt impact occurred but need not show that internal injuries occurred [73], [448]. This can occur in sports injuries where soft tissue injuries can escape detection [214].

A bruise profile models the shape of the bullet-armor impact and can help guide the examination after an armor gunshot. This is similar to a wound profile [151] that can help the examination of a gunshot wound. The bruise profile can indicate the affected internal tissue beneath the visible armor bruise.

I.2 Bullet-Armor Impact Experiments Measure Armor Deformations

Experimental Setup

Two experimental setups measured the bullet-armor impacts' depths and widths against a gelatin-block backing in the Orange County Indoor Shooting Range. The first setup used donated commercial armor to produce the deformation data. It fixed the bullet caliber (9-mm) and varied the distance between the target and the handgun. The distances were 5, 7, and 10 yards. These three short distances produced three measurably different bullet impacts because air friction quickly slows a bullet after it leaves the gun barrel.

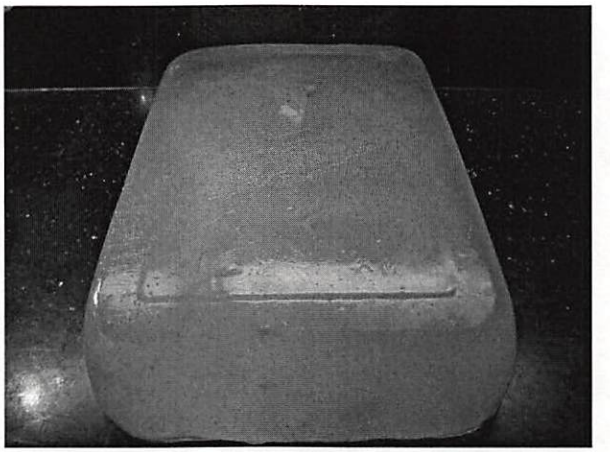

Figure 7.3: A sample 10% ordnance gelatin block. A target consisted of a generic armor-clad gelatin block. The gel block was the tissue simulant.

The second setup used generic armor that we made from eight layers of Kevlar fabric to produce the deformation data. It varied both the bullet caliber and the handguns' barrel lengths and fixed the distance (5 feet) between the target and the handguns. The setup used .22, .38, .40, and .45 caliber bullets. This choice of bullets gave a monotonic increase in bullet diameter and weight. We also used .357 magnum bullets that had weight similar to .38 caliber bullets and momentum similar to .45 caliber bullets due to higher speeds. A .44 magnum bullet penetrated the 8-layer generic armor. So we had no deformation data for the .44 magnum bullets. Hexcel Schwebel donated the Style 713 Aramid fabric that had 1000 deniers of Kevlar 29 fibers in plain weave.

The gel-backed experiments used 10% gelatin blocks to simulate tissue that backed the armor. Fig. 7.3 shows a sample gelatin block. The gelatin blocks consisted of one part Type 250A Ordnance Gelatin from Kind & Knox Gelatin and nine parts water by weight. We weighed the water-filled mold to find the 10% weight for the gelatin powder and weighed the mold while we added water to achieve the 1:9 ratio. Slowly stirring water into the gelatin powder reduced bubble formation. The mixture required refrigeration for 24 hours to prevent spoilage while the powder hydrated. This further

reduced air bubble formation. A warm water bath of about 40°C melted the mixture and prevented denaturing the gelatin. A cold water bath set the melted gelatin in molds that measured about 40 cm long by 30 cm wide by 12 cm thick.

Refrigeration hardened the gelatin blocks in 48–72 hours and ensured a uniform temperature of about 4°C in the blocks. The refrigerator ran for 24 hours before use to ensure that its temperature equilibrated in a range above freezing and below 4°C. This kept a gelatin block's temperature low while avoiding damage from ice crystals. We used ice chests to transport the gelatin blocks to and from the shooting range.

A BB shot calibrated each gelatin block before use by giving BB penetration at known temperatures. A model 760B BB Repeater Air Rifle from Crossman Air Guns can shoot a 5.5-grain BB at between 530–590 feet per second (ft/s) with 10 pumps. An outdoor thermometer measured the gelatin temperature before using the blocks.

We measured the bullet velocity at 12 feet or 3 yards and separate from the impact experiments. The Prochrono Plus optical chronometer from Competition Electronics complicated shot placement in the indoor shooting range. It required a separation of at least 10–15 feet from the handguns to prevent interference from the propellant smoke. The indoor lighting dictated a 12-ft separation between the chronometer and the handguns and a 58-inch separation between the chronometer and the floor. This was because the optical sensors required some minimal amount of light to detect a bullet's shadow as the bullet passed. The lack of a pistol holder allowed marksmanship to further complicate shot placement in the experiments.

The shooting range provided reloaded ammunition with full-copper-jacketed bullets. The 9-mm bullets weighed 115 grains on average. The mean velocity was 1216 feet per second (ft/s) for bullets from the same ammunition box. Table 7.2 shows the mean bullet speeds for each combination of bullet caliber and barrel length. The .22 caliber bullets had one mean weight (40 grains) and two different speeds (977 ft/s and 1059 ft/s on

		.22	.38	.40	.45	.357mag	.44mag
	WEIGHT	40	150	165	185	158	240
SPEED	Barrel 1	977	722	937	808	1135	1263
	Barrel 2	1059	751	N/A	897	N/A	N/A

Table 7.2: Average bullet speeds for the available combinations of bullet weight (caliber) and barrel length.

average). We used the data in Table 7.2 (except the .44 magnum bullets) for the weight and momentum that trained the fuzzy system.

Results of the Bullet-Armor Impact Experiments

The gelatin-backed bullet-armor experiments found that a bullet's impact depth correlated with it's distance to target d with the first setup and found that depth correlated with bullet properties that included the mean weight m, momentum $p = mv$, and kinetic energy $\frac{1}{2}mv^2$ in decreasing order with the second setup. Depth correlation with kinetic energy was much less than the correlations with weight or momentum. Impact depth also correlated with combinations of weight, momentum, and kinetic energy. The impact width similarly correlated with the bullet properties except distance. The impact depth and width correlated very little with a bullet's mean speed v. This held because the .45 caliber bullet-armor impacts were deeper and wider than both the .22 and .38 caliber impacts when the .22 caliber bullets were faster and the .38 caliber bullets were slower. Table 7.3 shows the regression statistics. The statistics were based on two subsets of the experimental data: Dataset (1) was complete and Dataset (2) excluded the .357 magnum data. The key results held for both datasets. Dataset (2) had stronger correlations (larger R^2) than Dataset (1). Deformation correlated with momentum more than it correlated with weight in Dataset (2).

Regression analysis fit the experimental data to a straight line. The simple linear model used functions of x and had smaller p-values than quadratic and cubic models while the quadratic and cubic models had marginally larger R^2 values. The R^2 measured

DEPTH REGRESSION	R^2	β_0	β_1	$H_0 : \beta_1 = 0$ t (p-value)	$H_0 : \beta_0, 1 = 0$ F (p-value)
WEIGHT (1)	0.880	5.385	0.280	19.892 ($p < 0.001$)	395.702 ($p < 0.001$)
(2)	0.893	5.424	0.283	19.210 ($p < 0.001$)	369.022 ($p < 0.001$)
MOMENTUM (1)	0.741	9.443	13.718	12.415 ($p < 0.001$)	154.135 ($p < 0.001$)
(2)	0.875	4.838	16.700	17.549 ($p < 0.001$)	307.966 ($p < 0.001$)
KINETIC ENERGY (1)	0.474	20.225	0.066	6.972 ($p < 0.001$)	48.606 ($p < 0.001$)
(2)	0.786	7.018	0.118	12.694 ($p < 0.001$)	161.138 ($p < 0.001$)
SPEED (1)	0.089	79.885	−0.124	−2.298 ($p = 0.025$)	5.280 ($p = 0.025$)
(2)	0.278	129.560	−0.314	−4.115 ($p < 0.001$)	16.929 ($p < 0.001$)
TARGET DISTANCE	0.415	29.328	−1.203	−4.453 ($p < 0.001$)	19.826 ($p < 0.001$)

WIDTH REGRESSION	R^2	β_0	β_1	$H_0 : \beta_1 = 0$ t (p-value)	$H_0 : \beta_0, 1 = 0$ F (p-value)
WEIGHT (1)	0.865	84.816	0.421	18.580 ($p < 0.001$)	345.214 ($p < 0.001$)
(2)	0.882	84.900	0.428	18.170 ($p < 0.001$)	330.141 ($p < 0.001$)
MOMENTUM (1)	0.745	90.295	20.870	12.566 ($p < 0.001$)	157.898 ($p < 0.001$)
(2)	0.906	82.612	25.844	20.589 ($p < 0.001$)	423.899 ($p < 0.001$)
KINETIC ENERGY (1)	0.482	106.478	0.101	7.094 ($p < 0.001$)	50.328 ($p < 0.001$)
(2)	0.851	84.692	0.186	15.842 ($p < 0.001$)	250.978 ($p < 0.001$)
SPEED (1)	0.079	194.170	−0.177	−2.153 ($p = 0.036$)	4.636 ($p = 0.036$)
(2)	0.220	258.890	−0.424	−3.521 ($p = 0.001$)	12.395 ($p = 0.001$)
TARGET DISTANCE	0.004	58.162	0.1082	0.340 ($p < 0.001$)	0.115 ($p = 0.737$)

DEPTH REGRESSION	R^2	β_0 t (p-value)	β_1 t (p-value)	β_2 t (p-value)	$H_0 : \beta_{0,1,2} = 0$ F (p-value)
WEIGHT AND (1)	0.881	5.550	0.304	−1.361	$F = 196.020$
MOMENTUM		2.616 ($p = 0.012$)	7.903 ($p < 0.001$)	−0.663 ($p = 0.510$)	$p < 0.001$
(2)	0.896	4.913	0.207	4.625	$F = 186.190$
		2.225 ($p = 0.031$)	2.988 ($p = 0.005$)	1.119 ($p = 0.270$)	$p < 0.001$
WEIGHT AND (1)	0.881	5.586	0.293	−0.006	$F = 196.851$
KINETIC ENERGY		2.638 ($p = 0.011$)	13.494 ($p < 0.001$)	−0.800 ($p = 0.427$)	$p < 0.001$
(2)	0.896	4.845	0.247	0.018	$F = 185.965$
		2.177 ($p = 0.035$)	6.782 ($p < 0.001$)	1.096 ($p = 0.279$)	$p < 0.001$
MOMENTUM AND (1)	0.887	5.574	31.388	−0.112	$F = 208.555$
KINETIC ENERGY		2.704 ($p = 0.009$)	13.943 ($p < 0.001$)	−8.305 ($p < 0.001$)	$p < 0.001$
(2)	0.897	5.348	29.484	−0.097	$F = 186.838$
		2.418 ($p = 0.020$)	6.810 ($p < 0.001$)	−3.015 ($p = 0.004$)	$p < 0.001$

WIDTH REGRESSION	R^2	β_0 t (p-value)	β_1 t (p-value)	β_2 t (p-value)	$H_0 : \beta_{0,1,2} = 0$ F (p-value)
WEIGHT AND (1)	0.865	84.846	0.425	−0.240	$F = 169.430$
MOMENTUM		24.742 ($p < 0.001$)	6.846 ($p < 0.001$)	−0.073 ($p = 0.942$)	$p < 0.001$
(2)	0.908	82.646	0.093	20.438	$F = 211.752$
		26.075 ($p < 0.001$)	0.932 ($p = 0.356$)	−0.073 ($p = 0.001$)	$p < 0.001$
WEIGHT AND (1)	0.865	84.967	0.431	−0.004	$F = 169.917$
KINETIC ENERGY		24.804 ($p < 0.001$)	12.261 ($p < 0.001$)	−0.370 ($p = 0.713$)	$p < 0.001$
(2)	0.907	82.342	0.267	0.078	$F = 209.355$
		25.661 ($p < 0.001$)	5.086 ($p < 0.001$)	3.361 ($p = 0.002$)	$p < 0.001$
MOMENTUM AND (1)	0.883	84.603	46.864	−0.165	$F = 200.376$
KINETIC ENERGY		26.588 ($p < 0.001$)	13.486 ($p < 0.001$)	−7.914 ($p < 0.001$)	$p < 0.001$
(2)	0.908	82.866	32.226	−0.048	$F = 212.991$
		26.139 ($p < 0.001$)	5.192 ($p < 0.001$)	−1.050 ($p = 0.300$)	$p < 0.001$

Table 7.3: Linear regression statistics for the gelatin-backed bullet-armor impact experiments. The statistics were based on two subsets of the experimental data: Dataset (1) was complete and Dataset (2) excluded the .357 magnum data. The key results held for both datasets. First was that deformation depth and width correlated with a bullet's weight, momentum, and kinetic energy while speed correlated little. Second was that kinetic energy had a weaker correlation with deformation than either weight or momentum. A bullet's weight monotonically increased with its caliber in Dataset (2) and could represent caliber by excluding the magnum data. Dataset (2) had stronger correlations (larger R^2) than Dataset (1). Momentum correlated with deformation more than weight in (2).

the strength of the correlation between the dependent and the independent variables. The first gel-backed experiments used a regression equation of the form

$$y = \beta_0 + \beta_1 x \tag{7.1}$$

where y was the deformation depth or width in millimeters (mm) and x was the distance between the target and the handgun in yards.

The second gel-backed experiments used the simple linear regression equation (7.1) to model how deformation depends on the individual bullet properties such as mean weight, speed, momentum, and kinetic energy. Multiple linear regression modeled how deformation depends on weight, momentum, and kinetic energy. The multiple regression equation had the form

$$y = \beta_0 + \beta_1 x_1 + \beta_2 x_2 \tag{7.2}$$

where y was the deformation depth or width in mm and x_1 and x_2 were the weights in grains, momentum in kilograms meter per second (kg m/s), or kinetic energy in kilograms meter squared per second squared (kg m^2/s^2).

We applied the simple linear model in (7.1) to test whether bullet deformation correlated with each of a bullet's properties. The null hypothesis $\mathbf{H}_0 : \beta_1 = 0$ stated that the slope β_1 of the regression line in (7.1) was zero and thus the impact deformation's depth and width (dependent variables) did not vary with a bullet's weight, momentum, kinetic energy, speed, or distance to target (independent variables). The p-value measures the credibility of $\mathbf{H}_0$. A statistical test rejects the null hypothesis $\mathbf{H}_0$ at a significance level α if the p-value is less than that significance level: Reject $\mathbf{H}_0$ if p-value $< \alpha$. The test rejected the null hypothesis $\mathbf{H}_0$ at the standard significance levels $\alpha = 0.05$ and $\alpha = 0.01$ because p-value < 0.001.

We applied the multiple regression in (7.2) for combinations of a bullet's property such as weight and momentum and tested the null hypothesis $\mathbf{H}_0 : \beta_i = 0$ for $i = 0, 1, 2$ that all the parameters were statistically insignificant. This tested whether the deformation's depth and width varied with the combination of a bullet's weight and

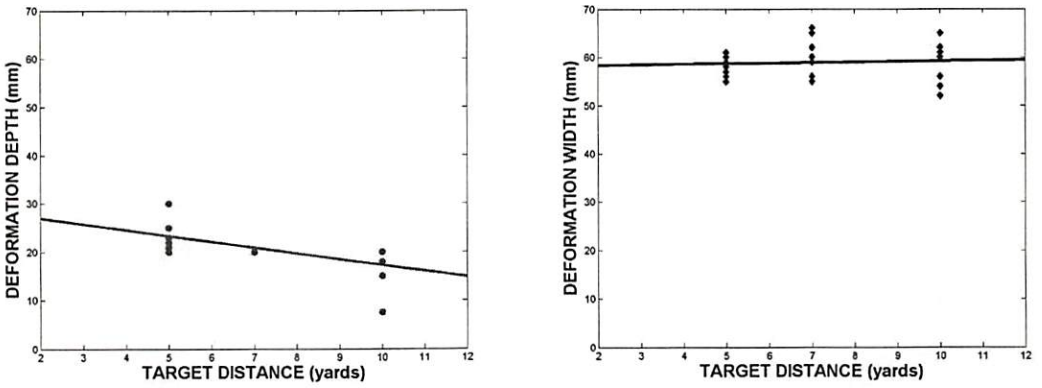

(a) DEPTH (b) WIDTH

Figure 7.4: Impact data from the first gelatin-backed bullet-armor experiments. (a) The impact depth correlates with distance to target. The correlation was $R^2 = 0.415$ and linear regression gave $y_1 = 29.328 - 1.203x$ with p-value < 0.001 where x was the distance in yards and y_1 was the deformation depth in mm. (b) The impact width correlates poorly with distance: $R^2 = 0.004$. The regression equation was $y_2 = 58.162 + 0.1082x$. Note that the regression line is nearly horizontal.

momentum. The test found that the regression coefficient for weight was statistically more significant than the coefficients for momentum or kinetic energy (see Table 7.3). This helped guide our choice of weight and momentum as the inputs of the fuzzy system.

Fig. 7.4 shows the depth and the width of the bullet-armor deformation after each impact in the first gelatin-backed experiments. The deformation depth decreased as target distance increased. Linear regression (see Table 7.3) gave $R^2 = 0.415$, regression equation $y_1 = 29.328 - 1.203x$, and p-value < 0.001 where x was the distance in yards and y_1 was the deformation depth in mm. The width y_2 did not appear to vary with target distance for $R^2 = 0.004$, $y_2 = 58.162 + 0.1082x$, and p-value < 0.001. These statistics suggested a non-zero slope but almost no correlation for $R^2 = 0.004$. The correlations between deformation and target distance also held for between deformation and momentum because bullet weight was approximately constant and velocity was

a monotonic function of distance. The limited number of data points was due to the availability of the donated armor. The shots should overlap as little as possible and avoid the armor panel edges for consistency. Marksmanship further decreased the number of shots as distance increased.

Fig. 7.5 shows the complete deformation depth data in (a) and the complete width data in (b) of the bullet-armor deformation as a function of bullet weight and momentum in the second gelatin-backed experiments. The regression planes suggested that depth correlated with bullet momentum more than weight and that width correlated with weight more than momentum. Excluding the magnum data in (c) and (d) changed the depth regression plane: It suggested that deformation depth correlated with both a bullet's weight and momentum. The correlation strengths were $R^2 = 0.881$ for the depth and $R^2 = 0.865$ for the width using the complete set of experimental data. The depth equation was $y_1 = 5.550 + 0.304x_1 - 1.361x_2$ where x_1 was bullet weight (grain) and x_2 was momentum (kg m/s). The width equation was $y_2 = 84.846 + 0.425x_1 - 0.240x_2$. The test statistics for depth correlation were $F = 196.020$ and p-value < 0.001. The test statistics for width correlation were $F = 169.430$ and p-value < 0.001. The test rejected the null hypothesis $\mathbf{H}_0$ at the standard significance levels $\alpha = 0.05$ and $\alpha = 0.01$.

The experiments used five bullet calibers (.22, .38, .40, and .45 caliber and .357 magnum, see Fig. 7.2) and two different speeds (such as on average 808 ft/s and 897 ft/s for the .45, see Table 7.2) per caliber to produce 56 sets of input-output data. This gave the sparse sampling of the input space in Fig. 7.5.

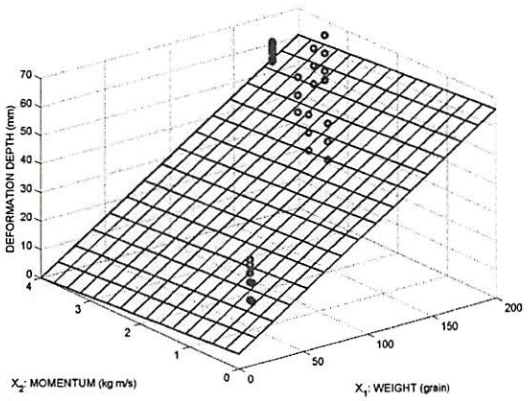

(a) DEPTH

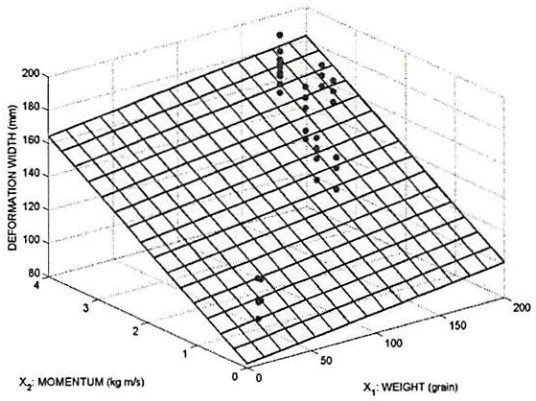

(b) WIDTH

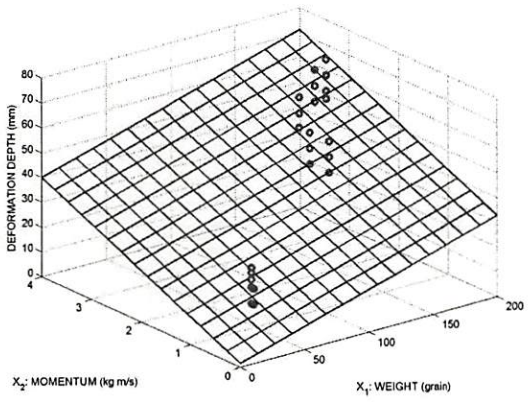

(c) DEPTH EXCLUDE MAGNUM

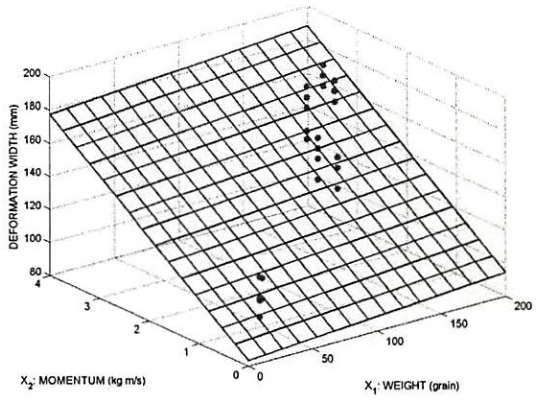

(d) WIDTH EXCLUDE MAGNUM

Figure 7.5: Impact data from the second gelatin-backed bullet-armor experiments. The figures show the complete set of experimental depth data in (a) and width data in (b) and their fit to regression planes as functions of weight (X_1) and momentum (X_2). (c) and (d) show a subset of the data that excluded the .357 magnum experiments. The regression planes consist of those points that satisfy the regression equations: $y_1 = 5.550 + 0.304x_1 - 1.361x_2$ for depth in (a), $y_2 = 84.846 + 0.425x_1 - 0.240x_2$ for width in (b), $y_1 = 4.913 + 0.207x_1 + 4.625x_2$ for depth in (c), and $y_2 = 82.646 + 0.093x_1 + 20.438x_2$ for width in (d).

I.3 Baseball Impact Experiments Compare Handgun Bullets and Baseballs

Experimental Setup

Two putty-backed experimental setups compared the baseball impacts to bullet-armor impacts. The baseball setup measured baseball impacts on tubs of Oatey's Plumber's

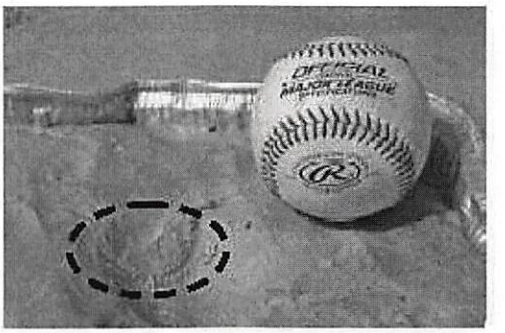

Figure 7.6: A regulation baseball and a crater of its impact. Pitching machines threw baseballs at tubs of Plumber's Putty. A chronograph measured the speed of each baseball. The baseball speeds were approximately 40, 50, 60, 70, 80, and 90 miles per hour.

Putty at the Home Run Park in Anaheim, California. The outdoor batting cage used pitching machines that threw baseballs at 40, 50, 60, 70, 80, and 90 miles per hour (mph). The chronometer used sunlight and a baseball's passing shadow to measure the baseball speed. We placed the chronometer approximately a half foot from the putty target. The putty-filled tubs were approximately three to five feet from the pitching machines. Each tub consisted of at least 15 pounds of the putty. Fig. 7.6 shows one sample deformation that a baseball made in putty.

The bullet-armor setup shot bullets at putty-backed soft body armor. The experiments shot .22, .38, .40, and .45 caliber bullets and .357 magnum and .44 magnum bullets. The armor was the Superfeatherlite model from Second Chance. The target was 5 feet from the handguns. Fig. 7.7 shows the depths of the putty deformations from baseball impacts next to the depths of the putty deformations from bullet-armor impacts. The deformations deepened as baseball speeds increased and as bullet caliber increased. The baseball impact experiments used regulation baseballs (Fig. 7.6) to produce at least 10 data points for each of the six different speeds. The putty deformed and recorded each impact. The baseballs' weight was constant so plotting the deformation depth against momentum preserved the proportion of plotting against speed. We plotted depth against

Bullet Caliber	.22	.38	.40	.357	.45	.44
Depth (mm)	5	15	19	21	22	40
Baseball Speed (mph)	40	70	80	90		n/a
Depth (mm)	6.5	13.6	17.0	21.6		n/a

Table 7.4: Baseballs deformed Plumber's Putty similar to handgun bullets. For instance: The mean impact depth was 21.6 mm for 90-mph baseballs and the bullet-armor impact depth was 21 mm for a .357 magnum bullet and 22 mm for a .45 caliber bullet. The .44 magnum bullet-armor impact deformed the putty to a depth of 40 mm that was about twice the effect of the fastest baseball available so had no comparable highspeed baseball impact.

momentum in Fig. 7.7 because the gelatin-backed bullet-armor experiments found that momentum correlated better with deformation depth than it correlated with weight or speed alone.

Results of the Baseball Impact Experiments

The baseball experiments compared bullet-armor impacts to baseball impacts in two ways: Deformation depth in putty and the slopes of the fitted regression lines. The first way compared how the two types of projectile deformations differed. Baseball impacts and bullet-armor impacts had similar depths in Oatey's Plumber's Putty (Table 7.4). The similarity of impact depths suggested that handgun shots on soft body armor would feel like baseball impacts without armor. Fast-baseball impact depths were comparable to bullet-armor impact depths: Getting shot with a .22 caliber bullet when wearing soft body armor resembles getting hit on the chest with a 40-mph baseball. Getting shot with a .45 caliber bullet resembles getting hit with a 90-mph baseball.

Fast baseballs were similar to large caliber bullets (on armor) in denting putty (see Fig. 7.7) except for the .44 magnum. The .44 magnum dented the putty to a 40 mm-depth or about twice the depth of the 90-mph baseballs. The 90-mph baseballs made 21.6 mm-deep dents in putty on average. This is similar to the depths of the dents from a .40 caliber (19 mm), a .45 caliber (22 mm), and a .357 magnum (21 mm) bullets. A

.38 caliber bullet made a 15-mm-deep dent in armor-clad putty. This depth is between the mean depth values of the 70-mph (13.6 mm) and the 80-mph (17 mm) baseballs. Table 7.4 summarizes these results.

The second way compared the correlation and regression slopes of the two types of impacts. The experiments found that the mean depth of a baseball's impact and the depth of a bullet's armor-impact both correlated with projectile momentum (see Fig. 7.7). The baseball impacts had correlation $R^2 = 0.93$, regression equation $y = -6.155 + 5.188x$, and p-value < 0.001 where x was a baseball's momentum in kilograms meter per second (kg m/s) and y was the putty deformation depth in millimeters (mm). The bullet-armor impacts had similar correlation $R^2 = 0.97$, regression equation $y = -2.12 + 4.76x$, and p-value < 0.001.

The putty-impact regression lines had similar slopes $\beta_1 \approx 5$ for the baseball impacts ($\beta_1 = 5.188$) and the bullet-armor impacts ($\beta_1 = 4.766$). Fig. 7.7 suggests that the two lines are parallel: Same slope with different intercepts. But the multiple-regression-based Chow test [389], [85] gave only that the two regression lines differed for $F = 61.826$, degrees of freedom $(2, 62)$, and p-value < 0.001. So we applied a modified Chow test (Gujarati-Chow test [189]) to test whether the slope terms β_1 differed, the intercept terms β_0 differed or both.

The Gujarati-Chow test was a multiple regression analysis with a dummy variable approach [389], [189] that compared two groups of data. It used a binary dummy variable D (see Appendix) to test separately whether the slope terms β_1 differed and whether the intercept terms β_0 differed. The slope-term (β_1) test statistics were $t = 0.855$ and p-value $= 0.396$. The two putty-impact regression lines had statistically indistinguishable slopes because we retained the null hypothesis that the slope terms were identical at the standard significance levels $\alpha = 0.05$ and $\alpha = 0.01$. This confirmed

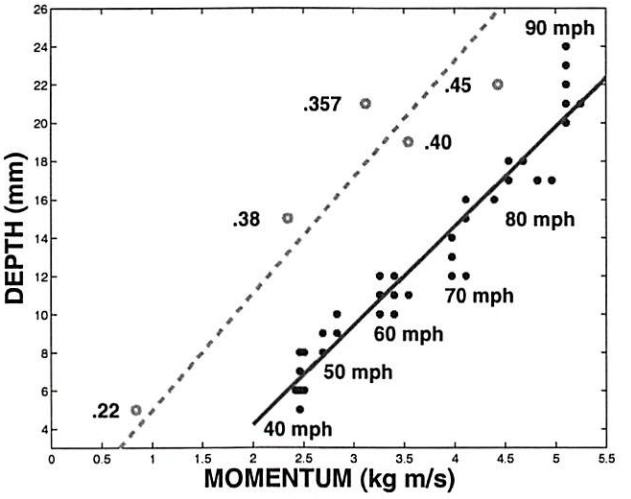

Figure 7.7: Baseball and bullet impact depths in Plumber's Putty versus momentum. The baseball impact depth correlated with baseball momentum $R^2 = 0.93$ and p-value < 0.001 for the null hypothesis: $\beta_1 = 0$. The solid line on the right is the regression line for the baseball impacts (blue dots) $y = -6.155 + 5.188x$ where x is baseball momentum and y is putty deformation depth. Only two data points fell outside of the 95% confidence bounds. Bullet-armor impact depths correlated with bullet momentum $R^2 = 0.97$. The green dashed line on the left is the regression line for the bullet-armor impacts (green circles) $y = 2.124 + 4.766x$ where x is bullet momentum and y is depth. The two regression lines have the similar slope $\beta_1 \approx 5$. A multiple regression analysis with dummy variables (Gujarati-Chow test) could not reject the null hypothesis $H_0 : \beta_1(\text{baseball}) = \beta_1(\text{armor})$ for the test statistics $t = 0.855$ and p-value $= 0.396$. So the test retained the null hypothesis that the two types of impacts had the same slope.

that the putty-backed baseball impacts and the bullet-armor impacts had the same slope β_1 in their regression lines as Fig. 7.7 suggested.

The intercept-term (β_0) test statistics were $t = -4.995$ and p-value < 0.001. The putty-impact regression lines had statistically distinct intercepts because we rejected the null hypothesis that the intercept terms were identical at the standard significance levels $\alpha = 0.05$ and $\alpha = 0.01$. This confirmed the Chow-test result that the two regression lines were distinct.

We note that the regulation baseball's constant weight implied that the correlation between deformation and speed was the same as the correlation between deformation

(a) DEPTH RULES	X_2: MOMENTUM							
	VS	SM	MS	MD	ML	LG	VL
X_1 WEIGHT	VL	MD	MD	MD	LG	LG	LG	VL
	LG	MD	MD	MD	LG	LG	LG	VL
	ML	MD	MD	MD	MD	MD	MD	LG
	MD	SM	MD	MD	MD	MD	MD	LG
	MS	SM	SM	SM	SM	SM	MD	LG
	SM	SM	SM	SM	SM	SM	MD	MD
	VS	VS	VS	VS	SM	SM	MD	MD

(b) WIDTH RULES	X_2: MOMENTUM							
	VS	SM	MS	MD	ML	LG	VL
X_1 WEIGHT	VL	MD	MD	MD	MD	LG	LG	VL
	LG	SM	SM	MD	SM	LG	LG	VL
	ML	SM	SM	SM	SM	MD	LG	VL
	MD	SM	SM	SM	SM	MD	MD	LG
	MS	VS	VS	VS	VS	SM	MD	LG
	SM	VS	VS	VS	VS	SM	MD	MD
	VS	VS	VS	VS	VS	SM	MD	MD

(c) THEN-PART DISPERSION	X_2: MOMENTUM							
	VS	SM	MS	MD	ML	LG	VL
X_1 WEIGHT	VL	LG	LG	MD	MD	LG	MD	SM
	LG	LG	LG	MD	MD	MD	SM	SM
	ML	LG	MD	MD	MD	MD	SM	SM
	MD	MD	MD	MD	SM	SM	SM	SM
	MS	MD	MD	MD	SM	SM	SM	MD
	SM	SM	SM	MD	MD	MD	LG	LG
	VS	SM	SM	MD	MD	MD	LG	LG

Table 7.5: Initial fuzzy rules for the function approximation. Each entry represented one rule for the depth subsystem in (a) and width subsystem in (b). We based the 49 initial fuzzy rules for the armor-deformation depth and width on the experimenters' ballistic judgment and experience. The rules had two-dimensional if-part sets and two parallel scalar then-part sets. A typical rule (highlighted) had the word form "If the bullet's weight X_1 is medium small (MS) and the momentum X_2 is medium (MD) then the armor deformation depth Y_1 is small (SM) and the width Y_2 is very small (VS)." The then-part set functions b_j had center parameters c_j based on the entries in (a) and (b). The area parameters V_j were based on the entries in (c). Seven if-part fuzzy sets described the bullet's weight and momentum {Very Small (VS), SMall (SM), Medium Small (MS), MeDium (MD), Medium Large (ML), LarGe (LG), Very Large (VL)}. Five then-part fuzzy sets described the armor deformation {VS, SM, MD, LG, VL}. Three volume or area values in (c) described the rule uncertainty {SM, MD, LG} by fixing the dispersion or width of the then-part sets.

and momentum. This corroborated the results from the first gelatin-backed bullet-armor experiments.

I.4 Fuzzy Systems Analyze Gunshot Armor Bruise

Adaptive Fuzzy Systems

Bullet-impact experiments trained an adaptive fuzzy system to model the depth and width of the bullet-armor impact given a handgun bullet's weight and momentum.

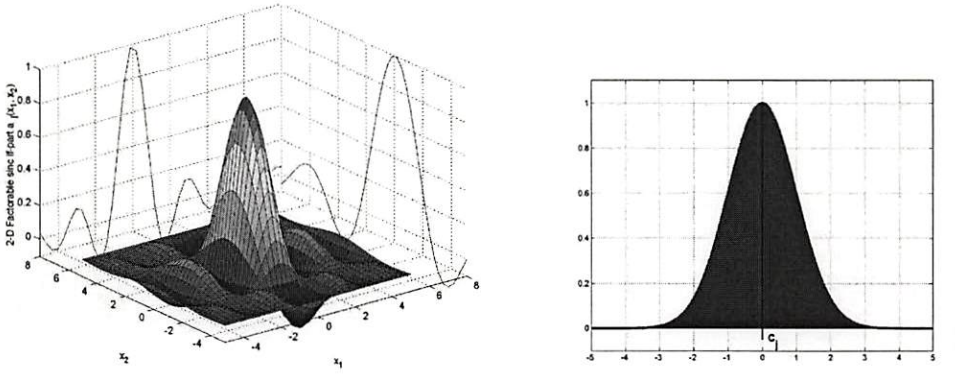

(a) SAMPLE IF-PART SET (b) SAMPLE THEN-PART SET

Figure 7.8: Sample if-part and then-part fuzzy sets. (a) Joint (product) sinc if-part set function for two-dimensional input case [24]. The joint set function has the factorable form $a_j(x) = a_j(x_1, x_2) = a_j^1(x_1) \times a_j^2(x_2)$. The shadows show the scalar sinc set functions $a_j^i : R \rightarrow R$ for $i = 1, 2$ that generate $a_j : R^2 \rightarrow R$. (b) Scalar Gaussian then-part set function centered at c_j.

We picked the fuzzy system's initial rules in Table 7.5 based on the correlations in the experimental data (Table 7.1) and based on our ballistic judgment and experience. Similar rules described the depth and width subsystems. A typical rule in Table 7.5 was "If a bullet's weight is small (SM) and its momentum is very small (VS) then the armor deformation depth is SM and the width is VS." A rule's volume (or dispersion) reflected its uncertainty. The gunshot data tuned the rules in an adaptive standard-additive-model (SAM) function approximation.

We applied two scalar-valued additive fuzzy systems [252], [334] $F : R^n \rightarrow R^p$ (for $p = 1$) in parallel that used two-dimensional inputs ($n = 2$) to model the depth and width of a bullet-armor impact. These systems approximated some unknown function $f : R^2 \rightarrow R$ by covering the graph of f with m fuzzy rule patches and averaging patches that overlap. An if-then rule of the form "If X is A then Y is B" defined a fuzzy Cartesian patch $A \times B$ in the input-output space $X \times Y$. The rules could use fuzzy sets of any shape for either their if-part sets A or then-part sets B. This held for the feedforward

standard additive model (SAM) fuzzy systems discussed below. Their generality further permitted any scheme for combining if-part vector components because all theorems assumed only that the set function mapped to numbers as in $a : R^n \rightarrow [u, v]$. Fig. 7.8 shows a sample two-dimensional if-part set that used a joint factorable sinc function. The general fuzzy approximation theorem allows any choice of if-part sets or then-part sets for a general additive model and specifically allows any choice of if-part sets for the SAM case (which in turn includes most fuzzy systems in use) [334]. These nonlinear systems can approximate any continuous (or bounded measurable) function on a compact domain [252].

The if-part fuzzy sets $A_j \subset R^n$ and then-part fuzzy sets $B_j \subset R^p$ had set functions $a_j : R^2 \rightarrow [0, 1]$ and $b_j : R \rightarrow [0, 1]$ for $n = 2$ and $p = 1$. An additive fuzzy system [252], [334] summed the "fired" then-part sets B'_j

$$B(x) \quad = \quad \sum_{j=1}^{m} w_j B'_j \quad = \quad \sum_{j=1}^{m} w_j a_j(x) B_j. \tag{7.3}$$

The scaling choice $B'_j = a_j(x)B_j$ gave an SAM. The SAM output F was the centroid of $B(x)$ in (7.3): $F(x) = \text{Centroid}\,(B(x))$.

The shape of if-part sets A_j affected how well the feedforward SAM output F approximates a function f and how quickly an adaptive SAM output F approximated it when learning based on input-output samples from f tuned the parameters of A_j and the centroids c_j and volumes V_j of the then-part set B_j. The shape of the then-part sets B_j did not affect the *first-order* behavior of a feedforward SAM output F beyond the

effect of the volume V_j and centroid c_j. This held because the SAM output computed a convex-weighted sum of the then-part centroids c_j for each vector input x

$$F(x) = \frac{\sum_{j=1}^{m} w_j a_j(x) V_j c_j}{\sum_{j=1}^{m} w_j a_j(x) V_j} \tag{7.4}$$

$$= \sum_{j=1}^{m} p_j(x) c_j = E[Y|X = x] \tag{7.5}$$

for if-part joint set function $a_j : R^n \to [0, 1]$ that defined the if-part set $A_j \subset R^n$, rule weights $w_j \geq 0$, $p_j(x) \geq 0$, and $\sum_{j=1}^{m} p_j(x) = 1$ for each $x \in R^2$. Fig. 7.9(a) and 7.9(c) are examples of the SAM output F based on the rules in Table 7.5 with two-dimensional joint factorable sinc if-part set functions. The convex coefficient

$$p_j(x) = \frac{w_j a_j(x) V_j}{\sum_{i=1}^{m} w_i a_i(x) V_i} \tag{7.6}$$

depended on then-part set B_j only through its volume or area V_j (and perhaps through its rule weight w_j).

The fuzzy output $F(x)$ in (7.4) equals the conditional expectation $E[Y|X = x]$ in (7.5) because the then-part set functions b_j are non-negative and have finite volume (area) and because $F(x)$ is the centroid of $B(x)$. Appendix II shows that these two conditions give a well-defined conditional probability density function $p(y|x)$ in $F(x) = \int_{-\infty}^{\infty} yp(y|x)dy$ [252]. So the SAM output describes the *first-order* behavior of the fuzzy system and does not depend on the shape of the then-part sets B_j. But the shape of

B_j did affect the *second-order* uncertainty or conditional variance $V[Y|X = x]$ of the SAM output $F(x)$ [252]:

$$V[Y|X = x] = \sum_{j=1}^{m} p_j(x)\sigma_{B_j}^2 + \sum_{j=1}^{m} p_j(x)[c_j - F(x)]^2 \tag{7.7}$$

where $\sigma_{B_j}^2$ is the then-part set variance

$$\sigma_{B_j}^2 = \int_{-\infty}^{\infty} (y - c_j)^2 p_{B_j}(y)dy \tag{7.8}$$

where $p_{B_j}(y) = b_j(y)/V_j$ is an integrable probability density function and $b_j : R \rightarrow [0, 1]$ is the integrable scalar set function of then-part set B_j. Fig. 7.9(b) and 7.9(d) show examples of the conditional variance $V[Y|X = x]$ based on the rules in Table 7.5 with Gaussian then-parts. The first term on the right side of (7.7) gave an input-weighted sum of the then-part set uncertainties. The second term measured the *interpolation penalty* that resulted from computing the SAM output $F(x)$ in (7.4) as the weighted sum of centroids. The second-order structure of a fuzzy system's output depended crucially on the size and shape of the then-part sets B_j.

Learning tuned the volumes V_j and centroids c_j of the then-part sets B_j in our adaptive function-approximation. The adaptive SAM fuzzy system learned from data with learning laws that updated the fuzzy rules so as to reduce the squared error of the function approximation. The two-dimensional joint factorable sinc if-part (see Fig. 7.8(a)) had learning laws that updated the two-dimensional vector center m_j and dispersion (or width) d_j parameters:

$$\begin{aligned} m_j^k(t+1) = & \quad m_j^k(t) \\ & + \mu_t \varepsilon_t \frac{p_j(x)}{a_j(x)} \frac{a_j(x)}{a_j^k(x_k)} (c_j - F(x))(a_j(x) - \cos(\frac{x - m_j^k(t)}{d_j(t)})) \frac{1}{x - m_j^k(t)} \end{aligned} \tag{7.9}$$

$$d_j^k(t+1) = d_j^k(t) + \mu_t \varepsilon_t \frac{p_j(x)}{a_j(x)} \frac{a_j(x)}{a_j^k(x_k)} (c_j - F(x))(a_j(x) - \cos(\frac{x - m_j^k(t)}{d_j(t)})) \frac{1}{d_j^k(t)} \quad (7.10)$$

where μ_t was a learning rate at iteration t and ε_t was the approximation error or the difference between the fuzzy output $F(x)$ and the approximand f. The Gaussian then-part parameters had learning laws that updated the scalar centroid c_j and volume V:

$$c_j(t+1) = c_j(t) + \mu_t \varepsilon_t(x) p_j(x) \quad (7.11)$$

$$V_j(t+1) = V_j(t) - \mu_t \varepsilon_t(x) \frac{p_j(x)}{V_j} [c_j - F(x)] \quad (7.12)$$

where the volume or area of a scalar Gaussian then-part set was a function of the standard deviation: $V = \sqrt{2\pi\sigma_{B_j}^2} = \sigma_{B_j}\sqrt{2\pi}$. This related the dispersion or width of a then-part set to its volume and so related the volume parameter V to the set variance $\sigma_{B_j}^2$ that contributed to the conditional variance.

Fuzzy systems $F : R^n \rightarrow R^p$ suffer from rule explosion in high dimensions. A fuzzy system F needs on the order of k^{n+p-1} rules to cover the graph and thus to approximate a vector function $f : R^n \rightarrow R^p$. Optimal rules can help deal with the exponential rule explosion. Lone or local mean-squared optimal rule patches cover the extrema of the approximand f: They patch the bumps [252]. Better learning schemes move rule patches to or near extrema and then fill in between extrema with extra rule patches if the rule budget allows.

Fuzzy System Setup

The adaptive SAM fuzzy system used the learning laws (7.9), (7.10), (7.11), (7.12) to learn from the gelatin-backed bullet-armor experimental data. We used the two-dimensional joint factorable sinc function (see Fig. 7.8) for the if-part fuzzy sets A_j.

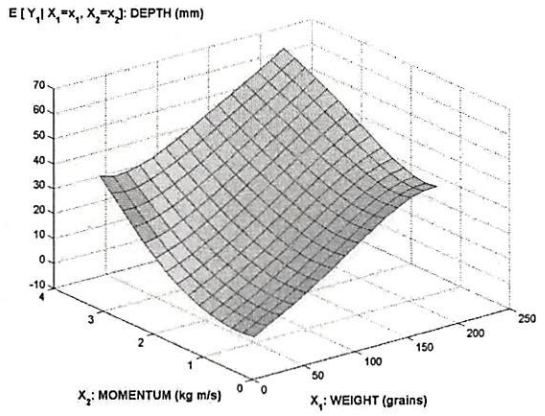

(a) DEPTH: $F_1(x_1, x_2) = E[Y_1|X_1 = x_1, X_2 = x_2]$

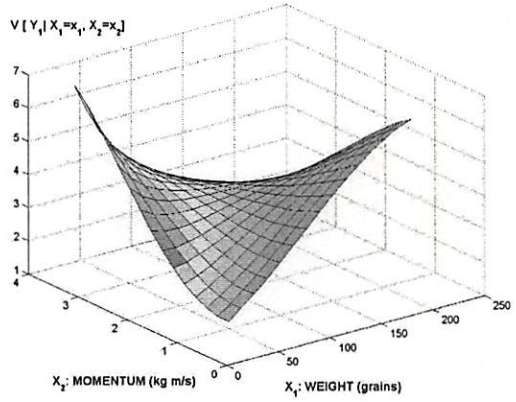

(b) $V[Y_1|X_1 = x_1, X_2 = x_2]$

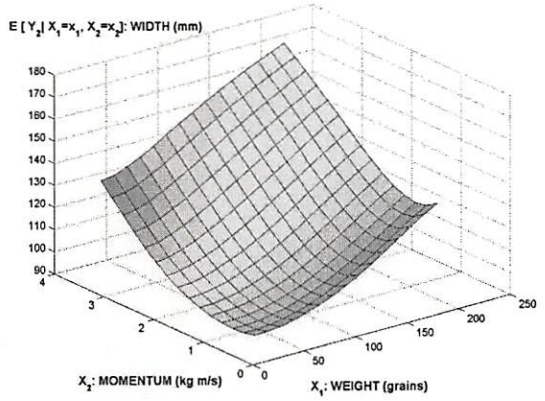

(c) WIDTH: $F_2(x_1, x_2) = E[Y_2|X_1 = x_1, X_2 = x_2]$

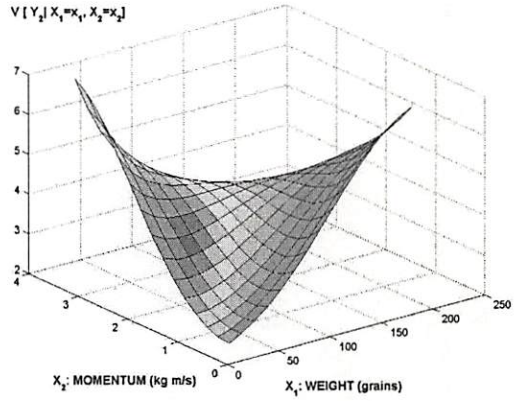

(d) $V[Y_2|X_1 = x_1, X_2 = x_2]$

Figure 7.9: Initial fuzzy system output and conditional variance. An adaptive fuzzy system used two parallel scalar fuzzy systems to model the depth and width (mm) of a bullet-armor deformation given the bullet's weight (grain) and momentum (kilograms meter per second). The output gave the depth and width of the bruise profile. Each surface plots the output against the momentum to the left and the weight to the right. The first-order outputs are the depth in (a) and width in (c). The depth and the width subsystems produced similar surfaces. Both the depth and width increased as the bullet weight and momentum increased. The second-order uncertainties are the conditional variance in (b) and (d) for the depth and width outputs. We picked the initial fuzzy rules based on the correlations in the experimental data (see Table 1) and the fuzzy sets in Table 2. The left and right side rules were less certain because their if-parts covered untested combinations of bullet weight and momentum. So their then-parts had larger set variances and gave larger conditional variances.

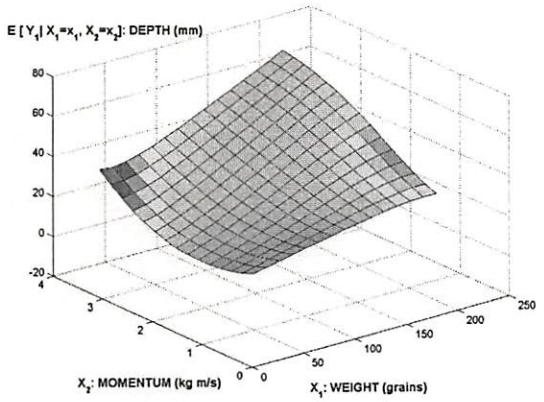

(a) TUNED DEPTH: $E[Y_1|X_1 = x_1, X_2 = x_2]$

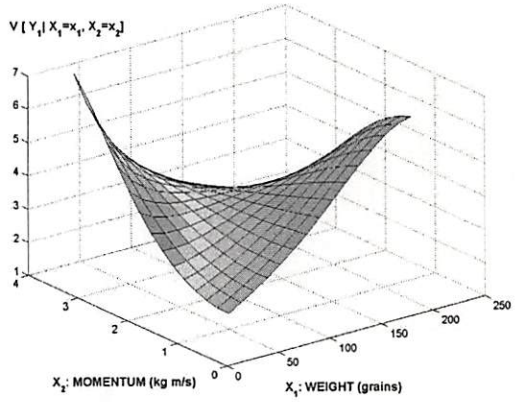

(b) $V[Y_1|X_1 = x_1, X_2 = x_2]$

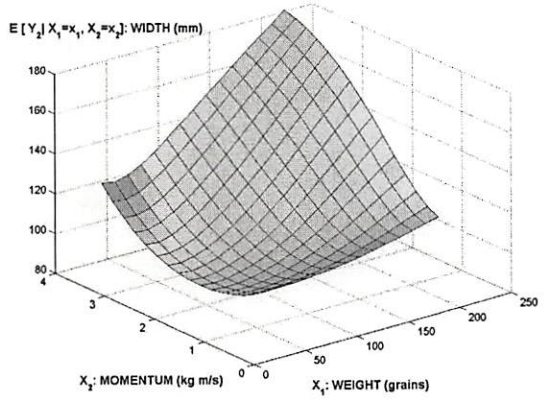

(c) TUNED WIDTH: $E[Y_2|X_1 = x_1, X_2 = x_2]$

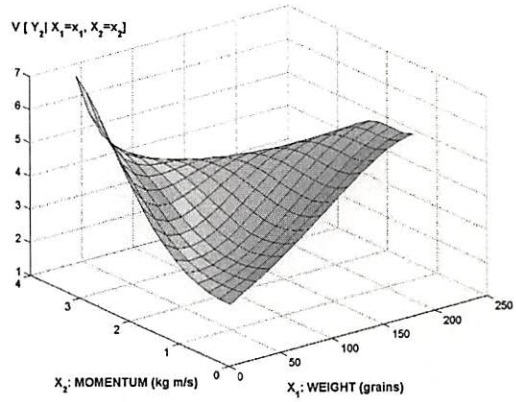

(d) $V[Y_2|X_1 = x_1, X_2 = x_2]$

Figure 7.10: Tuned fuzzy system output and conditional variance. The complete set of experimental data trained the fuzzy system from the initial states in Fig. 3.

Sinc sets often converge faster and with greater accuracy than do triangles, Gaussian bell curves, Cauchy bell curves, and other familiar set shapes [334]. We used scalar Gaussian set functions for the one-dimensional then-part fuzzy sets B_j. This gave the set variance $\sigma^2_{B_j}$ from the then-part set volume V_j : $\sigma^2_{B_j} = V_j^2/2\pi$.

A larger then-part rule volume V_j produced more uncertainty in the j^{th} rule and so should result in less weight. So we weighted each rule with the inverse of its squared volume [252]: $w_j = 1/V_j^2$. This gave the final form of the SAM output F from (7.4)

$$F(x) = \frac{\sum_{j=1}^{m} \frac{a_j(x)}{V_j} c_j}{\sum_{j=1}^{m} \frac{a_j(x)}{V_j}} = \sum_{j=1}^{m} p_j(x) c_j \tag{7.13}$$

A larger volume V_j also gave a larger conditional variance.

We picked the fuzzy system's initial rules according to the observed correlations in Table 7.1: Same-weight bullets hit harder if they were faster. Same-speed bullets hit harder if they were heavier. But heavier and slower handgun bullets can hit harder than some lighter and faster ones. The adaptive SAM system used 49 rules according to Table 7.5. The if-part set functions a_j used center and width parameters to uniformly cover the input space. The then-part set functions b_j used center parameters or centroids c_j that gave an output according to Table 7.5 (a) and (b) and used volume or dispersion parameters in (c) that reflected the uncertainty of the rules. The fuzzy sets in Table 7.5 listed the initial rules that we created based on our experience with ballistics and soft body armor. The volume V_j was a function of the then-part's dispersion or width parameter. A rule was less certain if its if-part covered untested combinations of bullet weight and momentum so its then-part had a larger set variance. Fig. 7.9 shows the fuzzy system's initial first-order output $F(x) = E[Y|X = x]$ and second-order uncertainty $V[Y|X = x]$.

A random resampling scheme selected half of the sparse experimental data as the bootstrapped training set and the remaining half as the test set. A bootstrap scheme [496] sampled the training data with replacement at random to generate 300 sets of input-output data to tune the fuzzy system.

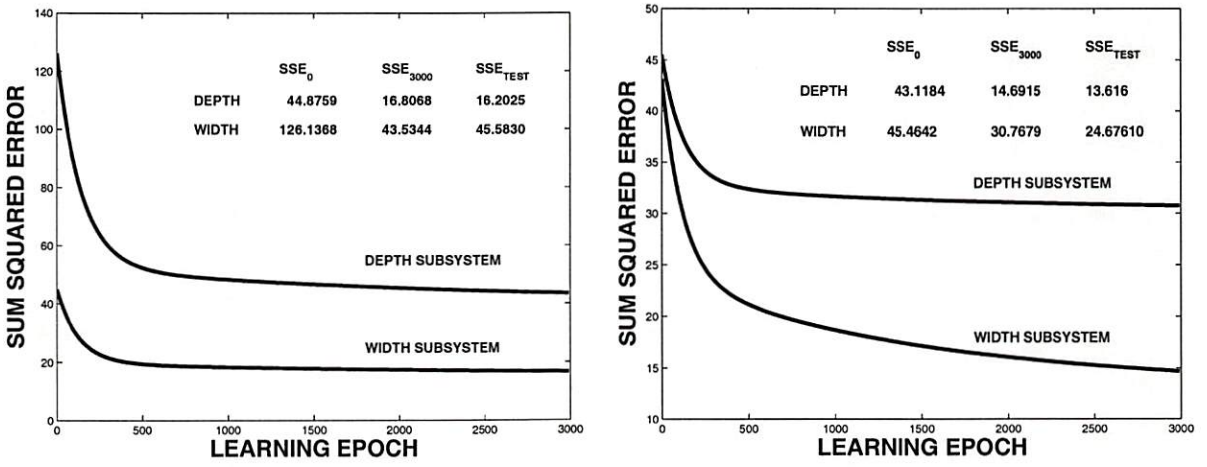

(a) Complete Dataset

(b) Exclude Magnum Data

Figure 7.11: Learning curve. Tuning reduced the fuzzy system's sum squared error (SSE) of the function approximation for two subsets of data: Dataset (a) was complete and Dataset (b) excluded the .357 magnum data. The depth subsystem in (a) reduced its SSE from 45 to 17 over 3000 epochs of learning and had test SSE = 16. The width subsystem in (a) reduced its SSE from 126 to 44 and had test SSE = 46. The depth subsystem in (b) reduced its SSE from 43 to 15 and had test SSE = 14. The width subsystem in (b) reduced its SSE from 45 to 31 and had test SSE = 25.

Fuzzy System Predicts Armor Bruise

We used two sets of the experimental data to train the fuzzy system: Dataset (1) was complete and Dataset (2) excluded the .357-magnum data. Tuning with Dataset (1) reduced the fuzzy system's error function SSE= $\sum_x (f(x) - F(x))^2$ that summed the squared approximation error $f - F$ for 3000 epochs of learning. Fig. 7.10 shows the tuned system output $F(x) = E[Y|X = x]$ and its conditional variance $V[Y|X = x]$. The tuning was effective because the depth subsystem had an initial error of SSE = 45, final error of SSE = 17, and low test error of SSE = 16 and the width subsystem had initial SSE = 126, final SSE = 44, and low test SSE = 46 (see Fig. 7.11(a)).

Tuning with Dataset (2) produced system output $F(x)$ and conditional variance $V[Y|X = x]$ similar to the initial state in Fig. 7.9. The fuzzy system's final SSE

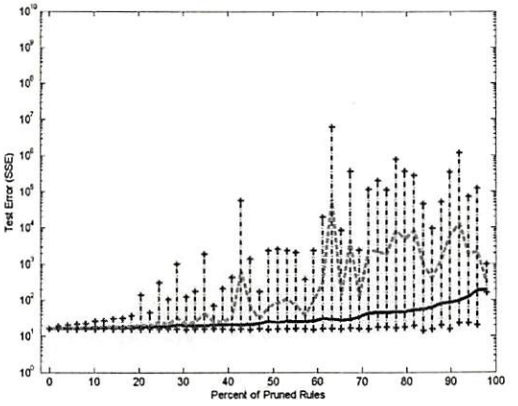

(a) DEPTH RULE PRUNING

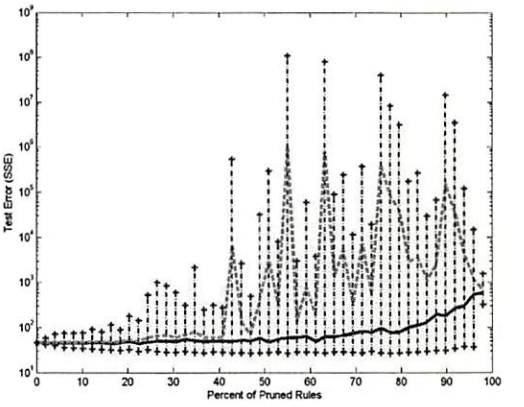

(b) WIDTH RULE PRUNING

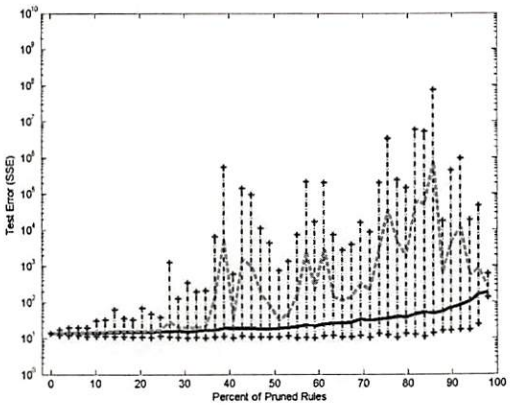

(c) DEPTH EXCLUDE MAGNUM

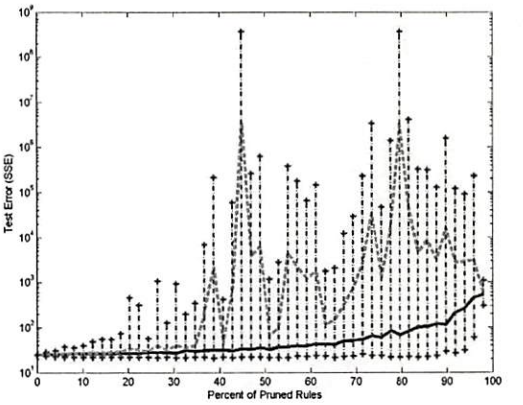

(d) WIDTH EXCLUDE MAGNUM

Figure 7.12: Rule pruning plot shows fuzzy system robustness. The fuzzy system was robust against random pruning. The figure plots the system's test error in log scale versus the percent of pruned depth rules in (a). Similar results hold for random pruning of width rules in (b) and for pruning rules that trained without magnum data in (c) and (d). The vertical bars show the maximal and minimal range of 100 trials. The solid polygonal line interpolates the median of those trials. The dashed line interpolates the mean. The maximal error remained below 100 sum squared error (SSE) for up to 20% of randomly pruned rules. Both the mean and median error remained low for rule losses of up to 35%.

resembled its initial SSE after tuning even though the low test SSE suggested that the tuning was effective: The depth subsystem had an initial error of SSE = 43, final error

of SSE = 15, and test error of SSE = 14 and the width subsystem had initial SSE = 45, final SSE = 31, and test SSE = 25 (see Fig. I.4).

We tested the robustness of the tuned fuzzy system by randomly pruning its rules (see Fig. 7.12). The fuzzy system proved robust both when the learning included the magnum data and when it did not. Pruning randomly removed a fraction of the rules over 100 trials. The depth and the width subsystems gave similar results. The maximal test error remained low (SSE $<$ 100) for random rule loss of up to 20 percent using Dataset (1) and up to 10 percent using Dataset (2). The low test SSE was comparable to the approximation errors in data tuning. Both the mean and the median of the test error remained low for random pruning that removed up to 30 percent of the rules using Dataset (1) and 20 percent using Dataset (2).

I.5 Journal Appendix: Standard Additive Model (SAM) Theorem

This Appendix derives the basic ratio structure (1) of a standard additive model fuzzy system [252], [334].

SAM Theorem: Suppose the fuzzy system $F : R^n \rightarrow R^p$ is a standard additive model: $F(x)$ = Centroid $(B(x))$ = Centroid $(\sum_{j=1}^{m} w_j a_j(x) B_j)$ for if-part joint set function $a_j : R^n \rightarrow [0, 1]$, rule weights $w_j \geq 0$, and then-part fuzzy set $B_j \subset R^p$. Then $F(x)$ is a convex sum of the m then-part set centroids

$$F(x) = \frac{\sum_{j=1}^{m} w_j a_j(x) V_j c_j}{\sum_{j=1}^{m} w_j a_j(x) V_j} = \sum_{j=1}^{m} p_j(x) c_j \tag{7.14}$$

The convex coefficients or discrete probability weights $p_1(x), \ldots, p_m(x)$ depend on the input x through

$$p_j(x) = \frac{w_j a_j(x) V_j}{\sum_{i=1}^{m} w_i a_i(x) V_i} \tag{7.15}$$

V_j is the finite positive volume (or area if $p = 1$) and c_j is the centroid of then-part set B_j

$$V_j = \int_{R^p} b_j(y_1, \ldots, y_p)\, dy_1 \ldots dy_p > 0 \tag{7.16}$$

$$c_j = \frac{\int_{R^p} b_j(y_1, \ldots, y_p)\, dy_1 \ldots dy_p}{\int_{R^p} b_j(y_1, \ldots, y_p)\, dy_1 \ldots dy_p}. \tag{7.17}$$

Proof: There is no loss of generality to prove the theorem for the scalar-output case $p = 1$ when $F : R^n \rightarrow R^p$. This simplifies the notation. We need but replace the scalar integrals over R with the p-multiple or volume integrals over R^p in the proof to prove the general case. The scalar case $p = 1$ gives (7.16) and (7.17) as

$$V_j = \int_{-\infty}^{\infty} b_j(y)\, dy \tag{7.18}$$

$$c_j = \frac{\int_{-\infty}^{\infty} y b_j(y)\, dy}{\int_{-\infty}^{\infty} b_j(y)\, dy} \tag{7.19}$$

Then the theorem follows if we expand the centroid of B and invoke the SAM assumption $F(x)$ = Centroid $(B(x))$ = Centroid $(\sum_{j=1}^{m} w_j a_j(x) B_j)$to rearrange terms

$$F(x) = \text{Centroid}(B(x)) = \frac{\int_{-\infty}^{\infty} y b(y)\, dy}{\int_{-\infty}^{\infty} b(y)\, dy} \tag{7.20}$$

$$= \frac{\int_{-\infty}^{\infty} y \sum_{j=1}^{m} w_j b_j'(y) dy}{\int_{-\infty}^{\infty} \sum_{j=1}^{m} w_j b_j'(y) dy} \tag{7.21}$$

$$= \frac{\int_{-\infty}^{\infty} y \sum_{j=1}^{m} w_j a_j(x)\, b_j(y) dy}{\int_{-\infty}^{\infty} \sum_{j=1}^{m} w_j a_j(x)\, b_j(y) dy} \tag{7.22}$$

$$= \frac{\sum_{j=1}^{m} w_j a_j(x) \int_{-\infty}^{\infty} y b_j(y)\, dy}{\sum_{j=1}^{m} w_j a_j(x) \int_{-\infty}^{\infty} b_j(y)\, dy} \tag{7.23}$$

$$= \frac{\sum_{j=1}^{m} w_j a_j(x) V_j \frac{\int_{-\infty}^{\infty} y b_j(y)\, dy}{V_j}}{\sum_{j=1}^{m} w_j a_j(x) V_j} \tag{7.24}$$

$$= \frac{\sum_{j=1}^{m} w_j a_j(x) V_j c_j}{\sum_{j=1}^{m} w_j a_j(x) V_j} \tag{7.25}$$

I.6 Journal Appendix: Additive Statistics Theorem [252]

Suppose F: $R^n \rightarrow R$ is an additive fuzzy system with scalar output such that $F(x) = \text{Centroid}(B(x))$ and $B(x) = \sum_{j=1}^{m} w_j B'_j(x)$. Then

$$F(x) = E[Y|X = x] = \sum_{j=1}^{m} p_j(x) E_{B'_j}[Y|X = x] \tag{7.26}$$

$$V[Y|X = x] = \sum_{j=1}^{m} p_j(x) V[Y|X = x,\ B'_j] \tag{7.27}$$

the convex coefficients $p_j(x)$ are weighted volume ratios of the "fired" sets B'_j:

$$p_j(x) = \frac{w_j V'_j(x)}{\sum_{k=1}^{m} w_k V'_k(x)} \tag{7.28}$$

where

$$V_j'(x) = \int b_j'(x, y)dy \tag{7.29}$$

Proof: The proof that centroidal fuzzy systems are conditional means follows from the ratio structure of the centroid and the boundedness and non-negativity of the set values $b(x, y) \geq 0$ of the combined set B of "fired" then-part sets B_j. Each input x gives its own $B(x)$ and thus its own output $F(x)$:

$$\begin{aligned} F(x) &= \text{Centroid}(B(x)) && (7.30) \\ &= \frac{\int_{R^p} yb(x, y)dy}{\int_{R^p} b(x, y)dy} && (7.31) \\ &= \int_{R^p} yp(y|x)dy && (7.32) \\ &= E[Y|X = x] && (7.33) \end{aligned}$$

for each $x \in R^n$. This holds because the ratio of the joint distribution to the marginal defines a proper conditional probability density

$$p(y|x) = \frac{b(x, y)}{\int_{R^p} b(x, y)dy} \tag{7.34}$$

even though $b(x,y) > 1$ may hold.

Then we continue the same chain of equalities to show that $F(x)$ is a convex sum of local conditional mean realizations or centroids:

$$F(x) = \frac{\sum_{j=1}^{m} w_j \int_{-\infty}^{\infty} yb_j'(x, y)dy}{\sum_{j=1}^{m} w_j \int_{-\infty}^{\infty} yb_j'(x, y)dy} \tag{7.35}$$

$$= \frac{\sum_{j=1}^{m} w_j \int_{-\infty}^{\infty} b'_j(x,y)dy \frac{\int_{-\infty}^{\infty} y b'_j(x,y)dy}{\int_{-\infty}^{\infty} b'_j(x,y)dy}}{\sum_{j=1}^{m} w_j \int_{-\infty}^{\infty} y b'_j(x,y)dy} \tag{7.36}$$

$$= \frac{\sum_{j=1}^{m} w_j V'_j \int_{-\infty}^{\infty} y b'_j(y|x)dy}{\sum_{j=1}^{m} w_j V'_j} \tag{7.37}$$

$$= \sum_{j=1}^{m} p_j(x) E_{B'_j}[Y|X=x] \tag{7.38}$$

$$= \sum_{j=1}^{m} p_j(x) c'_j \tag{7.39}$$

The variance (covariance) result follows in the same way:

$$V = [Y|X=x] = \frac{\int_{-\infty}^{\infty} (y - E[Y|X=x])^2 b(x,y)dy}{\int_{-\infty}^{\infty} b(x,y)dy} \tag{7.40}$$

$$= \sum_{j=1}^{m} p_j(x) \int_{-\infty}^{\infty} (y - E[Y|X=x])^2 p_{B'_j}(y|x)dy \tag{7.41}$$

$$= \sum_{j=1}^{m} p_j(x) V[Y|X=x,\ B'_j] \tag{7.42}$$

The SAM structure $B'_j(x) = a_j(x)B_j$ simplifies the conditional variance $V_{B'_j}[Y|X = x]$ because the conditional probability density $p_{B'_j}(y|x)$ does not depend on the input x for $a_j(x) > 0$:

$$p_{B'_j}(y|x) = \frac{a_j(x)b_j(y)}{a_j(x)\int_{R^p} b_j(y)dy} \tag{7.43}$$

$$= \frac{b_j(y)}{\int_{R^p} b_j(y)dy} = \frac{b_j(y)}{V_j} = p_{B_j}(y) \tag{7.44}$$

The marginal density $p_{B'_j}(y)$ lets us define the variance of the (implicitly normalized) then-part set B_j:

$$\sigma^2_{B_j} = \int_{-\infty}^{\infty} (y - E_{B_j}[y])^2 p_{B_j}(y)dy \tag{7.45}$$

$$= \int_{-\infty}^{\infty} (y - c_j)^2 p_{B_j}(y)dy \tag{7.46}$$

This holds since the then-part set centroid c_j is just the mean with respect to the j^{th} then-part marginal density $p_{B'_j}(y)$:

$$c_j = \frac{\int_{-\infty}^{\infty} y b_j(y)dy}{\int_{-\infty}^{\infty} b_j(y)dy} \tag{7.47}$$

$$= \int_{-\infty}^{\infty} y p_{B_j}(y)dy \tag{7.48}$$

$$= E_{B_j}[y] \tag{7.49}$$

Then we use these facts to simplify the first-order and second-order conditional statistics of a SAM system. It gives the SAM conditional variance as a convex sum of the local then-part variances plus a global dispersion term.

Corollary (SAM Statistics): The scalar-valued SAM system

$$F(x) = \text{Centroid}(\sum_{j=1}^{m} w_j a_j(x) B_j) \tag{7.50}$$

has conditional mean and variance

$$E[Y|X = x] = F(x) = \sum_{j=1}^{m} p_j(x) c_j \tag{7.51}$$

$$V[Y|X = x] = \sum_{j=1}^{m} p_j(x) \sigma_{B_j}^2 + \sum_{j=1}^{m} p_j(x)(c_j - F(x))^2 \tag{7.52}$$

with convex coefficients

$$p_j(x) = \frac{w_j a_j(x) V_j}{\sum_{k=1}^{m} w_j a_j(x) V_j} \tag{7.53}$$

The second term in (7.52) acts as a penalty term. It is positive if and only if some j^{th} rule fires ($a_j(x) > 0$ and thus $p_j(x) > 0$) and $c_j \neq F(x)$. So it is positive iff the fuzzy system F interpolates to reach the output $F(x)$. Each rule comes with its own output uncertainty $\sigma_{B_j}^2$. Interpolated outputs have more variance than just the sum of these weighted rule variances. Combining two uncertain structures gives a still less certain third structure.

I.7 Journal Appendix: Learning Laws for Scalar and Joint-Factorable If-Part Sets

This appendix derives the learning laws for scalar and joint factorable if-part sets [334]. Supervised gradient descent can tune all the parameters in the SAM (7.4). A gradient descent learning law for a SAM parameter ξ has the form

$$\xi(t+1) = \xi(t) - \mu_t \frac{\partial E}{\partial \xi} \tag{7.54}$$

where μ_t is a learning rate at iteration t. We seek to minimize the squared error $E(x) = \frac{1}{2}(f(x) - F(x))^2$ of the function approximation. The vector function $f : R^n \rightarrow R^p$ has components $f(x) = (f_1(x), \ldots, f_p(x))^T$ and so does the vector function $F(x)$. We consider the case when $p = 1$. A general form for multiple output when $p > 1$ expands the error function $E(x) = \|f(x) - F(x)\|$ for some norm $\|.\|$. Let ξ_j^k denote the k^{th} parameter in the set function a_j. Then the chain rule gives the gradient of the error function with respect to the if-part set parameter ξ_j^k, with respect to the then-part set centroid $c_j = (c_j^1, \ldots, c_j^p)^T$, and with respect to the then-part set volume V_j

$$\frac{\partial E}{\partial \xi_k^j} = \frac{\partial E}{\partial F}\frac{\partial F}{\partial a_j}\frac{\partial a_j}{\partial \xi_k^j}, \frac{\partial E}{\partial c_j} = \frac{\partial E}{\partial F}\frac{\partial F}{\partial c_j}, \text{ and } \frac{\partial E}{\partial V_j} = \frac{\partial E}{\partial F}\frac{\partial F}{\partial V_j} \tag{7.55}$$

where

$$\frac{\partial E}{\partial F} = -[f(x) - F(x)] = -\varepsilon(x) \text{ and } \frac{\partial F}{\partial a_j} = (c_j - F(x))\frac{p_j(x)}{a_j(x)}. \tag{7.56}$$

The SAM ratios (7.4) with inverse-squared-volume rule weights $w_j = 1/V_j^2$ give

$$\frac{\partial F}{\partial c_j} = \frac{a_j(x)/V_j}{\sum_{j=1}^{m} a_j(x)/V_j} = p_j(x) \tag{7.57}$$

$$\frac{\partial F}{\partial V_j} = -\frac{p_j(x)}{V_j}(c_j - F(x)) \tag{7.58}$$

Then the learning laws for the then-part set centroids c_j and volumes V_j have the form

$$c_j(t+1) = c_j(t) + \mu_t \varepsilon_t(x) p_j(x) \tag{7.59}$$

$$V_j(t+1) = V_j(t) - \mu_t \varepsilon_t(x) \frac{p_j(x)}{V_j} [c_j - F(x)] \tag{7.60}$$

The learning laws for the if-part set parameters follow in like manner for both scalar and joint sets as we show below. Chain rule gives for scalar sinc set function

$$\frac{\partial E}{\partial m_j^k} = \frac{\partial E}{\partial F}\frac{\partial F}{\partial a_j}\frac{\partial a_j}{\partial m_j^k} \text{ and } \frac{\partial E}{\partial d_j^k} = \frac{\partial E}{\partial F}\frac{\partial F}{\partial a_j}\frac{\partial a_j}{\partial d_j^k} \tag{7.61}$$

A joint factorable set function $a_j(x) = a_j^1(x) \dots a_j^n(x)$ leads to a new form for the error gradient. The gradient with respect to the parameter of the j^{th} set function a_j has the form

$$\frac{\partial E}{\partial m_j^k} = \frac{\partial E}{\partial F}\frac{\partial F}{\partial a_j}\frac{\partial a_j}{\partial a_j^k}\frac{\partial a_j^k}{\partial m_j^k} \text{ where } \frac{\partial a_j}{\partial a_j^k} = \prod_{i \neq k}^{n} a_j^i(x_i) = \frac{a_j(x)}{a_j^k(x_k)}. \tag{7.62}$$

Combining (7.54), (7.55), (7.61), and (7.62) gives the if-part learning laws:

$$\begin{aligned} m_j^k(t+1) = & \quad m_j^k(t) \\ & + \mu_t \varepsilon_t \frac{p_j(x)}{a_j(x)} \frac{a_j(x)}{a_j^k(x_k)} (c_j - F(x))(a_j(x) - \cos(\tfrac{x - m_j^k(t)}{d_j(t)})) \tfrac{1}{x - m_j^k(t)} \end{aligned} \tag{7.63}$$

$$\begin{aligned} d_j^k(t+1) = & \quad d_j^k(t) \\ & + \mu_t \varepsilon_t \frac{p_j(x)}{a_j(x)} \frac{a_j(x)}{a_j^k(x_k)} (c_j - F(x))(a_j(x) - \cos(\tfrac{x - m_j^k(t)}{d_j(t)})) \tfrac{1}{d_j^k(t)}. \end{aligned} \tag{7.64}$$

I.8 Journal Appendix: Hypothesis test for simple linear regression

This section reviews the hypothesis test whether the slope term of a simple linear regression equation has a certain value c: $\mathbf{H}_0 : \beta_1 = c$ versus $\mathbf{H}_a : \beta_1 \neq c$ [392]. The *simple* linear regression model for n observations has the form

$$y = \beta_0 + \beta_1 x + \epsilon \tag{7.65}$$

where the independent variable x, dependent variable y, and error term ϵ are $n \times 1$ vector representations of the n observations. The prediction equation

$$y = \hat{\beta}_0 + \hat{\beta}_1 x \tag{7.66}$$

uses the least squares estimators

$$\hat{\beta}_1 = \frac{\sum_{i=1}^{n} (x_i - \bar{x})(y_i - \bar{y})}{\sum_{i=1}^{n} (x_i - \bar{x})^2} \tag{7.67}$$

$$\hat{\beta}_0 = \bar{y} - \hat{\beta}_1 \bar{x}. \tag{7.68}$$

The test statistic is

$$t = \frac{\hat{\beta}_1 - c}{s / \sqrt{\sum_{i=1}^{n} (x_i - \bar{x})^2}}. \tag{7.69}$$

where

$$s^2 = \frac{SSE}{n-2} \text{ and } SSE = \sum_{i=1}^{n} (y_i - \hat{y}_i)^2 \tag{7.70}$$

The test rejects the null hypothesis $\mathbf{H}_0$ if the test statistic $|t| \geq t_{\alpha/2,n-2}$. We note that t has a noncentral distribution $t(n-2,\delta)$ with noncentrality parameter δ that has the form

$$\delta = \frac{E(\hat{\beta}_1)}{\sqrt{var(\hat{\beta}_1)}} = \frac{\beta_1}{\sigma / \sum_{i=1}^{n} (x_i - \bar{x})^2}. \tag{7.71}$$

The hypothesis test for $\mathbf{H}_0 : \beta_1 = 0$ versus $\mathbf{H}_a : \beta_1 \neq 0$ can use (7.69)–(7.71) for $c = 0$ and $\delta = 0$.

I.9 Journal Appendix Multiple Regression Analysis and the Dummy Variable Approach (Gujarati-Chow test)

Multiple regression [389] can compare two groups with unequal numbers of samples. The dummy variable approach [189] can compare the two groups' linear regression coefficients to see whether they have different intercepts, different slopes, or both. This modifies the Chow test [85] that tests whether both the intercepts and slopes differ between the two groups.

The Gujarati-Chow test is a multiple regression analysis that uses a dummy variable D [189], [389] to create interaction terms. The test concatenates the data from the two groups and uses the binary dummy variable D to determine whether a data sample belongs to Group A or Group B:

$$D = \begin{cases} 1 & \text{if the observation lies in Group A} \\ & \text{(of } N_1 \text{ observations).} \\ 0 & \text{if the observation lies in Group B} \\ & \text{(of } N_2 \text{ observations).} \end{cases}$$

The dummy-variable regression equation has the form

$$y = a_0 + a_1 D + a_2 x + a_3 (Dx) \tag{7.72}$$

where x is the independent variable and y is the dependent variable for both groups of data. The dummy variable D is in both an additive and a multiplicative forms. The constants a_1 and a_3 are the *differential intercept* and *differential slope* coefficients. The Gujarati-Chow test performs a multiple linear regression and can test two null hypothesis: $\mathbf{H}_0^{a_1} : a_1 = 0$ and $\mathbf{H}_0^{a_3} : a_3 = 0$.

The intercept value of Group A's data is $a_1 + a_0$ if a_1 is statistically significant then a_0 is the intercept value of Group B's data in this case. Else a_0 estimates the intercept term of both groups of data if a_1 is statistically insignificant (large p-value).

The slope of Group A's data is $a_3 + a_2$ if a_3 is statistically significant then a_2 is the slope of Group B's data in this case. Else a_2 estimates the slope term of both groups of data if a_3 is statistically insignificant (large p-value). The additive and multiplicative dummies give whether two linear regressions differ either in the intercept or the slope or both.

We want to test the null hypothesis $\mathbf{H}_0$ that the two regression slopes are identical for the bullet-armor impact data (Group A) and the baseball impact data (Group B). This tests the hypothesis $\mathbf{H}_0 : a_3 = 0$ versus $\mathbf{H}_a : a_3 \neq 0$. The hypothesis test retains the null hypothesis for a high p-value: a_3 is not statistically significant and a_2 estimates the slope term of both the bullet-armor data and the baseball data.